



Vacuum evaporation of pharmaceutical molecules for the creation of medically active nanostructures with enhanced activities



Dissertation

Zur Erlangung des akademischen Grades

Doktor der Ingenieurwissenschaften

(Dr.-Ing.)

der Technischen Fakultät

der Christian-Albrechts-Universität zu Kiel

Eman Zarie

Kiel 2013

1. Gutachter: Prof. Dr. Rainer Adlung

2. Gutachter : Prof. Dr. Hartwig Steckel

(ggf.3. Gutachter)

Datum der mündlichen Prüfung: 5.07.2013

Self Declaration

I hereby declare that the work represented in this PhD thesis is my own except some cited sources.

I declare that this thesis: **“Vacuum evaporation of pharmaceutical molecules for the creation of medically active nanostructures with enhanced activities”** has not been prepared with any illegal help. I also assert that other authors’ contributions used in the thesis or led to some ideas in it are properly referenced in written form. I am aware that a PhD thesis, developed under guidance, is part of the examination and may not be commercially used or transferred to a third party without written permission from my supervising professor.

Kiel,

.....

Signature

Acknowledgements

First and foremost, thanks are due to Allah, the Almighty, for giving me health, time and patience to complete this PhD thesis.

I would like to express my deepest gratitude to my supervisor, **Prof. Dr. Rainer Adelung** for his guidance, ideas, encouragement, and understanding. His consistent and considerate support, insight advice, fruitful scientific discussions, generosity in sharing his expertise helped me throughout the development of this work and made it all possible. I am also grateful to him for warm welcome and help during my stay in Germany, the very thing that I will never forget. His supervision not only improved my research abilities but also broadened my view and my interest in the field of science and nano-science.

Also, I would like to express my heartiest thanks to **Prof. Dr. Hartwig Steckel** (Director of the Pharmaceutics and Biopharmaceutics, Christian Albrechts University Kiel) for his efforts, guidance, ideas, encouragement, and understanding. I honestly state that this thesis wouldn't have been possible without his modifications, continuous encouragement, enthusiasm, and innovative ideas.

I wish to thank **Dr. Franz H. Furkert**, and **Dr. Regina Scherließ** who have initiated this project and provided experimental facilities, chemicals and technical guidance on biological applications. This biological screening of this research project has been conducted by **Prof. Dr. Hartwig Steckel**, **Dr. Franz H. Furkert**, and **Dr. Regina Scherließ** at the Department of Pharmaceutics and Biopharmaceutics, Christian Albrechts University Kiel.

Also, I would like to express my heartiest thanks to **Prof. Dr. Franz Faupel** and **Prof. Dr. Mady Elbahri** for their invaluable support and for allowing me to work in their laboratories.

I am grateful to thank **Dr. Yogendra K. Mishra** and **Dr. Seid Jebril** for their assistance, fruitful scientific discussions and support in several descriptive studies as well as in Laboratory experiments. My sincere gratitude is directed to **MSc. Dawit Gedamu** for his cooperation in measuring field effect transistor and electrical current. My deep thanks are to **Dr.-Ing. Sebastian Wille** and **Dr. Dipl. -Ing. Kristina Schlüter** for teaching me how to use atomic force microscopy.

I would like to express my genuine appreciation to engineers **Dipl.-Ing. Stefan Rehders** and **Dipl.-Ing. Christoph Ochmann** who construct the deposition chamber and solve technical problems. Also, thanks are to **Dipl.-Ing. Rainer Kloth** and **Christian Neue** for computer support. My sincere gratitude is to our secretaries **Dipl.-Geol. Beate Minten**, **Mrs. Christiane Otte-Hüls**, **Dipl.-Chem. Sieglinde Kastaun** and for their help concerning official work. I thank **Dipl.-Min. Marlies Schwitzke** for teaching me how to use the scanning electron microscopy. It is a pleasure for me to express my sincere thanks to **Prof. Dr. Klaus Raetzke** for teaching me how to use the X-Ray Diffraction.

Special thanks to **MSc. Ramzy Abdelaziz** for his kind help performing certain measurements (SEM) for my thesis.

I also thank all members in the group of Functional Nanomaterials and Multicomponent Materials who helped me in completing my thesis successfully and in creating a very good working atmosphere. I would like to thank **hiwi** students who did many of the experiments during their master and bachelor thesis: **MSc. Charline Wolpert** and **MSc. Viktor Kaidas**.

Certainly, I greatly appreciate the financial support extended to me by the **Egyptian government**. I am very thankful to **my professors** in National Research Centre, Dokki, Cairo, Egypt, for encouraging and motivating me throughout my study.

I would like to express my utmost gratitude and debt towards my **brothers and sisters** whose continuous love, help, patience and encouragement motivated me to overcome all the obstacles to complete my work.

I dedicate this thesis to my father Said Zarie and my mother for they have supported me with their prayers and motivation the whole way through from Egypt.

Special thanks to **Duygu Disci** for being good friend of mine.

Finally, I wish to express my sincere gratitude to **my husband Ramzy** and **my kids** who were patient and encouraging, and without whose unending support and assistance this work would have never been brought into light.

Table of Contents	Page
Acknowledgements	i
List of Figures.....	xii
List of Tables	xxii
Chapter 1	1
1 Introduction.....	1
Chapter 2	5
2 Theoretical Considerations	5
2.1 Limitations of Techniques for Solubility Enhancement	5
2.2 Vacuum deposition	8
2.2.1 Thermal evaporation	9
2.2.1.1 Thermal evaporation of organic materials	9
2.2.1.2 Evaporation of Metals by vacuum deposition	11
2.2.2 Sputter Deposition	14
2.3 Growth mechanism	16
2.4 Growth mechanism equations.....	18
2.5 Nanotechnological aspects.....	20
2.6 Potential applications of thermal evaporation in medical science	22
2.6.1 Stents.....	22
2.6.2 Biofilm formation as microbial development.....	24
Chapter 3	27
3 Characterization Techniques.....	27
3.1 Light Microscopy.....	27
3.2 Atomic force microscopy (AFM)	29
3.2.1 Probe-sample interaction	31
3.2.2 Contact Mode.....	31
3.2.3 Non-contact Mode	32
3.3 Scanning electron microscopy (SEM)	33
3.3.1 Basic principle	33
3.3.2 Instrumentation	34
3.3.3 Interaction volume	37
3.4 Energy Dispersive X-Ray Analysis	39
3.5 Raman Spectroscopy (RS)	40

3.6 X-Ray Diffraction (XRD).....	43
3.7 Profilometer	46
Chapter 4	48
4 Experimental part.....	48
4.1 Introduction.....	48
4.2 Evaporation chamber	48
4.3 Evaporation of Materials.....	50
4.3.1 Evaporation of active selected pharmaceutical molecules.....	50
4.3.2 Evaporation of polymer	58
4.4 Biological screening of vacuum deposited pharmaceutical molecules.....	58
4.5 Current-Voltage (FET) Response	59
4.6 Analysis by Optical, Atomic Force, Scanning Electron and Raman Microscopies	60
Chapter 5	64
Results and Discussions	64
5.1 Results	68
5.1.1 Structural engineering of Parabens	68
5.1.1.1 Optical microscopy results of Nipasol nano-microstructures	68
5.1.1.2 AFM of Nipasol	69
5.1.1.3 SEM of Nipasol.....	71
5.1.1.4 Raman spectrum of Nipasol.....	71
5.1.1.5 Raman spectrum of Nipagin	72
5.1.2 Structural engineering of Pilocarpine-HCl	74
5.1.2.1 Optical microscopy of Pilocarpine-HCl.....	74
5.1.2.2 SEM of Pilocarpine-HCl.....	75
5.1.2.3 Raman Spectroscopy of Pilocarpine-HCl	75
5.1.2.3.1 Raman Spectroscopy of Pilocarpine-HCl on Ti.....	75
5.1.2.3.2 Raman Spectroscopy of Pilocarpine-HCl on polymer foil	76
5.1.3 Structural engineering of Pindolol	77
5.1.3.1 Optical microscopy of Pindolol nano-microstructures	77
5.1.3.2 AFM of Pindolol nano-microstructures	78
5.1.3.3 Raman Spectroscopy of Pindolol nano-microstructures.....	79
5.1.3.3.1 Raman Spectroscopy of Pindolol nano-microstructures on Ti	79
5.1.3.3.2 Raman Spectroscopy of Pindolol deposited on Si	79

5.1.4 Structural engineering of 5-Fluorouracil	81
5.1.4.1 Optical spectroscopy of 5-Fluorouracil	81
5.1.4.2 AFM of 5- Fluorouracil	81
5.1.4.3 Raman microscopy of 5-Fluorouracil nano- microstructures	82
5.1.5 Structural engineering of Chloramphenicol.....	84
5.1.5.1 Optical spectroscopy of Chloramphenicol.....	84
5.1.5.2 Raman spectroscopy of Chloramphenicol nano-microstructures	86
5.1.6 Structural engineering of Tetracaine-HCl.....	88
5.1.6.1 SEM of Tetracaine-HCl nano-microstructures	88
5.1.6.2 AFM of Tetracaine-HCl nanomicrostructures	90
5.1.6.3 Raman Spectroscopy of Tetracaine-HCl	90
5.1.6.4 EDX Results of Tetracaine-HCl nano-microstructures with silver and gold.....	92
5.1.7. Structural engineering of Acetyl Salicylic acid	93
5.1.7.1 SEM of Acetylsalicylic acid	93
5.1.7.2 AFM of Acetylsalicylic acid.....	94
5.1.7.3 Raman spectrum of Acetylsalicylic acid.....	94
5.1.8 Structural engineering of Metronidazole	95
5.1.8.1 SEM of Metronidazole.....	95
5.1.8.2 AFM of Metronidazole nano-microstructures	95
5.1.8.3 Raman spectrum of Metronidazole.....	96
5.1.9 Structural engineering of Clotrimazole.....	97
5.1.9.1 Optical Light Spectrum of Clotrimazole nano-microstructures.....	97
5.1.9.2 AFM of Clotrimazole nano-microstructures.....	98
5.1.9.3 SEM of Clotrimazole nano-microstructures	98
5.1.9.4 Raman Spectrum of Clotrimazole nano-microstructures.....	99
5.1.10 Structural engineering of Trimethoprim	100
5.1.10.1 AFM of Trimethoprim nano-microstructures	100
5.1.10.2 Raman spectrum of Trimethoprim nano-microstructures.....	101
5.1.10.3 XRD Spectrum of Trimethoprim nano-microstructures	103
5.1.11 Structural engineering of Sulphathiazole.....	104
5.1.11.1 AFM of Sulphathiazole nano-microstructures.....	104
5.1.12 Characterization of Tetracycline-HCl nano-microstructures.....	105
5.1.12.1 AFM of Tetracycline-HCl nano-microstructures.....	105

5.1.13 Structural engineering of Erythromycin	105
5.1.13.1 AFM of Erythromycin nano-microstructures	105
5.1.14 Structural engineering of Tobramycin	106
5.1.14.1 AFM of Tobramycin nano- microstructures	106
5.1.15 Structural engineering of Ascorbic acid	107
5.1.15.1 SEM of Ascorbic acid nano-microstructures	107
5.1.16 Characterization of Adipic acid nano-microstructures	108
5.1.16.1 SEM of Adipic acid micro-nanostructures	108
5.1.16.2 Raman Spectrum of Adipic acid nano-microstructures	109
5.1.17 Structural engineering of Caffeine.....	110
5.1.17.1 SEM of Caffeine nano-microstructures	110
5.1.17.2 Raman spectrum of Caffeine nano-microstructures	110
5.1.18 Structural engineering of Cholesterol	112
5.1.18.1 SEM of Cholesterol nano-microstructures.....	112
5.1.18.2 Raman-spectra of Cholesterol nano-microstructures.....	113
5.1.19 Structural engineering of SM nano-microstructures.....	114
5.1.19.1 Optical image of SM nano-micro structures.....	114
5.1.19.3 AFM of SM nano-microstructures.....	115
5.1.20.1 SEM image of PLGA.....	116
5.1.21 Structural engineering of Indometacin.....	117
5.1.21.1 SEM of Indometacin nano-microstructures.....	117
5.1.21.2 Raman spectrum of Indometacin nano-microstructures.	117
5.1.22 Structural engineering of multilayers.....	119
5.1.22.1 Characterization of two layers	119
5.1.22.2 Characterization of (4 Layers)	120
5.2 Discussion.....	120
5.2.1 Control over the crystallinity of the deposited drug films and their morphology	120
5.2.2 Time-related Process.....	125
5.2.3 Temperature-related Process.....	128
5.2.4 Control over the lateral structuring of the deposited drug films	130
5.2.5 Characterisation of chemical composition and Raman shifting	131
5.3.6 Sequential deposition: Multilayers of different drugs and hybrid materials	137

Chapter 6	143
6-Application of Thermal Evaporation.....	143
6.1 Antimicrobial screening:.....	143
6.2 Controlled drug release from biodegradable polymers.....	151
6.3 Thermal evaporation for enhanced activities.....	152
6.4 Pharmaceutical field effect transistor (PFET).....	153
6.5 Room Temperature Current - Voltage Characteristic.....	155
6.6 The unique requirements of thermal evaporation	156
Chapter 7	158
7 Summary and Outlook	158
Bibliography	i

List of Figures

Chapter 2

Figure 2.1: Setup for thermal evaporation of organic materials.	10
Figure 2.2: The sketch shows the metal evaporator with a power feed through (a), and both the external (b) and the internal (c) part of the metal evaporator cell.	12
Figure 2.3: (a) Crucible rack for thermal evaporation, (b) Target material distribution from a small area source, (c) Distribution of evaporated material following cosine-law. (These images were taken from the following website, http://www.ep4.rub.de/imperia/md/content/skripte/ss04/thinfilmmagnetism/hcs.pdf).	14
Figure 2.4: Picture of magnetron sputtering chamber a) outer part b) inner part, the numbers in the inside chamber correspond to parts of the (1) Pt magnetron (2) Copper magnetron (3) quartz monitors (4) sample holder.	16
Figure 2.5: Thin film growth mechanisms. (a): Volmer-Weber (island) growth, (b): Frank-van-der-Merwe (layer-by-layer) growth, (c): Stranski-Krastanov growth	18
Figure 2.6: The growth mechanism of a thin film layer through evaporation of molecules is demonstrated schematically.	20
Figure 2.7: shows the differing patterns of restenosis and in- stent restenosis (ISR). (source of this image in website: cvi.med.nyu.edu).....	22
Figure 2.8: Pathophysiology of in-stent restenosis and the mechanisms of action of different therapeutic agents . (Abbreviations: ECM, extracellular matrix; SMC, smooth muscle cells).....	23
Figure 2.9: Schematic representation of biofilm formation	25

Chapter 3

Figure 3.1: Optical microscope: (a) optical path of the light beam in an optical microscope, (b) Picture of a typically optical microscope.....	29
Figure 3.2: Schematic representation of general components of an AFM and their function (a), the inset shows the close view of the tip-surface interaction. The tip-effect (b) and the force-displacement curve (c) are also shown.	30

Figure 3.3: Sketch depicting contact mode (a) and noncontact mode (b) of the AFM.	33
Figure 3.4: Schematic diagram of a scanning electron microscope (a), and Ray paths in SEM; standard arrangement for image formation (b)	34
Figure 3.5: Schematic diagram illustrating the volume of material that is probed by an incident electron beam together with the volumes from which x-rays and backscattered, Auger and secondary electrons emanates.	38
Figure 3.6: EDX spectra of the as-synthesized Tetracaine-HCl with Ag which confirms the presence of Cl, C, O, N as well as Ag.	39
Figure 3.7: Schematic of the sample, incident light and collection optics in The Raman spectrometer where illumination and collection are performed through microscope objective.	40
Figure 3.8: Three types of scattering by a molecule are excited by a photon with energy $E = h\nu$. The most common transition is marked with bold arrows.	43
Figure 3.9: The sketch shows the schematic diagram of the setup for XRD and Schematic of incoming x-rays diffracted at lattice planes under a specific angle fulfilling Bragg's law.....	45
Figure 3.10: The sketch shows Dektak 8000 profilometer (Veeco) (a), and diamond tip scanning over the surface of the sample (b).	47

Chapter 4

Figure 4.1: Schematic showing the deposition chamber used for thin film preparation: photo (a) and inner part of evaporation chamber(b).....	49
Figure 4.2: Photographs of the evaporator. In the middle the fitting for the crucible is situated. The crucible itself is shown in (b) and (c) with its dimensions tagged.	49
Figure 4.3: Illustrated the optical image of titanium substrate before deposition (a) and the growth of thin film by vapour deposition on titanium plate (b).....	57
Figure 4.4: This is a photo of the microchip holder device which was used to measure the electrical properties of various pharmaceutical molecules. The inset (top left) shows the microchip consists of horizontal organic molecules at each of the contact junctions, and the number refers to the contact points.....	60

Chapter 5

- Figure 5.1:** (a-d) Optical images of various Nipasol micro-nanostructured morphologies on different substrates like Ti (a) Si pre-coated with 8 nm thick Au thin film (b), glass (c), polymer foil (d), Si Pre-coated with ZnO 50 nm thick thin film (e and f) respectively..... 68
- Figure 5.2:** Three-dimensional AFM height image of Nipasol grown on Ti substrate at various substrate temperatures ranging from -100 °C with different magnifications (a-b) to room temperature (c)..... 69
- Figure 5.3:** Two-dimensional AFM height image of Nipasol on Ti substrate at different evaporation temperatures @ ~ 165 °C (10 min) (a) and @ ~ 220°C (27 min)(b). 70
- Figure 5.4:** SEM images of Nipasol deposited on ZnO nanostructures at different magnifications (a and b) and microspheres on titanium substrate with substrate temperature at -100 °C (c)..... 71
- Figure 5.5:** The Raman spectrum of Nipasol control sample. The inset shows the optical microscope image of the control sample..... 72
- Figure 5.6:** The Raman spectrum of Nipasol deposited sample. The inset shows the optical microscope image of the deposited sample..... 72
- Figure 5.7:** The Raman spectrum of Nipagin control sample. The inset shows the optical microscope image of the control sample..... 73
- Figure 5.8:** The Raman spectrum of Nipagin deposited sample. The inset shows the optical microscope image of the deposited sample..... 73
- Figure 5.9:** a-e Representative optical images of various pilocarpine-HCl micro or nano structured morphologies on different substrates like polymer foil (a), glass (b), Ti (c), soft contact lens (d), copper grid on Ti substrate (e) and large grains size deposited on ZnO substrate (f)..... 74
- Figure 5.10:** (a-c) SEM images of Pilocarpine-HCl micro-nanostructures grown on Si pre-coated with 50 nm thickness ZnO thin film with different magnifications..... 75
- Figure 5.11:** Example of Raman identification (green: spectrum of Pilocarpin-HCl raw material, red: spectrum of Pilocarpine-HCl layer vacuum deposited on titanium carrier)..... 76
- Figure 5.12:** Raman-spectrum and optical microscope image (inset) of Pilocarpine-HCl reference drug..... 77

Figure 5.13: Pilocarpine-HCl sample after deposition on polymer foil with its optical image(inset) and Raman-spectrum.	77
Figure 5.14: Both optical images show deposited Pindolol on polymer foil (a) and Ti substrate (b) respectively.	78
Figure 5.15: a-b Two- and three dimensional AFM (non contact mode) images of Pindolol nano-microparticles deposited on Ti substrate.....	78
Figure 5.16: Raman identification (red: spectrum of Pindolol raw material, blue: spectrum of Pindolol layer vacuum deposited on Ti carrier).....	79
Figure 5.17: The Raman spectrum of Pindolol control sample. The inset shows the optical microscope image of the control sample.....	80
Figure 5.18: Raman-spectrum with its appropriate optical image (inset) of Pindolol sample after deposition.	80
Figure 5.19: Optical images of 5-Fluorouracil with (a) 20 x and (b) 50 x magnification grown on titanium substrate that show crystallization process after thermal evaporation deposition.....	81
Figure 5.20: Two-dimensional AFM height images of 5-Fluorouracil on Ti substrate with a scan area of (a) 5 x 5 μm^2 , (b) 1 x 1 μm^2 . Also, three-dimensional AFM height image of Fluorouracil on Ti is shown with a scan area of 1 x 1 μm^2 and a maximum height of 0.1 μm	82
Figure 5.21: Raman spectrum and optical image (inset) of 5- Fluorouracil reference drug.	83
Figure 5.22: Raman spectrum and optical image (inset) of 5- Fluorouracil after deposition.....	83
Figure 5.23: (a) and (b): Images for different positions on the sample show Chloramphenicol deposited on glass illustrated with a magnification of 10 x. Images were taken 1 min after evaporation. Images (c) and (d) were taken 3h after evaporation. They show different positions on glass sample with droplets of deposited Chloramphenicol. The magnification is 10 x.....	84
Figure 5.24: Chloramphenico microstructures deposited on glass substrate after 1 day (10 x magnification)(a, and b) after 2 days (c).	85
Figure 5.25: Optical micrographs show the initial specific area of Chloramphenicol on glass after 10 days (a) and its higher surface area Blossom-like crystalline structure after heating 1 h at 100 °C on glass at lower and higher magnification b and c	

respectively. Chloramphenicol on polymer foil appears after 1 month (d). b) after 2 days (c).....	85
Figure 5.26: Raman spectrum and optical image (inset) of Chloramphenicol reference drug.	86
Figure 5.27: Raman spectrum and optical image (inset) of Chloramphenicol deposited drug directly after evaporation.	87
Figure 5.28: Raman-spectrum and optical image (inset) of deposited Chloramphenicol sample after a certain time.	87
Figure 5.29: a-h Representative SEM images of various Tetracaine-HCl nanostructures morphologies grow on different substrates: Silicon wafer at higher temperature (a), Silicon wafer at lower temperature (b), Titanium substrate(c), Silicon coated with 20 nm Au thin film (d), Silicon coated with 4 nm Au thin film(e) co-deposition of Tetracaine-HCl with Ag on silicon wafer(f) and Ti substrate (g) and co-deposition of Tetracaine-HCl with Au on Si substrate(h) The inset is a high-magnification SEM images.....	89
Figure 5.30: Two-dimensional AFM height image of Tetracaine-HCl on Ti. The scan area is about 20 μm x 20 μm	90
Figure 5.31: The Raman spectrum of Tetracaine-HCl control sample. The inset shows the optical microscope image of the control sample.....	91
Figure 5.32: Tetracaine-HCl sample is shown after deposition with its appropriate optical image (inset) and Raman-spectrum.....	91
Figure 5.33: EDX spectrum of co- deposition of Tetracaine-HCl nanostructures with Ag by thermal evaporation.....	92
Figure 5.34: EDX spectrum of co-deposition of Tetracaine-HCl nanostructures with Au by thermal evaporation.....	92
Figure 5.35: Representative SEM images of Acetylsalicylic acid grown on Ti substrate (a, b) and through a copper grid as micro scale shadow mask (c, d) with different magnifications.	93
Figure 5.36: Two-and-three dimensional image of the topography of Acetylsalicylic acid with a scan area of 10 x 10 μm^2	94
Figure 5.37: Microscopic images of Acetylsalicylic acid deposited on Ti substrate and copper grid through a microscopic shadow mask (a, b) respectively and Raman spectra of the deposited and reference Acetylsalicylic acid (c).....	94

Figure 5.38: a-c SEM images of Metronidazole nano-microstructures fabricated on titanium substrate with different magnifications.	95
Figure 5.39: AFM 2D and 3D images of Metronidazole deposited on glass substrate with a scan area of (a, b) $10 \times 10 \mu\text{m}^2$	95
Figure 5.40: The reference sample of Metronidazole with optical microscope image (inset) and its Raman spectrum.....	96
Figure 5.41: Metronidazole sample after deposition with its appropriate optical image (inset) and Raman-spectrum.	97
Figure 5.42: Optical images of Clotrimazole micro-nanostructures deposited on Si coated with ZnO nanostructures (a) and Ti substrate (b).....	97
Figure 5.43: Two-dimensional and three-dimensional AFM height images of Clotrimazole growing on Ti (a and b) and two-dimensional AFM of clotrimazole on glass substrate(c).	98
Figure 5.44: SEM images of Clotrimazole deposited on Ti substrate.	99
Figure 5.45: The reference sample of Clotrimazole with optical image (inset) and its Raman-spectrum.	99
Figure 5.46: Clotrimazole sample after deposition with its appropriate optical image (inset) and Raman-spectrum.	100
Figure 5.47: Two dimensional AFM and a three-dimensional AFM height image of Trimethoprim on Ti with different scan area of $10 \times 10 \mu\text{m}^2$ (a-b) and $6 \times 6 \mu\text{m}^2$ (c-d)	101
Figure 5.48: The reference sample of Trimethoprim shows optical image (inset)) with its Raman-spectrum.	102
Figure 5.49: Trimethoprim sample after deposition with appropriate optical image (inset) and it's Raman-spectrum.	102
Figure 5.50: XRD pattern of Trimethoprim deposited on glass substrate at different growth times after 1h (blue line), 3 day (red line)s and ten days (black line).	103
Figure 5.51: AFM 2D and 3D image of Sulphathiazole deposited on Ti with different magnifications.....	104
Figure 5.52: AFM 2D and 3D images of Tetracycline-HCl deposited on Ti(a-b) and glass (c-d) with different scan area.	105
Figure 5.53: AFM 2D and 3D images of Erythromycin deposited on Ti with different magnifications.....	106

Figure 5.54: AFM 2D image of Tobramycin deposited on Ti. The scan area is about 10 μm x 10 μm . The surface roughness is minor as the legend on the left implies a maximum height of < 30 nm.....	107
Figure 5.55: AFM 3D image of Tobramycin on Ti is shown with a scan area of 10 μm x 10 μm and a maximum height of 0.1 μm	107
Figure 5.56: a-c SEM images of Ascorbic acid on Ti substrate with different magnifications.....	108
Figure 5.57: (a-c) SEM images of Adipic acid grown on Ti substrate with different magnifications.....	108
Figure 5.58: The Raman spectrum of Adipic acid control sample. The inset shows the optical microscope image of the control sample.....	109
Figure 5.59: The Raman spectrum of Adipic acid deposited sample. The inset shows the optical microscope image of the deposited sample.....	109
Figure 5.60: SEM images show different magnifications of Caffeine nanostructures deposited on Ti substrate.	110
Figure 5.61: The Raman spectrum of Caffeine control sample. The inset shows the optical microscope image of the control sample.....	111
Figure 5.62: Caffeine sample after deposition with its appropriate optical image (inset) and Raman-spectrum.	111
Figure 5.63: SEM image of Cholesterol nanostructures deposited on Ti (a, b) and Si coated with 4 nm Au thickness (c, d) with different magnifications.	112
Figure 5.64: Raman spectrum and optical image (inset) of Cholesterol reference drug.	113
Figure 5.65: Raman-spectrum and optical microscope image (inset) of Cholesterol sample after evaporation.	113
Figure 5.66: (a) Small droplets of SM directly after deposition on glass sample with a magnification of 50 x. (b) shows droplets of SM also directly after deposition but on titanium sample with a magnification of 20x.	114
Figure 5.67: a-c SEM images of SM grown on Ti with different magnifications revealing uniform dispersity.	115
Figure 5.68: AFM 2D image of SM on Ti substrate. The lighter parts in the image display particles that are higher than 2 μm . The particle size amounts roughly < 2 μm	115

Figure 5.69: AFM 3D images of SM. (a) has a scan area of 10 x 10 μm^2 whereas (b) has a scan area of 2 x 2 μm^2 . The maximum height is around 1.5 μm .	116
Figure 5.70: SEM image of PLGA on Ti substrate. The images are taken directly after evaporation. They show small droplets of PLGA.	116
Figure 5.71: SEM images of Indometacin with hierarchical structures growing on Ti with different magnifications.	117
Figure 5.72: Microscopic image of Indometacin deposited on titan (film (a) reference sample (b) its Raman spectra of Indometacin reference substance (blue) and as film deposited substance on titanium substrate (red).	118
Figure 5.73: Microscopic image of Indometacin deposited on polymer foil (film (a) reference sample (b) its Raman spectra of Indometacin reference substance (blue) and as film deposited substance on polymer foil (red).	118
Figure 5.74: Raman spectra of Indometacin reference substance (blue) and deposited substance crystal on titanium substrate (red) after one week.	119
Figure 5.75: SEM of two layers sample composed of (1) Metronidazole, (2) PLGA with higher and lower magnification a and b respectively.	119
Figure 5.76: SEM of a four-layers sample composed of (1) SM, (2) Cholesterol, (3) Fluorouracil and (4) SM on Ti substrate with higher and lower magnification a and b respectively. Thicknesses of the single layers are: (1) >20 μm , (2) 15 μm , (3) few nm, (4) >20 μm .	120
Figure 5.77: SEM images of Acetylsalicylic acid on Ti substrate after and before deposition a and b respectively. The inset shows higher magnification SEM image.	122
Figure 5.78: a-c SEM images of Tetracaine HCl deposited on Si pre-coated with 20 nm Au thin film at different magnifications.	123
Figure 5.79: a-b SEM images of Tetracaine- HCl Si pre-coated with 4 nm Au thin film at different magnifications.	124
Figure 5.80: SEM images of Tetracaine-HCl grown on Si substrate at different evaporation times with 16 min (a), 23 min (b) and 30 min (c).	127
Figure 5.81: SEM images of Chloroamphenicol deposited on glass substrate which obtained after 3 h.(a) and 10 days(b) respectively.	128
Figure 5.82: XRD pattern of Chloroamphenicol deposited on glass substrate at different times of 3h and 10 days.	128

Figure 5.83: Representative Structure-zone model after Movchan and Diminishin relating the substrate temperature to the corresponding arising thin film structure .	129
Figure 5.84: SEM images of lateral structures of Pilocarpine-HCl (a) and Acetylsalicylic acid (b) respectively.	131
Figure 5.85: Raman spectra of the deposited and reference 5-Fluorouracil, showing clear Raman peaks in the thermally deposited 5-Flurouracil on titanium substrate..	132
Figure 5.86: Raman spectra of the deposited and reference Metronidazole.	132
Figure 5.87: Raman spectra of the deposited and reference Clotrimazole.	133
Figure 5.88: Raman spectra of the deposited and reference Adipic acid.	133
Figure 5.89: Raman spectra of the deposited (on polymer foil) and reference Pilocarpine-HCl.	135
Figure 5.90: Raman spectra of the deposited (on glass at different time) and reference Chloroamphenicol.	136
Figure 5.91: Raman spectra of the deposited and reference Nipagin.	136
Figure 5.92: SEM images of co-deposition of Tetracaine-HCl with gold (a and b) and silver (c and d).	139
Figure 5.93: a-d SEM images of Nipasol coated on the surface of ZnO nano-microstructures.	141
Figure 5. 94: EDX spectra of the as-synthesized Nipasol grown on ZnO nano structures which confirms the presence of Zinc, carbon as well as oxygen.	142

Chapter 6

Figure 6.1: shows the antimicrobial activity of Erythromycin against <i>Staphylococcus aureus</i> , positive control (a), deposited film (b).	144
Figure 6.2: SEM images of Erythromycin as bulk material before evaporation (a) and deposited film after evaporation (b).	144
Figure 6.3: illustrates the antimicrobial activities of deposited films of Nipasol (a), Tetracycline-HCl (b), Chloramphenicol (c) against <i>Staphylococcus aureus</i> .	145
Figure 6.4: The antimicrobial activity of Itraconazole against <i>Candida albicans</i> , positive control (a), deposited drug (b) by evaporation under vacuum.	146
Figure 6.5: SEM images of Itraconazole as bulk material (a) and deposited drug (b) by evaporation under vacuum.	146

Figure 6.6: Illustrates the antimicrobial activity of Tobramycin against Staph aureus, Negative Control (Anod. Ti type II) (a), Positive Control (Tobramycin) (b), deposited Tobramycin film grown on Titanium oxide (c), Titanium (d), stainless steel (e). 149

Figure 6.7: 3D AFM images of nano-microstructured pharmaceutically active molecules. 150

Figure 6.8: Illustrates drug release profile of Metronidazole. 151

Figure 6.9: SEM images of Metronidazole as bulk material (a) and deposited drug (b) by vacuum evaporation. The inset shows higher magnification SEM image. 152

Figure 6.10: The basic layout and conductivity curves of a PFET based on Pilocarpine-HCl by deposition through a shadow mask directly on a silicon microchip. 154

Figure 6.11: The I-V characteristic of pilocarpine-HCl thin film deposited on glass substrate. 155

List of Tables

Table 4.1: Overview of thermally evaporated different drug substances. First part (1-12) lists the materials which have been successfully nanostructured by thermal evaporation and have been tested with disk diffusion method. The second part (13-30) lists the successfully deposited materials. However, the biological tests are under progress. The last part (31-34) lists the pharmaceutical substances which are not suitable for thermal evaporation as they are decomposed during deposition..... 52

Table 5.1: Overview of thermally evaporated different drug substances. First part (1-30) lists the materials which have been successfully nanostructured by thermal evaporation and have been tested with disk diffusion method. The last part (31-34) lists the pharmaceutical substances which are not suitable for thermal evaporation as they are decomposed during deposition. 65

Table 6.1: The bacteriostatic effect of various antibiotics and of Nipasol deposited by evaporation under vacuum against *Staphylococcus aureus* ATCC 6538.....145

Table 6.2: The fungistatic effect of antimycotics deposited by evaporation under vacuum against *Candida albicans* ATCC 10231..... 146

Chapter 1

1 Introduction

Nanoscience can be defined as the systematic study of materials with properties that depend critically on length scales on the order of nanometers, see e.g. the definition by the Royal Society and the Royal Academy of Engineering in 2004 defines nanotechnology as designing, classification, creation, and maintaining of structures or systems by controlling their shape and size at the nanometre scale [1].

Nanostructures are functional structures with at least one characteristic dimension being between 1 nm and 100 nm. Such materials and systems can be designed to exhibit novel and significantly improved physical, chemical and biological properties as a result of the limited size of their constituent particles or molecules. Nowadays, there are different types of nanostructured materials and systems essentially differing in the number of dimensions which lie within the nanometer range: such as systems confined to one dimension (nanofilms, nanolayers), systems confined to two dimensions (nanowires, nanorods, nanocolumn, nanotubes), and systems confined to three dimensions (nanoclusters of different shapes).

By reducing the particle size, nanosystems can reveal several multifunctional physical effects based on quantum phenomena like quantum entanglement, electron confinement, electron tunnelling, ballistic transport, and near-field optical properties. Furthermore, a very important aspect of nanoscale objects is their increased surface area to volume (S/V) ratio. Nanotechnology exhibits huge potential for different applications such as semiconductor industry, metrology, electronics, biotechnology, biomedical engineering, military technology, agriculture and space applications. But one of the most promising societal impacts of nanotechnology is in the area of nanomedicine.

As stated earlier, the most common characteristic of nanotechnology is very small scale of the involved matter, which is below 100 nm. In general, there are two

different approaches for producing structures in nanometer regime: top-down and bottom-up. In the top-down approach a reduction of a source material from bulk size to nanoscale is carried out by: grinding processes, electron-beam lithography [2] and pattern-dependent oxidation methods [3, 4]. On the other hand, the bottom-up approach is a procedure to make nanostructures by agglomerating smaller entities, i.e., atoms and molecules in a controlled way and a few examples are molecular beam epitaxy (MBE), [5] chemical precipitation, [6] sol-gel process, [7] thermal evaporation, [8, 9] chemical vapour deposition (CVD), [10, 11] laser ablation, [12] and sputtering [13, 14].

An interesting biomedical aspect of synthetically constructed nano/micro structures is that their size is smaller than or similar to the natural units such as a cell (10–100 μm), a virus (20–450 nm), a protein (5–50 nm) or a gene (2 nm wide and 10–100 nm long). This means that they can deeply interact with biological systems or can be very close to a biological unit of interest [15].

More than 10 years ago, increasing attention was paid to optimize the pharmacological and pharmacokinetic properties of already available drugs through chemical and physical modifications. A promising approach in this respect is developing the nano/micro scale drug delivery carriers and small-molecule drugs to reach specifically targeted areas.

Currently, less than 10% of new drug candidates have both high solubility and permeability [16]. The chemistry of a drug by itself is not alone responsible for this effect rather its physical structure [17]. The increasing number of drug with poor water solubility demands development of technologies to improve drug solubility, reducing the toxic effects, and for promoting the therapeutic benefits. Therapeutic effectiveness of a drug depends on the bioavailability and hence on the solubility of drug molecules. Solubility is one of the important parameters to achieve desired concentrations of drugs in circulatory system of the body for a pharmacological response. Lower solubility of drugs leads to stability problems, fatal side-effects, lower bioavailability as well as an increased dose required for the treatment of patient. Reduction of drug particles size is necessary to facilitate the targeted drug delivery which has been a topic of renewed interest in pharmaceutical industries. There is a

variety of techniques employed to reduce the particle size including solid dispersion, salt formation, spray drying, milling, grinding, super critical fluid, freeze drying, solvent evaporation, coacervation and in situ polymerization. These techniques usually include the use of large amount of toxic solvents and/or surfactants which themselves require further purifying steps for removal the remaining solvent. Therefore, research efforts have been directed to develop the environmentally safe methods to produce the drug-loaded micron and submicron size particles. If solvent impurities remain in the drug-loaded NPs, then these become toxic and may degrade the pharmaceuticals within the polymer matrix. Important tasks for pharmaceutical engineering are the molecular scale mixing and structuring of pharmaceutical drugs for increased solubility. Nanostructuring of drug delivery systems offers many promising applications like precise control of dissolution and release kinetics, enhanced activities, flexibility in terms of surface coatings, integration into implants, designing the appropriate scaffolds or even integrating into microelectronic chips etc. for different desired applications. In general such kind of structuring is difficult due to unintentional mixing of chemical solvents used during drug formulations.

In surface science, many techniques exist to form nanostructures and surface coatings of nanoscopic thickness. Thermal evaporation (TE) processes have already been used to deposit individual atoms or molecules to form micro or nanostructured thin films since the last 50 years. The evaporation of drug molecules and their emission to a specific surface under vacuum led to controlled assembling of the molecules from vapour phase to solid phase. The most important aspects of thermal evaporation technique are: solvent-free, precise control of size, possibility of fabricating multilayer/hybrid, and free choice of substrates.

The aim of this thesis deals with the combination of nanotechnological methods, explicitly thermal evaporation, with pharmaceutical research to control the particle size/shape of pharmaceutical ingredients to overcome the aforementioned problem of drug insolubility. Furthermore nano and micro-structured thin films of active and non-active pharmaceutical layers shall be fabricated using the lowest drug concentration and decreasing the adverse effects related with drugs. This includes coating of implants for multifunctional applications, or creation of hybrids/ multilayers from

different drugs and carriers for designing the controlled and sequential release of drugs.

In general, the dissertation is devoted to the following two strategies: firstly, the synthesis of both pharmaceutical thin film and their multilayer structures; and secondly, the integration of these functional nano-microstructures into medical science. This dissertation is categorized into seven chapters including the current one.

Chapter 2 discusses some of the theoretical concepts of vacuum evaporation system. It begins with introducing the limitations of the conventional techniques which are used for improving drug solubility. The thin film deposition technique and some of its basic concepts regarding the atomistic thin film growth mechanisms are also discussed.

Chapter 3 discusses the successful experimental technique used by thermal evaporation for producing thin film from various pharmaceutical molecules, polymers and metals. Details about the thin film preparation and multilayer processes by co-evaporation used mainly for increasing the solubility of drugs and controlling the drug release are given. The antimicrobial experiment is also illustrated.

The description of techniques used for elemental, morphological, and structural analysis of these nano/microstructures appears briefly in chapter 4. The next two chapters focus on the main work of the dissertation including experimental results and discussion.

Chapter 5 describes the most important results of different spectroscopic techniques regarding the nucleation and growth of pharmaceutical thin films on various substrates prepared by thermal evaporation. Chapter 6 presents the application of thermal evaporation in medicine and electrical engineering, such as biological screening of deposited films, control the release of drug and field effect transistor.

Finally, chapter 7 concludes the dissertation with a summary of the obtained results and a brief discussion of the experiments followed by an outlook.

Chapter 2

2 Theoretical Considerations

Due to the interdisciplinary character of this thesis, it is necessary to give a basic background about pharmaceutical and materials science aspects which are important in this work. This chapter is divided into three main sections. First, important pharmaceutical aspects about solubility and hydrophobicity of drugs are introduced in the subchapter 2.1, the basic concepts regarding to the advantages and limitations associated with each process used for preparing drug delivery systems are discussed. The second section, subchapters 2.2- 2.5, presents the material science aspects ranging from vacuum vapour deposition techniques for various thin film depositions and the basic concepts of the growth mechanism, as well as a few words on nanotechnology. The last section discusses stents (subchapter 2.6.1) and biofilm formation (subchapter 2.6.2), both are important for potential applications of the thermal evaporation in biomedical research which is introduced in the following chapter.

2.1 Limitations of Techniques for Solubility Enhancement

In current medical scenario, the main challenge is to development different forms of drugs with appropriate size, defined solubilities/wettabilities, and desired functionalities in a versatile way. Indeed, various new drugs failed to reach the market due to their hydrophobic nature [18, 19] which lead to stability problems and high dose therapy. It is mainly difficult to build up a novel molecule with high-quality pharmacological activity and preferred solubility and permeability. According to the biopharmaceutical and classification system, class II drugs are solubility-limited and are estimated to account for about 30% of both commercial and developmental drugs [20, 21]. The solubility of a solute can be identified as the maximum quantity of solute that can be dissolved in a certain quantity of solvent to form a solution at a specific temperature. Therefore, drug dissolution is defined as ‘drug molecules

undergo from a solid phase to a solution phase'. In addition, water insoluble drugs show lower dissolution rates [22]. The solubility behaviour of active pharmaceutical substances remains one of the most challenging aspects in formulation development [23]. From pharmaceutical point of view, solubility is one of the most important parameters to achieve the desired concentrations of drugs in systemic circulation for a pharmacological response. The poorly soluble drugs have a number of disadvantages such as repetition of the dosage, administration frequency, stability problem and the resultant occurrence of side effects. In general, therapeutic effectiveness of a drug depends on the bioavailability and solubility of the drug molecules. Important tasks in pharmaceutical engineering are the molecular scale mixing and structuring of pharmaceutical drugs for increased solubility. This includes coating of implants for creation of hybrids and multilayers from different drugs and carriers for designing the drug controlled release and multifunctional applications. However, due to the nature of fluids this multilayer formation is difficult to achieve with conventional solvent based methods.

The chemistry of a drug by itself is not alone responsible for its effect. Therefore, different techniques are employed for engineering the drug particles through processing protocols for example, spray coating [24], supercritical point drying [25], drug precipitation, milling, or matrix assisted pulsed laser deposition (PLD) [26]. Impressively, PLD was already used to deposit complex proteins like glucose oxidase. To carry out the aforementioned approaches, however, methods are rare in which solvent is not used. The degradation and toxicity of pharmaceutical molecules might result from the remaining of solvent with them during their formulation.

Current formulation strategies that are used to improve solubility and dissolution rate of poorly water soluble drugs are associated with some disadvantages. For instance, adjustment of lattice structure or crystallinity to form polymorphs, solvates, or anhydrous solids acquire stability problem due to their metastable nature [27, 28]. Synthesis of new derivatives to get water soluble compounds by chemical method needs a lot of efforts to evaluate the effectiveness and safety of novel products. Altering chemical structure might drastically vary pharmacological activity by modifying the affinity of the drug for its receptor. Development of water-soluble

derivatives is costly however because of the need to investigate efficacy and safety of the new chemical species.

The use of solubilizing excipients in drug solubilization is limited due to their toxicity. Higher concentrations of surfactants can also cause toxicity problem and allergic reactions in definite individuals [29]. For example, adding Cremophor EL as a vehicle to Paclitaxel (Taxol) to improve its solubility. It was found that Cremophor EL can cause serious hypersensitivity reactions and nephrotoxicity in human subjects [30, 31].

Crystal and particle engineering strategies have notable potential to solve the problems of low aqueous solubility of drug substances [32]. These methods are applicable not only to molecules of a specific physical and chemical nature, but also to a wide range of crystalline materials.

The methods discussed above require the use of organic solvents, which are hazardous to the environment as well as to the physiological system [33]. While supercritical fluid technology is suitable for mass production, it has disadvantages. For instance, the majority of polymers show little or no solubility in supercritical fluids [34]. Modification of pH method might cause chemical instability and local tissue irritation or necrosis near the injection site at significant pH.

Besides chemical methods, which have their own side-effects and limited applicability, one can resort to physical aspect of the drug particles too for improving the solubility. Although micronisation increases the dissolution rate of drugs through increased surface area, it does not increase equilibrium solubility [35]. It was found that micronisation is not satisfactory because micronized products like amorphous materials exhibit the tendency of agglomeration, which leads to decrease in the effective the surface area to volume (S/A) ratio required for dissolution higher rate. From an engineering point of view the control over the drug particle size is very essential for increasing the (S/A) ratio. A smaller particle size (particularly in nanodimensions) leads to higher rates of dissolution [36, 37]. Considerably, the general physical activity of a material can be tuned by adjusting its shape or size. In addition, enhancement of drug solubility resulted from increasing the surface area of drug by diminishing the particle size of the solid materials obtainable for dissolving

compound and/or by improving the wetting characteristics of the compound surface as discussed by Noyes Whitney equation [38].

The effect of particle size on the solubility can be also described by the following equation [39].

$$\log \frac{S}{S_0} = \frac{2\gamma V}{2.303RT r} \quad (2.1)$$

Where S is the solubility of infinitely large particles, S₀ is the solubility of fine particles, V is molar volume, γ is the surface tension of the solid, and r is the radius of the fine particle.

Therefore, design features like particle size, surface energy, distribution, surface rugosity, surface area, particle density, porosity, and micro viscosity must be controlled by all different techniques used for improving solubility such as spray drying.

High absorption of pharmaceutical materials through inhalation can be achieved by controlling all of the above mentioned features. For example, engineered particles are employed for immune modulation. The delivery of antibodies and inhaled vaccines achieved by continuous proceed are anticipated by using smart therapeutics are capable of active targeting and intracellular trafficking [40].

Considering advantages and the limiting efficacy of all methods mentioned above of preparation and formulation of drugs, there is still room for alternative methods in drug processing.

2.2 Vacuum deposition

Physical vapour deposition (PVD) is referred to as vacuum deposition for coating processes, "physical" means without further reaction. In the other hand, if the source of material includes the chemical vapor precursors which they chemically reacted to produce desired deposit in higher performance, this process is called chemical vapour deposition (CVD). PVD is one of the most essential techniques used in coating technology of electronic devices. Nowadays it is even used for the formation of biomaterial compounds. PVD is a fast and easy method to deposit micro and nano structured thin films from various materials on different substrates with desired thicknesses. Generally, physical approaches involve heating the solid materials to be vaporized. The vaporized molecules then travel across a region of preferably low

pressure. Finally, they reach the substrate, where they condense and form the desired thin film deposited. Several kinds of methods underlie this principle, e.g., evaporation, sputter deposition, pulsed laser deposition or molecular beam epitaxy to assist the transfer of the atoms from a solid or molten source onto a substrate. The thin film depositions in this work were done using an ultra high vacuum chamber. Finally, it could be interesting for introducing some information about thin film deposited by thermal evaporation and sputtering technique.

2.2.1 Thermal evaporation

2.2.1.1 Thermal evaporation of organic materials

Thermal evaporation (TE) processes [41] have been used to deposit individual atoms or molecules to form micro or nanostructured thin films since at last 50 years. While thermal evaporation is mainly used for inorganic or ceramic materials [42], a widespread variant of the thermal evaporation in vacuum is known as thermal organic vapour phase deposition which is commercially used for the fabrication of organic light emitting diodes (OLED) [43] for flat panel displays. The main advantage of thermal evaporation is that it is a solvent free technique and can be routinely used to fabricate specimens which require a shape control down to the nanoscale. As a bottom up growth technique, individual atoms or molecules can be evaporated and assembled on the desired substrates of larger units and in new structures. Even the fabrication of multilayers is possible by using thermal evaporation. Laterally structured systems are possibility formed with the help of lithographic techniques or shadow masks. Even without further structuring, the internal deposited structure can be controlled [44]. Growth of thin films in vacuum is very well understood for decades [45]. Only by varying the deposition parameters like evaporation rate [46], oven or substrate temperature, the degree of organization of the deposited materials from amorphous to single crystalline and the surface roughness from atomically flat to macroscopically rough can be tuned.

Figure 2.1 shows a typical setup, a substrate holder is placed in the vacuum chamber in such a way that it is directly facing to the crucible containing the precursor materials to be evaporated. A vacuum of at least 10^{-5} mbar is maintained because a lower pressure entails a higher mean free path (MFP) of the evaporated particles. The MFP can be a multiple of the distance between target and substrate. In general, 100

mm to 1 km can be attained within high vacuum [47]. If the MFP is high, the effective evaporation rate meaning molecules that reach the substrate holder is higher. Besides, pressure has always to be kept below the gas pressure of the evaporating material. The whole thermal evaporation process can be divided into three main events: evaporation, transport and condensation. Considering the evaporation procedure, the solid material is in a graphite or refractory metal crucible and has to be heated to allow vapor particles to travel directly to the target object (substrate), where they might condense back to a solid state. The evaporation process takes place above the melting temperature in vacuum to transform into vapor phase [48]. Increasing the temperature means providing more energy to leave the crucible on the one hand, on the other hand there is more energy to break the bonds of the organic chemical compounds that are evaporated. Typically, the crucible is heated by resistive heating elements connected with a regulated power supply, the heating temperature can be adjusted by changing the current.

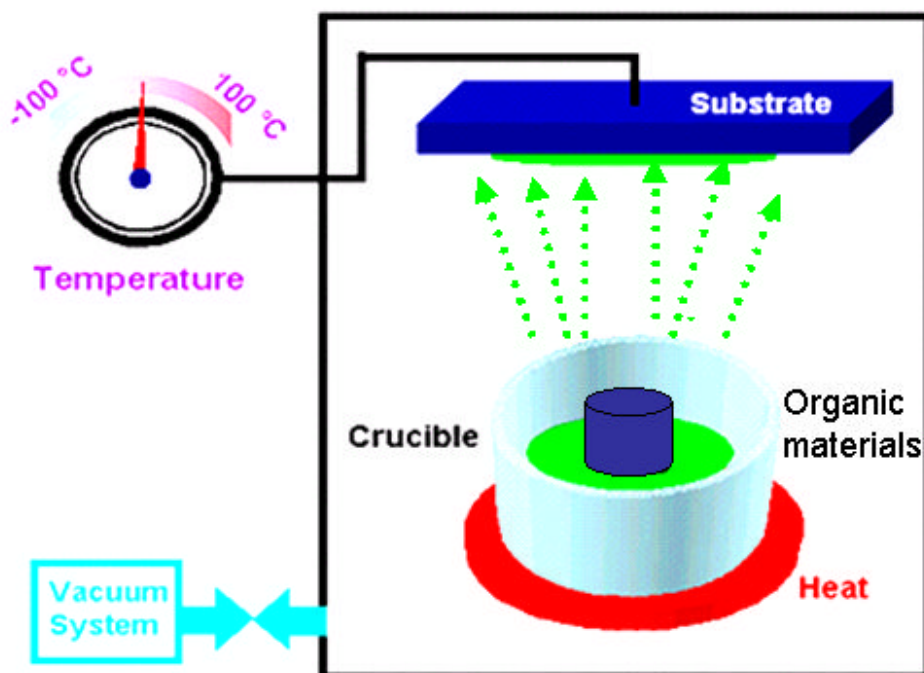


Figure 2.1: Setup for thermal evaporation of organic materials.

2.2.1.2 Evaporation of Metals by vacuum deposition

While molecular organic substances are tightly bound within the molecule by strong covalent bonds, weak van der Waals forces or polar control the interaction between individual molecules. In contrast, metals are characterized by metallic bonds. In metals the outermost valance electrons of each atom form part of a collective free electron cloud or gas that permeates through entire lattice. This free-electron gas has a strong electrostatic attraction with the positive ion cores. On the application of metals in medical science, chemotherapeutic drugs including Platin such as Oxaliplatin, Cisplatin, and Carboplatin are able to be passively targeted to solid tumours during the enhanced permeability and retention effect [49]. Moreover, gold nanoparticles (NPs) have various potential applications as catalysis, bioanalysis, and imaging. Gold NPs can also be used as an ideal drug-delivery scaffold due to their non-toxicity and non-immunogenicity behaviours [50]. On the other hand, Platinum-based chemotherapy drugs and gold nanoparticles can be used for solid tumours and leukaemia treatment. Surface modifications may be introduced through conjugation with targeting moieties (e.g., antibodies, peptides, small molecules, aptamers, fluorescence dyes, genes, or drugs) to provide multimodal functionalities [51, 52]. Exposure of metal NPs to infrared light or magnetic fields [53] resulted in generation of hyperthermia for solid tumour treatment [54]. Furthermore, it is known that silver ions have been used against gram positive and gram negative bacteria. Various generic forms of silver have been confirmed to be efficient against burns, severe chronic osteomyelitis, urinary tract infection and central venous catheter infections [55]. Furthermore, Nanostructures from silver and gold nanoparticles capped with mercaptoethane sulfonate can be used as antiviral activities [56, 57]. In addition, it was found that cobalt/silica carriers are presently being examined for their use in eye surgery to fix disconnected retinas [58].

This method is capable of using the film-forming material making up the thin layer with higher efficiency owing to heating materials while preventing the substrate and the thin layer from being adversely affected by heat from the heating source materials. When a sufficient vacuum, e.g., 10^{-6} mbar is achieved, the crucible is heated above the melting temperature of the contained material. The external and internal schematic designs of a typical metal evaporator of Knudsen cell type, which is used in this work, are illustrated in **Figure 2.2**.

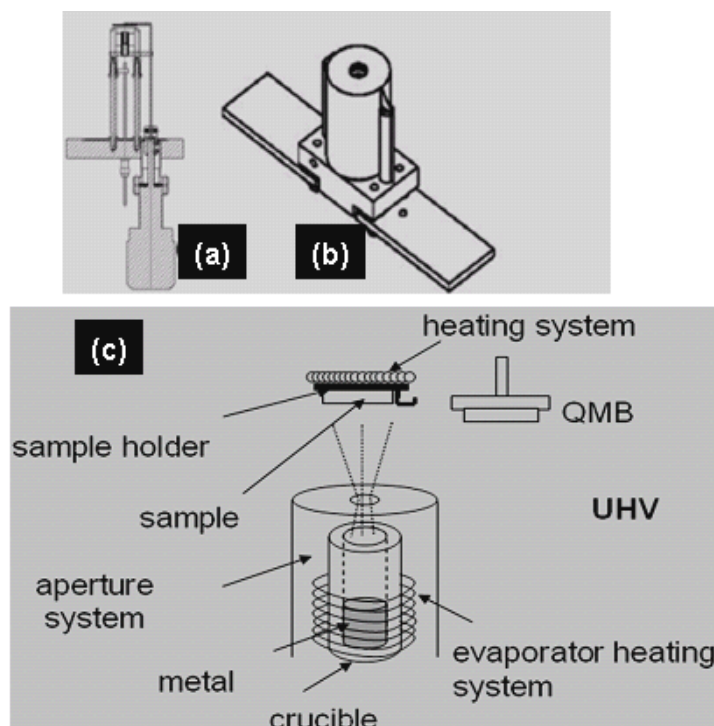


Figure 2.2: The sketch shows the metal evaporator with a power feed through (a), and both the external (b) and the internal (c) part of the metal evaporator cell.

The Tantalum (Ta) heater coil filament was selected to transmit the high current and produce the heat required to evaporate the charge. Ta also has a high melting point, a sufficient degree of thermal shock resistance, and a high ductility among the refractory metals. Basically, the rate of deposition of metal atoms in resistively heated evaporators depends on the temperature of the crucible which is itself controlled by the electrical power and the amount of exporting material. In general, compared with the evaporation of organic material, the evaporation rate of metals is very low, typically at least a factor of 10. In this design, the Ta heater coil is minimally supported within notched ceramic support rods to reduce heat sinking. The coil extends well below the bottom of the crucible so that the thermocouple touching the crucible bottom is immersed within the same heating environment as the crucible and thus stabilizes at the same temperature.

Moreover, the coil is extended towards the crucible mouth, above the level of the evaporation material, which leads the mouth of the crucible to be at higher temperature than the temperature of the evaporation material. This prevents condensation of evaporant droplets at the mouth and also prevents evaporants which

wet the crucible from migrating out of it. In addition, the radiation heat shielding consists of several wraps of corrugated Ta foil is used to reflect radiation from the coil and crucible, thereby improving source temperature and reducing out gassing of nearby hardware.

A cup shaped crucible sources (length =17 mm, and inner diameter =3 mm) made of aluminium oxide, molybdenum, and boron nitride can be used as a source of the evaporant. The boron nitride crucible was found to be the best type for the evaporation of Au and Ag as compared to others. In some cases, diffusion of evaporant materials into the crucible material and crack formation in the crucible was observed in case of Au evaporant and molybdenum crucible. Crucible materials should be chosen whose residual contaminants are the least harmful to the film being deposited. However, much of the volatile contaminants were removed from the crucibles and associated components by firing it at a higher temperature than the desired evaporation temperature prior to the filling with new evaporant. The areic evaporation rate results from equation:

$$a_v = \alpha_c \cdot 4.4 \cdot 10^{-4} \cdot p_s \cdot \sqrt{\frac{M}{T}} \quad (2.2)$$

α_v indicates evaporation rate, meaning the evaporated mass per time and unit area in $g/(cm^2 \cdot s)$, α_c is the evaporation coefficient (being 1 for ideal evaporation), p_s is the saturation vapour pressure of evaporation material at evaporation temperature in Pa and M is the atomic/molecular mass of evaporation particles in g/mol [59]. This explains why the rate of deposition of organic molecules is in general much higher than in metals.

The characteristic propagation of the evaporated material depends on the geometry of the evaporation source. In this work a crucible is used as a small area source. A small area source is defined as having small dimensions of the evaporating area compared to its distance to the substrate (r). The evaporation rate is a directional quantity. Concerning the angle φ between substrate position and the vertical to the source, the rate also depends on the distribution of the evaporating material. Thereby it follows a cosine law:

$$a_v = \cos^n \varphi \cdot \cos \phi \quad (2.3)$$

with $n \geq 0$, the bigger n the more directed the flux as shown in **Figure 2.3**.

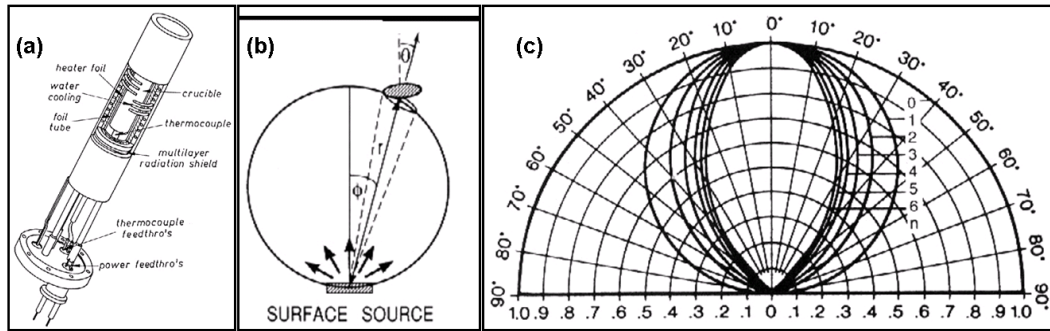


Figure 2.3: (a) Crucible rack for thermal evaporation, (b) Target material distribution from a small area source, (c) Distribution of evaporated material following cosine-law. (These images were taken from the following website, <http://www.ep4.rub.de/imperia/md/content/skripte/ss04/thinfilmmagnetism/hcs.pdf>).

2.2.2 Sputter Deposition

This is a commonly used process for thin film deposition, etching and analytical techniques. Compared to evaporation of metals, it has a much higher deposition rate. In sputtering, atoms are ejected from a solid material under the bombardment by fast, heavy and by positive-ion (Ar^+) of typical energies 500 eV-10 keV, ejection of atoms of binding energies 1-5 eV. Thus, a minimum binding energy needed to supply to the atoms in order that sputtering may occur since sputtering is driven by momentum exchange between the ions and atoms in the material due to collisions. The incident ions set off collision cascades in the target. When such cascades recoil and reach the target surface with energy above the surface binding energy, an atom can be ejected. Sputtering is widely used for thin film depositions because it has unique combination of advantages over the other techniques. Any material can be volatilized by sputtering, compounds are volatilized stoichiometrically, and the film deposition rate can be maintained uniform over very large areas. Here, the deposition of metals (such as gold, platinum, palladium etc. with 99.99% purity) was mainly done by magnetron sputtering.

Sputtering has a wide variety of applications on metals, metal alloys, semiconductors, or insulators. Due to the high impact energies of the ions, it can not be utilized for

organic molecules. For these different materials, different modes of sputtering such as DC, RF, magnetron, or reactive sputtering are used. The choice of the techniques for example depends on the type of the target used in sputtering it out. For instance, DC sputtering is used for conducting targets and RF sputtering for insulator targets. Magnetron sputtering is widely used variant of DC sputtering. In addition, magnetron sputtering is practiced in RF and reactive variants which can significantly increase the efficiency of the process. Magnetron sputtering is presently the most widely commercially practiced sputtering method due to its high deposition rates. These are typically order of higher rates than attained by conventional sputtering techniques. It incorporates a crosswise magnetic field over the cathode which prolongs the electrons residence time in the plasma and thus enhances the probability of ion collision.

The electron within the dual field (i.e. both magnetic- and electric fields) experiences the well known Lorentz force in addition to an electric field force:

$$F = \frac{mdu}{dt} = -q(E + u \times B) \quad (2.4)$$

Where q , m and u are the electron charge, mass and velocity, respectively. This leads to the larger discharge current and thus increased sputter deposition rate. In other words, this magnetic field greatly increases their mean free path length before they finally escape to the anode by scattering. Because the path of electrons is much longer than the electrode gap, the minimum pressure to sustain the plasma is much lower for the magnetron than for the planar diode. The sputtered atoms retain most of their kinetic energy on reaching the substrate. Besides, the deposition rate is increased because of reduced scattering and re-deposition of sputtered atoms on the cathode.

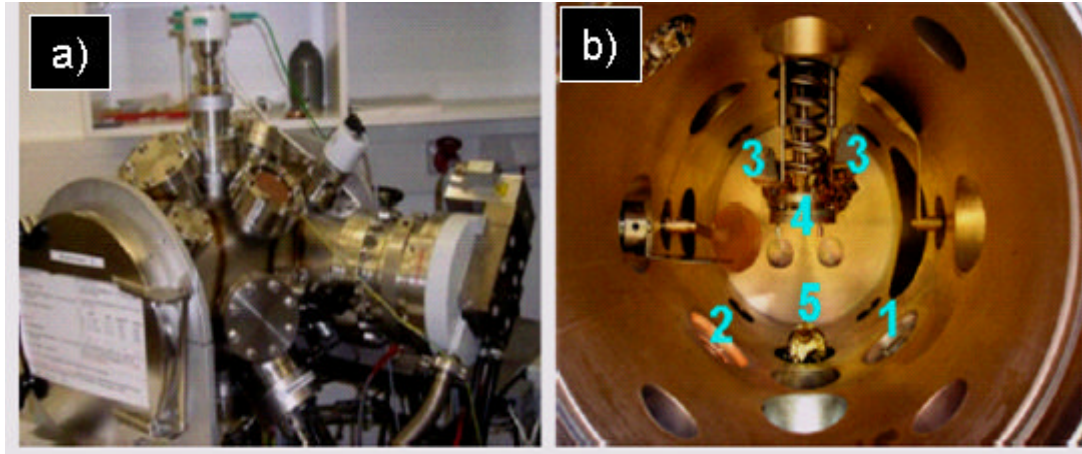


Figure 2.4: Picture of magnetron sputtering chamber a) outer part b) inner part, the numbers in the inside chamber correspond to parts of the (1) Pt magnetron (2) Copper magnetron (3) quartz monitors (4) sample holder.

Figure 2.4 shows the image of the magnetron chamber used in our laboratory for sample preparation. The chamber consists of sputter targets, evaporation sources, two quartz microbalances for an in-situ film thickness monitoring and a sample holder. The Chamber is equipped with a rotary pump (Pfeiffer DUO 005 M), to generate the pre-vacuum (10^{-1} torr) together with a turbomolecular pump (Pfeiffer TMU 260) that is used for creating the end-vacuum in the range of 10^{-7} - 10^{-8} torr. A relatively good vacuum condition is required to reduce collision of the transported material with the residual gas. Thus, the reduction in the rate of deposition and oxidation of the materials are prevented. During thin film deposition process, the target must be well bonded to a water-cooled Cu backing plate to dissipate. The heat is created by bombardment to prevent out gassing or melting of the target material.

2.3 Growth mechanism

Growth of thin films, as in the phase of transformation, involves the processes of nucleation and growth on the substrate surface. The nucleation process plays a very important role in determining the crystallinity and microstructure of the resultant films. For the deposition of thin films with thickness in the nanometer region, the initial nucleation process is important. From a thermodynamic point of view, the size and the shape of the initial nuclei are assumed to be solely dependent on the change of the volume of Gibbs free energy due to supersaturation, and the combined effect of surface and interface energies governed by Young's equation. No other interactions

between the film or nuclei and the substrate were taken into consideration. In practice, the interaction between film and substrate plays a very important role in determining the initial nucleation and the film growth. Therefore, the condensed atoms have to form clusters. When these clusters reach a critical radius, where they are thermodynamically stable, a nucleus is formed. Three major growing mechanisms of film formation have pointed basic growth modes island (Volmer-Weber), layer-by-layer (Frank-van der Merwe), and Stranski-Krastanov. **Figure 2.5** demonstrates these three basic modes of initial nucleation in the film growth. The Volmer-Weber mechanism is also called island growth mechanism. The deposited atoms are bound together in three-dimensional islands where the cohesive forces are stronger than the adhesive forces to the substrate. Nucleation starts from small clusters that form on the substrate. Further arriving atoms bind to the already existing islands and enlarge them until they coalesce and build up a uniform thin layer. The Frank-van-der-Merwe mechanism is also called layer-by-layer growth. The adhesive forces between deposited atoms and surface atoms are stronger than the cohesive forces. After the first two-dimensional monolayer has formed the second layer starts to grow. The Stranski-Krastanov mechanism combines the previous mechanisms. Initially the Frank-van-der-Merwe is predominant until a critical layer thickness is reached. This critical layer thickness is dependent on physical and chemical properties of the substrate and the film. Many systems of metals or organic materials on insulator substrates, alkali halides, graphite and mica substrates display the Volmer-Weber mechanism [60], this type of nucleation during the initial film deposition. Subsequent growth results in the islands to coalesce to form a continuous film. The layer growth is the opposite of the island growth, where growth species are bound more powerfully to the substrate than to each other. First complete monolayer is formed, before the deposition of second layer occurs. The most important examples of layer growth mode are the epitaxial growth of single crystal films. The island-layer growth is an intermediate combination of layer growth and island growth. Such a growth mode typically involves the stress, which is developed during the formation of the nuclei or films.

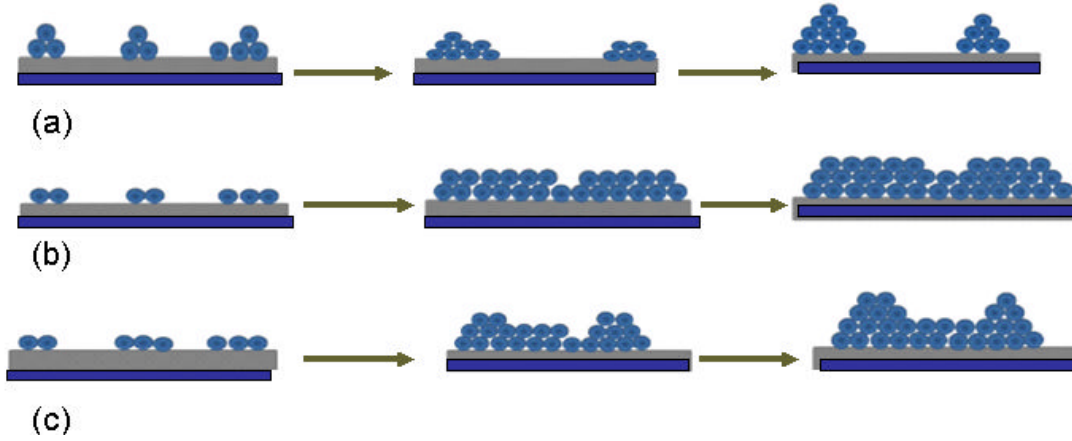


Figure 2.5: Thin film growth mechanisms. (a): Volmer-Weber (island) growth, (b): Frank-van-der-Merwe (layer-by-layer) growth, (c): Stranski-Krastanov growth [61].

2. 4 Growth mechanism equations

As indicated by optical microscope, atomic force microscopy (AFM) and scanning electron microscopy (SEM) results (see **chapter 5**), the thin film formation starts with island growth. For instance, the nucleation process has to be considered. When the material vapour condenses at the substrate surface, interfaces are formed between the film and substrate due to change in the Gibbs free energy. An energy gain comes from the formation of new volume, and a loss of energy arises from the creation of a new surface. The change in energy can be given by the equation (2.5).

$$\Delta G = \frac{4}{3}\pi \cdot r^3 \cdot G_v + 4\pi \cdot r^2 \cdot \alpha \quad (2.5)$$

The free energy change accompanying the formation of an aggregate of mean dimension r is given by

$$\Delta G = \alpha_3 r^3 \Delta G_v + a_{1fv} r^2 \gamma_{fv} + a_2 r^2 \gamma_{sf} - a_2 r^2 \gamma_{sv} \quad (2.6)$$

The chemical free-energy change per unit volume, ΔG_v , drives the condensation reaction. There are several interfacial tensions, and these are identified by the subscript f, s, and v representing film, substrate and vapour, respectively. The formation of new phases results a reduction of Gibbs free energy, but an increase in the total surface energy. The nucleation is stable only when its size is larger than the critical size, i.e., $r > r^*$:

$$r^* = \frac{-2(\alpha_1\gamma_{vf} + \alpha_2\gamma_{fs} - \alpha_2\gamma_{sv})}{3\alpha_3\Delta G_v} \quad (2.7)$$

Correspondingly, ΔG_v evaluated at $r = r^*$ is

$$\Delta G^* = \frac{4(\alpha_1\gamma_{vf} + \alpha_2\gamma_{fs} - \alpha_2\gamma_{sv})^3}{27\alpha_3^2\Delta G_v^2} \quad (2.8)$$

where G_v is the free energy change per unit volume, r is the radius of nucleus formed, α is the surface tension, a and γ indicate the interfacial areas and energies and f , v and s stand for film, vapour and solid, respectively. For three different cases of layer, island and layer-island growth the relations between the interface energies are varied. For island growth, the surface energy between solid and vapour will be smaller than the sum of the other two as:

$$\gamma_{sv} < \gamma_{sf} + \gamma_{fv} \quad (2.9)$$

For layer growth, the interface energy between solid and vapour equals the sum of the other two because the substrate will be covered completely. So, one gets:

$$\gamma_{sv} = \gamma_{sf} + \gamma_{fv} \quad (2.10)$$

When both mechanisms are combined, the surface energy between solid and vapour is bigger due to in- situ induced stresses during growing process [62].

$$\gamma_{sv} > \gamma_{sf} + \gamma_{fv} \quad (2.11)$$

To explain the thin film growing within thermal evaporation, the fundamental properties of the material should be considered during evaporation like melting point, and density. In this thesis, organic compounds and particularly pharmaceutical substances are deposited by a thermal evaporation process. The materials are heated to their specific melting points. If the surface of the sample material in the crucible has enough energy, evaporation will start. Thus small-sized particles attain to the vapour flux and condense at the substrate. They will increase in size when further molecules reach there. Due to stability issues, some monomers are not able to stay at the top of the islands (see **Figure 2.6**). But, they rather fall down on the substrate surface where they have been bound to surface layer atoms. This is the point where layer formation arises. The corresponding surface energies are referred to equations mentioned above. The nucleation and growth processes depend on different factors. For instance, the substrate surface plays a key role on island formation. High roughness of the surface may lead to non-uniform thin films or different island sizes

and heights. Also the concentration of the evaporated material is relevant because higher concentration means more molecules reaching the substrate. This might lead to faster layer formation as the molecules coalesce at numerous places to small islands which will in turn coalesce, as the inter-island distance is small. Also, aspects considering diffusion processes are the energies of the evaporated molecules as well as the time component of evaporation itself. The more energy and time is available during the whole process, the higher the probability to form clusters on the surface. This will be elaborated more precisely in **chapter 5**. Bulk diffusion does not matter because the organic molecules are quite big if compared to the substrate atoms and thus will not diffuse into the substrate. In addition, it is possible that not only monomers can be evaporated but also possible to evaporate the dimers or even trimers.

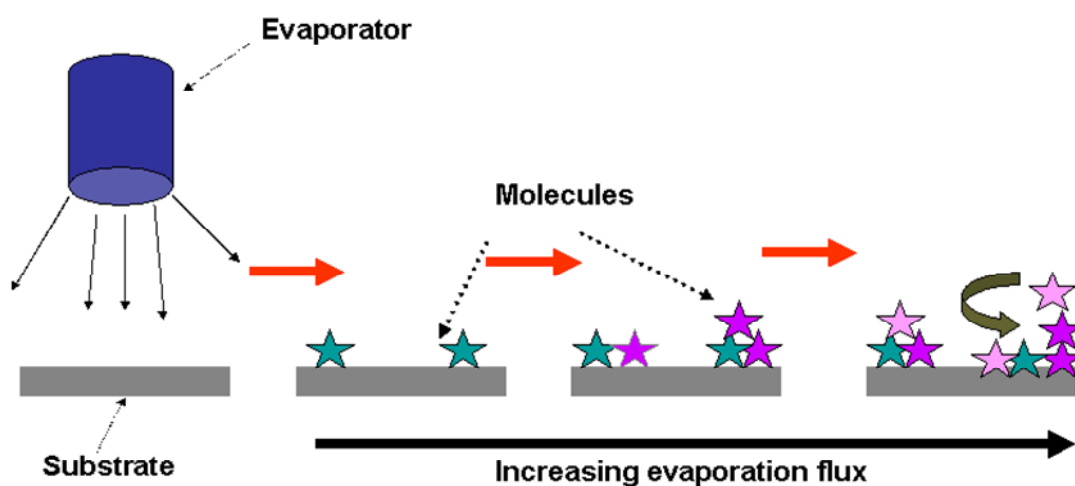


Figure 2.6: The growth mechanism of a thin film layer through evaporation of molecules is demonstrated schematically.

The different colours of the molecules should signify the different stages of molecule arrivals. Firstly individual small islands form until a whole layer derives. The outer right part shows the instability of a molecule on top of an island and its degradation.

2.5 Nanotechnological aspects

Nanotechnology approaches are necessary to study the materials and structures at the nanoscale level of around 1-100 nanometers (nm) or fewer. Generally, nanoscience provides the study of matter and system in atomic and molecular levels. The objects

studied in this range of sizes, are larger than atoms and small molecules. But, these objects are smaller than the structures typically produced for using microtechnologies (e.g., microelectronics, photonics, MEMS, and microfluidics). The dimensions of these systems are often equal to or smaller than the length scales that define the physical properties of materials. The unique physical properties of nanostructures, in general, can be attributed to different origins: for example the relatively large fraction of surface atoms, large surface energy, and spatial confinement. At these sizes, nanosystems can exhibit useful physical actions based on quantum phenomena (electron confinement, near-field optical effects, quantum entangle). Some of the observed phenomena are as follows:

- Significantly low melting point or phase transition temperature and appreciably reduce constant lattice due to huge fraction of surface atoms.
- One or two order magnitude higher mechanical strength. This effect could be due to reducing the probability of defects.
- A high resistivity due to dominant surface and grain boundary scattering.
- Significantly different optical properties due to an increase in band gap.

The dimensional dependence of these properties shows that the general physical activity of a material can be tuned considerably by adjusting its shape or size.

Reduced dimensionality arises when at least one dimension of a physically active region is in nanoscale region. A condensed matter exhibits some remarkable properties when their dimension changes from bulk to nanoscale. The properties observed in this nanoscale dimension material significantly differ from their bulk counter parts. It was found that the size, surface characteristic and shape of nanoparticles are playing important role in their biodistribution in vivo [63]. The design of engineering NPs for therapeutic applications is important since particles of less than 5 nm are quickly removed from distribution during extravasations or renal clearance [64], and the particles of size ranging $\sim 15 \mu\text{m}$ and above to accumulate in the liver, the spleen and the bone marrow [65]. Therefore, particles should be in the size ranging $\sim 10 \text{ nm}$ to $\sim 15 \mu\text{m}$ to promote cellular targeted and systematic circulation [66]. In general, the high surface to volume ratio of nanoparticles induces a higher decomposition rate. Targeted drug delivery is a process of transporting the medication to a patient with higher concentration in the tissue of interest without destroying the healthy tissue and organs [67, 68]. The design of nanostructured drug carriers will

assist to go through or overcome these barriers to drug delivery as described by Courrier et al. [69].

2.6 Potential applications of thermal evaporation in medical science

2.6.1 Stents

Nowadays, coronary artery disease (CAD) is one of the dangerous diseases leading to cause heart-related death and disability in the advanced world. CAD is associated with the development of atherosclerosis or arteriosclerotic vascular disease within one or more of the coronary arteries which transport oxygen and essential nutrients to the heart muscle. It was found that smoking, hypertension, diabetes, higher levels of fatty substances as cholesterol [70], cellular waste, calcium and other substances in the internal layer of any artery caused numerous risks such as sufficiently narrow lumen, limited blood flow to a portion of the heart and result in angina pectoris. From this finding, the treatment of re-narrowing artery should be done in-stent restenosis (ISR) [71, 72], as demonstrated in **Figure 2.7**.

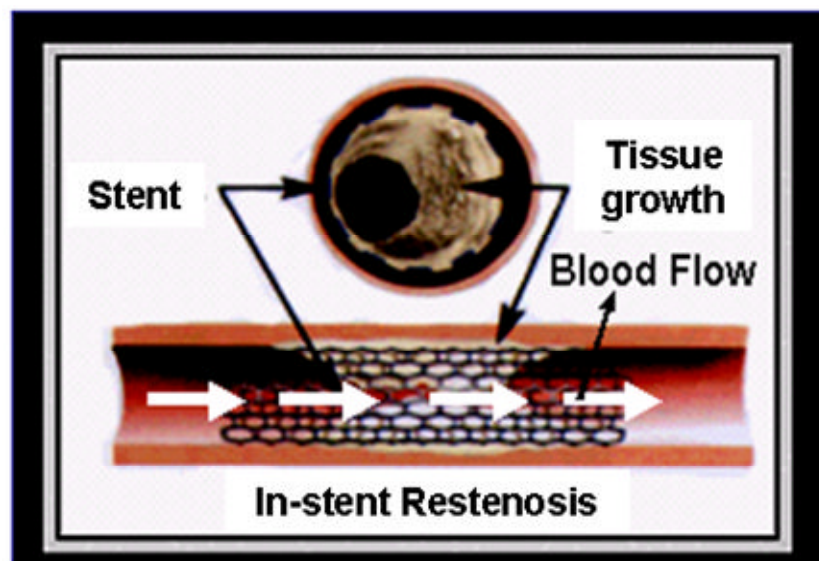


*Figure 2.7: shows the differing patterns of restenosis and in- stent restenosis (ISR).
(source of this image in website: cvi.med.nyu.edu)*

There are two kinds of stents.

(1) **Bare-metal stent (BMS)** is non coating stent which is a mesh-like tube of thin wire. Metal stent is fabricated from metals which do not decompose in biological

system. Stainless steel and Cobalt-chromium alloy are widely used in cardiac arteries treatment. Normally, a BMS is a small, tubular, wire-mesh device which is pre-loaded in a collapsed form onto a catheter balloon, threaded to the narrowed section of the artery and expanded within the vessel.

(2) Drug-eluting stents (DES)

DES represents one of the most promising advances in interventional cardiology and radiology. The major development of ISR is at the site of injury as there is locally smooth muscle cell activation and replication. Three different routes are concerned in the pathogenesis of ISR as illustrated in **Figure 2.8**. These consist of: (1) instant vessel recoil after stretch injury, (2) negative arterial remodelling, and (3) neointimal hyperplasia.

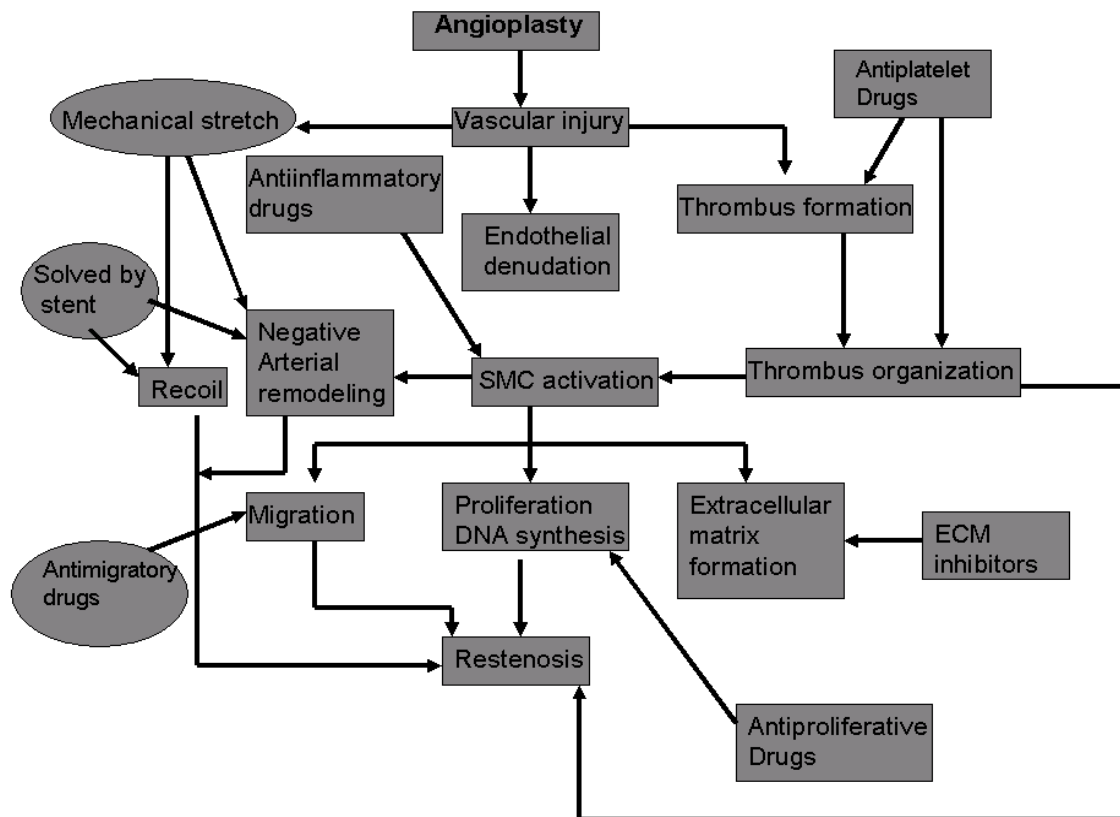


Figure 2.8: Pathophysiology of in-stent restenosis and the mechanisms of action of different therapeutic agents [73]. (Abbreviations: ECM, extracellular matrix; SMC, smooth muscle cells).

Consequently, the most important thing in a stent-based drug delivery system is to locally deliver a suitable concentration of active molecules to prevent this process and

toxic effects. The successful system would consist of three components: (1) a metallic platform, (2) a drug carrier vehicle that stores a therapeutic agent as well as allows the agent to diffuse into the vascular tissue in a controlled fashion, and (3) an effective therapeutic agent that reduces the neointimal growth induced by stent implantation. To facilitate better interaction or adhesion between drug releasing matrix and stent, using of stable synthetic polymer coating materials such as polyethylene-co-vinyl acetate (PEVA), poly-n-butyl methacrylate (PBMA), and the tri-block copolymer poly(styrene-b-isobutylene-b-styrene) (SIBS). The most successful method has been applied to the surface of the stent stage by using anti-restenotic drugs with polymers to coat the stents surface. Upon deployment, drug-delivery is driven by diffusion from the polymeric matrix and the rate of this diffusion is stated by the type, composition and number of polymers used in the drug-polymer matrix. Through the operation of a DES, any mechanical injury acquired in the vessel leads to an immediate healing response in the arterial wall. This healing response is firstly described by the creation of platelets within the intima, leading to thrombus development and the recruitment of blood-borne monocytes, neutrophils and lymphocytes. These cells produce mitogenic and chemotactic factors which trigger the activation of smooth muscle cells (SMCs) which undergo unrestrained proliferation and migration toward the intimal layer resulting in neointimal growth and ISR [74]. Consequently, the use of the perfect anti-restenotic substances should show potent antiproliferative effects but protect vascular healing. In clinical treatment, using several immunosuppressive agents, such as Sirolimus, Zotarolimus and Everolimus prevent SMC proliferation in response to cytokine and growth factor stimulation by binding to the cytosolic FK binding protein 12 (FKBP12). This prevents the activation of the mammalian target of rapamycin (mTOR) and leads to interruption of the cell-cycle in the G1-S phase. Paclitaxel is known as a strong antiproliferative agent, suppresses neointimal growth by binding with and stabilising microtubules.

2.6.2 Biofilm formation as microbial development

Many patients need an internal fixation device or artificial cooperative in advanced countries [75]. The most familiar diseases which cause bone failure or loss are periodontitis, perio-implantitis, osteomyelitis and rheumatoid arthritis. These diseases are caused by bacterial infections such as (gram negative and gram positive bacteria)

and inflammation reactions [76, 77]. Biofilms can be defined as the ability of microorganisms attached to a surface of solid materials or medical devices [78]. The contamination of medical implants and devices might come from: (1) a contaminated of the hands of medical teams during the surgical procedure, (2) the infection of the surface of implant/device, (3) the patient's own skin or mucus membrane, (4) isolated local contaminations in the patient, (5) infected antiseptic, (6) communication with other patients in the hospital, or family members after involvement [79, 80]. During the insertion on implant devises, blood or tissue proteins directly adhere to top of the surface of an implanted device (see **Figure 2.9a**). The adhesion or adsorption of larger biomolecules such as protein to a surface, but without actually penetrating the surface. Protein is of high physiological relevance, and adsorb with different mechanisms than their molecular or atomic analogs. Some of the major driving forces behind protein adsorption include Protein adhesion which depends on surface hydrophobicity, roughness, porosity, chemical composition, as well as composition and concentration of the protein solution, salt concentrations and pH [81, 82, 83, 84]. The deposition of adsorbed proteins layer has been revealed to be significant for sticking with free swimming bacteria which is called planktonic state [85]. It will in vivo adsorb these surface proteins as represented in (**Figure 2.9b**) [86, 87].

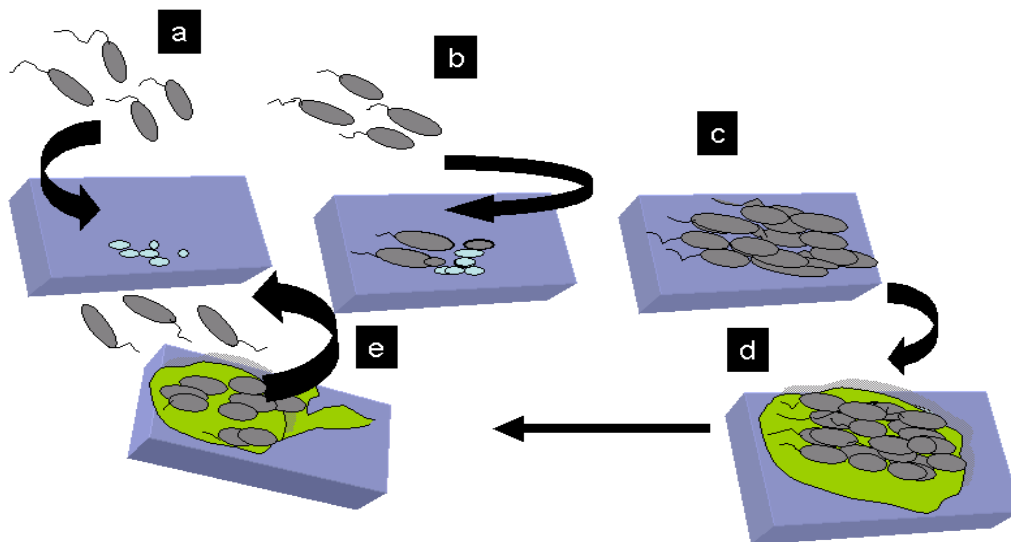


Figure 2.9: Schematic representation of biofilm formation [88].

The sticking bacteria grow rapidly by production or proliferation and mobilization of other bacteria from the immediate surroundings. Much more bacteria have stuck on the surface. These can change their gene appearance by mutation. Changing in bacterial genes might be initiated which are in charge for the production of additional

cellular polymeric materials, which are necessary in the construction of biofilm [89]. **Figure 2.9c** contains extracellular polymeric substances (EPS). In principal, the EPS matrix has changeable composition. And it includes polysaccharides [90]. Also, non-cellular materials from the direct environment can be formed. The biofilm gradually develops and microcolonies of bacteria form inside the biofilm as shown in (**Figure 2.9d**). Finally, small parts of the biofilm can fracture and planktonic bacteria run away from the biofilm as illustrated in (**Figure 2.9e**). The formation of biofilm sheet is required to protect the sessile bacteria from shear stress. It is attacked by the host's immune system and (awful or not comfortable for the patient) against antibiotic substances. The achievement of medical implants is not only based on the combination between bone and implant, but also on the occurrence of disinfection around the implant, which will prevent bacterial infection. Infection is one of the most serious complications that may arise after orthopaedic implant surgery. To regulate the best approach for fighting the infection of medical device, one can put in his consideration, the medical implant transported to the patient should be completely clean and pure. Fighting of foreign bacteria colonized the medical devices may be achieved by using thermal evaporation technique. Thermal evaporation provides better adhesion between substrate surfaces and deposited antimicrobial agents such as pharmaceutical molecules and inorganic materials like silver.

Furthermore, in the framework of the examinations of this thesis the ability to investigate and control the release of antibiotic and the antimicrobial agents to increase the activity of antibiotic and antimicrobial substances to prevent bacterial and fungal adhesion to the biomedical surfaces such as *Staphylococcus epidermis*, *staphylococcus aureus* and *Candida Albicans*. The PVD process is recognized as the best choice since it results in good adhesiveness and resistance of metallic or ceramic coatings and it is extensively used in technical and medical applications [91].

Chapter 3

3 Characterization Techniques

This chapter introduces the fundamentals of the characterization techniques used for the investigation of structural, chemical and physical properties of the deposited organic thin films fabricated by physical vapour deposition. The techniques used in this study include light optical microscopy, atomic force microscopy (AFM), scanning electron microscopy (SEM), profilometer for actual thickness measurement, Raman spectroscopy and x-ray diffraction (XRD).

3.1 Light Microscopy

Optical microscopes were introduced in multiple forms in the 17th century. It is used initially to look at the majority of the samples that give us first impetration for making further investigations. Optical microscopes are the oldest design of a microscope which get better resolution and sample contrast than the naked eye. The image from an optical microscope can be captured by normal light-sensitive cameras to generate a micrograph. It is an honestly simple instrument, being essentially an extension of human eyes which magnifies images of small objects, enabling to directly view structures that are below its resolving power (0.1 mm). Furthermore, samples could be used to routinely document the progress of an investigation. The significance of light microscope in our research appears in investigating the features of thin film of deposited active pharmaceutical ingredients fabricated by thermal evaporation. The characterization of thin film morphology, particularly, was often done at different magnification ranging from 25 x to 1000 x right after deposition. This helps to check the characteristics of deposited molecules. The arriving light will be reflected on the surface of the delaminated thin film. Modern established compound microscope use multiple lenses for magnification. Its optical path is shown in **Figure 3.1**. Progress includes better resolution, less aberrations, exchangeable objective lenses and add-on features like phase contrast or dark field imaging. Standard resolutions achieved that can be achieved are about 200 nm (half of the blue light wavelength). The light source, which mostly is a halogen lamp, is seated opposite to the ocular and below the sample. Condenser lenses focus the light onto the sample. A condenser aperture helps

to adjust the light intensity on the sample. Objective lenses that lie above the sample collect light from it and produce a magnified intermediate image. In order to obtain the total magnification of the final image, the magnification power of the objective lens and the eyepiece has to be multiplied. This results in a maximum magnification power of 1000x that is limited by the nature of the specimen, the objective lens, and the wavelength of light. Limitations to what can be seen in an optical microscope are not so much related to magnification as they are to resolution, illumination, and contrast.

Resolution

The optical microscope is limited to a resolution of about 200 nm. The resolution is related to the numerical aperture (NA) of the objective lens and the wavelength passing through the lens. Higher numerical aperture and shorter wavelength, better resolution. The numerical aperture of an optical system such as an objective lens is defined by

$$NA = n \cdot \sin\theta \quad (3.1)$$

n is the index of refraction of the medium in which the lens is working and θ is the half-angle of the maximum cone of light that can enter or exit the lens.

Illumination

In order to see the intricacies and detail of the viewed sample, a glare-free, bright and evenly dispersed light must be displayed from behind and across the viewing field. Proper illumination occurs through reflected, refracted and transmitted light, or a combination of all three.

Contrast

Contrast is related to the illumination system and can be adjusted by changing the intensity of light and the diaphragm or pinhole aperture. Also, chemical stains applied to the specimen can enhance contrast. In principle, lighting and contrast can be dramatically improved using modifications such as dark field, phase contrast, and differential interference contrast. In this thesis, mainly bright field mode is used to investigate the sample. Dark field mode has been used once to improve the image contrast.

Most common magnification here is 10 x. To get the real magnification of the final image one has to multiply the magnifications of the objective lenses and the ocular.

One very important advantage is that similar to the AFM, only a negligible influence of the technique on the organic film occurs that avoids e.g. decomposition of the molecules.

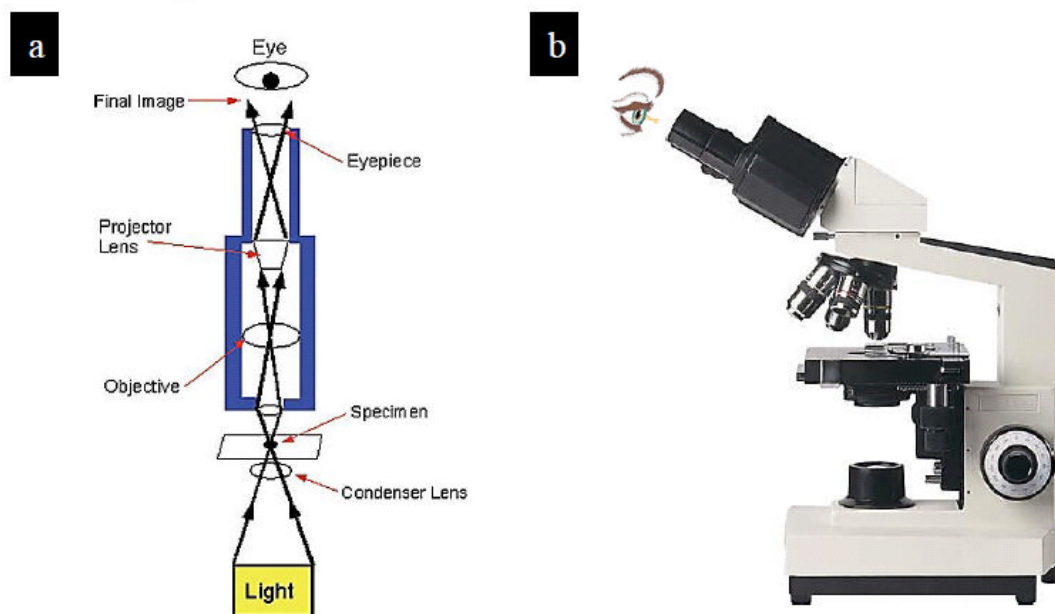


Figure 3.1: Optical microscope: (a) optical path of the light beam in an optical microscope, (b) Picture of a typically optical microscope.

3.2 Atomic force microscopy (AFM)

AFM is called atomic force microscope. AFM is an important technique in nanoscience and nanotechnology. Binnig and Quate established atomic force microscopy (AFM) about 26 years ago [92]. This enabled high-resolution visualization of structures at the atomic- and nanometer-scales for insulators in surface analysis for the first time. The materials under investigation include thin film of organic or inorganic materials, ceramics, composites, polymer, metals synthetic and biological membranes, and semiconductors. AFM is also used to investigate a wide range of sample types at ambient conditions and even in liquids or any kind of material in different gas phases. The fundamental principal of AFM is based on creation of high resolution topological image by moving sharp tip at the end of a cantilever on materials surface as illustrated in **Figure 3.2**. These measurements have been performed on scales from hundreds of microns down to nanometers and a maximum height on the order of 10-20 micrometers. The feature of AFM is providing three dimensional surface profiles. When the tip scans the surface by moving up and

down, the tip and the surface generate force which causes the cantilever to bend [93]. The deflection of the cantilever can be measured by optical lever including a laser beam reflected from the back site of cantilever which records a position-sensitive laser detector. The positional sensitive diode measures the changes of position of laser beam. A feed back loop will establish always a constant bending by moving the tip up and down accordingly.

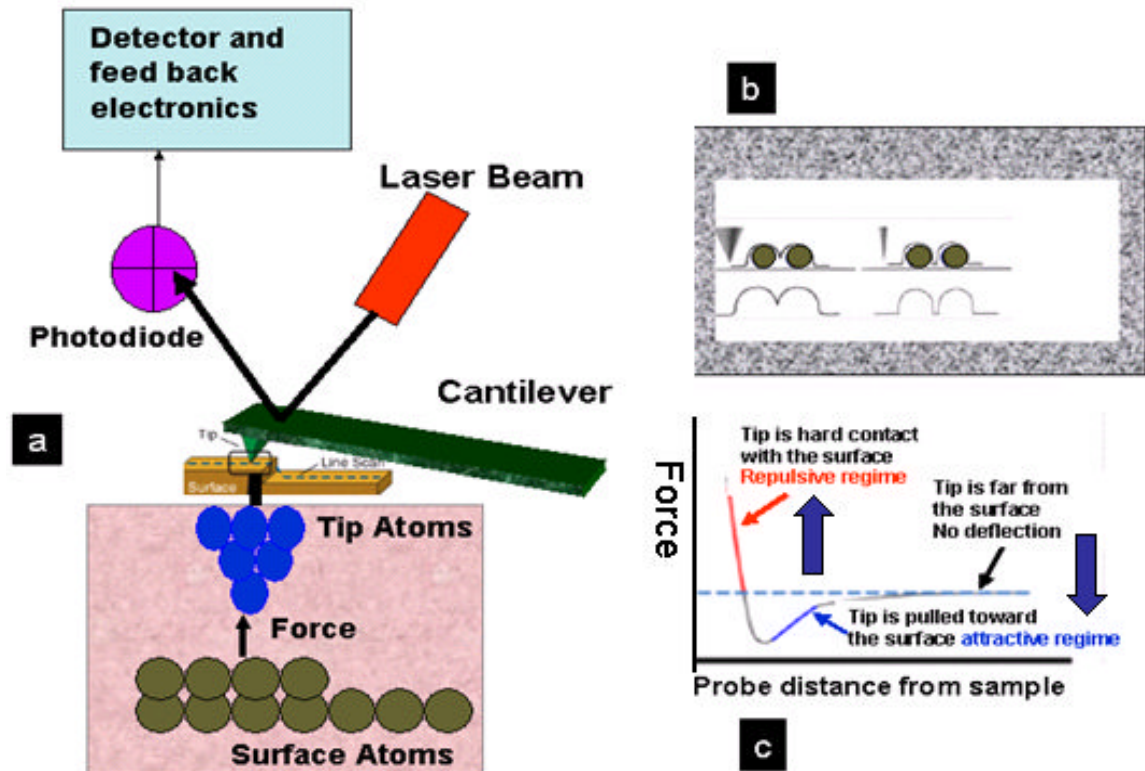


Figure 3.2 : Schematic representation of general components of an AFM and their function (a), the inset shows the close view of the tip-surface interaction. The tip-effect (b) and the force-displacement curve (c) are also shown.

The atomic forces between probe and sample surface atoms following Hooke's law which states

$$F = -k \cdot x \quad (3.2)$$

k is the spring constant of the cantilever and x is the deflection referred to the cantilevers equilibrium position. The atomic forces include at bottom mechanical forces (for contact mode), Van der Waals forces and electrostatic forces. The area of scanning can be up to $150 \times 150 \mu\text{m}^2$ where every scanning point will deliver a transferred image point. It is also possible to image single atoms. This functionality is

inherent in AFM, which is based on detection of more universal tip-sample mechanical forces. AFM uses a sharp tip (normally made from Si₃N₄ or Si) to investigate the surface under characterization. The tip is located at the last part of cantilever with a lower spring constant ($\sim 1 \text{ N.m}^{-2}$). It transports physical contact with the surface as shown in **Figure 3.2**. Nano sized tip is about 500 nm long and 100 nm wide. The position of the cantilever is very important for example, when the cantilever approaches the surface, weak attractive Van der Waals is forced between the cantilever atoms and the surface. Also, the cantilever is pouched into the surface repulsive forces obtained. Van der Waals force and repulsive forces displace or affect the cantilever. They are used to measure surface properties and topography as demonstrated in **Figure 3.2**.

3.2.1 Probe-sample interaction

This functionality is inherent to AFM. Image contrast obtained can be achieved in many ways a tip on a cantilever, forming a probe. The three main kinds of interaction are contact, tapping, and non-contact modes. Here, the non-contact mode is used for topographically analysing micro-nanostructures of different pharmaceutical thin films. Hence, the contact and non-contact modes are selectively discussed.

3.2.2 Contact Mode

In contact mode, when the cantilever is pushed into the materials surface, the tip and sample remain in close contact as the scanning proceeds resulted in the repulsive regime or repulsive force of the curve of the inter-molecular force recorded (see **Figure 3.2 b**). In this mode, the tip never leaves the surface as shown in **Figure 3.3 a**), so this mode can be used for high resolution image. The maximum vertical force is also controlled, so the compression of the sample can be limited. As the tip moves over the surface, the lateral forces can be a problem in some situations, and can be advantageous in others. The lateral deflection can give information about the friction between the tip and the sample, and can show areas that may have the same height, but different chemical properties. In contact mode, the set point value is the deflection of the cantilever, so a lower value of the set point gives a lower imaging force.

3.2.3 Non-contact Mode

This mode is suitable for samples with great differences in height and for damageable samples like polymers and active pharmaceutical molecules because the probe is only touching the surface slightly for a short time. In non-contact mode, the cantilever must be oscillated above the surface of the sample at such a distance that it is no longer in the repulsive regime of the curve of the inter-molecular force as demonstrated in **Figure 3.2b**. Its resonance frequency is stimulated through an external force. The resonance frequency can be calculated with the equation:

$$\omega = \sqrt{\frac{k}{m}} \quad (3.3)$$

where m is the effective mass. As the probe and the sample are not touching each other, mechanical forces do not act. Due to the distance, the attractive forces play a major role. Depending on the change in the distance, the resonance frequency shifts. This shift measures the interaction force like Van der Waals forces. Non-contact mode may be used when AFM imaging is very difficult to operate in ambient conditions. It can be used in organic materials to protect the surface from damaging by contact mode. The non-contact mode is a dynamic mode since the cantilever is oscillating at its resonance. The assembly can be seen in **Figure 3.3b**. The probe consists of the cantilever with a small fine tip at the end which is scanning the sample surface. A piezoelectric element moves the probe over the surface. Due to the interacting forces between tip and surface, the cantilever is deflected. As mentioned before, this deflection is measured with the help of a laser beam that is aimed on the top side of the cantilever. When the cantilever is deflected, the laser beam is reflected differently and is recorded in a photodiode.

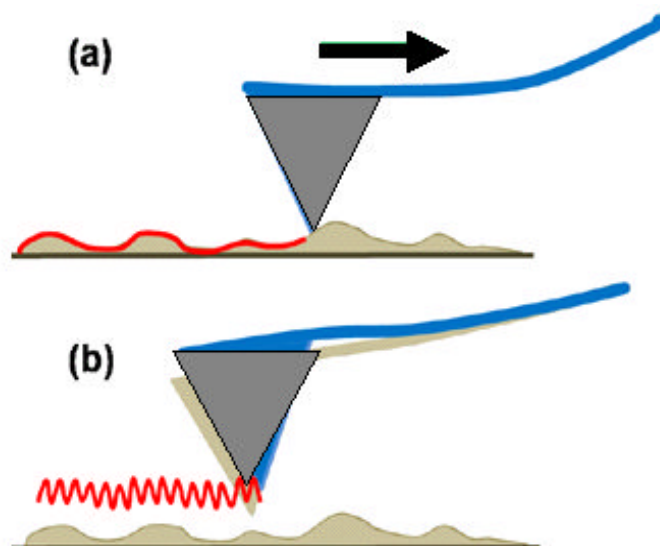


Figure 3.3: Sketch depicting contact mode (a) and noncontact mode (b) of the AFM.

3.3 Scanning electron microscopy (SEM)

3.3.1 Basic principle

Scanning electron microscopy (SEM) is one of the most popular tools used for the thin films characterization. The SEM has many advantages if compared to traditional optical microscopes. Since electrons are used instead of light which can produce a higher resolution in the range of nanometers. The accelerated electrons exhibit much shorter wavelengths than the visible light. Therefore, closely spaced specimens can be magnified at much higher levels. Moreover, SEM has a large depth of field about 1 nm. This allows more of a specimen to be in focus at one time.

The SEM is used for imaging the surface of the materials (e.g., topographical features) with the aid of signals resulting from the interface between the probe electrons and the specimen. The strength of the SEM lies in its inherent versatility due to the multiple signals generated, simple image formation process, wide magnification range, and excellent depth of field. Here in this work, the SEM (Philips X L 30) is used for thorough topological investigations of various micro nanostructures of different pharmaceutical molecules. The characteristic of the deposited thin film is also studied before the micro/ nano structured formations (see images in **Chapter 5**). The topography analysis of deposited pharmaceutical organic molecules was done after condensing the deposited material on different substrates by thermal

evaporation. The fundamental principle of the SEM is to accelerate electrons to go faster on sample or near surface and extract information about the later from interactions with the electrons to get a topographical image. The magnification can reach 1:1.000.000 with a high depth of field reaching 1 nm. The electron gun operates typically over a range 0-30 keV that sometimes extends up to 60 keV depending upon the type of instrument and application where the specimen is maintained at earth potential.

3.3.2 Instrumentation

Figure 3.4a illustrates a representative diagram of an electron optical column for two lenses of SEM how they are arranged.

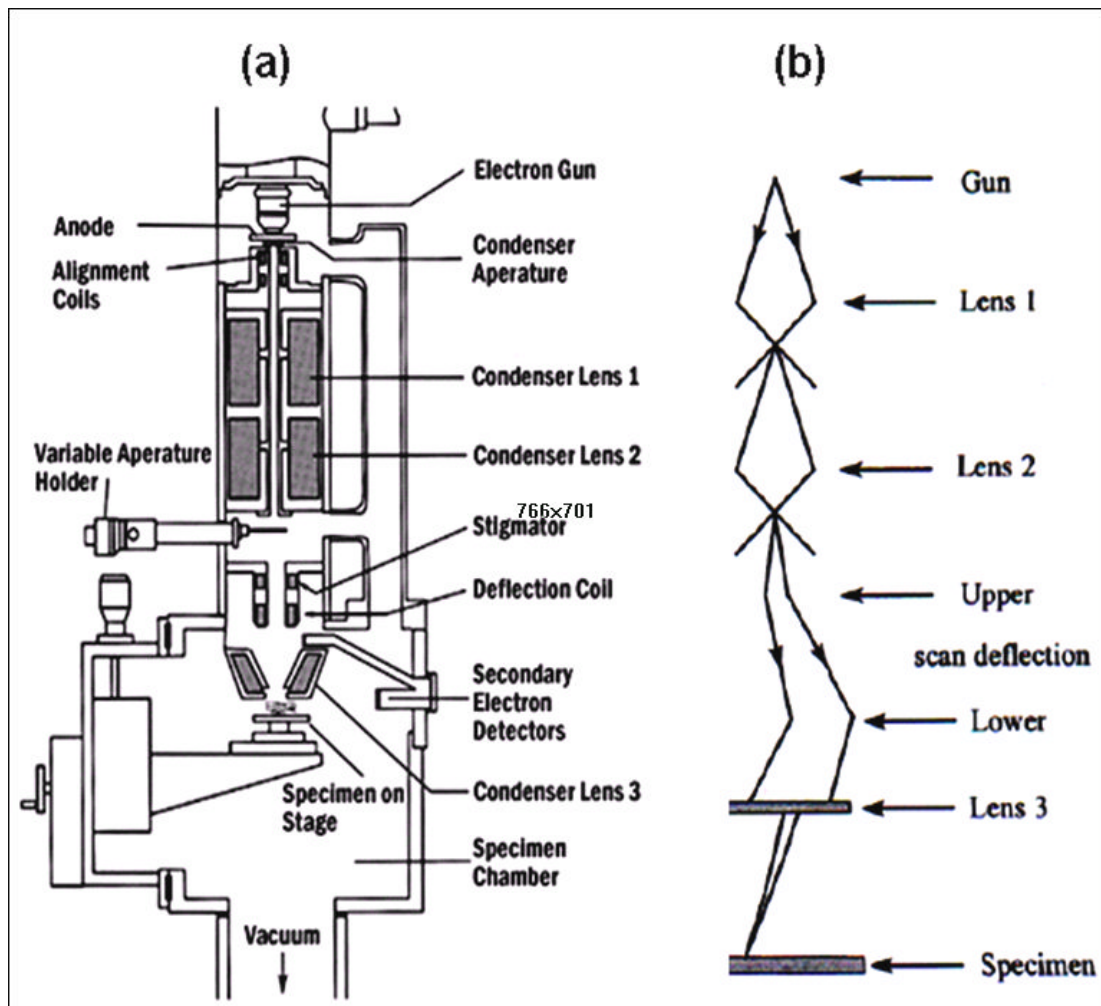


Figure 3.4: Schematic diagram of a scanning electron microscope (a), and Ray paths in SEM; standard arrangement for image formation (b) [94].

The setup of the SEM including a source of electron used in vacuum which focused into a fine probe that is scanned over the surface of the specimen. Vacuums are needed to stop electrical discharge in the gun assembly (lightning), and to permit the electrons to travel within the instrument without hindrance. As the electrons go on the surface, a number of interactions occurring results in releasing electrons or photons through the surface [308].

When a beam of electrons released from electron gun which passes through condenser lens and is developed into a thin stream, the objective lens fixes the electron beam onto the specimen. The objective lens contains a set of coils, which are energized with changeable voltages. The coils generate an electromagnetic field that applies a force on electron of electron beam into a sample by scanning it with a high-energy beam of electrons. The electromagnetic field of the coils also causes a spot of light on a cathode ray tube to shift at the same rate as the scanning electron beam. The microscope is a probe forming system where each lens condenses and de-magnifies the electron source to a focus spot at the specimen surface. The corresponding ray diagram for a complete microscope is illustrated in **Figure 3.4b**. Apertures are integrated at various positions to minimize divergence of the electron beam. To get the smallest diameter electron probes incident on the specimen the final condenser lens must have low aberrations. However, the resolution of the final image cannot be less than the diameter of the scanning electron beam. Small electron beam is of high resolution if the lens apertures are adjusted to an optimum size $\approx 150 \mu\text{m}$ diameter.

A large depth of focus is achieved for these instruments because the electron beam of the aperture is focused on the specimen surface over a distance of typically $\approx 15 \text{ mm}$. If the beam divergence is low ($\alpha \approx 3.3 \times 10^{-3} \text{ rad}$) this gives the depth focus of several millimetres. It is the combination of the high resolution with the large depth of focus which makes SEM suitable to examine topography of the materials such as thin film of pharmaceutical agents.

Three types of electron guns are in general use today: tungsten (W) and lanthanum hexaboride (LaB_6) thermionic electron guns, and the field emission gun. Tungsten and lanthanum hexaboride are used as filaments in thermionic electron guns, in which the filament (cathode) is heated by applying a current. Production of electrons occurs at high temperatures and requires the gun to be operated in a high vacuum to avoid oxidation.

The released electrons are accelerated to high energy by the submission of a negative voltage to the cathode and a bias voltage to the grid cap with the anode grounded. This triode system accelerates the electrons and provides an initial focusing into a probe. Tungsten is popular for its low cost, ease of replacement, and high current yield, while LaB₆ (used here) provides a brighter source (higher current density) useful for higher resolution. In the emission gun field, a fine tip is placed near a grid and electrons escape the surface due to the high extracting field created by the first grid. A second grid provides the accelerating voltage. Emission field requires ultra-high vacuum. When a beam of electron is emitted from the source and strikes the solid surface, it penetrates into the microstructure of the solid and interacts with its atoms.

During this procedure, two different interaction phenomena can take place: elastic and inelastic scattering. The electrons do not lose considerable energy during elastic scattering. Instead, they get deflected at the nucleus; it only changes its direction. Whereas the collision occurs between electrons of the atomic shell, it is accompanied by an energy transferred due to equal masses of the colliding particles (inelastic scattering). As a result of that, the incident electron does not only change its direction, but it also slows down. These two processes operate side by side and simultaneously. As a consequence of these different scattering events, an electron probe which originally focuses on vacuum spreads over a greater volume after penetrating the solid (see **Figure 3.5**). The shape and the size of this scattering quantity depend upon the material as well as on the energy and angle of rate of the probe electrons. The most accurate theoretical values for extension and shape of the scattering volume are obtained with the aid of Monte Carlo calculations [95, 96] to study of manipulate matters. The principal images produced in the SEM are of three types: secondary electrons (SE) images, backscattered electrons (BSE) images and elemental x ray maps. The elemental x ray maps is discussed in the following part. Secondary and backscattered electrons are conventionally separated according to their energies. The i_0 is a primary beam current, i_{BSE} is the BSE current, i_{SE} is the SE current, and the sample current transmitted through the specimen to the ground i_{SC} is defined as (according to Kirchoff current law) [97].

$$i_0 = i_{BSE} + i_{SE} + i_{SC} \quad (3.4)$$

These signals can be used to form complementary images. As the beam current increases, each current will also increase. The corresponding yields of the BSE η and SE δ , which refer to the number of BSE and SE emitted per incident electron, respectively, are defined by:

$$\eta = \frac{i_{BSE}}{i_0} \quad (3.5)$$

$$\delta = \frac{i_{SE}}{i_0} \quad (3.6)$$

This shows how they are arranged. In the upper part of the SEM, the electron source is located. It consists of a cathode, a Wehnelt cylinder and an anode. The electrons are generated in the cathode, bundled by the Wehnelt cylinder and accelerated towards the anode. Typical cathodes are thermionic emission guns or emission guns field. The principle of a thermionic emitter is to heat a small wire made of tungsten or lanthanum hexaboride (LaB_6). The energy needed overcomes the binding potential so electrons can be emitted. The emission field is based on the tunnelling effect. Strong electric fields around a thin tip consists of tungsten lower the potential wall for the electrons to be emitted. Although it is more expensive than thermionic emitters, it is still used nowadays for achieving higher beam intensities and image quality. The lens system contains two magnetic condenser lenses that bundle the electron beam, a magnetic objective lens that focuses the beam onto the sample, a deflection unit to scan the sample and apertures to avoid lens aberrations.

3.3.3 Interaction volume

As the electron beam reaches the sample, different reactions may occur as shown in **Figure 3.5** [98].

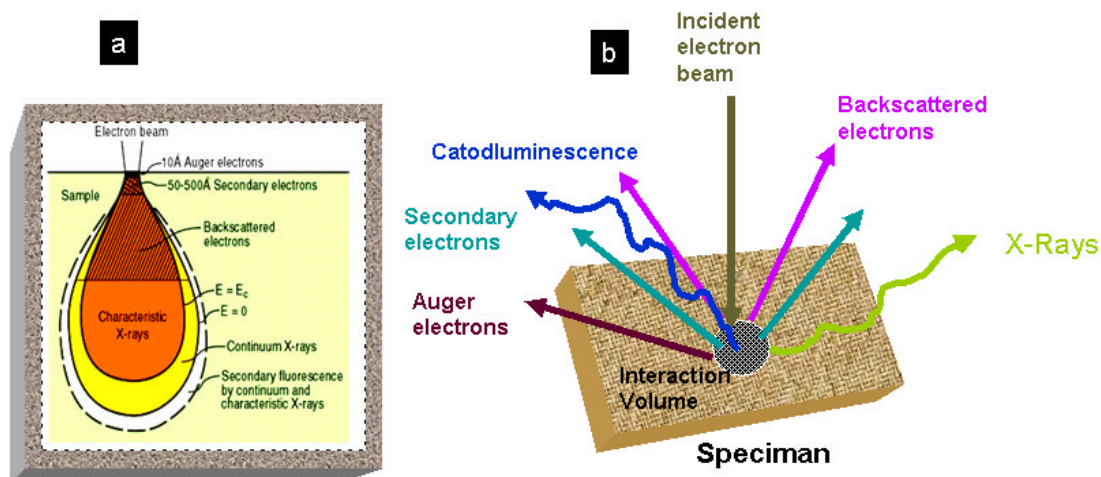


Figure 3.5: Schematic diagram illustrating the volume of material that is probed by an incident electron beam together with the volumes from which x-rays and backscattered, Auger and secondary electrons emanates.

Figure 3.5 represents the kind of information that the SEM gets from the sample and the depths that can be gathered from an electron beam-sample interaction and resulting signals. In other words, the most commonly interactions resulted from the electron beam with the specimen comprise secondary electrons (SE), backscattered electrons (BSE) and x-rays. From the surface of the specimen, Auger electrons are emitted. They are low energy electrons carrying atomic information. Secondary electrons (SE) can be found at a deeper volume. These electrons are the means of getting topographical images with SEM. Due to elastic scattering; the backscattered electrons (BSE) have energies close to primary beam electron energies. These electrons are used for the detection of contrast between areas of different chemical compositions.

Samples with high atomic numbers give better resolution due to heavy atoms backscattering electrons more strongly. Characteristic X-rays can be found at a larger volume. They give chemical compositional information An Everhart-Thornley-detector is used to collect the SE. They possess only low energies so they arise from the near-surface depth providing topographical information. The detection of BSE requires another detector because they are much more energetic than SE. The intensities of the signals are dependent on the atomic number of the material. Thus BSE provides information about the quantity materials in the sample and crystallinity.

The underlying effects are called material and phase contrast. X-ray detection is used to determine the element composition of the sample using a semiconductor detector. They are called EDX or WDX detectors, depending on the energy or wavelength dispersive x-rays. Generally, the x-ray intensities are characteristic for every material.

3.4 Energy Dispersive X-Ray Analysis

An Energy Dispersive X-ray Spectrometer (EDX) mounted in a scanning electron microscope (SEM) (Philips X L30) was used to identify and find out the local content of pharmaceutical thin films such Tetracaine-HCl co-deposited with silver which was done by thermal evaporation as shown in **Figure 3.6**. The transfer of energy from the primary electrons to the solid, i.e., the inelastic interaction, leads to various secondary process such as secondary electron (SE) emission, x-ray emission, Auger electron (AE) emission as shown in **Figure 3.5**.

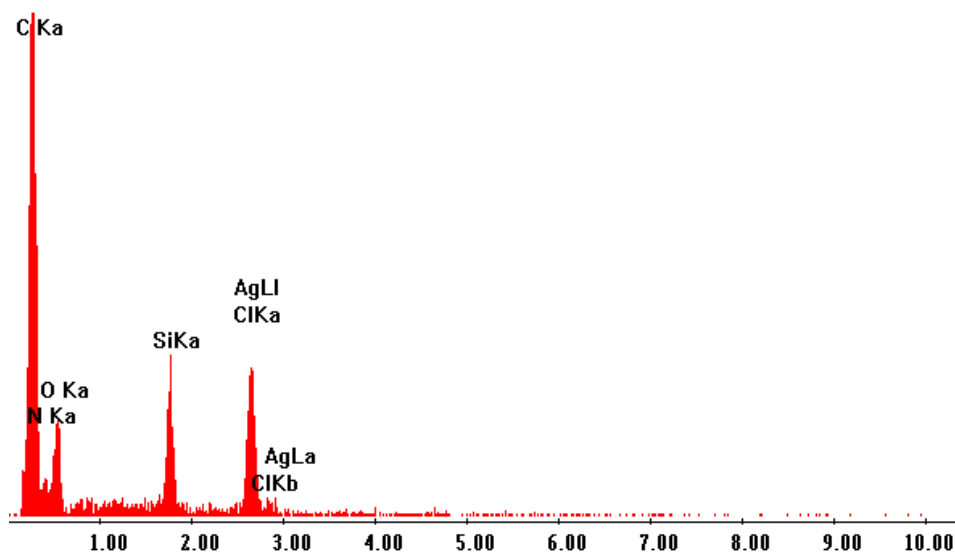


Figure 3.6: EDX spectra of the as-synthesized Tetracaine-HCl with Ag which confirms the presence of Cl, C, O, N as well as Ag.

A primary electron incident with sufficiently high energy originally removes an electron from an internal shell, for instance the K shell, and takes away it from the atom. As a result, the atom attains a higher energy state. When the atom returns to its ground state, an electron from an outer shell (e.g. L shell) fills the vacancy in the K shell. The energy released in this process leads to the either photon (x-ray) or another electron (Auger electron, e.g. from the L shell). The vacancy now left in the L shell is

filled with a further transition of an electron from an outer shell, with the associated emission of another x-ray or AE. This process will be repeated in a similar sequence until the final return of the atom to its neutral ground state.

3.5 Raman Spectroscopy (RS)

Raman spectroscopy is a spectroscopic technique depending on inelastic scattering of monochromatic light, typically from a laser source. Through inelastic scattering, the frequency of photons in monochromatic light changes when it interacts with the specimen.

Figure 3.7 showing the Raman system naturally contains four key components:

- Excitation source (Laser).
- Sample illumination system and light collection optics.
- Wavelength selector (Filter or Spectrophotometer).
- Detector (Photodiode array, CCD or PMT).

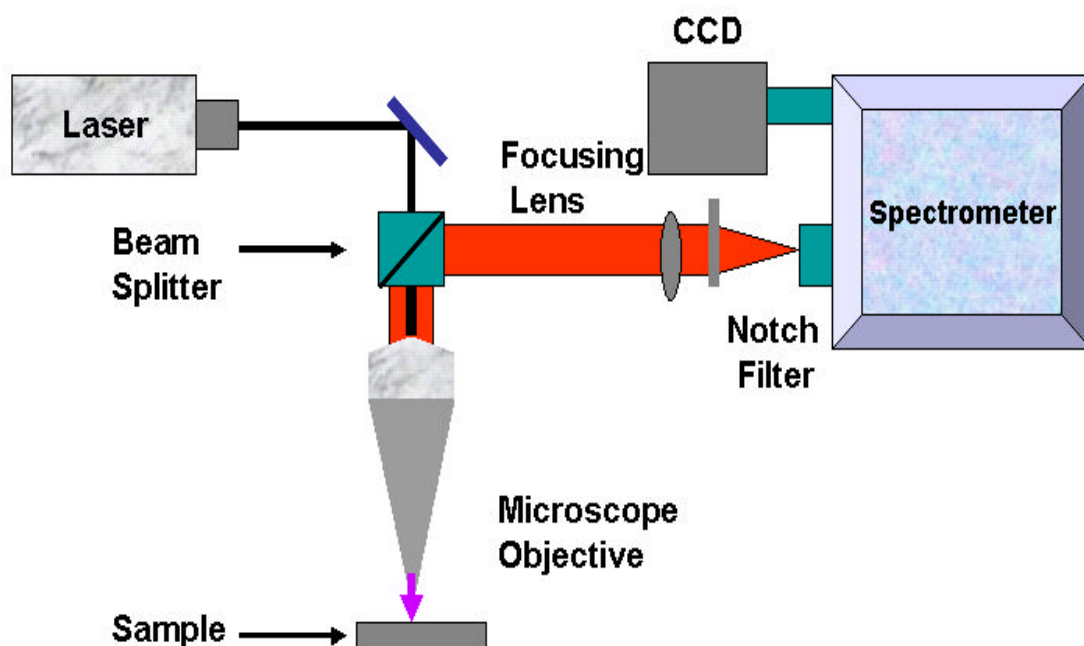


Figure 3.7: Schematic of the sample, incident light and collection optics in The Raman spectrometer where illumination and collection are performed through microscope objective.

RS is an essential fingerprint identification tool that distinguishes the chemical bonds and function groups of materials. Raman could be employed in evaluation qualitative and quantitative of chemical, biological, archaeological, semi conducting, polymeric and solid state physics. In our research, RS is used particularly for the examination of

the chemical composition of pharmaceutical samples after deposition, where characteristic peaks of deposited compounds on various substrates are clearly observed. Raman spectroscopy is also used to study the environment of molecular vibration and rotation which is mainly important in structure identification and molecular dynamics.

When the sample absorbs photons of the laser light and reemits frequency of the photons moving up or down in comparison with original monochromatic frequency which is called the Raman Effect. RS also identifies the polarizability change of a molecule. The Raman Effect is related to molecular deformations in electric field (E) which distinguished by molecular polarizability α . The laser beam can be considered as an oscillating electromagnetic wave with electrical vector E. Upon interaction with the sample, it induces electric dipole moment $P = \alpha E$ which deforms molecules. Because of periodical deformation, molecules start vibrating with characteristic frequency ν_m . a nuclear displacement is considered amplitude of vibration. Energy levels and transitions are connected to the Raman result: Laser- formed, monochromatic light of ultra- violet, visible, or infrared frequency used as the excitation source. In predictable Raman spectroscopy, visible lasers are used (e.g., Ar+, Kr+, Nd: YAG, He-Ne, diode) to motivate the molecules to high-energy "virtual" states of excitation. The Raman consequence takes place when light is focused on a molecule and it interacts with the electron cloud and the bonds of that molecule. The impulsive Raman Effect is a form of light scattering in which a photon excites the molecule from the ground state to a virtual energy state. When the molecule slows down, it emits a photon and it returns to a diverse rotational or vibrational state.

The difference in energy between the original state and this new state directs to a shift in the emitted photon's frequency away from the excitation wavelength. In other words, the underlying principle is a depolarisation of the incident monochromatic laser beam through molecular oscillations. The incident light waves interact with the electron clouds of the molecules and their bonds. In case of this study, only matter in solid state is taken into account, so molecular rotations can be ignored. The laser light is directed towards the sample where more than 90% is transmitted. A small amount

is elastically scattered and an even smaller amount is inelastically scattered at the molecules. The elastic scattering process is referred to the Rayleigh-scattering.

As one can see from **Figure 3.8**, the energy state or the frequency of the molecules will not change. The inelastic scattering process is referred to the Raman-scattering. All molecules perform certain oscillations in their initial state. Due to inelastic scattered photons, the molecules gain or lose some energy which will change the initial state to a virtually intermediate energy state. As the molecule relaxes, it falls down to a different exciting energy state whereupon a photon is emitted.

A change in frequency occurs. If the molecules gain some energy by reaching a higher energy level than the initial one, the frequency and energy of the scattered photons will be lower than $\nu_0 - \nu_m$. This process is called Stokes-scattering. However, Anti-stokes-scattering resulted from the higher frequency than $\nu_0 + \nu_m$ as well as the higher energy of the scattered photons. It is only possible if the molecule resides in a higher energy state before the collision with the photon taking place. The contributing factor is the energy difference between incident and scattered photon which is called Raman frequency shift. It is representative for every molecule. The energies of the photon for the different processes mentioned above can be clarified by the following equations. The energy E_I of the initial photon is:

$$E_I = h \cdot \nu_0 \tag{3.7}$$

The energy of the photon after Rayleigh-scattering is:

$$E_I = h \cdot \nu_0 \tag{3.8}$$

From this, the energy difference before and after striking is zero. The energy ESR of the photon after Stokes-Raman-scattering is:

$$E_{SR} = h \cdot \nu_0 - h \cdot \nu_R \tag{3.9}$$

This leads to an energy difference bigger than zero. The energy EASR of the photon after Anti-Stokes-Raman scattering is:

$$E_{ASR} = h \cdot \nu_0 + h \cdot \nu_R \tag{3.10}$$

It leads to an energy difference smaller than zero. In Rayleigh scattering including three steps, the molecule excites any virtual state then the molecule relaxes back to its original state. Finally, the photon is scattered elastically leaving with its original

energy. In Stokes scattering, the molecule excites any virtual state. After that, the molecule relaxes back to a higher vibrational state than it did originally. The photon leaves with energy $h\nu - \Delta E$ and has been scattered inelastically.

In scattering Anti-Stokes including 4 steps, the molecule starts in a vibrationally exciting state. Then, the molecule is exciting in any virtual state. After that, the molecule relaxes back to a lower vibrational state. In the end, the photon loses energy $h\nu + \Delta E$, and scatters elastically. Surface enhancing Raman usually occurs when a silver or gold colloid is used because Surface plasmons of silver and gold are animated by the laser resulting in amplifying the electric fields surrounding the metal. Particularly, Raman intensities are proportional to the electric field. So, the measured signal increases.

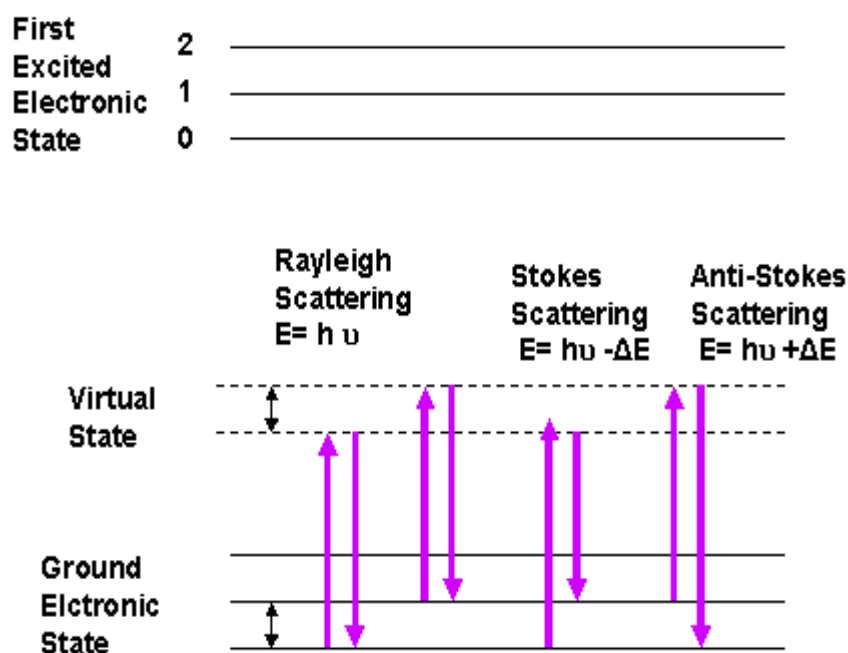


Figure 3.8: Three types of scattering by a molecule are excited by a photon with energy $E = h\nu$. The most common transition is marked with bold arrows.

3.6 X-Ray Diffraction (XRD)

The X-ray diffractometer from RICH SEIFERT & Co GmbH (XRD 3000TT) was used to investigate the nature of the deposited organic molecules which have been done by thermal evaporation. XRD is a non-destructive technique that describes the diffraction of monochromatic x-rays at a crystalline matter and can be used to define crystallographic orientations, symmetries, crystal structures, lattice parameters,

stresses and strains. Furthermore, XRD exposes information about the crystallographic arrangement, chemical composition, and physical properties of materials and thin films. It is also used to determine the size, shape inside stress of small crystalline regions, thickness of thin films and multi-layers structures. So, the crystal appears as a three-dimensional diffraction pattern for the incoming x-rays which are diffracted at the electron shells of the sample atoms. So, both constructive and destructive interference can occur. Destructive interference means that the optical path difference of incoming waves and diffracted waves are different which do not show an optical path difference. This phenomenon does only occur under specific conditions which are described by Bragg's law [99]:

$$n \lambda = 2d \sin \theta \quad (3.11)$$

N is a natural number that defines the order of the interference maximum starting from the middle, λ is the wavelength of the incoming x-rays, d is interplanar distance and θ is the angle toward the lattice plane as shown in **Figure 3.9**. Only if this law is fulfilled, constructive interferences occur in case of cubic crystals.

From that a diffraction pattern arises showing the constructive interferences as peaks which are directly related to the atomic distances. There are two main effects of x-rays, the Bremsstrahlung and the characteristic x-rays. X-rays have energy ranging from 120 eV to 120 KeV which is created whenever high-speed electrons have a collision with a metal objective. A source of electrons includes hot W filament, a high accelerating voltage between the cathode (W), the anode and the metal target like Cu, Al, Mo and Mg. To produce x-rays, electrons have to be accelerated from a coiled filament as cathode to an anode in an x-ray tube. At the anode, they are strongly decelerated whereby Bremsstrahlung is generated. Deceleration means that electrons give off their kinetic energy in terms of radiation. In addition, some electrons hit inner shell electrons of the anode material atoms which are knocked out.

The holes are filled again with other electrons from higher shells. Because these ones have higher energy than the inner shell electrons they have to give off the difference as radiation. They are called characteristic X-rays because the energy differences are specific elements. For the production of Bremsstrahlung, one can use synchrotron radiation. Electrons are accelerated in an acceleration ring where they are deflected from their direction of movement through magnetic coils. Concerning acceleration

movements, deflection is a particular form of deceleration whereby Bremsstrahlung also occurs.

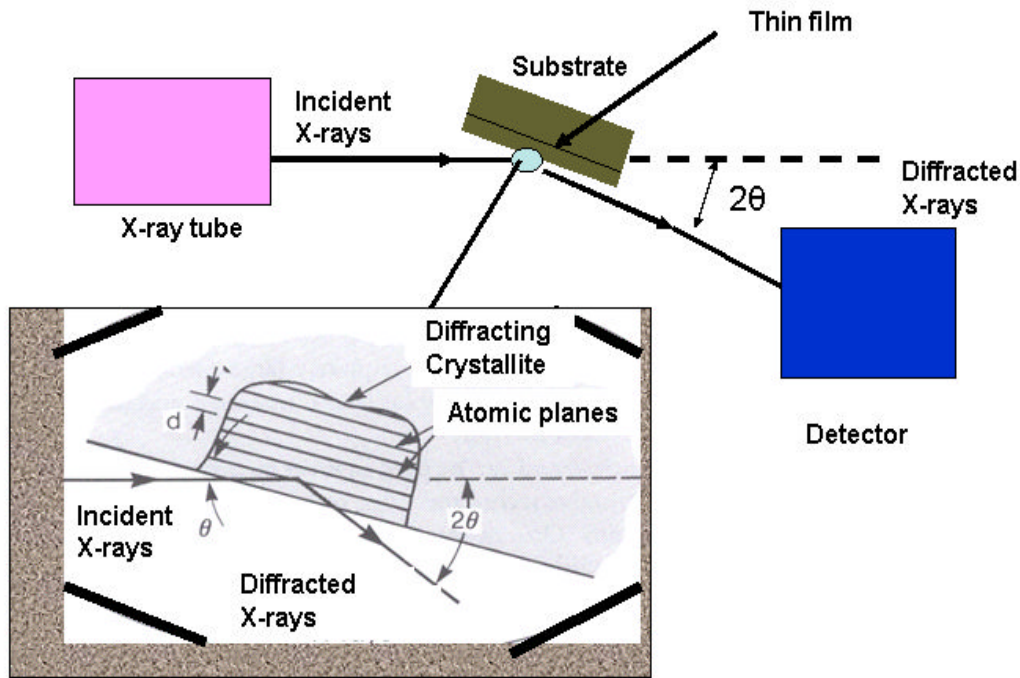


Figure 3.9: The sketch shows the schematic diagram of the setup for XRD and Schematic of incoming x-rays diffracted at lattice planes under a specific angle fulfilling Bragg's law.

In order to detect the diffracted x-rays, a counting tube, scintillation counter, or photographic films can be used as demonstrated in **Figure 3.9**. The mean grain size of the deposited film is calculated by using the Scherrer equation [100].

$$L = \frac{B \lambda}{\eta_{1/2} \cos \theta} \quad (3.12)$$

B is a constant equal to 0.9, λ is the wavelength of the radiation used, $\eta_{1/2}$ is the full width at half maximum intensity and θ is the Bragg angle corresponding to the peak considered. Crystalline parameters can be calculated from Scherrer equation. The grain size will decrease and the substrate temperature will be elevated. This is because an increasing substrate temperature causes surface energy to become higher and consequently make crystalline quality to become aggravated.

3.7 Profilometer

A profilometer is a measurement device which scans the surface of a sample to gauge its film thickness, Dektak 8000 profilometer (Veeco) was used for film thickness measurements and calibration of monitored thickness as shown in **Figure 3.10a**. Profilometer is a mechanical sensing system which measures also the roughness by the mechanical moment of a diamond stylus over the sample of interest as indicated in **Figure 3.10b**. In profilometer, the sharply pointed stylus has moves laterally across the sample in a specified distance and specified contact force where a direct contact to the surface and follows the height variations as the sample is moved. The height variations are converted into electrical signals, producing a profile. The resulting trace represents a cross-sectional view with height vertical resolution. The stylus force typically spans from 0.1 to 50 mg, enabling step heights from 0.5 nm to 800 μm . The radius of the stylus is 12.5 microns, and the horizontal resolution is controlled by the scan speed and scan length. There is a horizontal broadening factor which is a function of the radius of the stylus and of step height. This broadening factor is added to the horizontal dimensions of the steps. Moreover, the technique does not require a special sample preparation and almost any sample that will not be deformed by the stylus can be measured very rapidly. In these experiments, the steps used for thickness measurement were made by a thin narrow width mask before the film deposition process. Additional scratching of the films after the deposition process was also used as a method of conformation but not as a main method to determine the thickness of the film. The instrument can measure small surface variations in vertical stylus displacement as a function of position. The system provides a maximum of 65, 400 data points per scan for high horizontal resolution and excellent baseline stability for superior measurement repeatability. However, the accuracy of stylus measurements is affected by substrate roughness which gives excessive noise into the measurement and the vibration of the equipment.

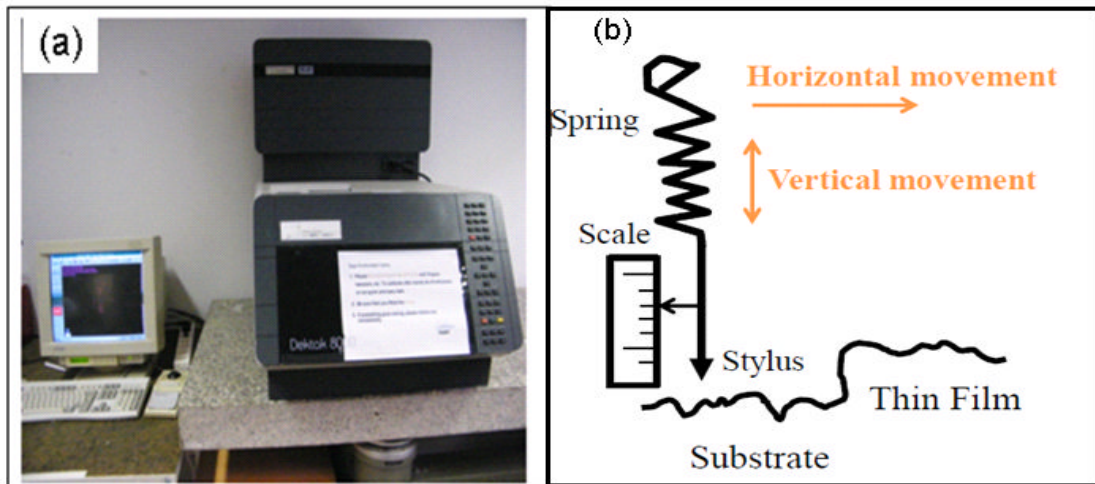


Figure 3.10: The sketch shows Dektak 8000 profilometer (Veeco) (a), and diamond tip scanning over the surface of the sample (b).

Chapter 4

4 Experimental part

4.1 Introduction

As mentioned before various chemical and physical methods can be used for the preparation of smaller drug particles. All these techniques have some limitations like utilization of toxic solvents, higher investment, consuming the time, extensive efforts and sometimes degradation the drug particles by mechanical stress. Indeed, thermal evaporation in vacuum has been investigated as an alternative and attractive technique to prepare and engineering the micro- and nano structures from organic molecules for microtechnologies, it provides an alternative approach for controlling particle size and crystal morphology. Hence, thermal evaporation method might be employed for promising drugs that would otherwise be abandoned due to aqueous insolubility.

This chapter introduces the experimental procedure and setup for the deposition experiments of active and non active ingredients by vacuum evaporation. This section also deals with deposition parameters, biological screening methods and the setup for current voltage measurements.

4.2 Evaporation chamber

The experiments were carried out in a vacuum chamber that was constructed by the Institute for Materials Science at CAU Kiel and modified in the framework of this thesis. The evaporation chamber was basically designed to evaporate pharmaceutical active molecules, inactive ingredients, polymers and metals. It allows to evaporate two different materials simultaneously on various substrates at room temperature, liquid nitrogen or various other temperatures as shown in **Figure 4.1**. The setup for vacuum deposition consists beside the two evaporators of the vacuum chamber, vacuum pumps, a pressure gauge, an observation window, substrate holder, crucible with supply connections, and shutter inside of the chamber. The shutter is placed between source and substrate and is used to control pausing or continuing the evaporation process. The sample holder is designed as spherical plate or rotatable to hold or fix the substrates which are typically made from metal. During deposition, the

distance between the sources and the substrate has been adjusted to the range of several decimetres. The evaporator itself is surrounded by a heating filament that is connected by an electrical power to heat the evaporator. In this case a lower-current filament is used with maximum current of 3 A. Thin film deposition involves a material undergoing a phase transition from a vapour phase, which is subsequently condensed onto a solid substrate [101].

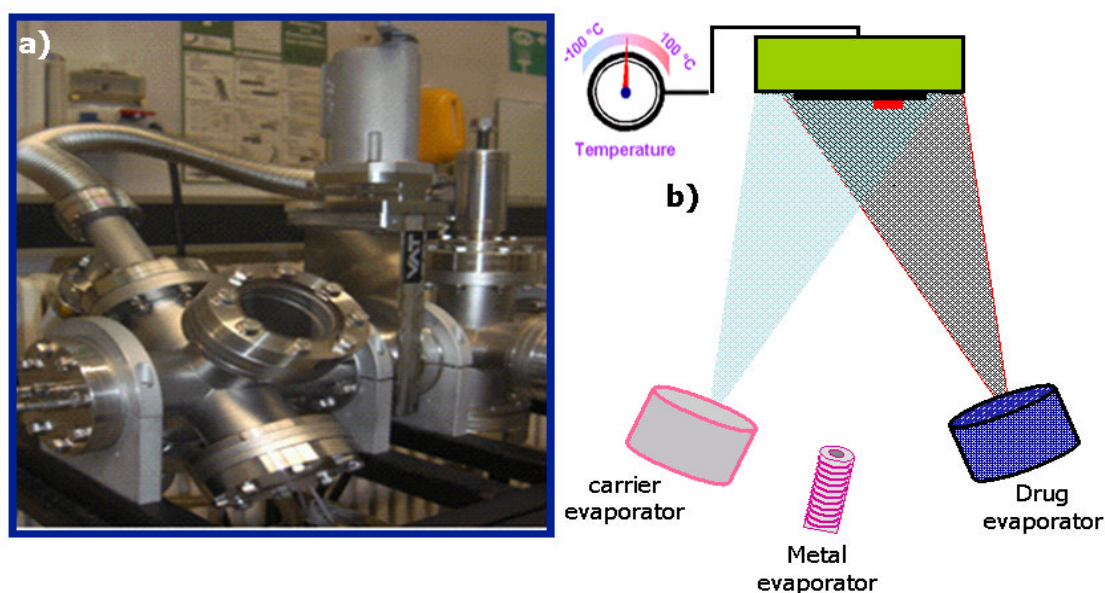


Figure 4.1: Schematic showing the deposition chamber used for thin film preparation: photo (a) and inner part of evaporation chamber (b).

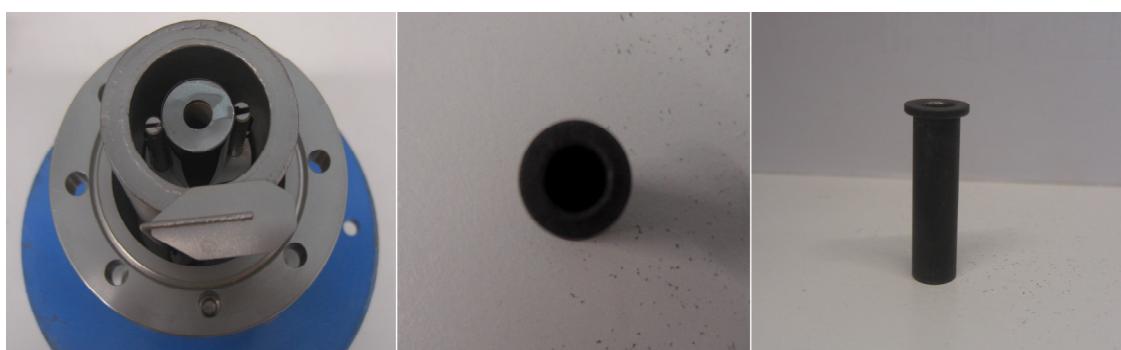


Figure 4.2: Photographs of the evaporator. In the middle the fitting for the crucible is situated. The crucible itself is shown in (b) and (c) with its dimensions tagged.

The centre is constructed in a way that allows the crucible with the dimensions to be launched into it. In this work, graphite, alumina and metal crucibles are used to guarantee ideal conditions for the evaporation for each individual material and the thin film deposition as illustrated in **Figure 4.2**. The higher vacuum is important for

this work to get the required mean free path. Vacuum should be at least 10^{-5} mbar range but in an optimal way it reaches 10^{-7} mbar. In order to reach a good vacuum, a standard setup of a pre-pump and a turbo molecular pump were used. The pre-pump creates the pre-vacuum of about 10^{-1} mbar while the turbo molecular pump provides the high-vacuum. The pre-pump was a scroll vacuum pump equipped with a set of active carbon filters in order to remove the high load of pharmaceuticals from the exhaust gas. To produce organic micro- nanostructure in various different shapes, two different materials can be evaporated from the two separate sources simultaneously, allowing a mixing on the molecular scale on the substrate. The observation window allows rotating and mounting the sample holder perpendicular to the evaporated materials.

4.3 Evaporation of Materials

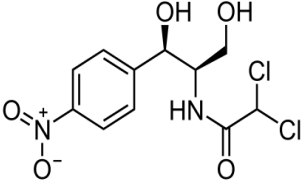
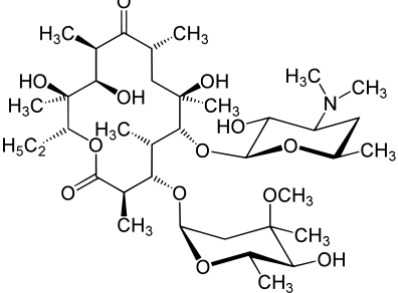
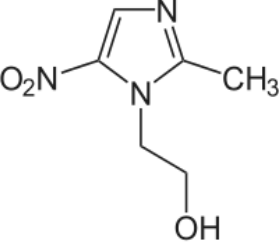
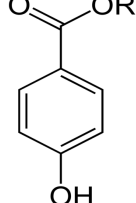
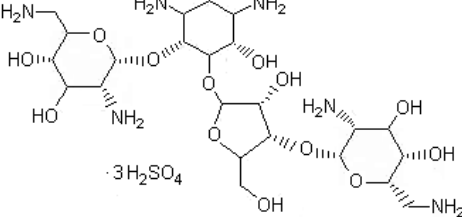
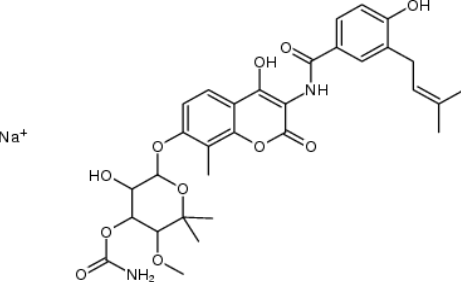
4.3.1 Evaporation of active selected pharmaceutical molecules

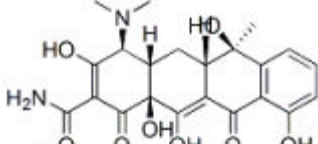
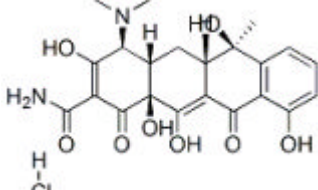
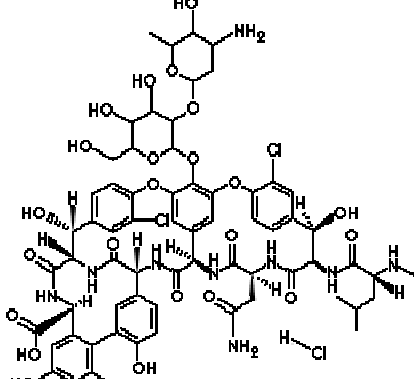
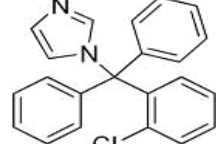
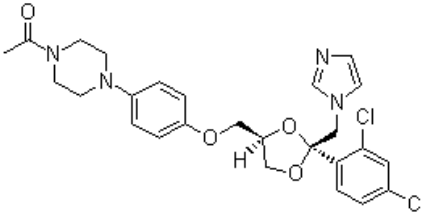
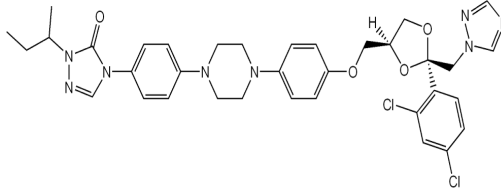
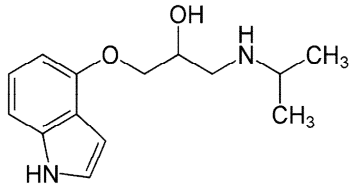
Various active pharmaceutical ingredients and excipients were selected for this study, see table 4.1. The large variety is necessary, as the evaporation of pharmaceuticals is carried out here for the first time. All substances are commercially available materials that are already in the market, most of them were provided by the collaboration partner in the department of Pharmaceutical Technology and Biopharmacy at the Christian-Albrechts-Universität zu Kiel.

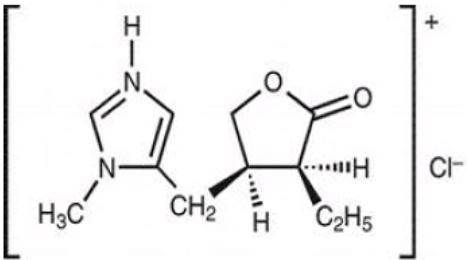
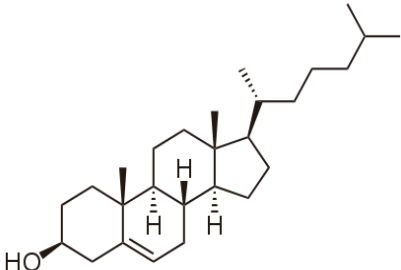
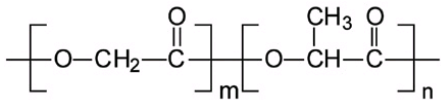
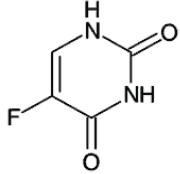
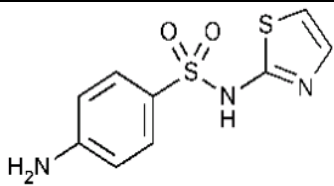
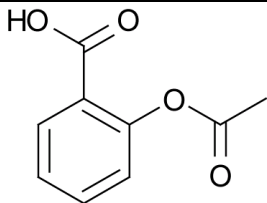
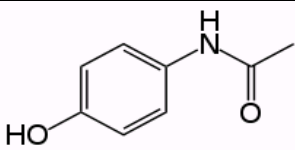
The standard evaporation procedure contains the following steps: In advance, the crucible is cleaned several times with isopropanol and acetone to remove residues. After that the sample holder has to be prepared. Different substrates such as titanium, silicon and steel are used in this study because of their potential applications. Silicon and glass have to cut into pieces with dimensions of about $2 \times 2 \text{ cm}^2$. The samples and the sample holder also have to be cleaned with isopropanol then acetone. The amount of the material to be evaporated is typically between 0.05 g and 0.2 g, depending on the nature of the individual materials and their applications, but a minimum filling height of about half of the crucible is valid for all materials to make sure that enough material is evaporated so that thin film growth can be achieved. Finally, the crucible is mounted in the evaporator.

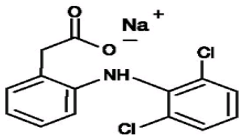
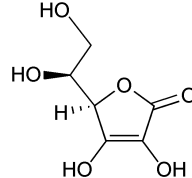
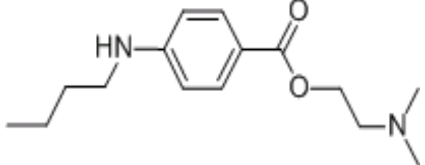
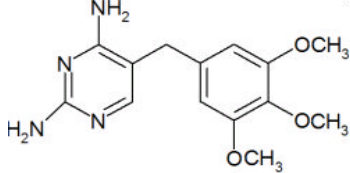
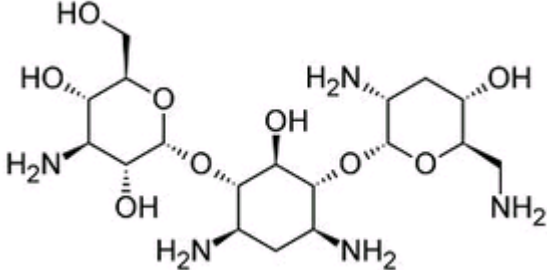
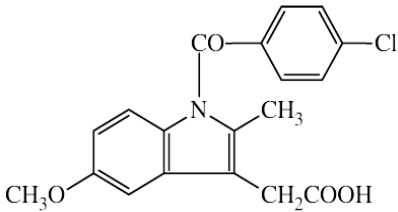
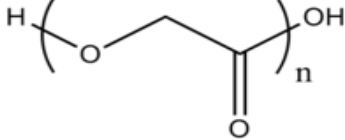
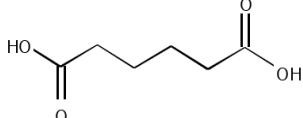
To mount the samples to the sample holder, special vacuum stable double bonded carbon tape is used. For the calibration of the deposited film thickness, a step edge in the deposited film was affected by covering parts of the samples with aluminium foil as illustrated in **Figure 4.3**. This is important for subsequent thickness measurements or thin film property analyses. After the sample holder is mounted in the chamber, it can be closed to draw the vacuum. For appropriate heating of the evaporator, the current through the heating-filament is raised to a value between 1.3 A and 1.7 A which lead to moderate temperatures in order to avoid or reduce damages in the chemical structure of the evaporated molecules. This depends individually on the melting point of each material. A thin layer of active pharmaceutical drugs on the surface of the substrate by vacuum evaporation is produced by heating materials to a temperature t ($^{\circ}\text{C}$) satisfying formula: $T_1 \leq t \leq T_2$ where T_1 is a melting point ($^{\circ}\text{C}$). T_2 is a boiling point ($^{\circ}\text{C}$) of the film-forming material. In a sequence of experiments, the optimum current was determined for each material. During the evaporation process a steep increase in pressure can be observed after the melting temperature is reached. This is due to the evaporated particles that migrate from the evaporation source to the sample holder. In order not to overshoot with the temperature the current is increased at the point of pressure increase. To maintain the temperature constant for a certain time, to make sure that all material in the crucible is evaporated, the current is kept changeless. After a certain period the current is switched off. The chamber should stay closed for some hours to avoid contamination with gas molecules that may diffuse from the chamber to the environment. Crucible materials should be chosen to avoid residual contaminants which are harmful to deposited film.

For the standard procedure, the ovens were heated stepwise over several minutes towards the desired evaporation temperature. After having reached the deposition temperature, shutters were opened allowing the deposition for a chosen time, followed by closing the shutter and reducing the temperature. For co-deposition, two ovens were mounted with an angle of 135° with respect to the sample holder that both ovens have an angle of 90° with respect to each other. Each vacuum oven is equipped with a mechanical shutter that permits blocking of the evaporated molecular flux. For simultaneous organic/inorganic evaporation experiments, metals were evaporated at temperatures much higher temperatures than the molecules, depending on their melting point even above 1000°C .

Test Material; <i>Indication and potential use of solvent free nanostructuring by TE</i>	Melting point at atmosphere (typical evaporation temperature range) [°C]	Chemical Structure of tested materials
1. Chloramphenicol; <i>Antibiotic, Increased solubility</i>	150 (~ 90-118)	
2. Erythromycin (base); <i>Antibiotic, Increased oral bioavailability</i>	190–193 (~ 100-137)	
3. Metronidazole; <i>Antibiotic, Dental implant coating</i>	159–163 (~100-194)	
4. Propyl-p-hydroxybenzoate (Nipazol); <i>Preservative, pre-preserved container</i>	95 - 98 (~ 85-165)	
5. Neomycin sulphate; <i>Antibiotic, Surface coating of wound dressings/implants</i>	250 - 260 (~ 160-300)	
6. Novobiocin sodium salt; <i>Antibiotic, Surface coating of wound dressings/implants</i>	215-220 (~ 150- 250)	

<p>7. Tetracycline hydrate; <i>Antibiotic, Device coating</i></p>	<p>170-175 (~ 100-223)</p>	
<p>8. Tetracycline HCl; <i>Antibiotic, Device coating</i></p>	<p>220-223 (~ 119-255)</p>	
<p>9. VancomycinHCl; <i>Antibiotic, Increased oral bioavailability</i></p>	<p>185 (~ 100-197)</p>	
<p>10. Clotrimazole; <i>Antimycotic, Improved nail coating</i></p>	<p>147-149 (~89-164)</p>	
<p>11. Itraconazole; <i>Antimycotic, Increased oral bioavailability</i></p>	<p>166,2 (~100-232)</p>	
<p>12. Ketoconazole; <i>Antimycotic, increased solubility</i></p>	<p>146 (~88-226)</p>	
<p>13. Pindolol; <i>Beta blocker, Contact lens coating</i></p>	<p>167-171 (~110-215)</p>	

<p>14. Pilocarpine HCl; <i>Parasympathomimetic, Contact lens coating</i></p>	<p>200 -203 (~117-250)</p>	
<p>15. Cholesterol; <i>Excipient, Biocompatible protection layer</i></p>	<p>148–150 (~90-165)</p>	
<p>16. PLGA; <i>Excipient, Controlled release layer</i></p>	<p>224 - 226 (~150-300)</p>	
<p>17. 5-Fluorouracil; <i>Antimetabolite (Anticancer)</i></p>	<p>283 (~115-250)</p>	
<p>18. Sulfathiazole; <i>Oral and topical antibiotic</i></p>	<p>200–203 (~110-250)</p>	
<p>19. Acetylsalicylic acid (ASA); <i>Non steroidal anti-inflammatory drug</i></p>	<p>135 (~90-140)</p>	
<p>20. Paracetamol; <i>Non steroidal anti-inflammatory drug</i></p>	<p>168 (~ 97-130)</p>	

<p>21. Diclofenac sodium; <i>Non steroidal anti-inflammatory drug</i></p>	<p>284 (~135-270)</p>	
<p>22. Ascorbic acid <i>Antioxidant</i></p>	<p>190-192 (~123-200)</p>	
<p>23. Tetracaine HCl; <i>Local anaesthetic</i></p>	<p>149 (~114-220)</p>	
<p>24. Trimethoprim; <i>Antibiotic</i></p>	<p>199-203 (~100-170)</p>	
<p>25. Tombramycin; <i>Antibiotic for surface coating of implants</i></p>	<p>168-178 (~153-260)</p>	
<p>26. Indometacin; <i>Non steroidal anti-inflammatory drug</i></p>	<p>155 (~150-190)</p>	
<p>27. Polyglycolic acid; <i>Biodegradable polymer, Control drug release</i></p>	<p>225-230 (~160-200)</p>	
<p>28. Adipic acid; <i>Excipient</i></p>	<p>152.1 (~119)</p>	

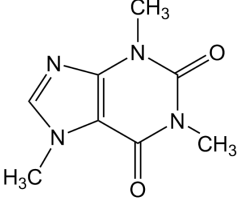
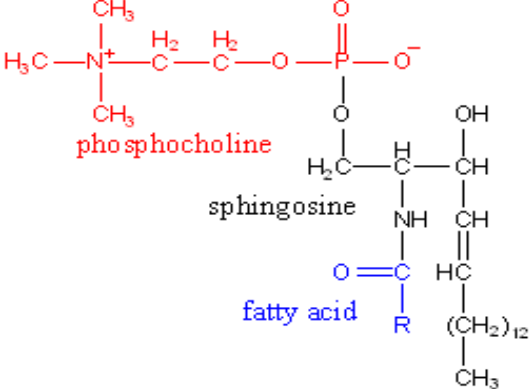
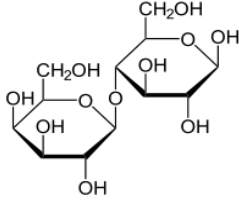
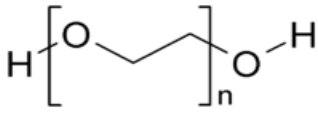
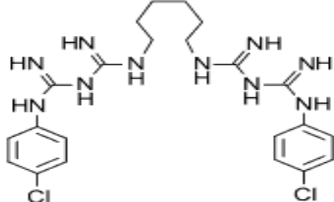
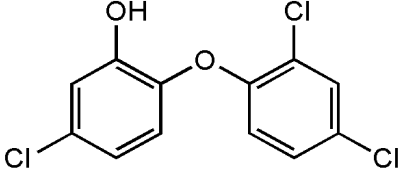
<p>29. Caffeine; <i>Psychoactive stimulant drug</i></p>	<p>227–228 (~120–250)</p>	
<p>30. Sphingomyelin (SM); <i>Excipient, phospholipide for liposomes</i></p>	<p>215 (~ 186–233)</p>	
<p>31. Lactose <i>Excipient</i></p>	<p>223</p>	
<p>32. Polyethylene glycol; <i>Excipient</i></p>	<p>49–53</p>	
<p>33. Chlorhexidine; <i>Antiseptic</i></p>	<p>134–136</p>	
<p>34. Triclosan; <i>Antibacterial and antifungal agent</i></p>	<p>56–58</p>	

Table 4.1: Overview of thermally evaporated different drug substances. First part (1–12) lists the materials which have been successfully nanostructured by thermal evaporation and have been tested with disk diffusion method. The second part (13–30)

lists the successfully deposited materials. However, the biological tests are under progress. The last part (31-34) lists the pharmaceutical substances which are not suitable for thermal evaporation as they are decomposed during deposition.

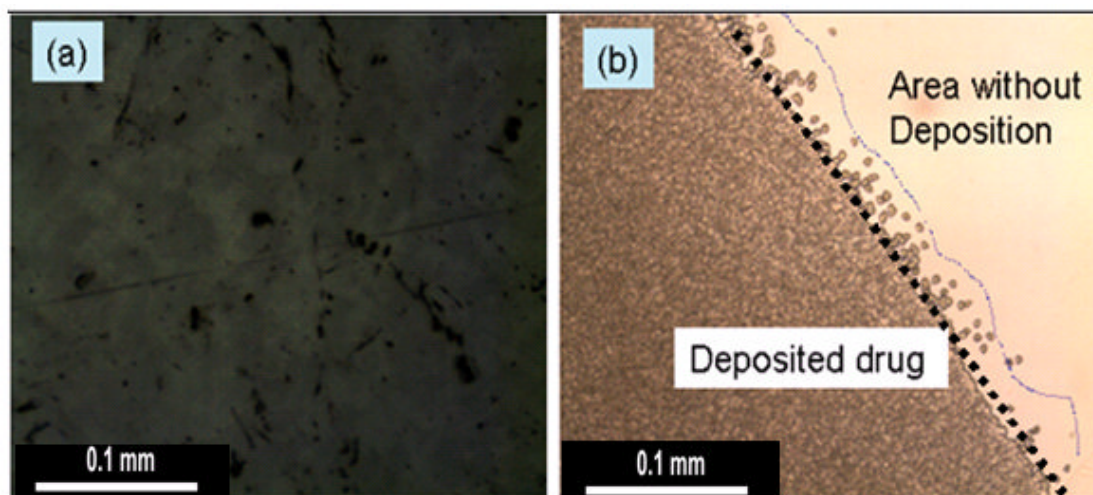


Figure 4.3: Illustrated the optical image of titanium substrate before deposition (a) and the growth of thin film by vapour deposition on titanium plate (b).

The film thicknesses of the evaporated materials is based on the substrate, geometry of chamber, distance between the source and substrate and experimental condition. Titanium, steel and silicon show high melting points (above 1400 °C) which make them ideal substrates for vacuum deposition due to their inertness. An advantage compared to glass is their conductivity which is beneficial for investigations in electron microscopes. Co-deposition of metals and active pharmaceutical molecules metals, typically gold and silver with 99.99% purity from "Goodfellow industry" are evaporated in a high vacuum chamber from an integral crucible-heater assembly. The internal representation design of the metal evaporator is illustrated in **Figure 2.2** (see **chapter 2**). Co-deposition permits the creation of a composite. This technique allows to fabricate metallic nanoclusters dispersed in a drug matrix by co-evaporation of one or more metals with drug from separate sources. In this case, a single metal is evaporated simultaneously with drugs in a controlled rate of deposition from two different sources.

Evaporation of metal and pharmaceutical materials at incident angles adjusted near the centre of the substrate surface to achieve a metal concentration gradient in the

composite film. This gradient films allow to examine, e.g., biological properties of the nanocomposites within a large range of metal concentrations prepared in one evaporation step under the same conditions. Moreover, these composite films were deposited on different substrates (Silicon wafer, titanium, Glass and polymer foil).

4.3.2 Evaporation of polymer

The same evaporator design (see **Figure 4.1**) that was used for the evaporation of the organic molecules was used to evaporate polymers as well. After the fabrication of the drug thin film, a second layer from polymer can be beneficial to protect the pharmaceutical molecules from degradation and controlling the drug release. In this study, PLGA is used as drug carrier which is a biocompatible material. The crucible is filled with PLGA powder or granulates. After applying a longer time or higher current than used for the organic molecules, maximum 2 A, the cell is heated up, the polymer melts and decomposes in molecular fragments like monomers which subsequently evaporate. Compared with the metal evaporator, this will give a high deposition rate, similar to the organic molecules. At enough rate of evaporation, molecular fragments reach the substrate and re-polymerization can occurs. Because of the high molecular of the polymer materials, the polymer thin films are traditionally prepared by chemical methods like solvent casting method or spin coating. However, this is not compatible with the vacuum process for coating the drugs and controlling release. Therefore vacuum deposition is used here even though it can be expected that a much lower molecular weight will be achieved compared to the traditional methods.

4.4 Biological screening of vacuum deposited pharmaceutical molecules

This biological screening of this research project has been conducted at department of Pharmaceutics and Biopharmaceutics, CAU Kiel. The efficacy of the preservatives, antibiotics and antimycotics vacuum-deposited on round titan plates (\emptyset 0.1 cm, thickness 0.04 cm) were examined by means of the agar diffusion test.

4.4.1 Sample preparation and antimicrobial test

The test organisms *Staphylococcus aureus* ATCC 6538 and *Candida albicans* ATCC 10231 were purchased from the German Collection of Microorganisms and Cell Cultures (Braunschweig, Germany). Muller Hinton Agar Medium, Sodium Chloride

Peptone Broth, buffered (SCPB), Tryptic Soy Broth and Tryptic Soy Agar Medium were delivered as dehydrated powders by Merck (Darmstadt, Germany). The test media were rehydrated with demineralised water and sterilized according to instructions by the supplier. For *Candida albicans* the Muller Hinton Agar was supplemented by 2 % glucose monohydrate prior to sterilization.

After sterilization and cooling down to about 50 °C, the agar medium was poured into Petri dishes (Ø 9 cm) in aliquots of 10 ml. The coagulating medium titan plates covered with vacuum deposited antimicrobial substances were placed on their sides in an upright position. Each titanium plate was deposited in the middle of the agar layer of a Petri dish. Test suspensions of *Staphylococcus aureus* and of *Candida albicans* were prepared from overnight cultures at 34 °C by floating the cultures using sterile sodium chloride peptone buffer. The cell concentrations in the resulting suspensions were assessed by means of spectrophotometer and the suspensions were diluted in order to adjust microbial numbers of 5×10^5 cfu/ml. 0.1 ml-aliquots of the suspensions were used to inoculate 5 ml-portions of sterilized and cooled down agar medium to achieve test concentrations of about 10^4 colony forming units per ml. Immediately after inoculation and mixing, these portions of the fluid agar medium were poured into the test dishes in order to get homogenous layers around the titan plates. Then the agar was allowed to gelate.

Control plates were prepared using paper discs (Ø 0.6 cm) which were impregnated with 20 µl of diluents containing the required test substance. In the case of poor water solubility, dimethylsulfoxide was used and hydrophilic substances were dissolved in sterile demineralised water. As final concentration per paper disc, 30 µg of the respective substance were chosen. The discs were placed on the surfaces of inoculated agar medium plates after their gelation. The test Petri dishes were incubated at 35 °C for 20 hours and then the extents of the inhibition areas were measured.

4.5 Current-Voltage (FET) Response

The field of electrically conductive organic substances got significantly broadened in recent years broad. It is applied in, for example, cell phone displays. But little is done with pharmaceutical molecules in this respect which in principle offer many opportunities. Visionary medical applications might utilize the deposited conductive pharmaceutical materials in a multifunctional manner, e.g. for treating cancer by

electrical induced hypothermia or controlling the amount of pharmaceuticals by measuring the electrical resistance through the organic thin film. Therefore, measurements of the current-voltage (I-V) and field effect transistor (FET) response of selected nanostructured pharmaceutical drugs which were fabricated directly on a microchip with gold contacts were carried out. Electrical characterization was done using a Keithley 6485 pico-amperemeter (optimised for measuring small signals) to measure current voltage curves at different gate voltages. The source and drain contacts were fabricated by deposition through a shadow mask and the gate contact was realised in the substrate consisting of a p^{++} -doped silicon wafer covered with a 100 nm thick gate oxide.

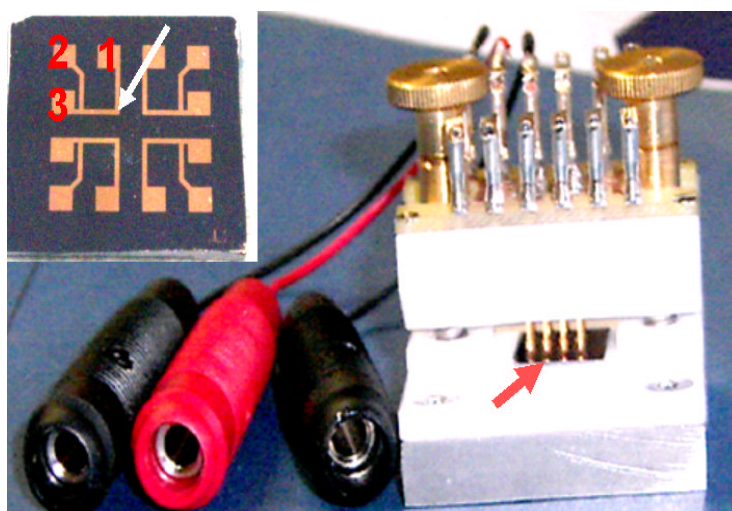


Figure 4.4: This is a photo of the microchip holder device which was used to measure the electrical properties of various pharmaceutical molecules. The inset (top left) shows the microchip consists of horizontal organic molecules at each of the contact junctions, and the number refers to the contact points.

4.6 Analysis by Optical, Atomic Force, Scanning Electron and Raman Microscopies

Bright field optical micrograph images of deposited drugs on different substrates were taken by Zeiss optical microscope equipped with a Leica DFC 280 digital camera system at different magnifications. Atomic force microscopy (AFM) images were recorded with Thermo Microscope-Veeco autoprobe AFM equipped with an optical unit and electronic module in contact and non contact mode. Standard silicon nitride tips mounted on cantilevers were used. Philips-FEI XL30 SEM equipped with an

EDAX EDX detector was used to analyse the structural geometry of nano- or micro-scale deposited drugs. In order to avoid the structural damage in the structures and the charging, acceleration voltages were kept as small as possible down to 2 kV and reduced currents were also applied. In order to get the actual morphologies of thermal evaporated pharmaceuticals, no further coating (of carbon or gold thin film) was performed on deposited drugs. This was the reason that the SEM images with higher magnification appear less focused. Raman spectra of raw drugs as well as thermally evaporated layers on different substrates were recorded to ensure the identity of substance using a Senterra Raman Microscope (Bruker Optik GmbH, Bremen, Germany) with OPUS software (Bruker). For the raw material, the sample was prepared on a sample holder or on a mirror plate to obtain a flat sample surface for measurement. The sample was mounted under the objective and the sample surface was brought in focus using the light microscopic image. For all measurements, a 20x magnification is identified as suitable and in combination with a slit aperture of 50 x 1000 μm ensures collection of the highest possible Raman intensity. Collection of the Raman spectra has been performed in the dark field with 535 nm (green light) laser excitation (50 mW) at a resolution of 3-5 cm^{-1} resulting in a full spectrum from 80 – 3500 cm^{-1} with 10 seconds integration time and 2 co-additions. The Raman shift was calibrated automatically using the SURECAL option of the instrument. For analysis, the Raman band positions in the fingerprint region of the vacuum deposited drugs were compared with respect to the Raman spectrum of the raw material.

Due to interference colours, a visible inspection of the substrate is sufficient to decide if a thin film is deposited on the substrates or not. To get a more detailed overview of the surface the light microscope is used. It uses an ocular with a magnification of 10 x, as the objective lenses have magnifications between 20 x and 50 x. With this microscope both bright field and dark field can be imaged. In bright field modus the light is transmitted through the sample from below and can be seen above. Thicker parts appear dark in the image. In dark field modus, the un-scattered beam is excluded from the image thus these parts of the sample appear dark. This feature may help to sharpen the contrast for various images. For further physical property investigations like thin film adhesion, thickness or general structural appearance of the sample SEM, AFM or profilometry can be applied. In certain cases, it is necessary to know the film thickness because in the field of drug therapy it exerts influences on the dosage of the medicament as well as on the release time. Film thicknesses measured for this thesis

differed between some hundred nanometres to about 35 μm for all materials used. Uniformly covered samples are also preferable. Leakages in the coating of a drug, for example, can bear unacceptable risks because release of the drug can proceed everywhere in the body without control. This in turn can have impact on the effect of the drug. The SEM used for this thesis is provided by the company Hitachi and is called "S-800". It uses the principle of thermionic emission with a LaB6-filament as described in chapter 4. The acceleration voltage of the electrons is 5 kV. For AFM operation the non-contact mode was used because it diminishes the damage of both probe and sample. The investigations were carried out in air. Concerning chemical properties, Raman-spectroscopy or XRD can be considered. Raman spectra are obtained from the raw material and the vacuum deposited layer on different carrier materials to ensure substance identity utilising a Senterra Raman Microscope (Bruker Optik GmbH, Bremen, Germany) with OPUS software (Bruker, Version). For the raw material, the sample is prepared on a sample holder or on a mirror plate to obtain a flat sample surface for measurement. The sample is mounted under the objective and the sample surface is brought in focus using the light microscopic image. For all measurements, a 20x magnification is identified as suitable and in combination with a slit aperture of $50 \times 1000 \mu\text{m}^2$ ensuring collection of the highest possible Raman intensity. Collection of the Raman spectra is performed in the dark field with 785 nm laser excitation (50 mW) at a resolution of $3\text{-}5 \text{ cm}^{-1}$ resulting in full spectra from $80 - 3500 \text{ cm}^{-1}$ with 10 seconds integration time and 2 co-additions. The Raman shift is calibrated automatically using the SURECAL option of the instrument. For analysis, the band positions in the fingerprint region of the vacuum deposited substance are compared to the spectrum of the raw material. The substance identity after vacuum deposition is verified by Raman spectroscopy for a range of substances. It appears that the substances are deposited without degradation on various carrier materials, whereas for some parameters, the resulting substance layer spectrum does not match the raw material indicating some changes during deposition.

Chemical compositions are important to be examined because a change in particular bonds may change the pharmaceuticals and their specific desired features. For biomedical applications, it is indispensable to know that changes occur during deposition because the biodegradability or biocompatibility can be influenced by that. As Raman-spectroscope Alpha A500 made by the company WiTec is used. X-ray

diffraction (XRD) is used here to differentiate between crystalline and amorphous state of the deposited material.

Chapter 5

Results and Discussions

This chapter discusses the most important results obtained from the experiments that are performed for the deposition of pharmaceutical molecules by thermal evaporation. For simplicity, the following subsections discuss different properties including the morphological and structural characterization corresponding to each individually deposited drug. The morphological and structural investigations of deposited micro-nanostructured material are also described by optical microscopy, atomic force microscopy and scanning electron microscopy techniques. The crystalline nature and chemical structures of the deposited organic molecules were confirmed by Raman spectroscopy and XRD techniques respectively. Successful fabrication of single, hybrid and multilayers from pharmaceutical drugs has been shown. The growth kinetics is also discussed.

This chapter also provides the overview of different pharmaceutical drugs structured on the micro scale by shadow mask lithography in a controlled manner. Preliminary results for multifunctional applications of these fabricated solvent-free pharmaceutical drugs are also presented. The data in this study also extend and confirm the present findings that reducing the particles size of poorly soluble pharmaceutical compounds may increase their efficiency. As a result, this procedure could be used to treat the side effects of the free drugs.

Here, Table 5.1 provides the overview of all the different thermally evaporated pharmaceutical substances. The first part includes the materials (1-30) which have been successfully nanostructured by thermal evaporation. The last part (31-34) lists the pharmaceutical substances which are not suitable for thermal evaporation as they are decomposed during deposition.

This thesis introduces the main results of the first 21 compounds (see table 5.1) which have been characterized by Optical microscopy, SEM, AFM and Raman spectroscopy. In the other hand, compounds (22-30) have been tested by disc diffusion method.

Test Material; Indication and potential use of solvent free nanostructuring by TE	Melting point at atmosphere (typical evaporation temperature range) [°C]	Deposition remarks and characterization tools
1. Parabens (Nipazol, Nipagin); <i>Preservative, pre-preserved container</i>	95 - 98 (~ 85-165)	Crystalline deposits Optical microscopy Raman spectra, SEM, AFM, diffusion test
2. Pilocarpine HCl; <i>Parasympatho-mimetic, Contact lens coating</i>	200 -203 (~117-250)	Crystalline deposits / Optical microscope, Raman Spectra, SEM,
3. Pindolol; <i>Beta blocker, Contact lens coating</i>	167–171 (~110-215)	Crystalline deposits / Raman Spectra, Optical microscopy , AFM
4. 5-Fluorouracil; <i>Antimetabolite (Anticancer)</i>	283 (~115-250)	Crystalline deposits Optical microscopy Raman Spectra , AFM
5. Chloramphenicol; <i>Antibiotic, Increased solubility</i>	150 (~ 90-118)	Amorphous and crystalline deposits; Raman spectra, Optical microscopy and diffusion test
6. Tetracaine HCl; <i>Local anaesthetic</i>	149 (~114-220)	Crystalline deposits SEM, AFM, Raman spectra, EDX
7. Acetylsalicylic acid (ASA); <i>Non steroidal anti-inflammatory drug</i>	135 (~90-140)	Crystalline deposits Raman spectra AFM
8. Metronidazole; <i>Antibiotic, Dental implant coating</i>	159–163 (~100-194)	Crystalline deposits; Raman spectra, SEM, AFM and diffusion test
9. Clotrimazole; <i>Antimycotic, Improved nail coating</i>	147–149 (~89-164)	Crystalline deposits; Raman spectra. AFM, diffusion test
10. Trimethoprim; <i>Antibiotic</i>	199–203 (~100-170)	Amorphous and crystalline deposits
11. Sulfathiazole; <i>Oral and topical antibiotic</i>	200–203 (~ 110-250)	Crystalline deposits AFM, Raman spectra and diffusion test
12. Tetracycline HCl; <i>Antibiotic, Device coating</i>	220-223 (~ 119-255)	Crystalline deposits AFM, diffusion test

13. Erythromycin (base); <i>Antibiotic, Increased oral bioavailability</i>	190–193 (~ 100-137)	Amorphous and crystalline deposits; Raman spectra and diffusion test
14. Tombramycin; <i>Antibiotic, surface coating of implants</i>	168-178 (~ 153-260)	Amorphous and crystalline deposits; Raman spectra AFM and diffusion Test
15. Ascorbic acid <i>Antioxidant</i>	190-192 (~123-200)	Crystalline deposits SEM
16. Adipic acid; Excipient	152.1(~ 119)	Crystalline deposits SEM, Raman Spectra
17. Caffeine; <i>Psychoactive stimulant drug</i>	227–228 (~120-250)	Crystalline deposits SEM, Raman spectra
18. Cholesterol; <i>Excipient, Biocompatible protection layer</i>	148–150 (~90-165)	Crystalline deposits SEM and Raman Spectra
19. Sphingomyelin (SM); <i>Excipient, phospholipide for liposomes</i>	215 (~186-230)	Amorphous and crystalline deposits Optical Microscopy, SEM and AFM
20. PLGA <i>Excipient, Controlled release layer</i>	224 - 226 (~ 150-300)	Amorphous deposits SEM
21. Indometacin; <i>Non steroidal anti-inflammatory drug</i>	155 (~150-190)	Amorphous and crystalline deposits SEM and Raman Spectra
22. Neomycin sulphate <i>Antibiotic, Surface coating of wound dressings/implants</i>	250 - 260 (~ 160-300)	Amorphous and crystalline deposits Diffusion test
23. Novobiocin sodium salt; <i>Antibiotic, Surface coating of wound dressings/implants</i>	215-220 (~ 150- 250)	Amorphous and crystalline deposits Diffusion test
24. Tetracycline hydrate; <i>Antibiotic, Device coating</i>	170-175 (~ 100-223)	Crystalline deposits Diffusion test
25. VancomycinHCl; <i>Antibiotic, Increased oral bioavailability</i>	185 (~ 100-197)	Amorphous and crystalline deposits Diffusion test
26. Itraconazole; <i>Antimycotic, Increased oral bioavailability</i>	166,2 (~100-232)	Amorphous and crystalline deposits Diffusion test
27. Ketoconazole; <i>Antimycotic, increased solubility</i>	146 (~88-226)	Amorphous and crystalline deposits Optical microscopy
28. Paracetamol; <i>Non steroidal anti-inflammatory drug</i>	168 (~ 97- 130)	Crystalline deposits

29. Diclofenac sodium; <i>Non steroidal anti-inflammatory drug</i>	284 (~135-270)	Crystalline deposits/ Raman spectra Optical microscopy
30. Polyglycolic acid; <i>Biodegradable polymer, Control drug release</i>	225-230 (~160-200)	Amorphous and crystalline deposits
31. Lactose <i>Excipient</i>	223	Deposition not possible
32. Polyethylene glycol; <i>Excipient</i>	49-53	Deposition not possible (decomposed to gas)
33. Chlorhexidine; <i>Antiseptic</i>	134–136	Decomposes, droplets on the surface of substrate
34. Triclosan; <i>Antibacterial and antifungal agent</i>	56–58	Deposition not possible (Degrades to dioxin)

Table 5.1: Overview of thermally evaporated different drug substances. First part (1-30) lists the materials which have been successfully nanostructured by thermal evaporation and have been tested with disk diffusion method. The last part (31-34) lists the pharmaceutical substances which are not suitable for thermal evaporation as they are decomposed during deposition.

5.1 Results

5.1.1 Structural engineering of Parabens

Parabens exhibit two classes of drugs called Nipasol and Nipagin. The following results show different properties including the morphological and structural characterization at different temperature regimes and different conditions.

5.1.1.1 Optical microscopy results of Nipasol nano-microstructures

Different characterization techniques such as AFM, SEM and light microscopy used to study the morphologies of as-synthesized Nipasol micro-nanostructures. Nipasol nano-microstructures has been deposited on various substrates by a simple thermal evaporation technique without using any solvent or catalyst. These optical images of Nipasol micro-nanostructures deposited on different substrates like silicon, titanium, Si pre-coated with 8 nm gold thin film, glass, Si pre-coated with 50 nm ZnO thin film.

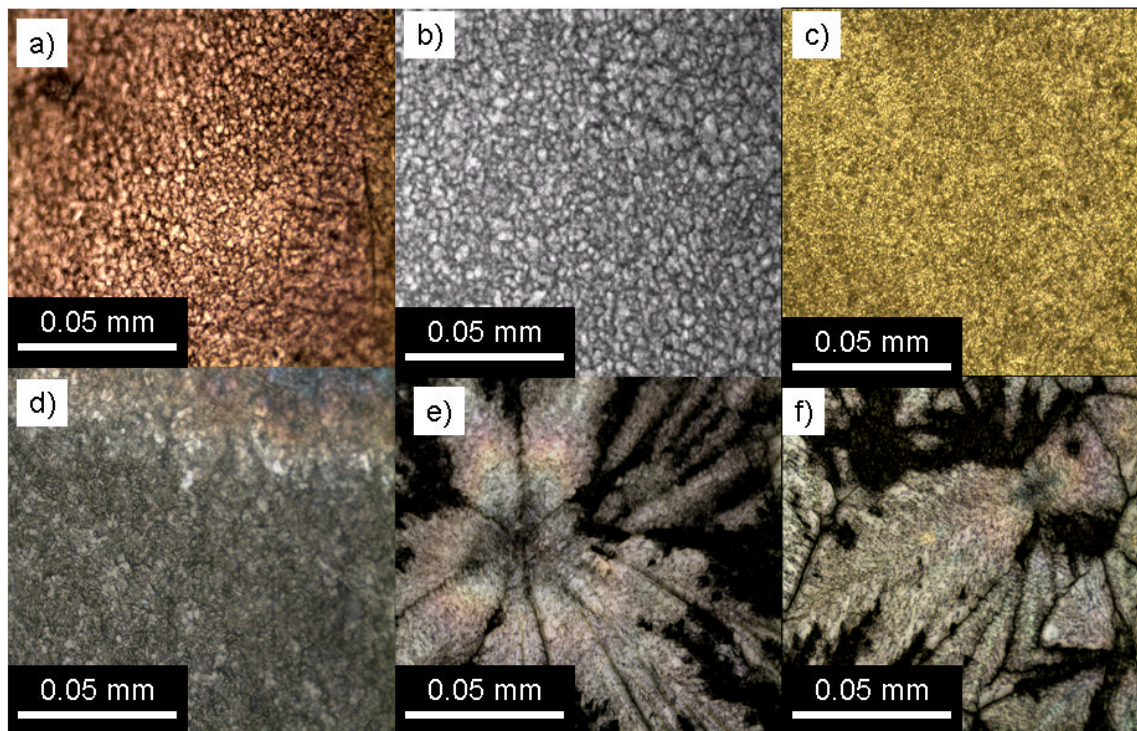


Figure 5.1: (a-d) Optical images of various Nipasol micro-nanostructured morphologies on different substrates like Ti (a) Si pre-coated with 8 nm thick Au thin film (b), glass (c), polymer foil (d), Si Pre-coated with ZnO 50 nm thick thin film (e and f) respectively.

Figure 5.1(a)-(f) shows the optical images of highly oriented Nipasol micro-nanostructures grown on different substrates at same condition. As expected, the coverage density and morphology of Nipasol micro-nanostructures on Ti, glass, Si pre-coated 8 nm Au thick thin film, Si pre-coated with ZnO 50 nm thick thin film, and polymer foil are significantly different. **Figure 5.1(d)** also shows the high density as-synthesized Nipasol structures consisting of micro-nanoparticles with various diameters and lengths of several micrometers. In the other hand, less adhesion of Nipasol nano-microstructures observed in case of utilizing glass substrate (c). It can be seen that the particles with an average size of 1 μ m were obtained by using the glass substrate. Meanwhile, as shown in **Figure 5.1(e)-(f)**, particles about 2 μ m by using Si Pr-coated with ZnO 50nm thick thin film. Obviously, the particles size of Nipasol nano-microstructures become much bigger and highly adhesion with the surface of ZnO as substrate (e and f) due to the polarity of ZnO. Reduction or increasing in particles diameter and the morphology of Nipasol can be observed in **Figure 5.1(a)-(d)** where the nucleation and further growth of the nanostructures occur. Here, the morphology of Nipasol nano-microstructures based on substrate surfaces.

5.1.1.2 AFM of Nipasol

Moreover, the morphology and microstructure of the deposited Nipasol were further studied by AFM. **Figure 5.2a-c** often shows dissimilarity in morphologies for Nipasol nano- microstructures deposited on Ti substrate at different substrate temperatures.

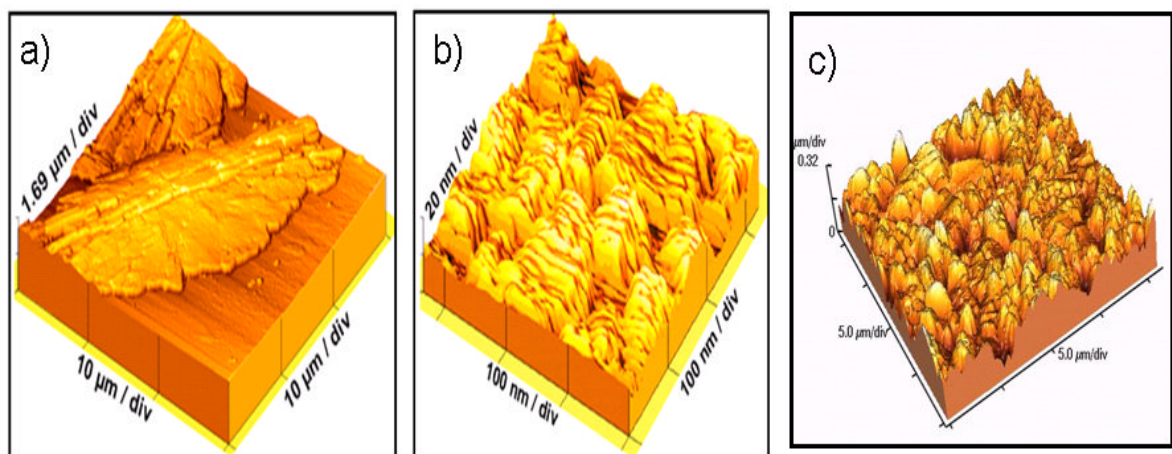


Figure 5.2: Three-dimensional AFM height image of Nipasol grown on Ti substrate at various substrate temperatures ranging from -100 $^{\circ}$ C with different magnifications (a-b) to room temperature (c).

Figure 5.3a-c shows three dimensional (3D) topographical views of Nipasol nano-microstructures grown on Ti substrate with different substrate temperatures. The scan area of $30 \times 30 \mu\text{m}^2$ and $20 \times 20 \mu\text{m}^2$. The product was dominated by various dimensions and structures.

The three-dimensional (3D) topographical view of Nipasol drug thin film grown on Ti substrate (see **Figure 5.2c**) depicts that uniform micro-crystalline covering the substrate at room temperature. **Figure 5.2a-b** illustrates that Nipasol drug film is nano-crystalline in the case of deposition at -100°C when substrate temperature which was maintained by using liquid N_2 . A height gradient from left to right is recognizable. The highest point in the left part of the scan is approximately $1.5 \mu\text{m}$ while on the right side it is around half of this value. Briefly, 3D AFM images of Nipasol grown on Ti substrate at room temperature resulting in a much larger crystal size as compared to that deposited at -100°C (see **Figure 5.3 a-c**).

Clearly, **Figure 5.3a-b** shows the grain sizes as a function of evaporation temperature and growth time. It was noted that @ $\sim 220^\circ\text{C}$ (27 min), the grain sizes of Nipasol deposited on Ti substrate are greater than the other temperature @ $\sim 165^\circ\text{C}$ (10 min) as illustrated in **Figure 5.3a-b**. With further increase in temperature a smoother surface might be expected due to an increased surface mobility of the species. According to our expectation, diffusion length of molecules along the substrate and re-evaporated of the molecules from substrate must be enhanced.

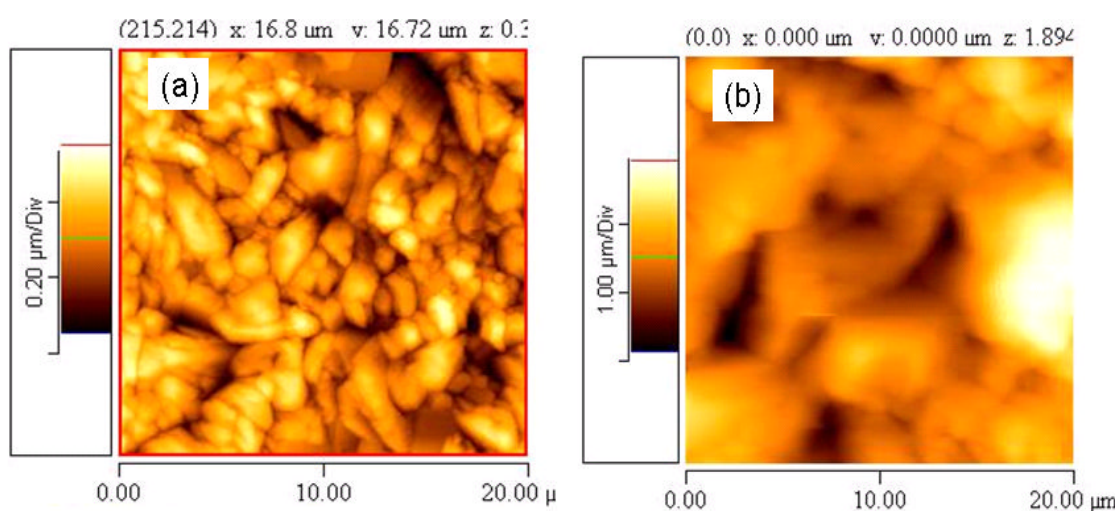


Figure 5.3: Two-dimensional AFM height image of Nipasol on Ti substrate at different evaporation temperatures @ $\sim 165^\circ\text{C}$ (10 min) (a) and @ $\sim 220^\circ\text{C}$ (27 min)(b).

5.1.1.3 SEM of Nipasol

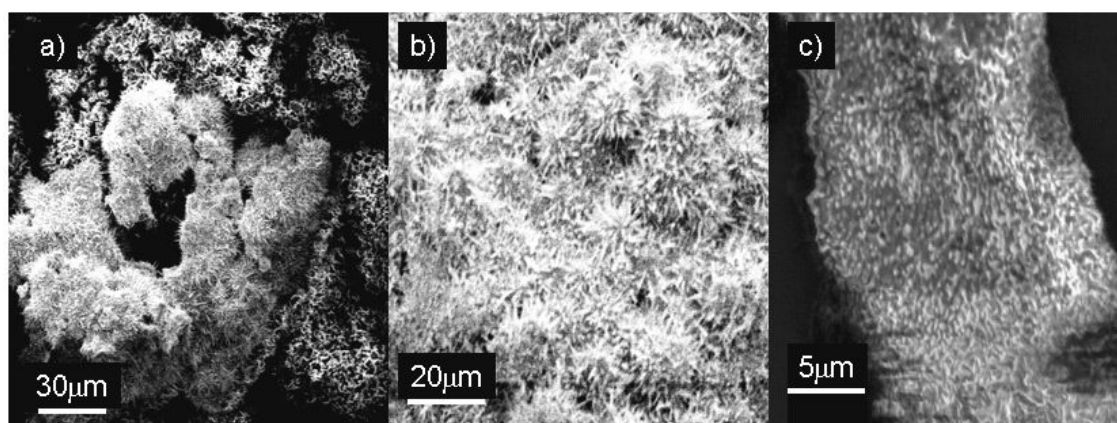


Figure 5.4: SEM images of Nipasol deposited on ZnO nanostructures at different magnifications (a and b) and microspheres on titanium substrate with substrate temperature at -100°C (c).

The SEM image (**Figure 5.4**) shows nanoneedles, nanorods and NPs like structure of Nipasol that are distributed homogeneously and uniformly over the surface.

The chemical intactness of synthesized Nipasol micro-nanostructures was further confirmed by Raman investigations. Raman spectroscopy was performed on each at sample to determine the structure of pharmaceutical ingredients and to identify the presence of specific functional groups within a specimen after deposition if compared to the control. The spectra of Raman microscopy of deposited pharmaceutical molecules on carrier and the reference spectrum are comparable which confirm that the chemical composition of deposited materials is same as their bulk.

5.1.1.4 Raman spectrum of Nipasol

Raman spectrum of Nipasol ($\nu_{\text{max}}/\text{cm}^{-1}$) shows a broad band at 3071 cm^{-1} which indicates the OH group. It is noted that bands located at 2958 cm^{-1} - 2880 cm^{-1} which are assigned principally to (C-H aromatic and C-H aliphatic). Sharp peaks located also at 1667 cm^{-1} and 1598 cm^{-1} which are corresponding to (C=O) and (C=C) respectively. As one can see here, other peaks can be observed at 1448 cm^{-1} , 1273 cm^{-1} and 1100 cm^{-1} which belong to (CH₂ bend, CH₃ bend and C-O-C) as illustrated in **Figures 5.5** and **5.6**.

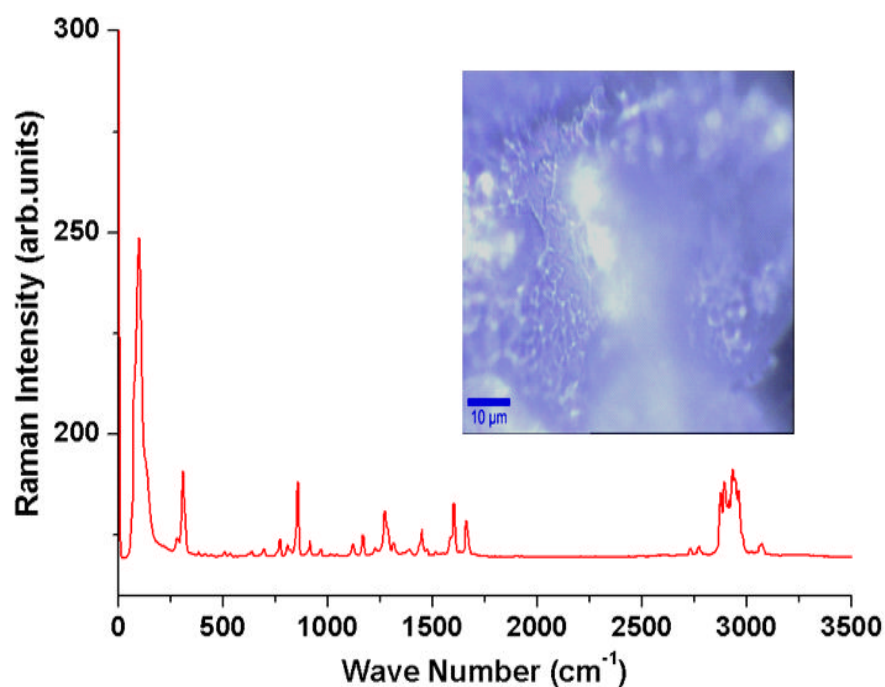


Figure 5.5: The Raman spectrum of Nipasol control sample. The inset shows the optical microscope image of the control sample.

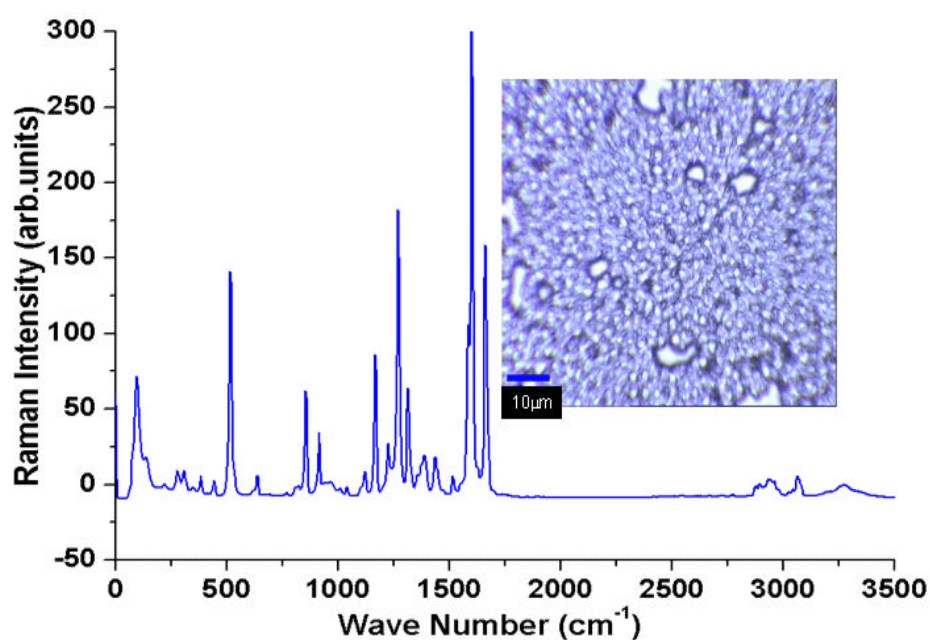


Figure 5.6: The Raman spectrum of Nipasol deposited sample. The inset shows the optical microscope image of the deposited sample.

5.1.1.5 Raman spectrum of Nipagin

Raman spectra of Nipagin (ν_{\max} /cm⁻¹) after and before deposition are similar to each other as shown in **Figure 5.7** and **Figure 5.8** respectively.

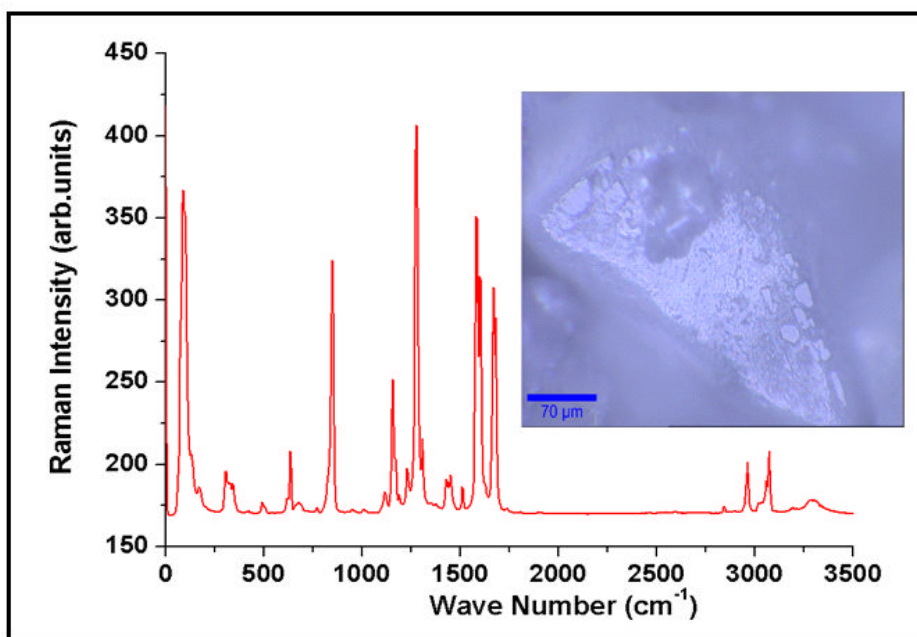


Figure 5.7: The Raman spectrum of Nipagin control sample. The inset shows the optical microscope image of the control sample.

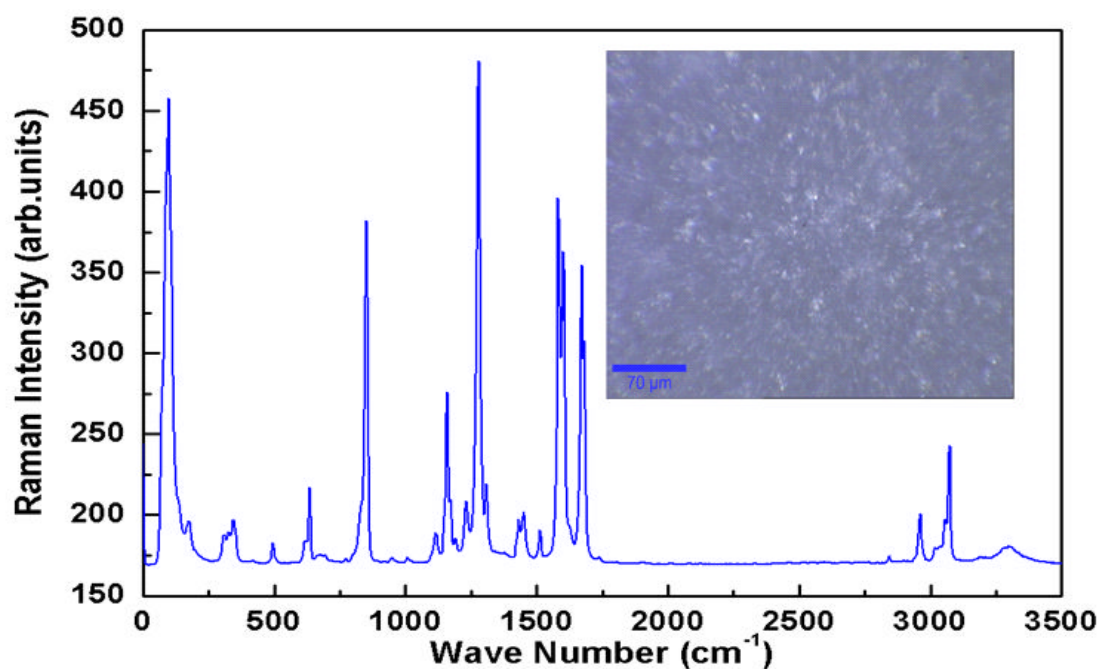


Figure 5.8: The Raman spectrum of Nipagin deposited sample. The inset shows the optical microscope image of the deposited sample.

One can expect that the presence of a broad intense band at $\sim 3303\text{ cm}^{-1}$ corresponding to the (OH stretch). The C-H aromatic located at 3083 cm^{-1} and C-H aliphatic at 2966 cm^{-1} . The Raman spectra of Nipagin also show sharp peaks located at 1675 cm^{-1} and 1579 cm^{-1} which assigned for (C=O stretch and C=C) respectively. It was shown that peaks

located at 1450 cm^{-1} for CH_2 bend and ring deformation, at 1252 cm^{-1} for (CH_3 bend) and at 1146 cm^{-1} for (C-O-C). Both spectra look similar to each other with relating to the Raman peaks which imply that the deposited sample did not exhibit any change in chemical structure. Therefore, one can assume that the deposition of crystalline Nipagin was successful.

5.1.2 Structural engineering of Pilocarpine-HCl

5.1.2.1 Optical microscopy of Pilocarpine-HCl

The deposition of Pilocarpine-HCl nano-microstructures in the range of $15\text{-}25\text{ }\mu\text{m}$ thicknesses is shown in **Figures 4.9a)-4.9d)** respectively.

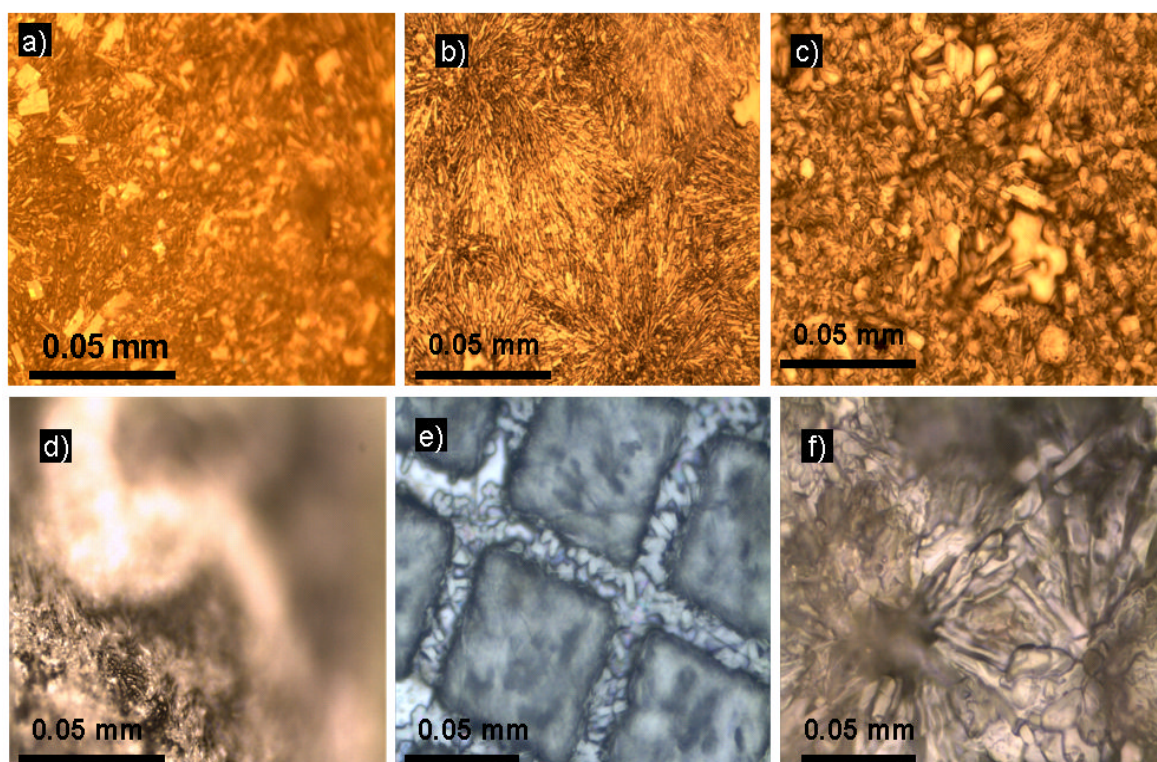


Figure 5.9: *a-e* Representative optical images of various pilocarpine-HCl micro or nano structured morphologies on different substrates like polymer foil (a), glass (b), Ti (c), soft contact lens (d), copper grid on Ti substrate (e) and large grains size deposited on ZnO substrate (f).

These structures typically exhibit high surface area to volume ratio which enable them to dissolve faster if compared to their bulk counterparts. As it is typical for thermal evaporation process, the substrate has a large influence on the structure especially in

terms of crystallinity and shape of the deposited free solvent drug. **Figures 5.9a)-5.9d)** show the differences in surface morphology of the deposition of Pilocarpine-HCl nano-microstructures grown on different substrates like polymer foil (a) glass (b), titanium substrate (c), soft contact lens (d), and through a copper grid as micro scale shadow mask on a Ti substrate (e).

5.2.2.2 SEM of Pilocarpine-HCl

The SEM image of Pilocarpine-HCl (**Figure 5.10**) shows a dense structure of rods arises from many small crystal nuclei that are distributed homogeneously and uniformly over the silicon substrate pre-coated with 50 nm ZnO thin film.

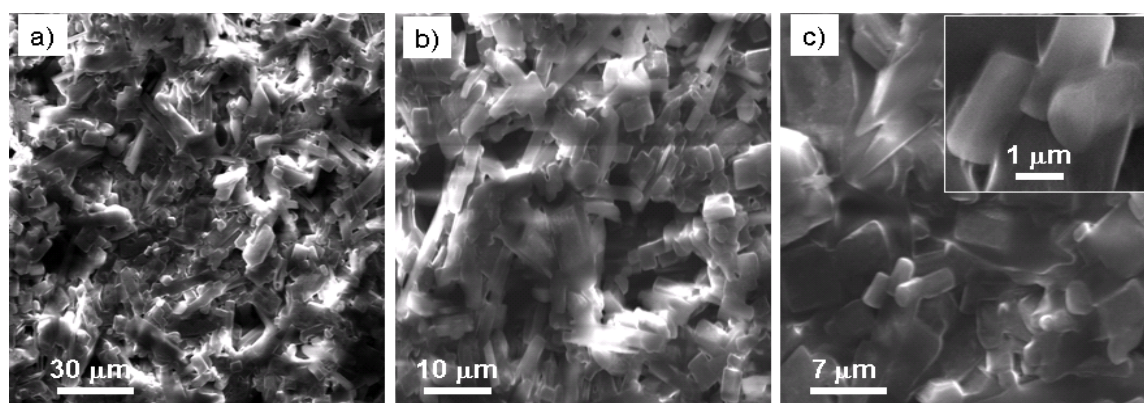


Figure 5.10: (a-c) SEM images of Pilocarpine-HCl micro-nanostructures grown on Si pre-coated with 50 nm thickness ZnO thin film with different magnifications.

5.1.2.3 Raman Spectroscopy of Pilocarpine-HCl

5.1.2.3.1 Raman Spectroscopy of Pilocarpine-HCl on Ti

The Raman shifts which imply that the deposited sample on Titanium plate (see **Figure 5.11**) never change its chemical composition. Therefore, the deposition of crystalline Pilocarpine-HCl is successful.

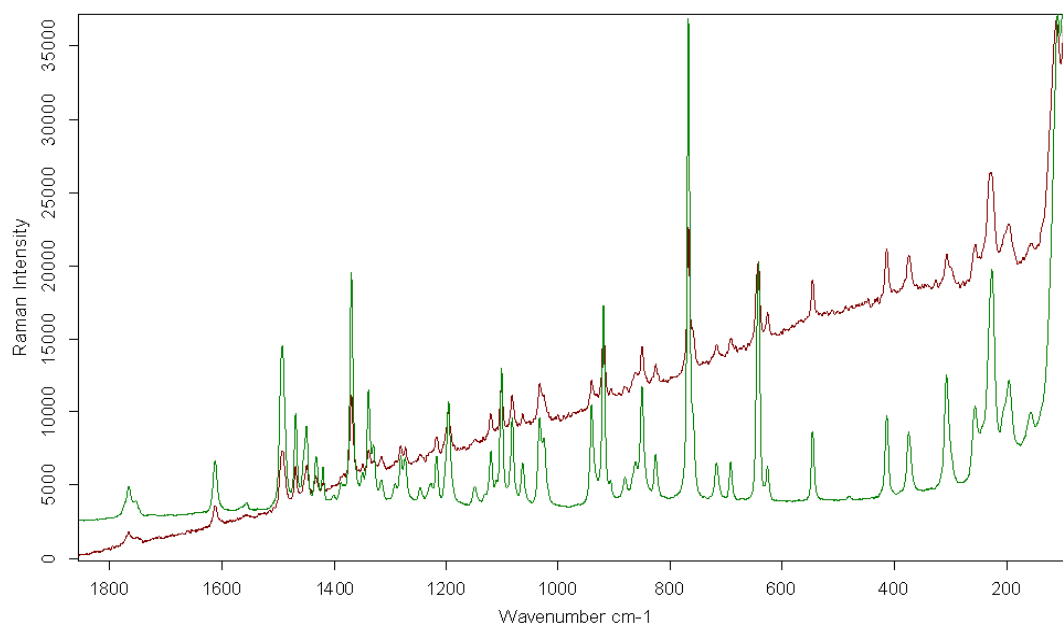


Figure 5.11: Example of Raman identification (green: spectrum of Pilocarpine-HCl raw material, red: spectrum of Pilocarpine-HCl layer vacuum deposited on titanium carrier).

5.1.2.3.2 Raman Spectroscopy of Pilocarpine-HCl on polymer foil

Both spectra in **Figure 5.12** and **Figure 5.13** contain the same functional groups of Pilocarpine-HCl. It looks to be related to the Raman shifts which imply that the deposited sample on titanium substrate does not change in chemical composition. However, in **Figure 5.13**, the foil carrier is very sensitive to energy input. It shows an irregular surface. The deposited layer shows a spectrum which is not truly 100% comparable to the reference spectrum of deposited materials. This is Raman spectrum of Pilocarpine-HCl ($\nu_{\max} / \text{cm}^{-1}$), **Figure 5.12** shows some characteristic peaks at 2944 cm^{-1} (CH aromatic), 2903 cm^{-1} (C-H aliphatic), broad peak in reference drug and sharp peak in deposited drug due to Raman signal might be enhanced by crystallinity. It is noted that characteristic peaks at 1598 cm^{-1} (C=O), 1487 cm^{-1} (C=C, C=N), 1429 cm^{-1} due to (CH_2 bend), 1367 cm^{-1} for (CH_3 bend) and 1022 cm^{-1} due to (C-O-C).

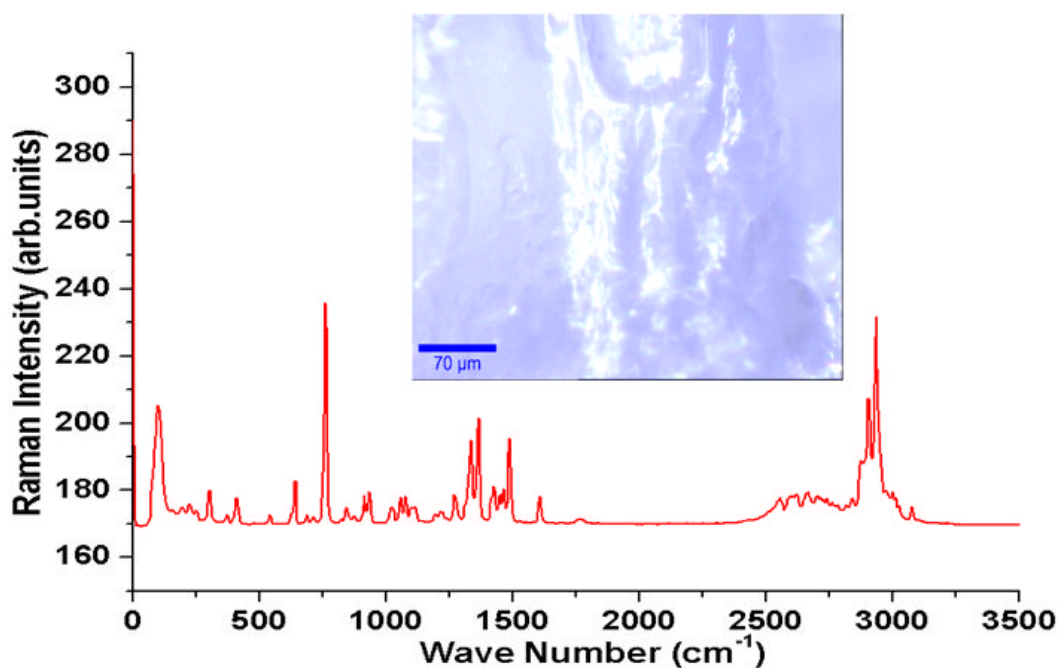


Figure 5.12: Raman-spectrum and optical microscope image (inset) of Pilocarpine-HCl reference drug.

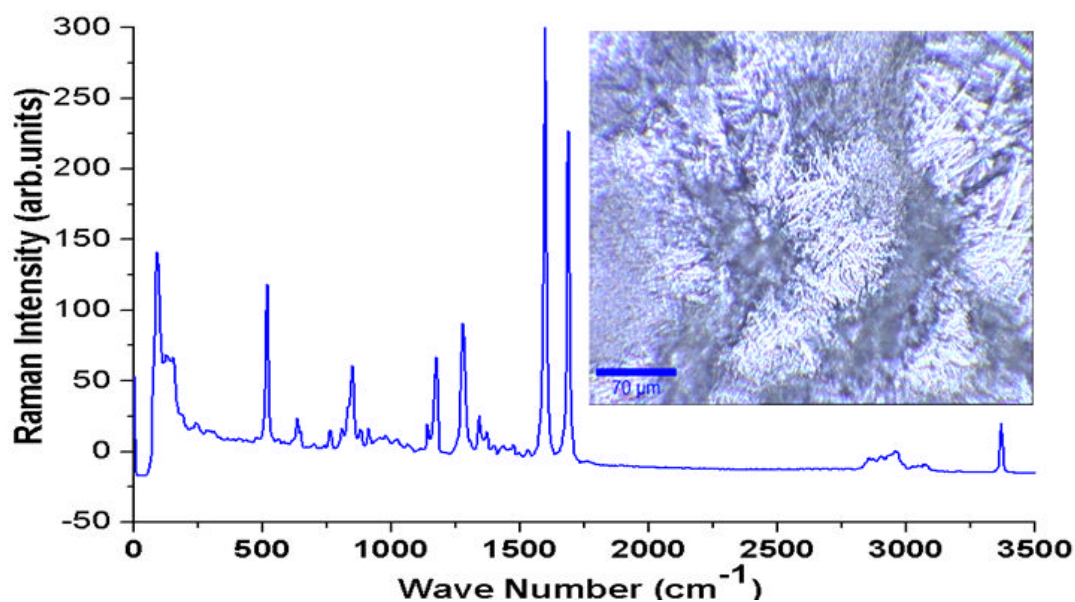


Figure 5.13: Pilocarpine-HCl sample after deposition on polymer foil with its optical image(inset) and Raman-spectrum.

5.1.3 Structural engineering of Pindolol

5.1.3.1 Optical microscopy of Pindolol nano-microstructures

The material is deposited on polymer foil and titanium substrate. **Figure 5.14a** shows small droplets of Pindolol grown on polymer foil with the magnification of 50 x. They

are < 300 nm as estimation can be done from the scale bar. They are randomly distributed over the whole sample surface. This may indicate that the island growth is the predominant mechanism. The substrate in the right figure is Titanium and Pindolol nuclei seem to be a densely porous structure.

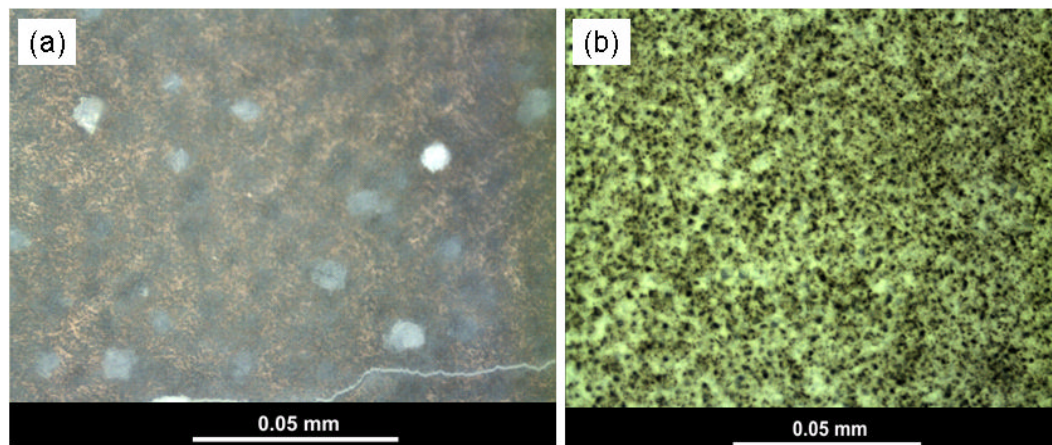


Figure 5.14: Both optical images show deposited Pindolol on polymer foil (a) and Ti substrate (b) respectively.

5.1.3.2 AFM of Pindolol nano-microstructures

Figure 5.15 depicts AFM images of vacuum evaporated Pindolol deposited on Ti substrate.

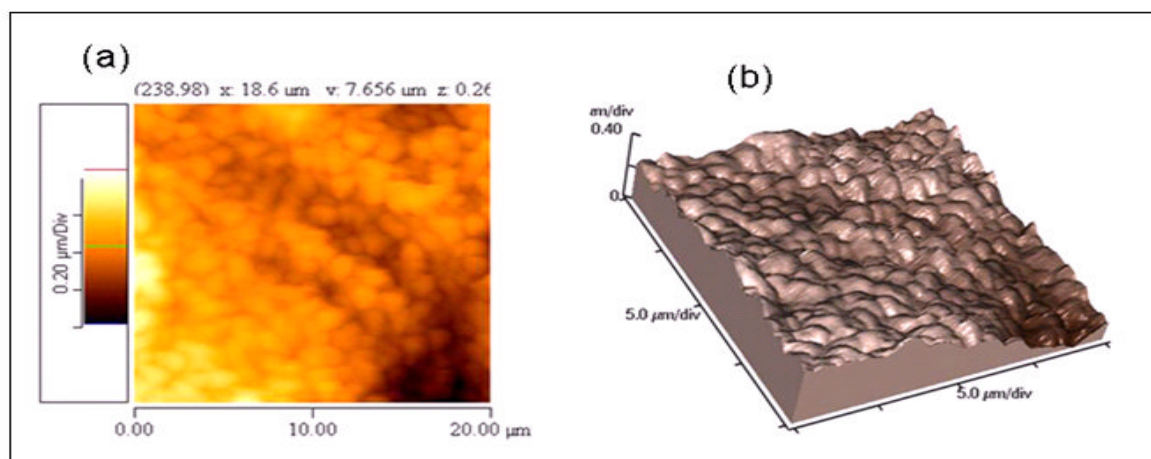


Figure 5.15: a-b Two- and three dimensional AFM (non contact mode) images of Pindolol nano-microparticles deposited on Ti substrate.

The 2D and 3d AFM images of Pindolol nano-microstructures were recorded in scan area at $20 \times 20 \mu\text{m}^2$. Obviously, uniform spherical particles were obtained and distributed homogeneously on the substrate surface and bounded to each other to make clusters. The

AFM image (**Figure 5.15**) shows surface features with an average diameter of ≥ 500 nm and a maximum height variation of 400 nm.

5.1.3.3 Raman Spectroscopy of Pindolol nano-microstructures

5.1.3.3.1 Raman Spectroscopy of Pindolol nano-microstructures on Ti

Figure 5.16 illustrates that the Raman spectra of Pindolol nano-microstructures are identical to each other (not changed) after evaporation.

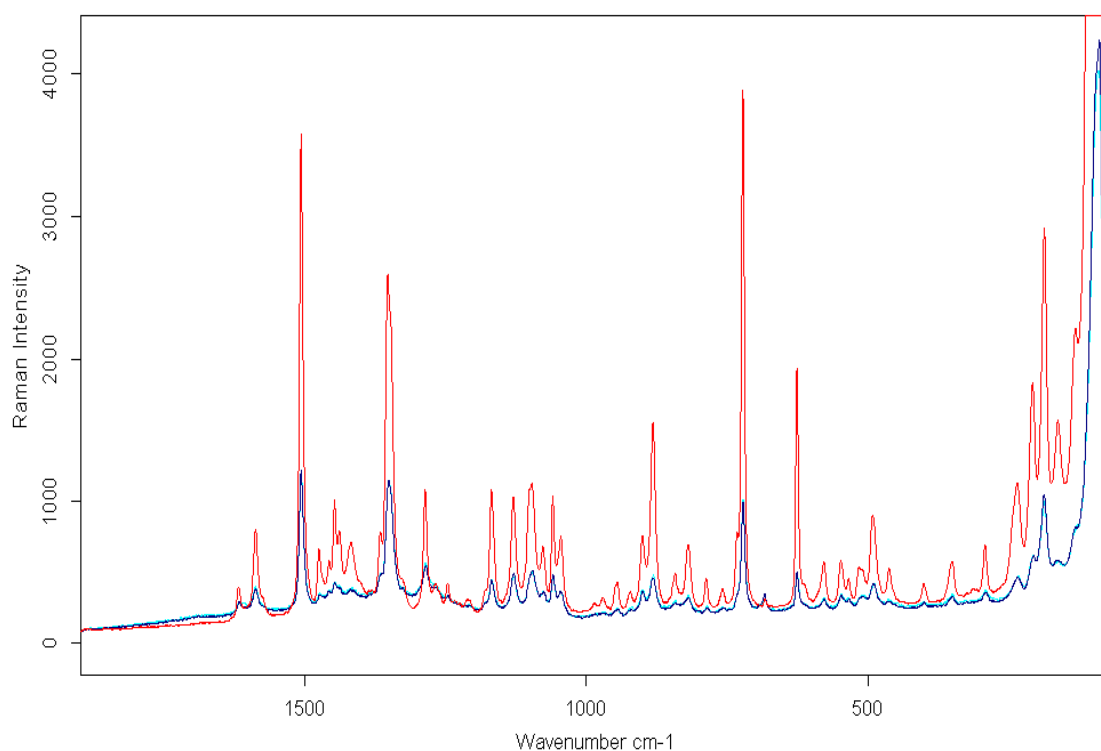


Figure 5.16: Raman identification (red: spectrum of Pindolol raw material, blue: spectrum of Pindolol layer vacuum deposited on Ti carrier).

5.1.3.3.2 Raman Spectroscopy of Pindolol deposited on Si

As shown in **Figure 5.17** and **Figure 5.18**, the spectra similar to each other and contain the same functional groups of Pindolol. This is Raman spectrum of Pindolol (ν_{\max} /cm⁻¹). **Figures 5.17** and **5.18** show characteristic peaks located at ~ 3293 cm⁻¹ (NH, OH), 3130 cm⁻¹ (C-H arom.), 2838 cm⁻¹ (CH aliph.), and 1580 cm⁻¹ (C=C), at 1500 - 1339 cm⁻¹ (CH₃

bend) and at 1098 cm^{-1} for (C-O-C), as a result the deposition of crystalline Pindolol is successful.

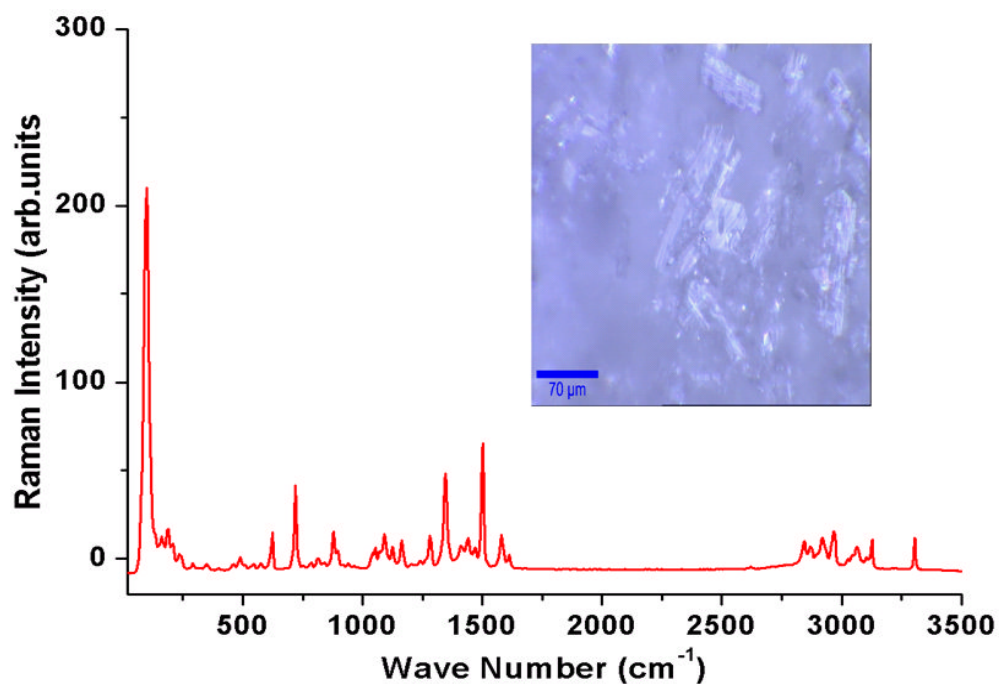


Figure 5.17: The Raman spectrum of Pindolol control sample. The inset shows the optical microscope image of the control sample.

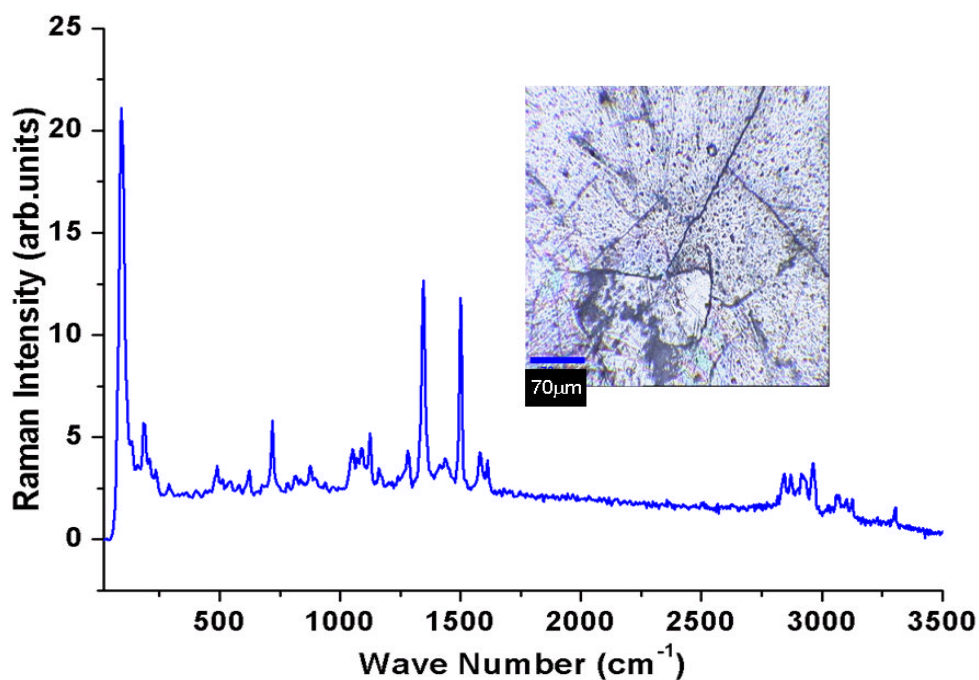


Figure 5.18: Raman-spectrum with its appropriate optical image (inset) of Pindolol sample after deposition.

5.1.4 Structural engineering of 5-Fluorouracil

5.1.4.1 Optical spectroscopy of 5-Fluorouracil

The optical images of 5-Fluorouracil show magnifications of 20 x on the left and 50 x on the right image of **Figure 5.19**. The material was deposited on Titanium substrate. From **Figure 5.19**, one can see Fluorouracil covers the sample surface uniformly although some scratches appear probably due to incautious handling with the tweezers when removed from the sample holder. The crystallization can be seen in the right image.

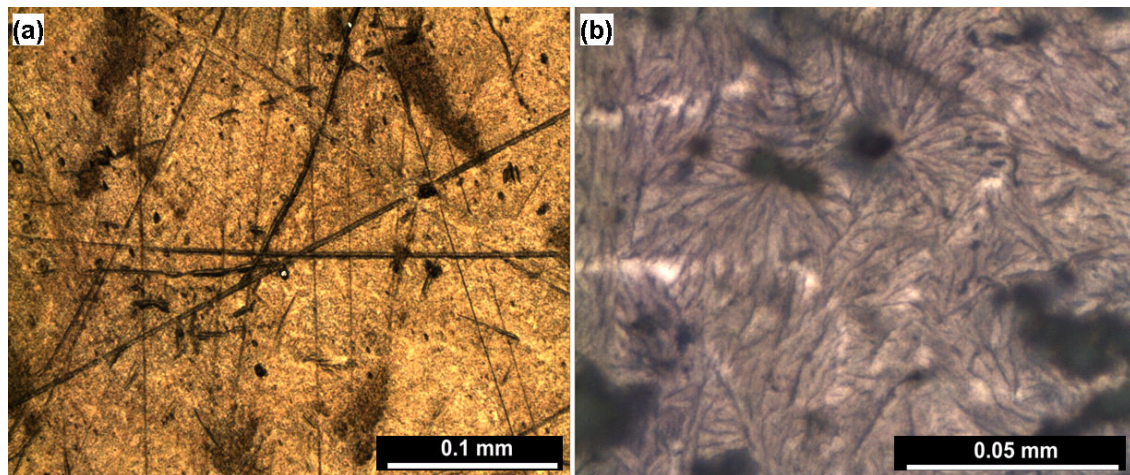


Figure 5.19: Optical images of 5-Fluorouracil with (a) 20 x and (b) 50 x magnification grown on titanium substrate that show crystallization process after thermal evaporation deposition.

5.1.4.2 AFM of 5- Fluorouracil

Figure 4.20 shows 2D and 3D topographical images of 5-Fluorouracil on Ti. The left scan has a scrutinizing area of $5 \mu\text{m} \times 5 \mu\text{m}^2$ whereas the right one is a zoomed-in scan with scan area of $1 \times 1 \mu\text{m}^2$. AFM images show surface features with an average diameter of 200 nm and a maximum height variation of 110 nm.

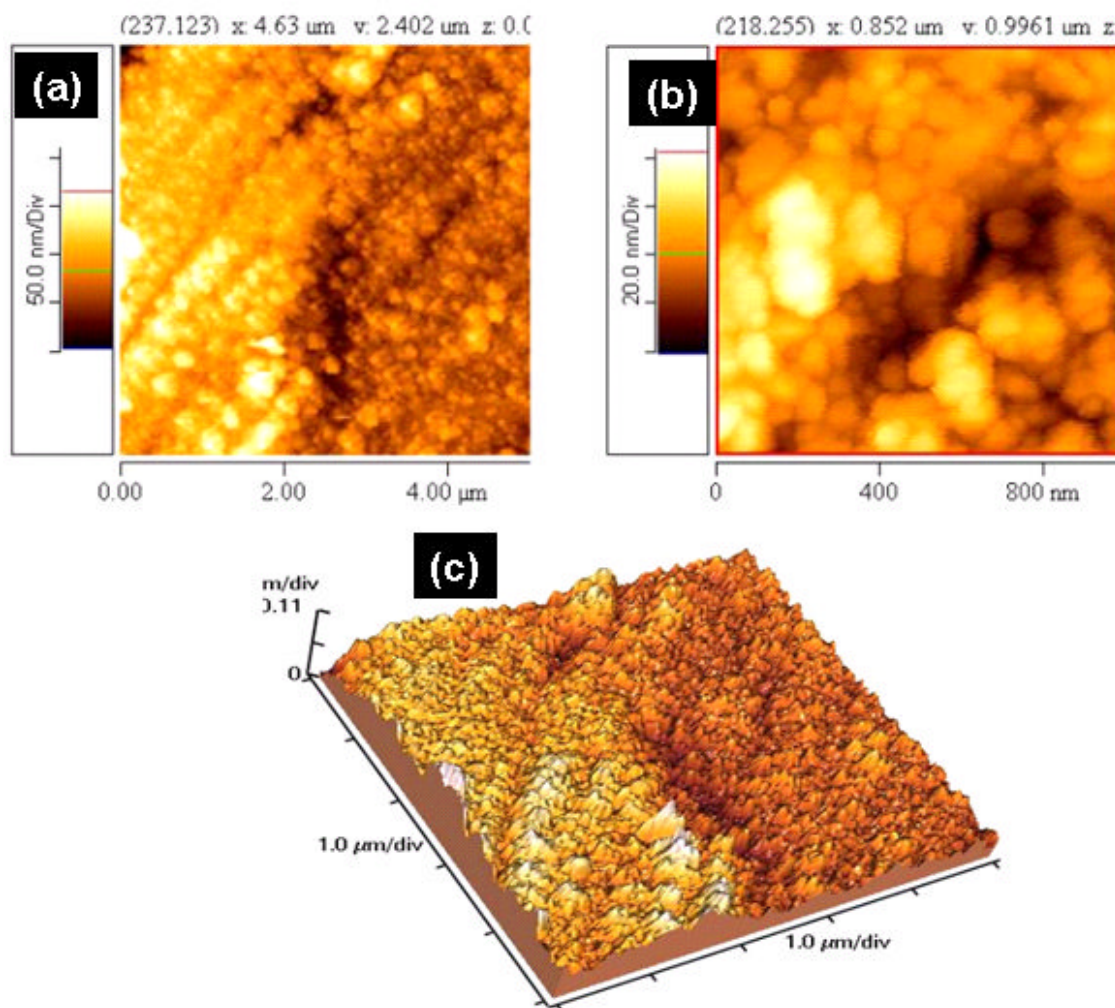


Figure 5.20: Two-dimensional AFM height images of 5-Fluorouracil on Ti substrate with a scan area of (a) $5 \times 5 \mu\text{m}^2$, (b) $1 \times 1 \mu\text{m}^2$. Also, three-dimensional AFM height image of Fluorouracil on Ti is shown with a scan area of $1 \times 1 \mu\text{m}^2$ and a maximum height of $0.1 \mu\text{m}$.

5.1.4.3 Raman microscopy of 5-Fluorouracil nano- microstructures

The confirmation of 5-Fluorouracil nano-microstructures synthesis was further determined by Raman microscopy. The spectra are very similar to each other with only very subtle differences. Raman signals in **Figures (5.21 and 5.22)** show that the three strong characteristic peaks located at $3100\text{-}3076 \text{ cm}^{-1}$ due to the presence of (OH, NH). It was noted that peaks located at 1660 cm^{-1} for (C=O), 1491 cm^{-1} for (C=N, C=C), and at $\sim 1227 \text{ cm}^{-1} - 737 \text{ cm}^{-1}$ for (C-F). **Figures 5.21 and 5.22** show the main functional groups and their specific Raman shifts. Both spectra contain the same functional groups as seen from the peaks in the spectra in **Figures 5.21 and 5.22** that seem similar. Thus, the

deposition of crystalline Fluorouracil was successful. Crystallization can be seen clearly from the enhancement of the Raman signal of deposited sample.

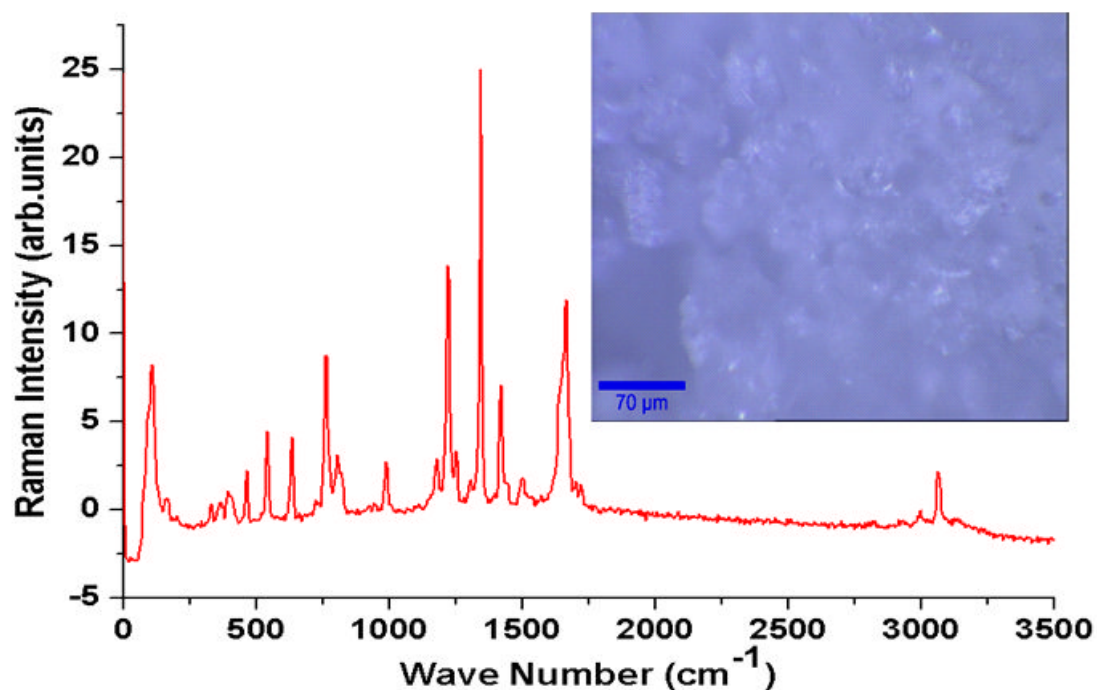


Figure 5.21: Raman spectrum and optical image (inset) of 5- Fluorouracil reference drug.

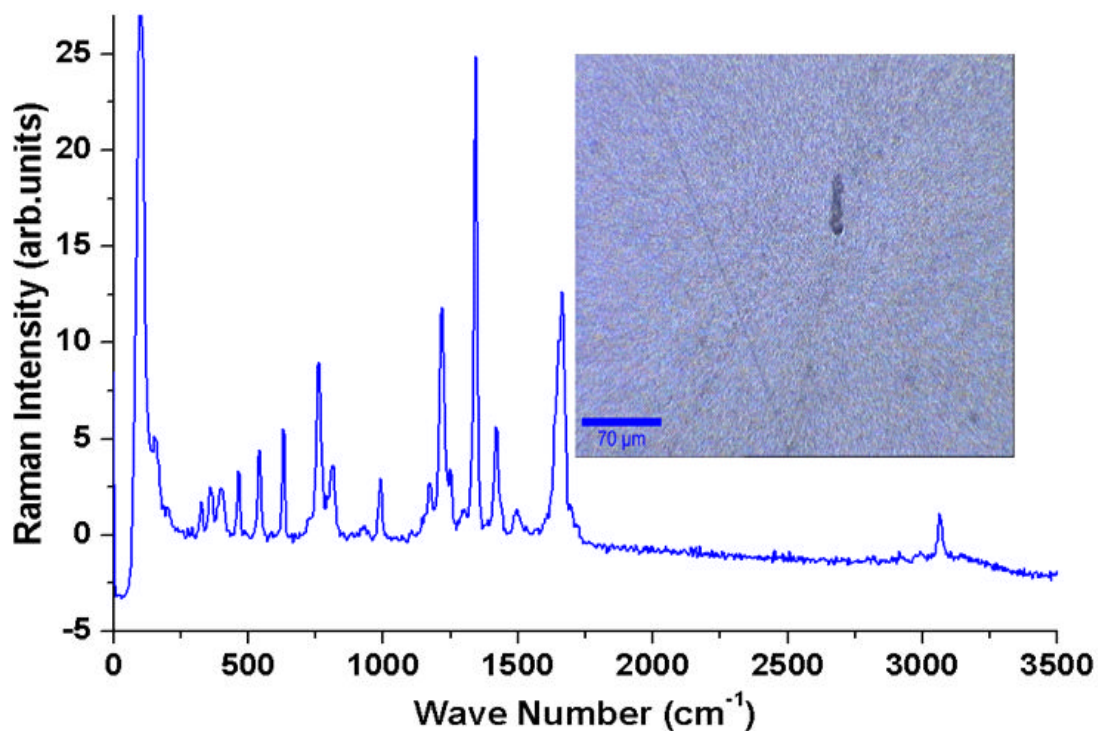


Figure 5.22: Raman spectrum and optical image (inset) of 5- Fluorouracil after deposition.

5.1.5 Structural engineering of Chloramphenicol

5.1.5.1 Optical spectroscopy of Chloramphenicol

The growth process of deposited Chloramphenicol is based on the growth time. The Chloramphenicol thin film is characterized by light microscopy where the images are taken after 1min, 3h and 1 day after evaporation process. **Figure 5.23** shows droplets of Chloramphenicol deposited on glass substrate. Concerning the upper left image, the diameter of the droplet in the upper left corner is approximately $240\ \mu\text{m}$ in diameter, the smallest in the upper middle part of the image is about $30\ \mu\text{m}$. Their distance to each other is quite big comparing to the whole sample surface area. The upper right image shows Chloramphenicol droplets with diameters between $100\ \mu\text{m}$ and $220\ \mu\text{m}$. concerning the same sample 3h after evaporation, the droplets expand a bit (see also **Figure 5.23**).

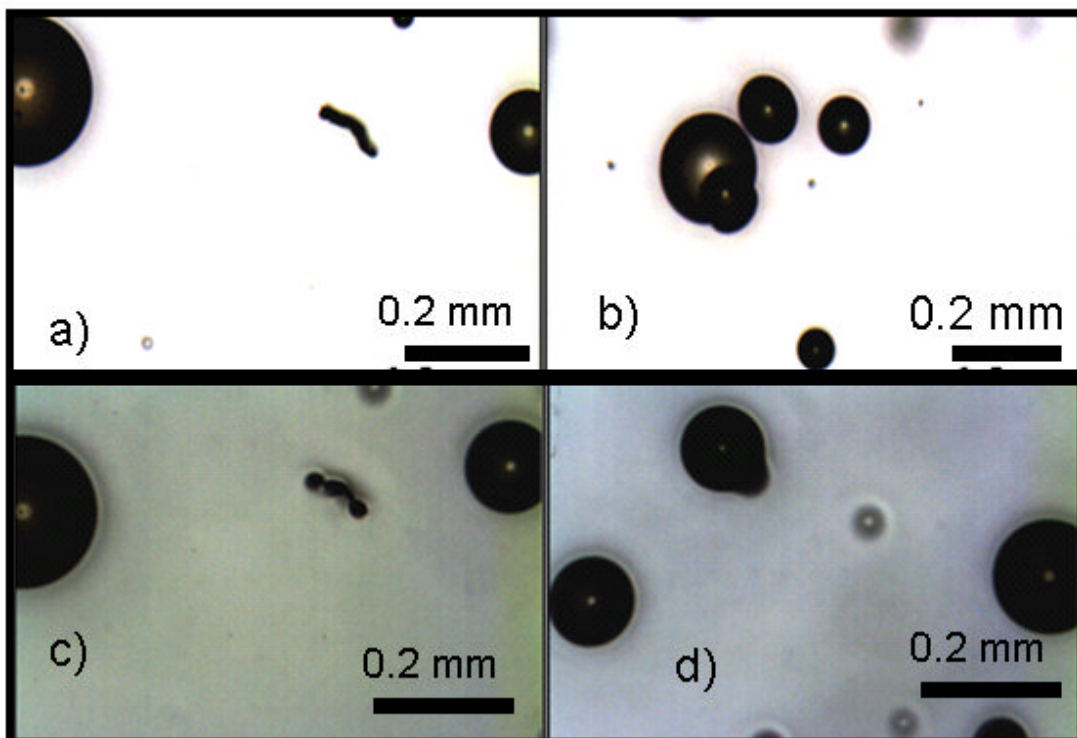


Figure 5.23: (a) and (b): Images for different positions on the sample show Chloramphenicol deposited on glass illustrated with a magnification of $10\times$. Images were taken 1 min after evaporation. Images (c) and (d) were taken 3h after evaporation. They show different positions on glass sample with droplets of deposited Chloramphenicol. The magnification is $10\times$.

When relating the diameter of the big droplet in the lower left image to the previous, its diameter increased to 280 μm . The small one actually increased to 60 μm in diameter. The droplets in the lower right image show diameters of about 100 μm to 200 μm . Considering the growth of the droplets after 1 day (see **Figure 5.24**). It is recognized that the diameter gained has incredible dimensions. The smaller one in the left image is about 350 μm . In the image on the right, two droplets start growing together. After two days, the agglomeration starts (c). Also, characterized Chloroamphenicol, after 10 days in the initial specific area, starts to produce. (**Figure 5.25a**). To accelerate the crystallization process, one sample with Chloramphenicol on glass was heated for 1 hour at about 50 $^{\circ}\text{C}$ after the evaporation process. The result can be seen in **Figure 5.25b** and **c**. The structure shows blossom-like or fan-like crystallites growing together.

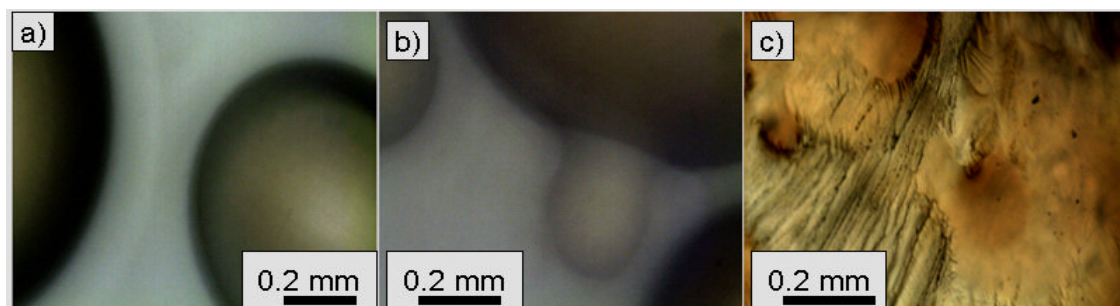


Figure 5.24: *Chloramphenicol microstructures deposited on glass substrate after 1 day (10 x magnification)(a, and b) after 2 days (c).*

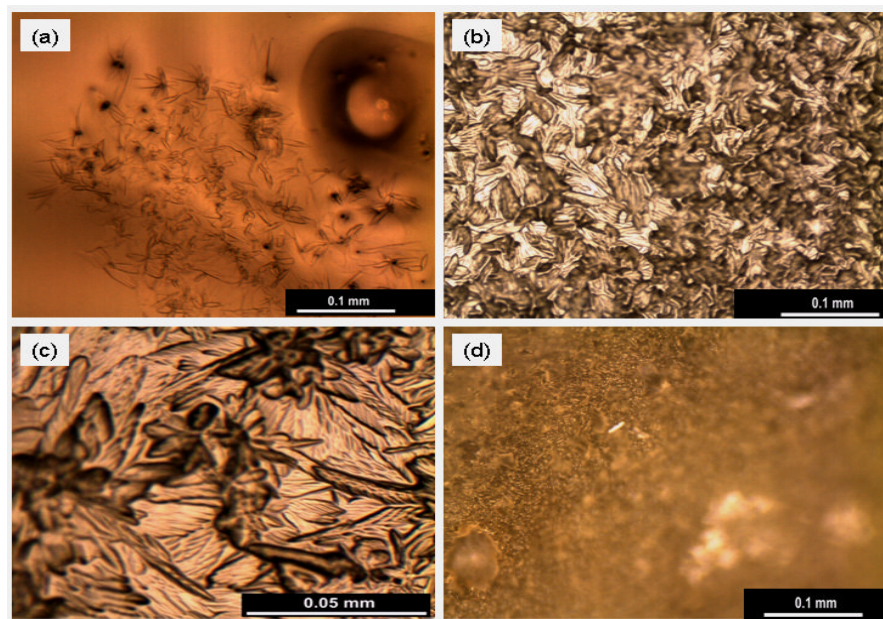


Figure 5.25: *Optical micrographs show the initial specific area of Chloramphenicol on glass after 10 days (a) and its higher surface area Blossom-like crystalline structure after*

heating 1 h at 100 °C on glass at lower and higher magnification *b* and *c* respectively. Chloramphenicol on polymer foil appears after 1 month (*d*). *b*) after 2 days (*c*).

5.1.5.2 Raman spectroscopy of Chloramphenicol nano-microstructures

Figures 5.26, 5.27 and 5.28 show Raman spectra consecutively recorded to examine the chemical structure of Chloramphenicol after and before thermal evaporation. The spectra are very similar to each other with only very subtle differences. The first one is the reference sample of Chloramphenicol powder. The second one shows the deposited Chloramphenicol immediately after evaporation process. and the third one after a certain time. Raman spectra of Chloramphenicol ($\nu_{\max}/\text{cm}^{-1}$) shows characteristic peaks placed at 3087 cm^{-1} (OH, NH), 2962 cm^{-1} (C-H aromatic), 1598 cm^{-1} (C=O) cm^{-1} and 1513 cm^{-1} (C=C). In the other hands, some peaks located at 849 cm^{-1} assigned to (C-Cl) and at $1345\text{-}1194\text{ cm}^{-1}$ for (NO_2) (see Figures 5.27 and 5.28).

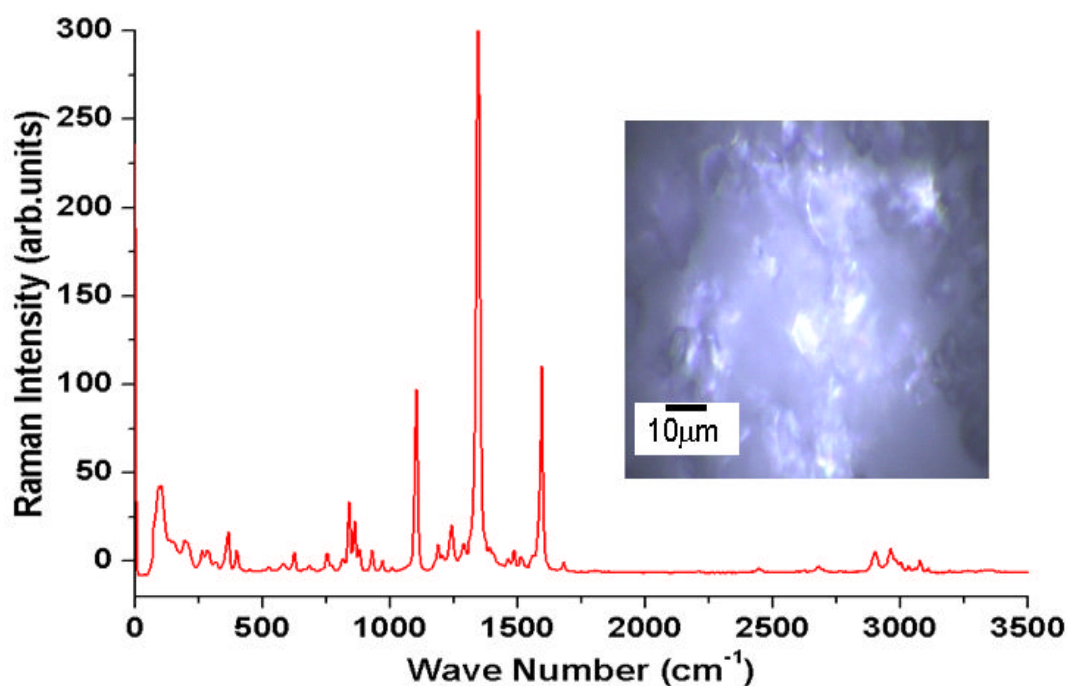


Figure 5.26: Raman spectrum and optical image (inset) of Chloramphenicol reference drug.

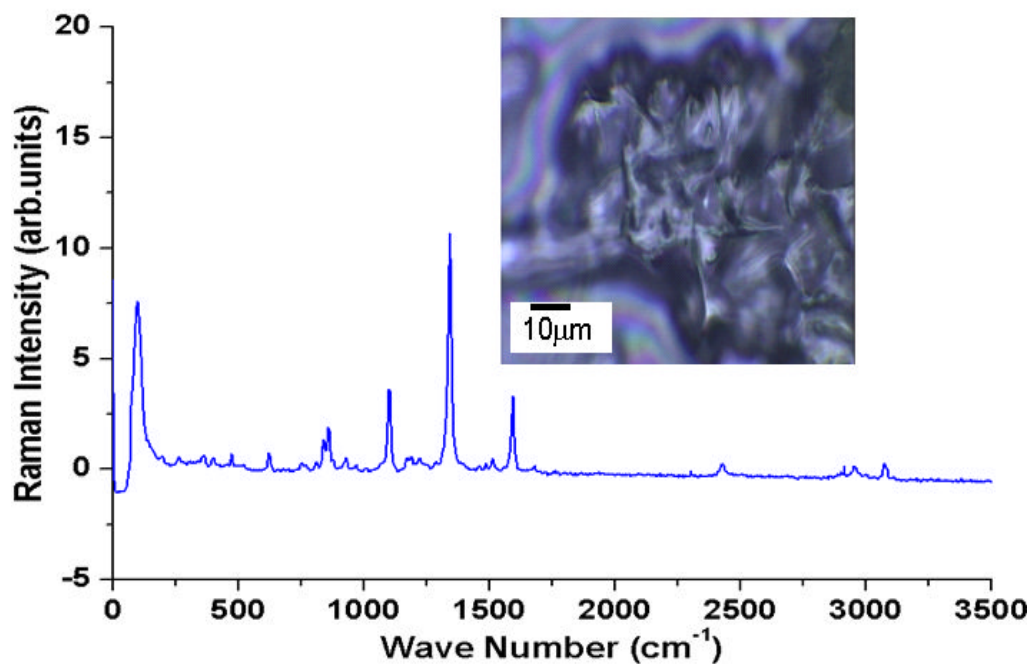


Figure 5.27: Raman spectrum and optical image (inset) of Chloramphenicol deposited drug directly after evaporation.

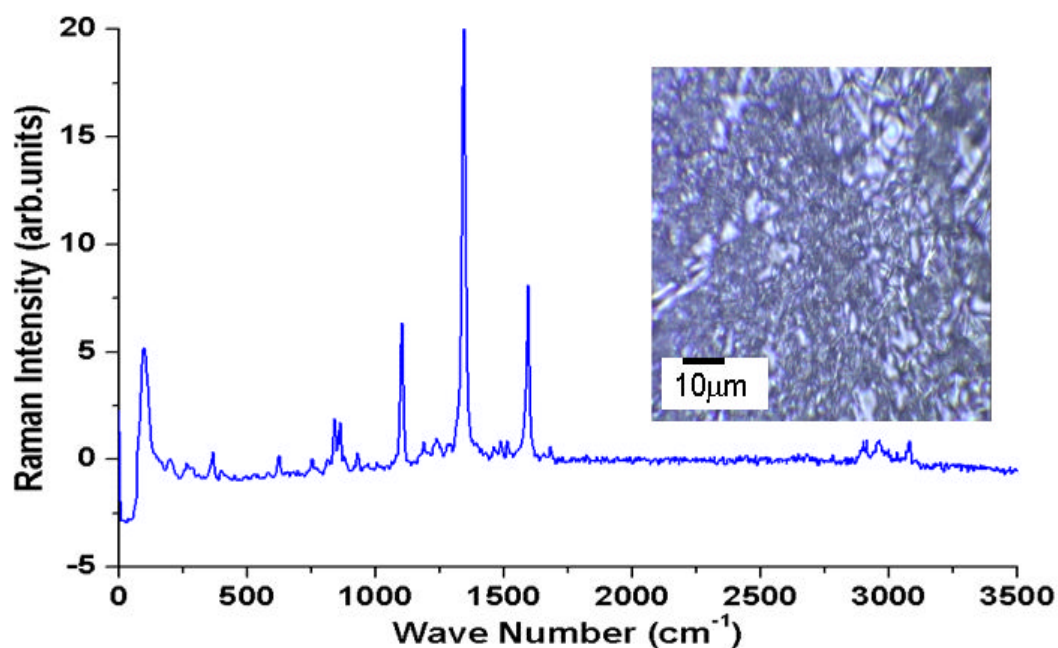


Figure 5.28: Raman-spectrum and optical image (inset) of deposited Chloramphenicol sample after a certain time.

It appears that Raman spectrum offers an overview of the most important functional groups and their dedicated Raman shift peaks. All peaks from **Figures 5.27** and **5.28** exhibit the specified Raman-shifts similar to the reference sample (**Figure 5.26**).

Additionally, the Raman intensity and the number of counts increased in the sample examined after a certain time. This is due to the advancing crystallization process of the material as shown in **Figure 5. 28**. Crystallinity has relationships with orientation and the polarizability of the material.

5.1.6 Structural engineering of Tetracaine-HCl

5.1.6.1 SEM of Tetracaine-HCl nano-microstructures

The SEM image of Tetracaine-HCl shows a dense structure of fibres, needles and tetrapods that are distributed homogeneously and uniformly over the surface. **Figure 5.29** shows further examples for different nanoscale roughnesses and large surface areas formed by self organisation during growth. The appearance of thermally evaporated films on different substrates visualised by scanning electron microscopy. Furthermore, when silicon substrate pre-coated with 20 nm gold thin film (e), in this case, much more materials deposited on the substrate. The surface morphology is flowers-like structure due to the hydrophilicity of the gold particles resulted in the aggregation and much adhesion of adsorbing molecules on substrate. In particular, inorganic-organic hybrids have attracted considerable attention as a subject of extensive research in materials chemistry because of the potential of combining distinct properties of organic and inorganic behaviours as shown in **Figure 5.29.g and h**.

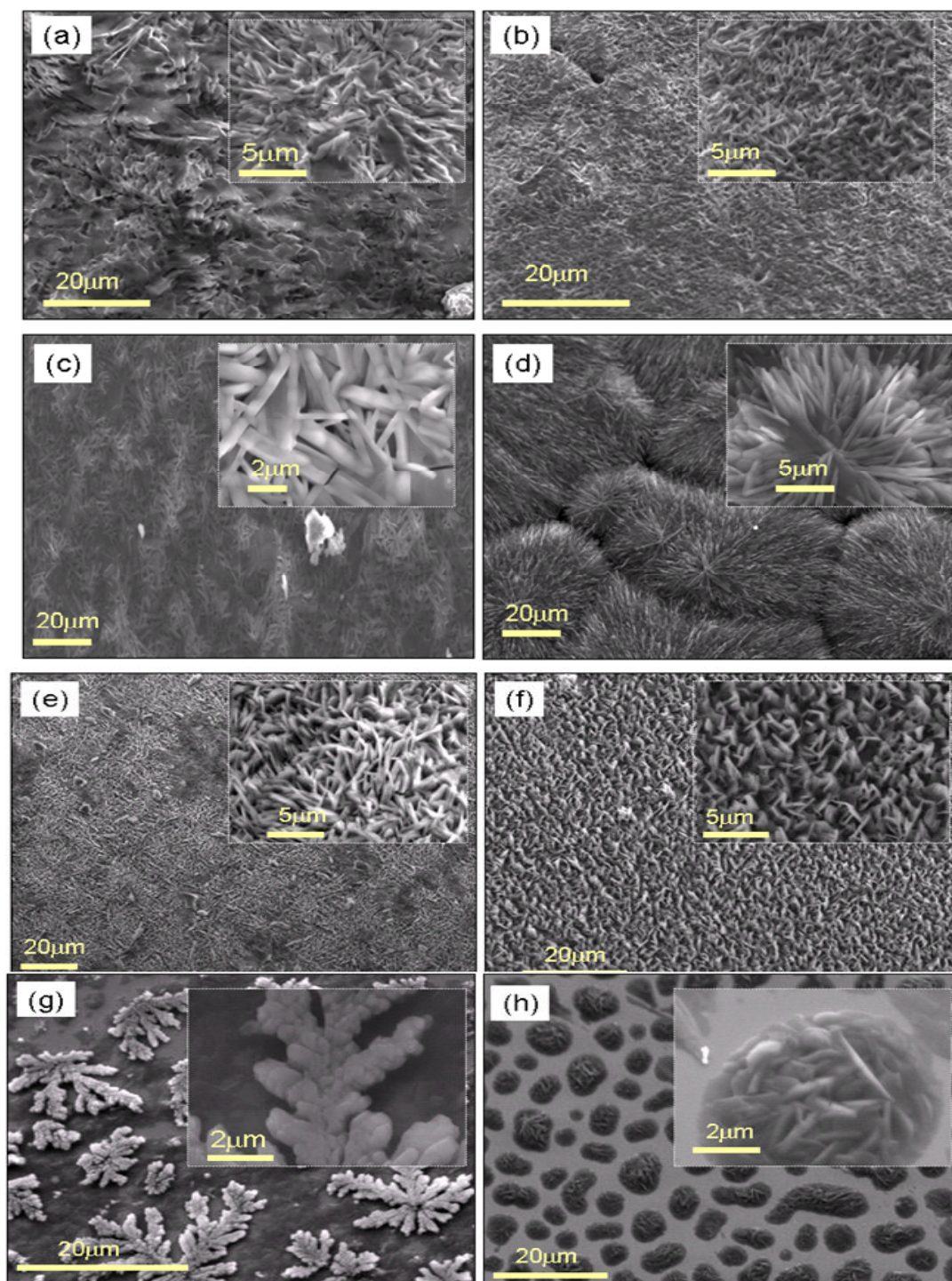


Figure 5.29: a-h Representative SEM images of various Tetracaine-HCl nanostructures morphologies grow on different substrates: Silicon wafer at higher temperature (a), Silicon wafer at lower temperature (b), Titanium substrate(c), Silicon coated with 20 nm Au thin film (d), Silicon coated with 4 nm Au thin film(e) co-deposition of Tetracaine-HCl with Ag on silicon wafer(f) and Ti substrate (g) and co-deposition of Tetracaine-HCl with Au on Si substrate(h) The inset is a high-magnification SEM images.

Figure 5.29 illustrates also the morphology and dimensions of the synthesized products depend on processing parameter adapted such as evaporation temperature, evaporation time period and substrate surfaces.

5.1.6.2 AFM of Tetracaine-HCl nanomicrostructures

The deposited Tetracaine-HCl nano-structures are also characterized by AFM to detect its morphology. AFM observations clearly showed 2D image of the topography of Tetracaine-HCl with a scan area of 20 x 20 μm^2 . Obviously, the film is homogeneous and comprises nanorods like structure of about 80–100 nm in size as shown in **Figure 5.30**.

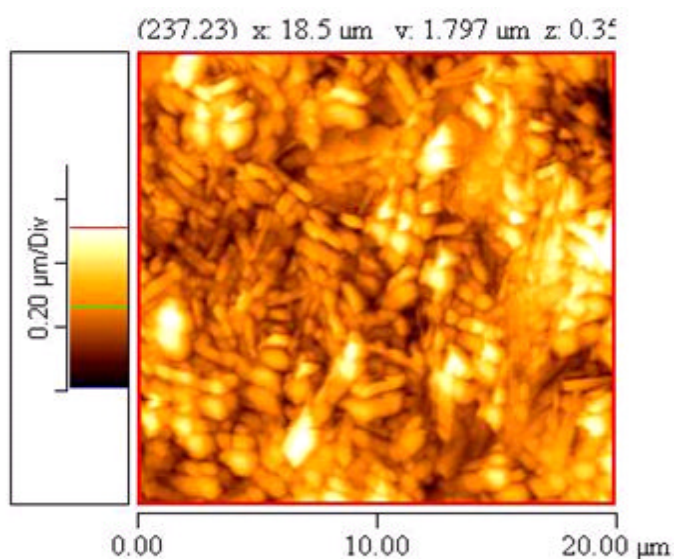


Figure 5.30: Two-dimensional AFM height image of Tetracaine-HCl on Ti. The scan area is about 20 μm x 20 μm .

5.1.6.3 Raman Spectroscopy of Tetracaine-HCl

The reference sample and deposited sample of Tetracaine-HCl are identified by Raman spectroscopy ($\nu_{\text{max}}/\text{cm}^{-1}$). Both spectra contain the same functional groups as seen from **Figures 5.31** and **5.32**.

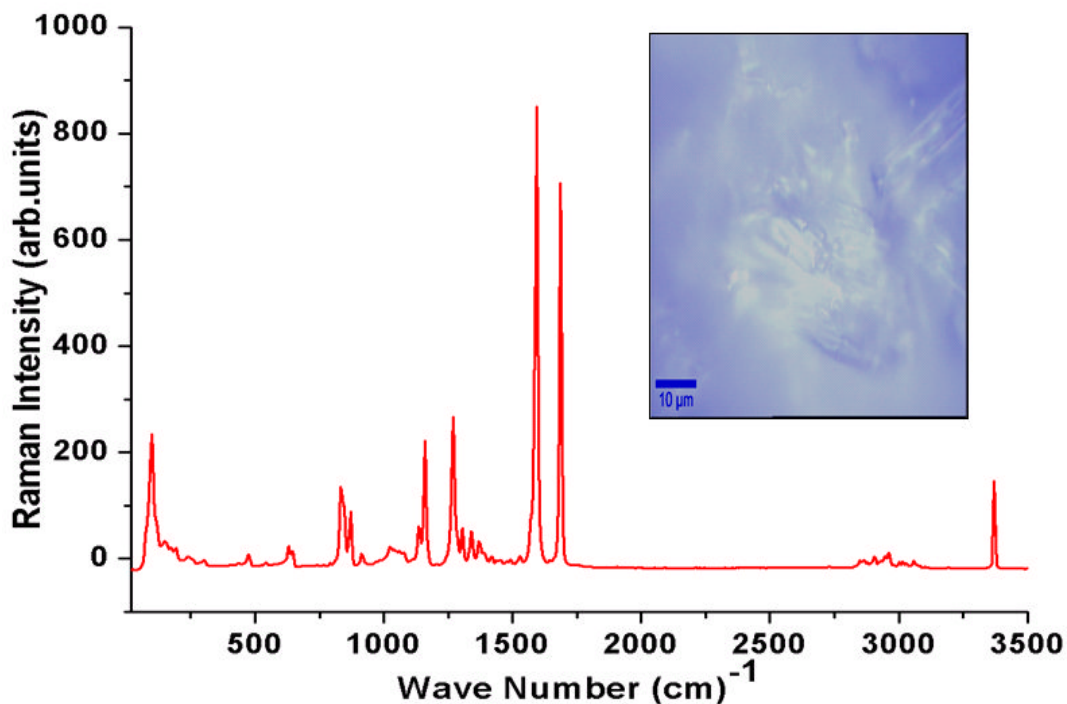


Figure 5.31: The Raman spectrum of Tetracaine-HCl control sample. The inset shows the optical microscope image of the control sample.

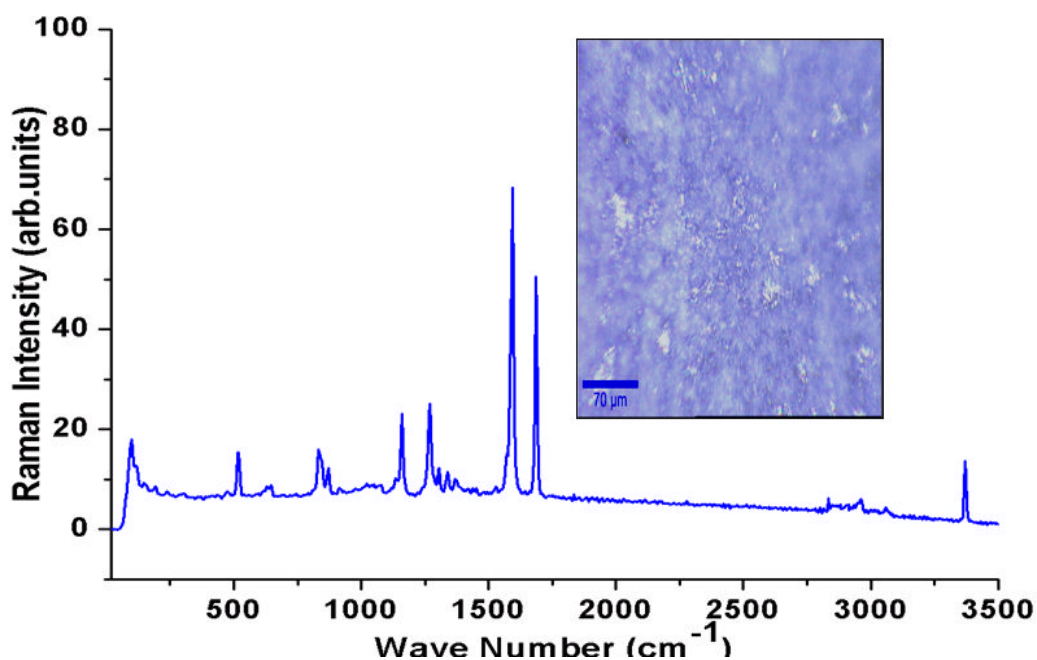


Figure 5.32: Tetracaine-HCl sample is shown after deposition with its appropriate optical image (inset) and Raman-spectrum.

The spectra are very similar to each other with only very subtle differences in Raman intensity. Raman spectrum of Tetracaine-HCl shows characteristic bands located at 3366 cm⁻¹ corresponding to the (NH), 3050 cm⁻¹ for (C-H aromatic) and 2958 cm⁻¹ for (C-H

aliphatic). Sharp peaks located at 1663 cm^{-1} and 1587 cm^{-1} which corresponding to (C=O) and (C=C). It is noted that peaks at 1260 cm^{-1} which belong to (CH₂ bend) and 1171 cm^{-1} for (CH₃ bend) and 1033 cm^{-1} for (C-O-C). Thus, the deposition of crystalline Tetracaine-HCl is functioning properly.

5.1.6.4 EDX Results of Tetracaine-HCl nano-microstructures with silver and gold

The EDX of Tetracaine-HCl samples are done by the SEM. The EDX reveals that the required phase has been presented. **Figures 5.33** and **5.34** show the existence of peaks related to Ag and Au in the samples after deposition. The EDX spectra of the analyzed thin films also confirm the presence of oxygen, chloride and carbon; these elements are the constituents of thin film of Tetracaine-HCl composite.

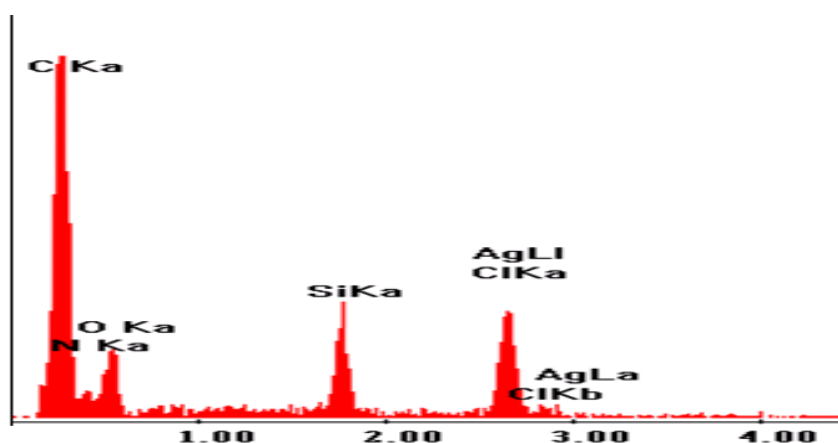


Figure 5.33: EDX spectrum of co- deposition of Tetracaine-HCl nanostructures with Ag by thermal evaporation.

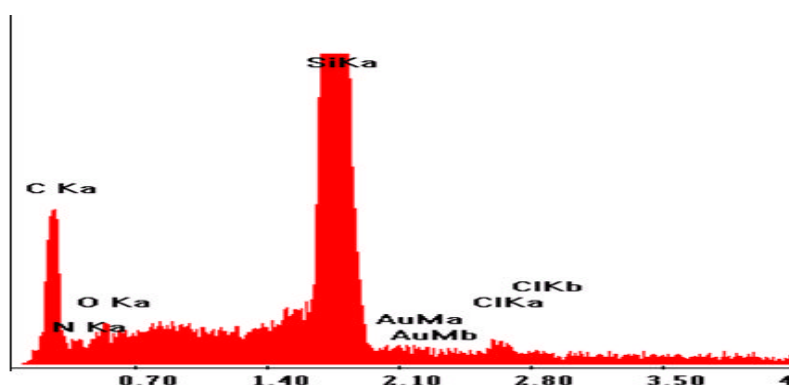


Figure 5.34: EDX spectrum of co-deposition of Tetracaine-HCl nanostructures with Au by thermal evaporation.

5.1.7. Structural engineering of Acetylsalicylic acid

5.1.7.1 SEM of Acetylsalicylic acid

Acetyl Salicylic acid is uniformly deposited on Ti substrate as seen in **Figure 5.35**. The microstructure appears to be uniformly and homogeneously composed of porous particles with higher surface area. Eventually, lateral structured systems are formed by using shadow masks which suited for the fabrication of micro-scale (or nanoscale) heterostructures on different substrates. When the shadow mask is in contact with the substrate ($h = 0$), the growth area is determined by the geometry of the mask apertures and the position of the mask on the substrate as demonstrated in **Figure 5.35 c, d**.

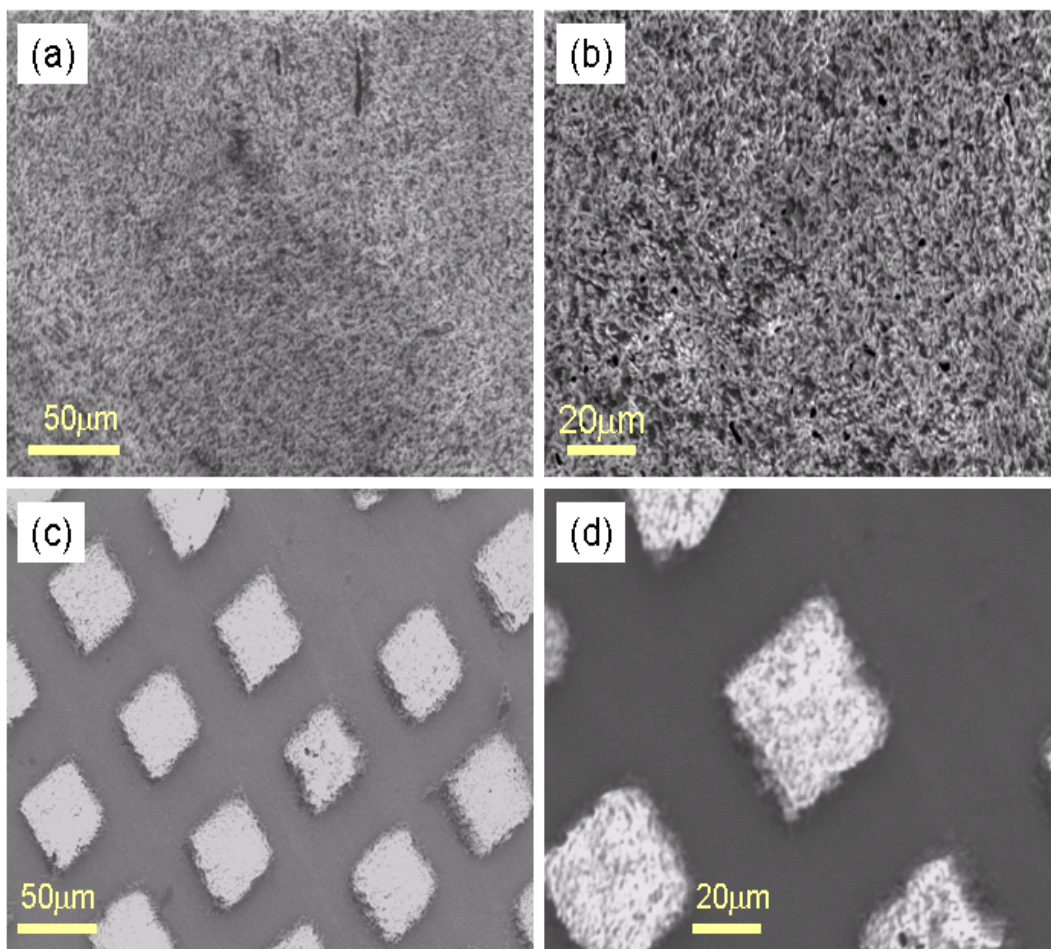


Figure 5.35: Representative SEM images of Acetylsalicylic acid grown on Ti substrate (a, b) and through a copper grid as micro scale shadow mask (c, d) with different magnifications.

5.1.7.2 AFM of Acetylsalicylic acid

Figure 5.36 shows a two-and-three dimensional image of the topography with a scan area of $10 \times 10 \mu\text{m}^2$. Obviously, a uniform crystalline structure is obtained. A uniform cover of the surface of titanium with Acetyl Salicylic acid can be observed as well as the crystalline structure of the deposited material. The shape of the nanostructured peaks resemble pyramided like structure.

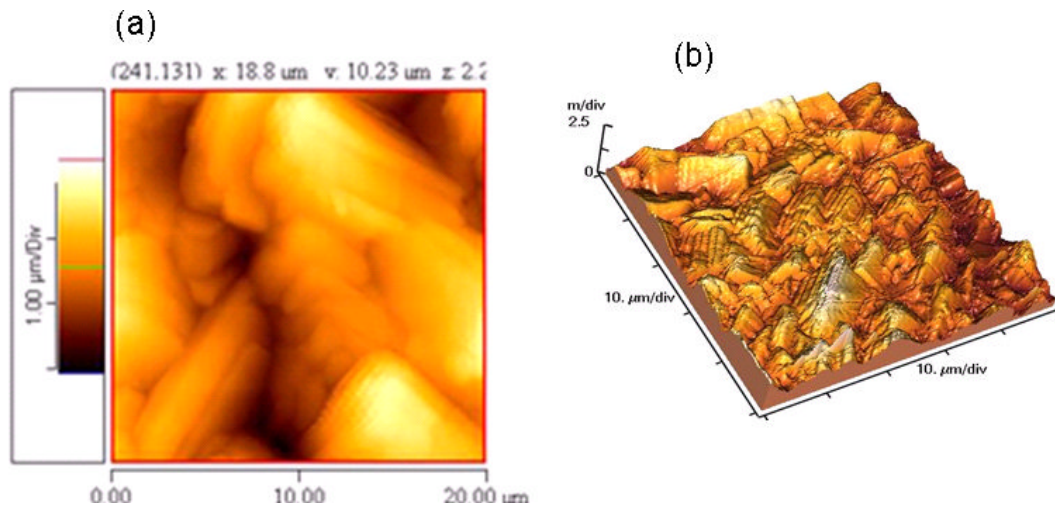


Figure 5.36: Two-and-three dimensional image of the topography of Acetylsalicylic acid with a scan area of $10 \times 10 \mu\text{m}^2$.

5.1.7.3 Raman spectrum of Acetyl Salicylic acid

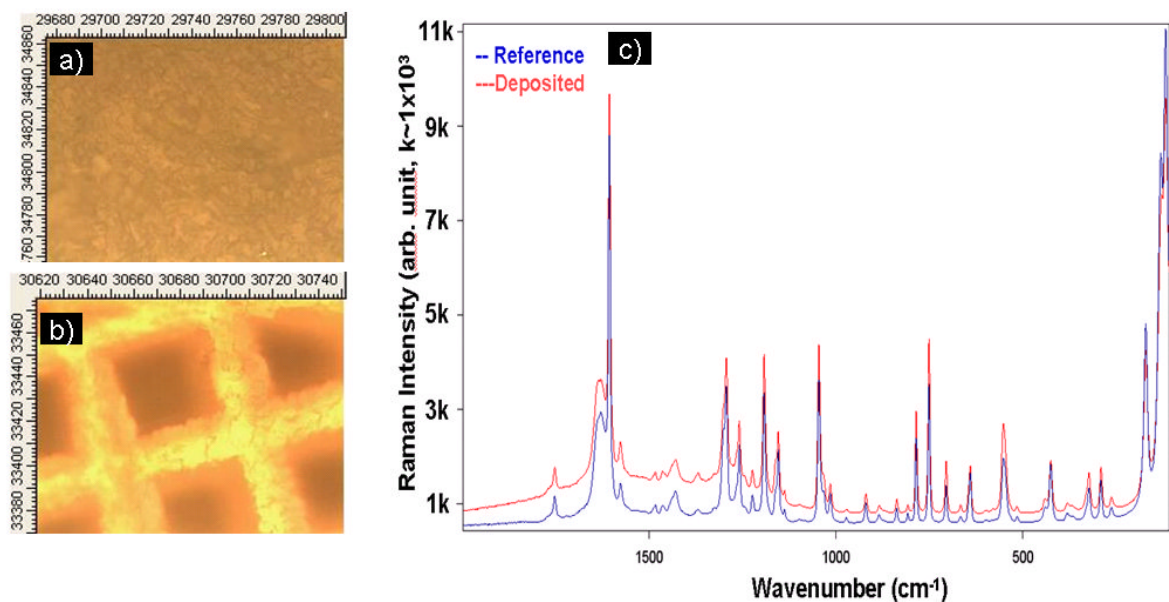


Figure 5.37: Microscopic images of Acetylsalicylic acid deposited on Ti substrate and copper grid through a microscopic shadow mask (a, b) respectively and Raman spectra of the deposited and reference Acetylsalicylic acid (c).

Raman-spectra also are recorded for Acetyl Salicylic acid analysis. **Figure 5.37** shows a clear Raman spectrum after deposition which is similar to the Raman of raw material.. The spectra are very similar to each other with only very subtle differences in intensity. The spectrum after deposition is identical to the reference spectrum, so the substance identity can be verified in **Figure 5.37**.

5.1.8 Structural engineering of Metronidazole

5.1.8.1 SEM of Metronidazole

Figure 5.38 shows the morphology of Metronidazole nano-microstructures deposited on Ti substrate. The structure appears to be pillars like structure with higher surface area.

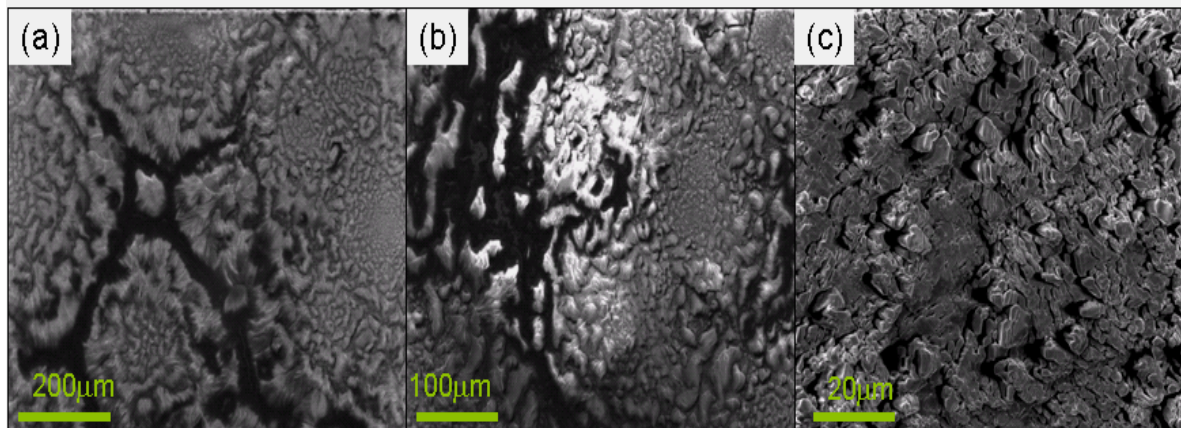


Figure 5.38: a-c SEM images of Metronidazole nano-microstructures fabricated on titanium substrate with different magnifications.

5.1.8.2 AFM of Metronidazole nano-microstructures

Figure 5.39 shows a two-dimensional image and three-dimensional topographical image with a scan area of $10 \times 10 \mu\text{m}^2$.

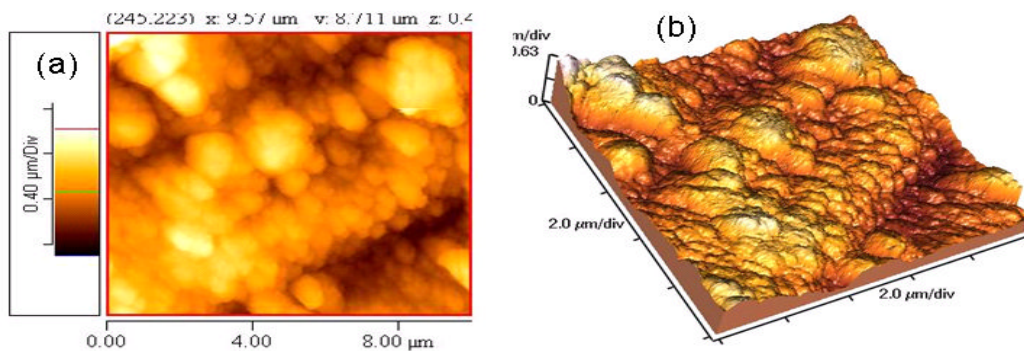


Figure 5.39: AFM 2D and 3D images of Metronidazole deposited on glass substrate with a scan area of (a, b) $10 \times 10 \mu\text{m}^2$.

Obviously, **Figure 5.39** shows the AFM images of as-prepared Metronidazole thin film. For Metronidazole thin film, the uniform grains are densely packed, implying a three-dimensional island. The AFM view of the image shows that the grain looks particles structure covering the substrate surface and coalescence to each other to form clusters. The surface is slightly roughness.

5.1.8.3 Raman spectrum of Metronidazole

The chemical composition of Metronidazole is examined with Raman spectroscopy. Raman spectra of Metronidazole (ν_{\max} / cm^{-1}) in both **Figures 5.40 and 5.41** contain the same functional groups. Figures below show characteristic bands observed at 3109 cm^{-1} for (OH), 3028 cm^{-1} for (C-H aromatic) and $\sim 2940\text{ cm}^{-1}$ for (C-H aliphatic). A sharp peak is located at 1543 cm^{-1} assigned to (C=C) and (C=N). Different bands observed at 1484 , 1260 cm^{-1} which are corresponding to (NO_2), band at 1458 cm^{-1} for (CH_2 bend) and band at 1389 cm^{-1} for (CH_3 bend).

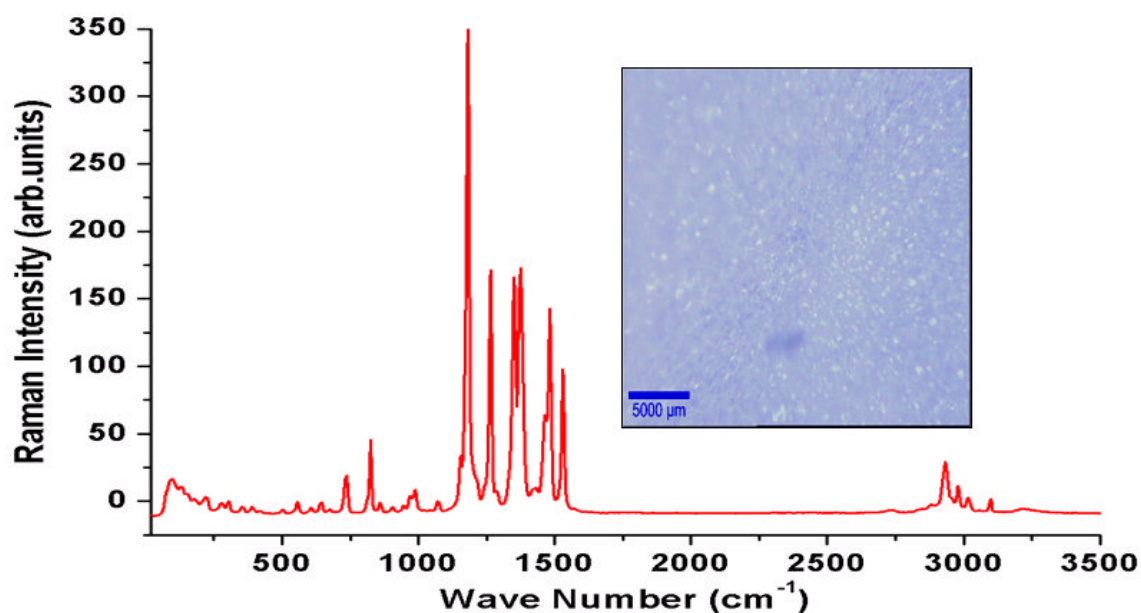


Figure 5.40: The reference sample of Metronidazole with optical microscope image (inset) and its Raman spectrum.

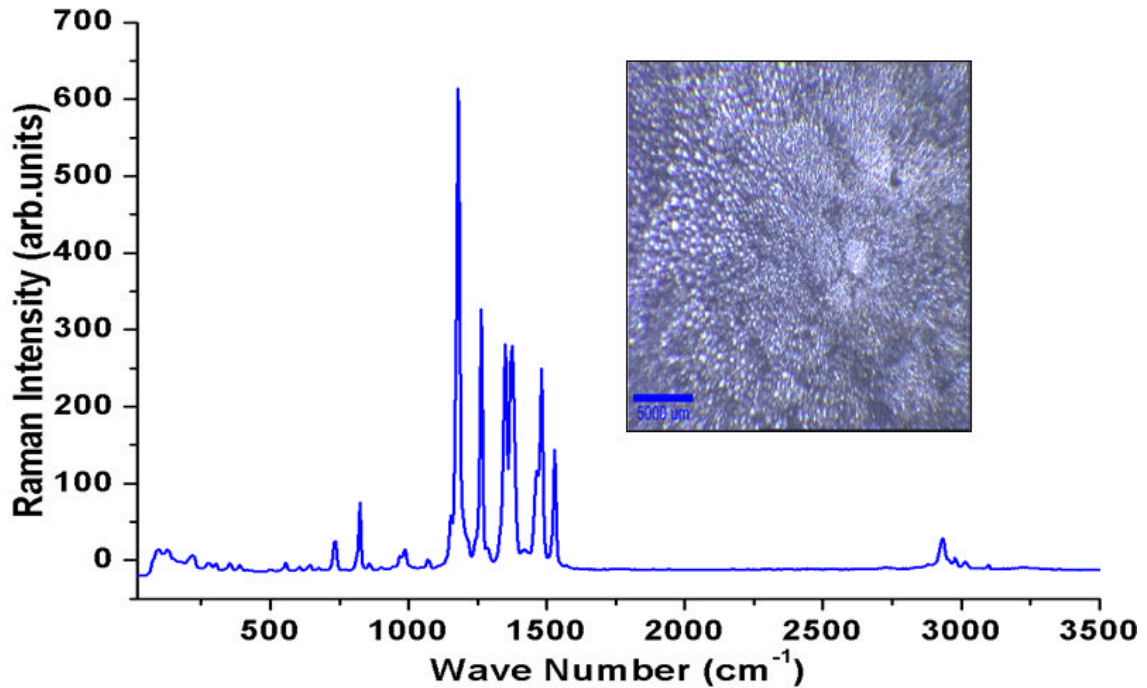


Figure 5.41: Metronidazole sample after deposition with its appropriate optical image (inset) and Raman-spectrum.

5.1.9 Structural engineering of Clotrimazole.

5.1.9.1 Optical Light Spectrum of Clotrimazole nano-microstructures

Figure 5.42 shows Clotrimazole deposited on Si pre-coated with ZnO nanostructures and Ti substrate with magnification of 50 x. Optical images show that the morphology of Clotrimazole depend on the employed substrate, where grains are slightly smaller and more dispersed.

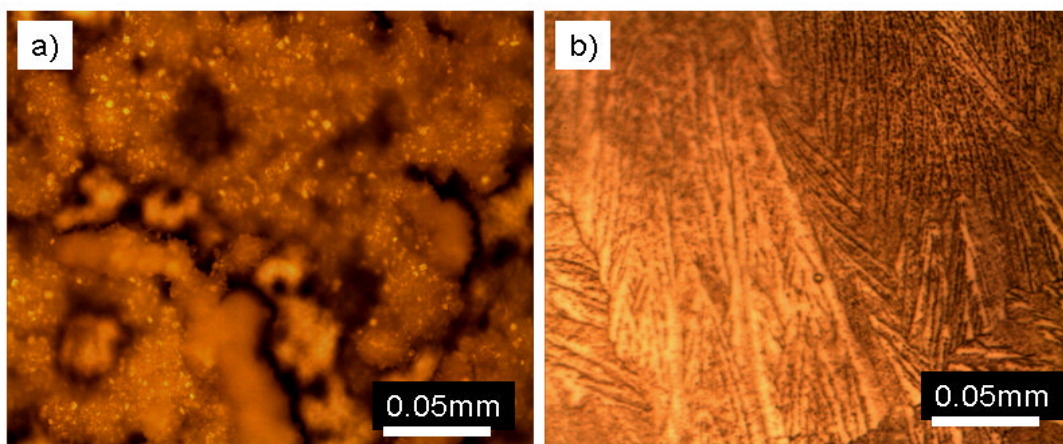


Figure 5.42: Optical images of Clotrimazole micro-nanostructures deposited on Si coated with ZnO nanostructures (a) and Ti substrate (b).

5.1.9.2 AFM of Clotrimazole nano-microstructures

AFM image was recorded from clotrimazole thin film which has been deposited on different substrates, the topography with a scan area of $20 \times 20 \mu\text{m}^2$. From Figure 5.43, it is clear that the surface morphology of the as-evaporated structures depend significantly on substrate surface. **Figure 5.43 a-b** shows uniform particles from Clotrimazole which distributed homogenously on Ti substrate. **Figure 5.43c** shows uniform Clotrimazole nano-microstructures covering the glass surface with growing rod like structures.

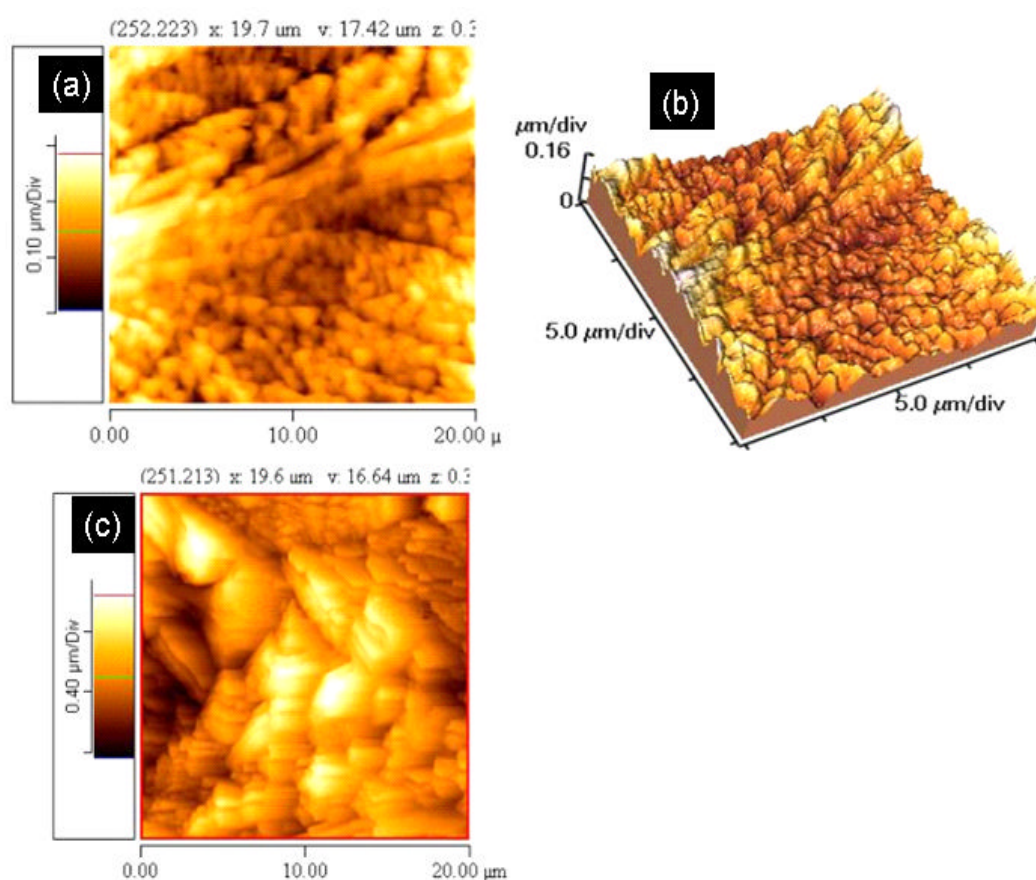


Figure 5.43: Two-dimensional and three-dimensional AFM height images of Clotrimazole growing on Ti (a and b) and two-dimensional AFM of clotrimazole on glass substrate(c).

5.1.9.3 SEM of Clotrimazole nano-microstructures

Figure 5.44. shows the SEM of Clotrimazole deposited on Ti substrate. It was noted that the surface of thin films consists different shapes of aggregates. These aggregates in thin

film are dendrite-like structures which grown after evaporation. The SEM image shows uniform formation of the seeds with an average size of $\sim 40\text{-}60\ \mu\text{m}$ on the film surface.

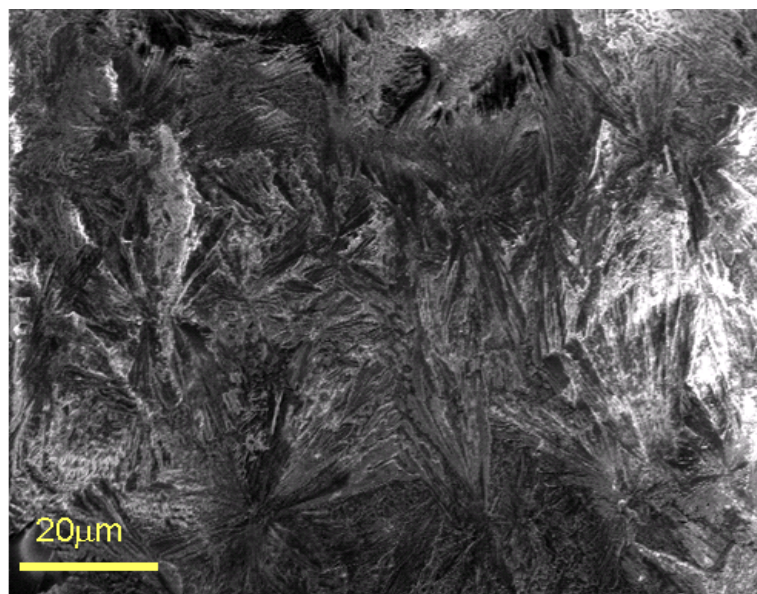


Figure 5.44: SEM images of Clotrimazole deposited on Ti substrate.

5.1.9.4 Raman Spectrum of Clotrimazole nano-microstructures

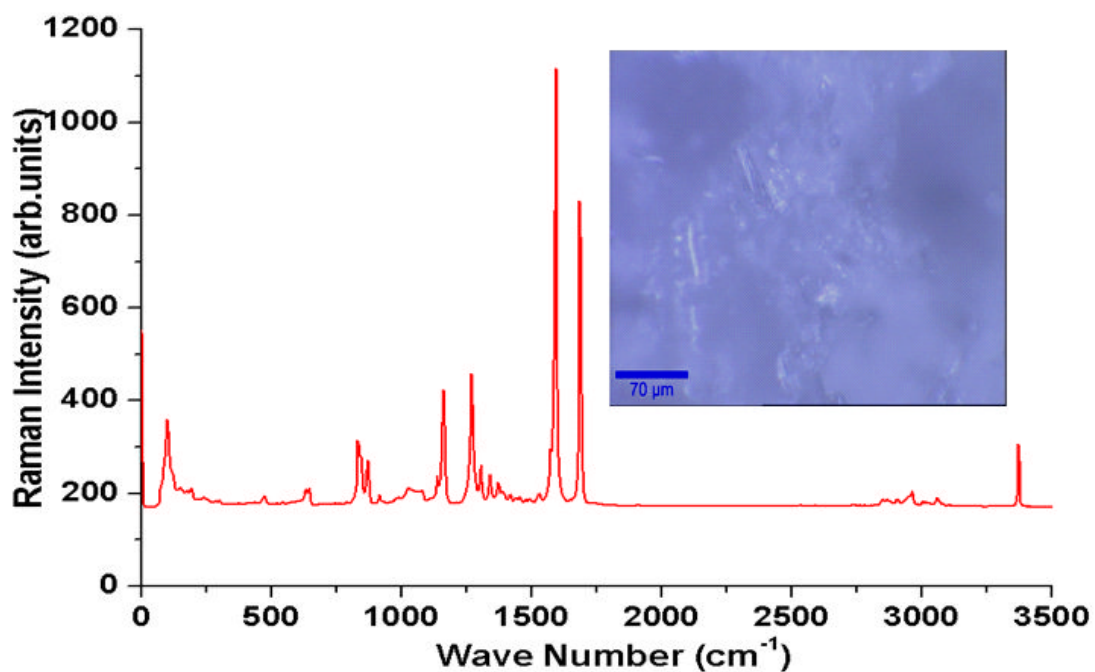


Figure 5.45: The reference sample of Clotrimazole with optical image (inset) and its Raman-spectrum.

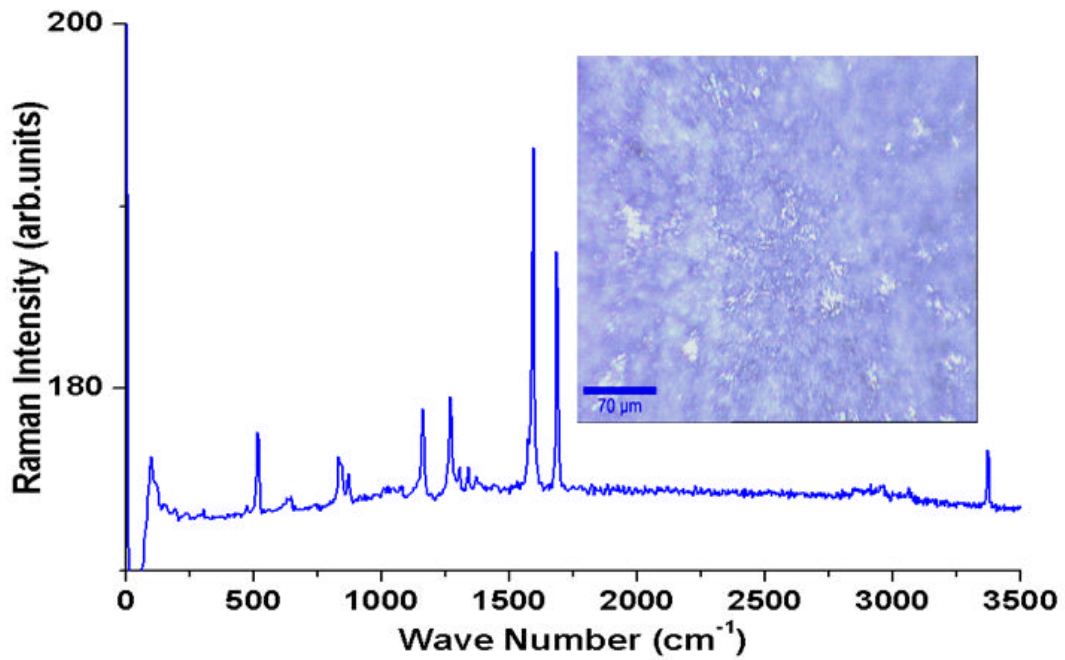


Figure 5.46: Clotrimazole sample after deposition with its appropriate optical image (inset) and Raman-spectrum.

The spectra are very similar to each other with only very subtle differences in Raman intensity. Both **Figures 5.45** and **5.46** show the functional groups of Clotrimazole. It is noted that the characteristic bands for Clotrimazole located at $\sim 3300\text{-}3100\text{ cm}^{-1}$ for (CH aromatic) and large bands located at 1689 cm^{-1} and 1583 cm^{-1} and 817 cm^{-1} for (C=C) and (C=N) and (C-Cl) respectively. The presence of these bands in deposited materials suggests the existence of Cotrimazole without decomposition.

5.1.10 Structural engineering of Trimethoprim

5.1.10.1 AFM of Trimethoprim nano-microstructures

Figure 5.47 shows 2D and 3D AFM images of Trimethoprim nano-microstructures deposited on Ti substrate with different scan area of $10 \times 10\ \mu\text{m}^2$ and $6 \times 6\ \mu\text{m}^2$. Obviously, a uniform film consists of many tiny particles with higher surface area which grown on Ti substrate. AFM images show surface features with an average diameter of $200\ \mu\text{m}$ and a maximum height variation of 390 nm. The surface is slightly roughness.

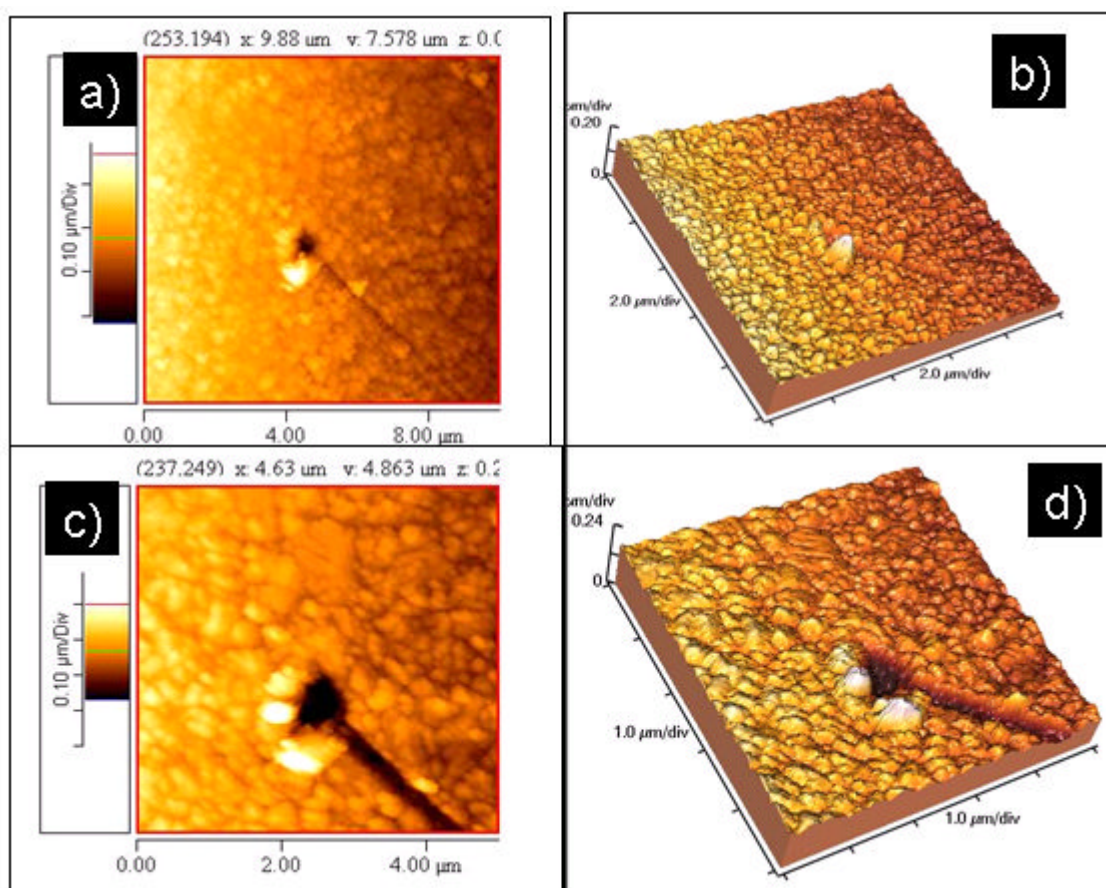


Figure 5.47: Two dimensional AFM and a three-dimensional AFM height image of Trimethoprim on Ti with different scan area of $10 \times 10 \mu\text{m}^2$ (a-b) and $6 \times 6 \mu\text{m}^2$ (c-d)

5.1.10.2 Raman spectrum of Trimethoprim nano-microstructures

Raman spectrum of Trimethoprim is ($\nu_{\text{max}} / \text{cm}^{-1}$). **Figure 5.49** shows observed peaks at $\sim 3474 \text{ cm}^{-1}$ which assigned to the (NH_2), at 3006 cm^{-1} for (CH aromatic), at $2900\text{-}2922.25 \text{ cm}^{-1}$ (CH aliphatic), the large band is located at 1587.77 cm^{-1} which is corresponding to ($\text{C}=\text{C}$) and ($\text{C}=\text{N}$), peaks located at 1350 cm^{-1} and 1448 cm^{-1} which are describing (CH_3 and CH bend), and at 1049 cm^{-1} for (C-O-C). The presence of these bands also in deposited materials suggests that the existence of Trimethoprim without decomposition.

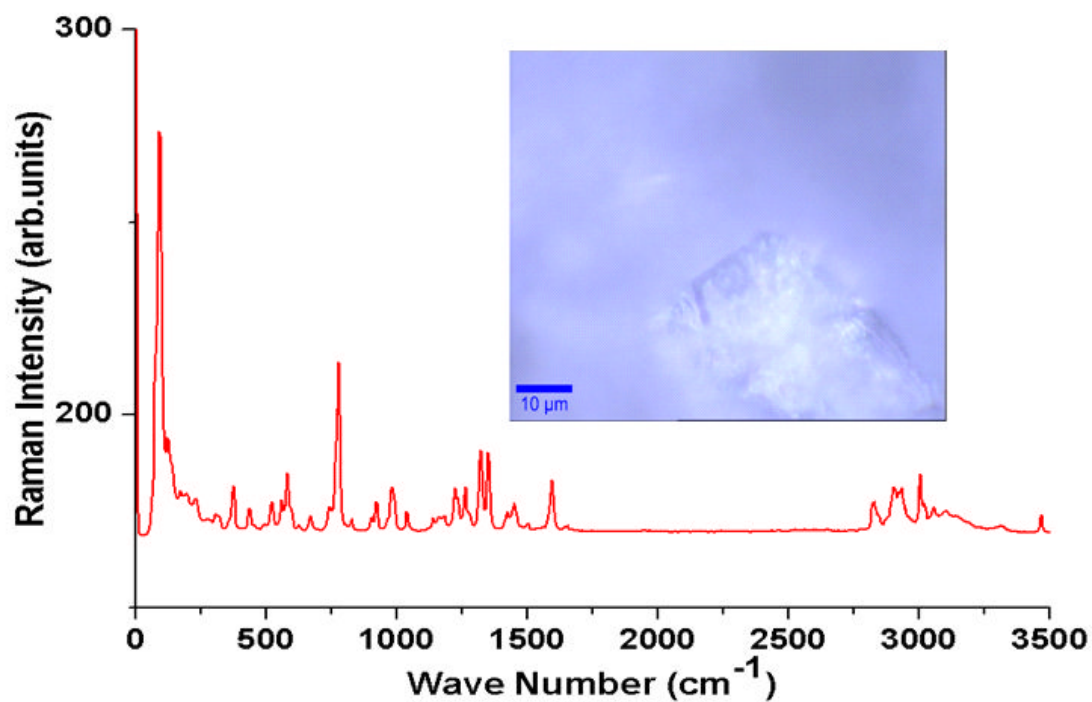


Figure 5.48: The reference sample of Trimethoprim shows optical image (inset)) with its Raman-spectrum.

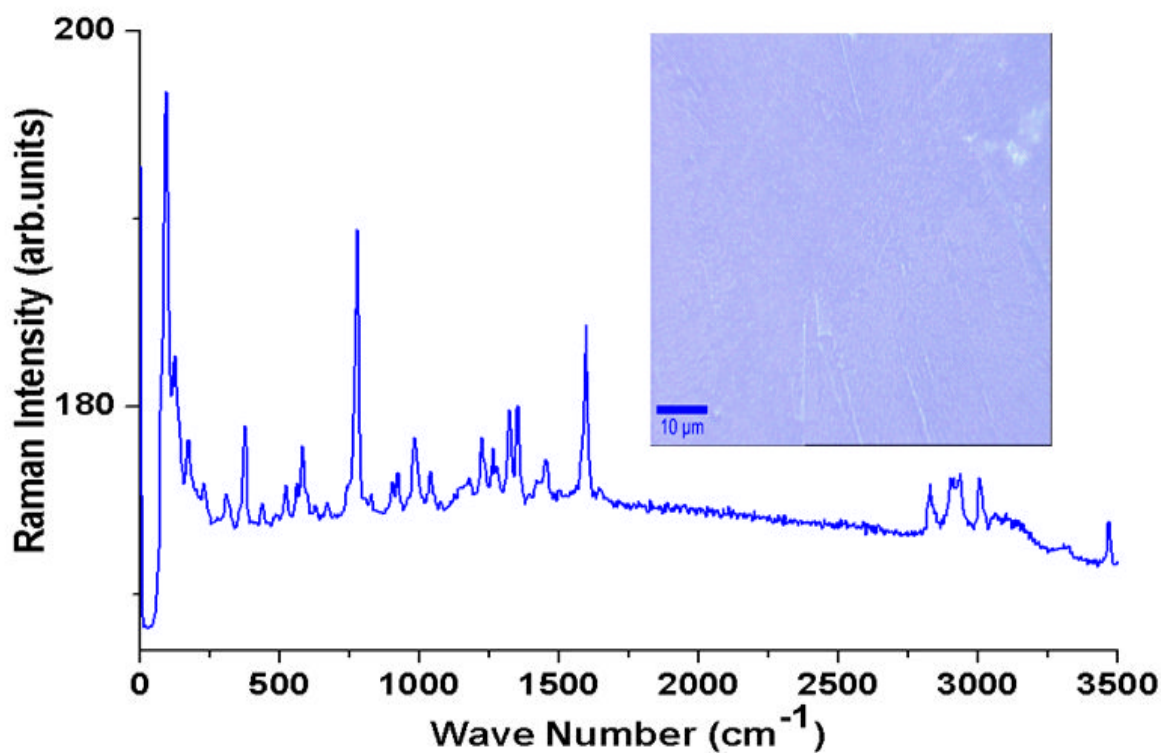


Figure 5.49: Trimethoprim sample after deposition with appropriate optical image (inset) and it's Raman-spectrum.

5.1.10.3 XRD Spectrum of Trimethoprim nano-microstructures

The XRD spectrum has been recorded to emphasize the statement that some materials are in amorphous state directly after deposition. In this case, Trimethoprim is being investigated.

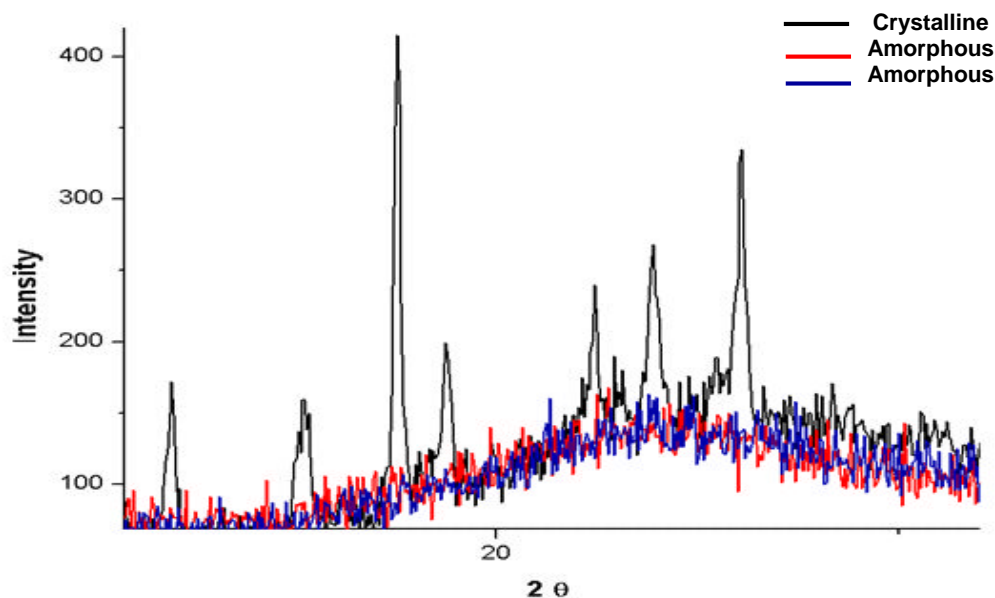


Figure 5.50: XRD pattern of Trimethoprim deposited on glass substrate at different growth times after 1h (blue line), 3 day (red line)s and ten days (black line).

The crystallinity of Trimethoprim drug thin film has been checked by XRD after evaporation immediately, 3 days and after 10 days as illustrated in **Figure 5.50**. The spectrum in **Figure 5.50** shows many peaks from different angles but without projecting single specific ones. This is typical for materials in amorphous state which have been investigated after one hour and three days. XRD results also show that the film of Trimethoprim is still in amorphous nature after 3 days. **Figure 5.50** represents that the good crystalline nature and sharp intense peaks of Trimethoprim achieved after 10 day due to the mobility of the condensing particles on the substrate surface is more which provides the crystallization and the growth of large crystals. Films of nano-microparticles can be also controlled by post deposition heat treatment. The Crystallization process started slowly with the formation of nuclei then growth follows. Obtaining this kind of information is important in the area of pharmaceutical formulations.

5.1.11 Structural engineering of Sulphathiazole

5.1.11.1 AFM of Sulphathiazole nano-microstructures

Figure 5.51 shows the AFM images of 2D and 3D Sulphathiazole thin films deposited on Ti. For thin films, the uniform grains are densely packed, implying a three-dimensional island. The enlarged view of the image shows that the grain looks rod-shaped (see **Figure 5.51d**). The AFM images show surface features with an average diameter of 450 nm and a maximum height variation of 480 nm.

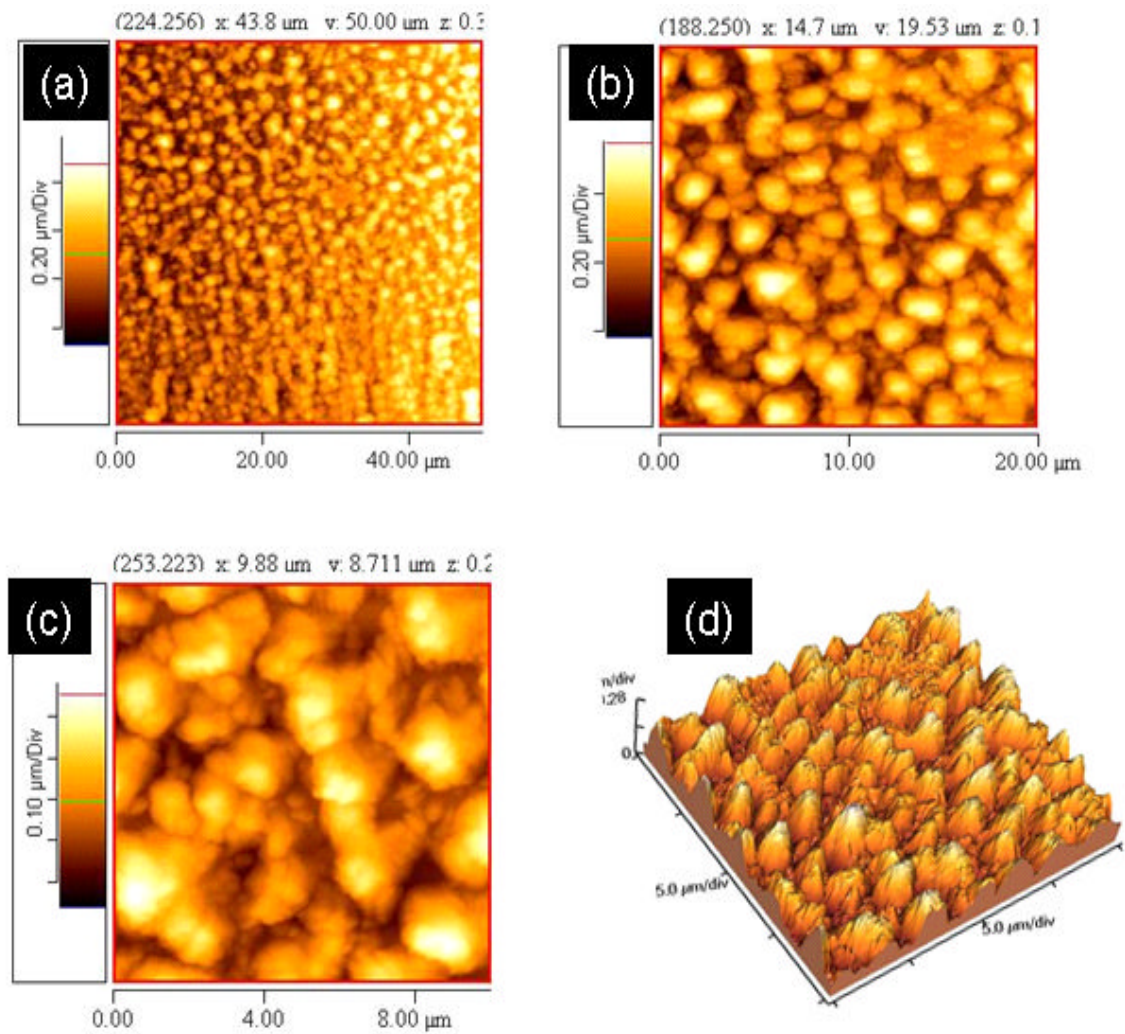


Figure 5.51: AFM 2D and 3D image of Sulphathiazole deposited on Ti with different magnifications.

5.1.12 Characterization of Tetracycline-HCl nano-microstructures

5.1.12.1 AFM of Tetracycline-HCl nano-microstructures

Figure 5.52a-d shows a two-dimensional image and three dimensional of the topography with different a scan area of $20 \times 20 \mu\text{m}^2$, $4 \times 4 \mu\text{m}^2$, $2 \times 2 \mu\text{m}^2$ and three dimensional image with a scan area of $20 \times 20 \mu\text{m}^2$ with various height 0.31, 0.013, 0.010. Clearly, uniform nanoparticles were obtained on titanium substrate (see **Figure 5.52a-b**) and glass substrate (**Figure 5.54c-d**). The AFM images shows surface features with an average diameter of $\sim 20 \text{ nm}$.

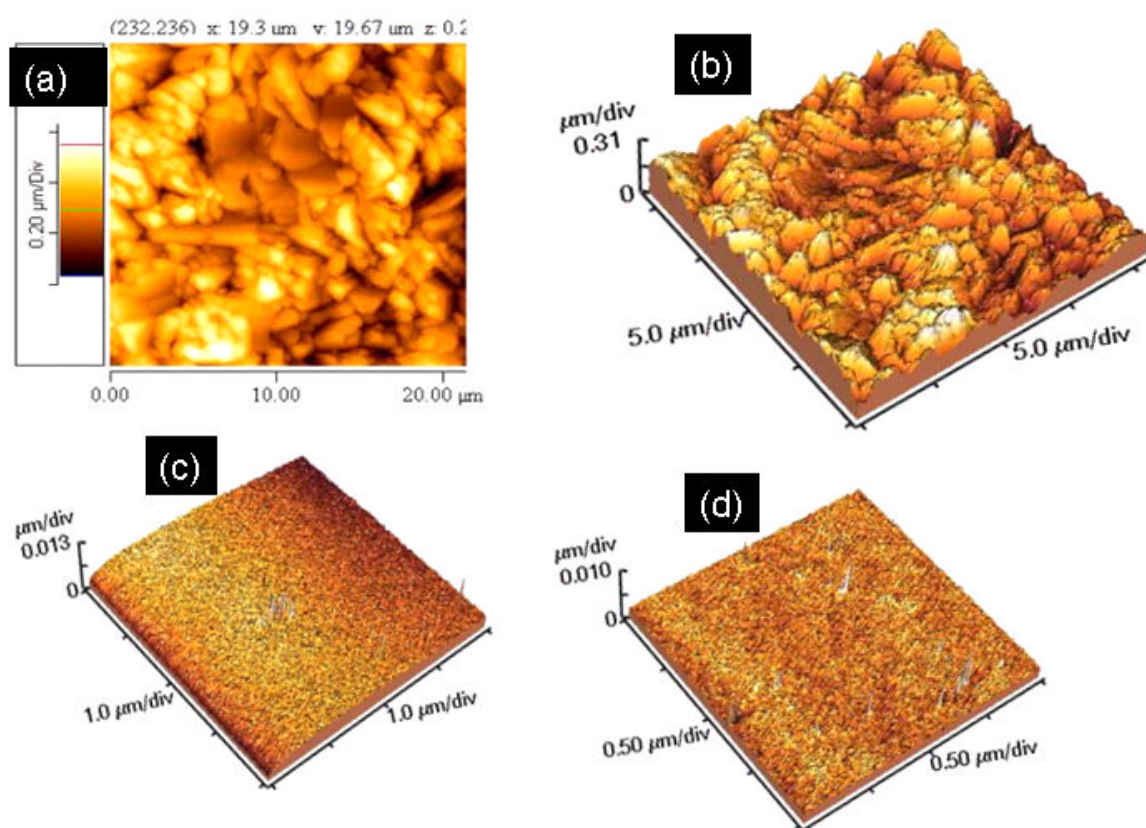


Figure 5.52: AFM 2D and 3D images of Tetracycline-HCl deposited on Ti(a-b) and glass (c-d) with different scan area.

5.1.13 Structural engineering of Erythromycin

5.1.13.1 AFM of Erythromycin nano-microstructures

Figure 5.53a-d shows 2D and 3D AFM images of the topography of Erythromycin with different a scan area of, $20 \times 20 \mu\text{m}^2$, $4 \times 4 \mu\text{m}^2$, $2 \times 2 \mu\text{m}^2$. Also 3D AFM image appears with a scan area of $20 \times 20 \mu\text{m}^2$ with various heights 0.31, 0.013, and 0.010. Clearly, a

uniform nanoparticles and smaller grain sizes for Erythromycin after evaporation covered and distributed on the titanium substrate with higher surface area as well as the crystalline form occurred after time.

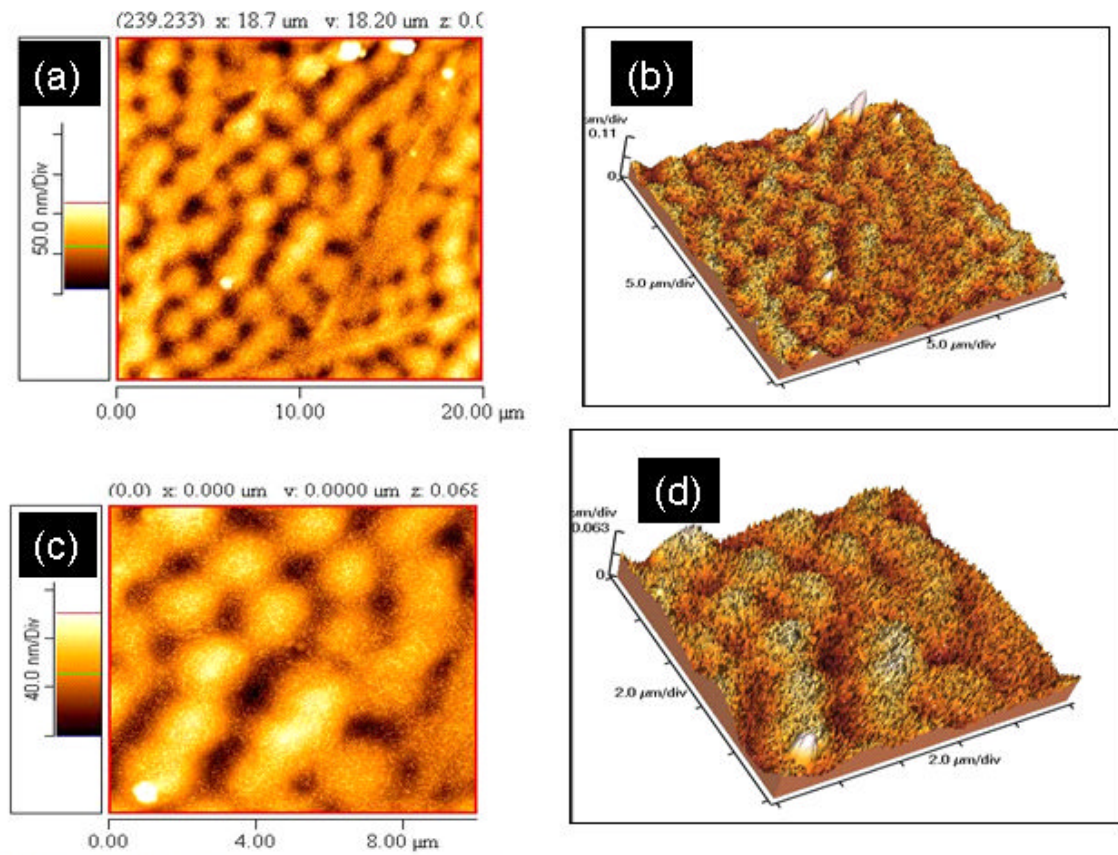


Figure 5.53: AFM 2D and 3D images of Erythromycin deposited on Ti with different magnifications.

5.1.14 Structural engineering of Tobramycin

5.1.14.1 AFM of Tobramycin nano- microstructures

Tobramycin is also deposited on Ti substrate. **Figure 5.54** shows 2D AFM image of the topographical scan with a scan area of $10 \times 10 \mu\text{m}^2$. Obviously, a uniform of crystalline structure is attained. In some regions, the deposited material not sufficient to cover all the surface. The overall roughness is low. The lighter parts on the upper and lower end of the scan arise from problems while scanning the sample and may falsify the actual image. A three-dimensional topographical scan of this area can be seen in **Figure 5.55**. It proves the previous conclusion about the surface structure. But, the irregularities on the upper and lower end of the scan occur. Nevertheless, the surface is rather smooth. The maximum height reaches about $0.1 \mu\text{m}$.

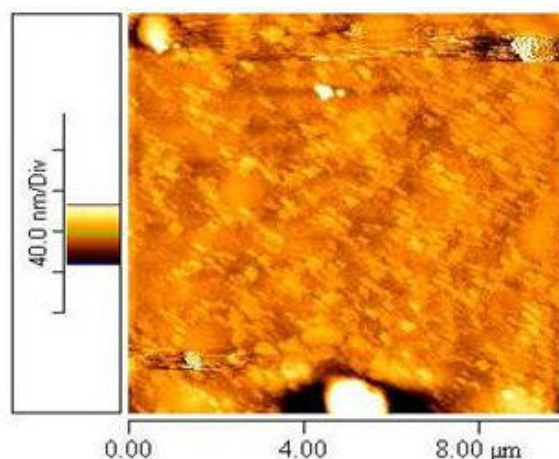


Figure 5.54: AFM 2D image of Tobramycin deposited on Ti. The scan area is about $10\ \mu\text{m} \times 10\ \mu\text{m}$. The surface roughness is minor as the legend on the left implies a maximum height of $< 30\ \text{nm}$.

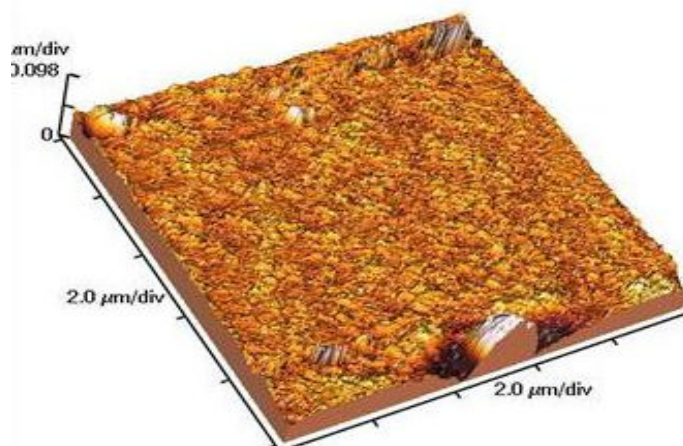


Figure 5.55: AFM 3D image of Tobramycin on Ti is shown with a scan area of $10\ \mu\text{m} \times 10\ \mu\text{m}$ and a maximum height of $0.1\ \mu\text{m}$.

5.1.15 Structural engineering of Ascorbic acid

5.1.15.1 SEM of Ascorbic acid nano-microstructures

Apart from the standard growth of nanoscale thin films with a certain degree of crystallinity, formation of rather complicated dendrite or hierarchical like structures may be triggered, as illustrated for Ascorbic acid in **Figure 5.56**. The SEM images show uniform formation of the hierarchical structures with an average size of $\sim 60\ \text{nm}$ on the film surface.

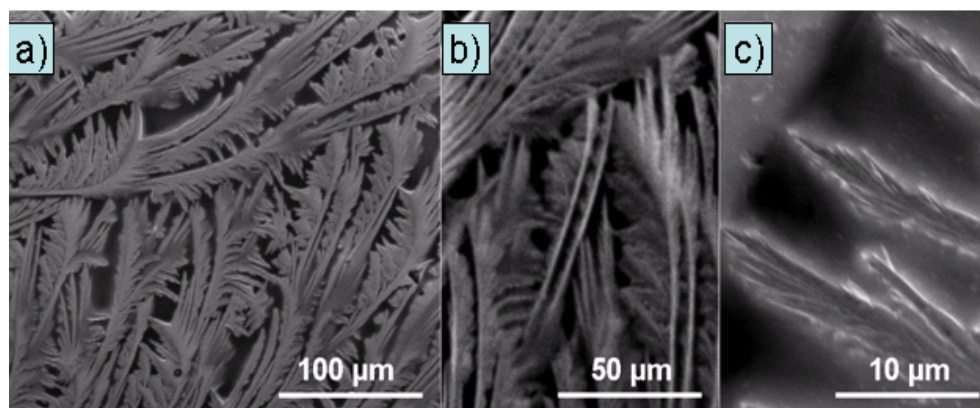


Figure 5.56: a-c SEM images of Ascorbic acid on Ti substrate with different magnifications.

5.1.16 Characterization of Adipic acid nano-microstructures

5.1.16.1 SEM of Adipic acid micro-nanostructures

The SEM image of Adipic acid shows dense structures of nano needles like structures that are distributed homogeneously and uniformly over the surface (see **Figure 5.57**).

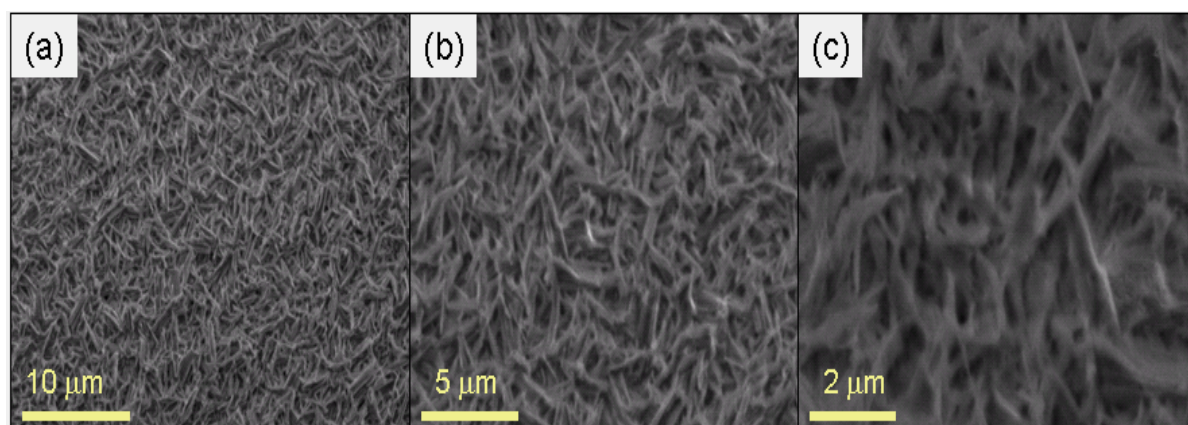


Figure 5.57: (a-c) SEM images of Adipic acid grown on Ti substrate with different magnifications.

5.1.16.2 Raman Spectrum of Adipic acid nano-microstructures

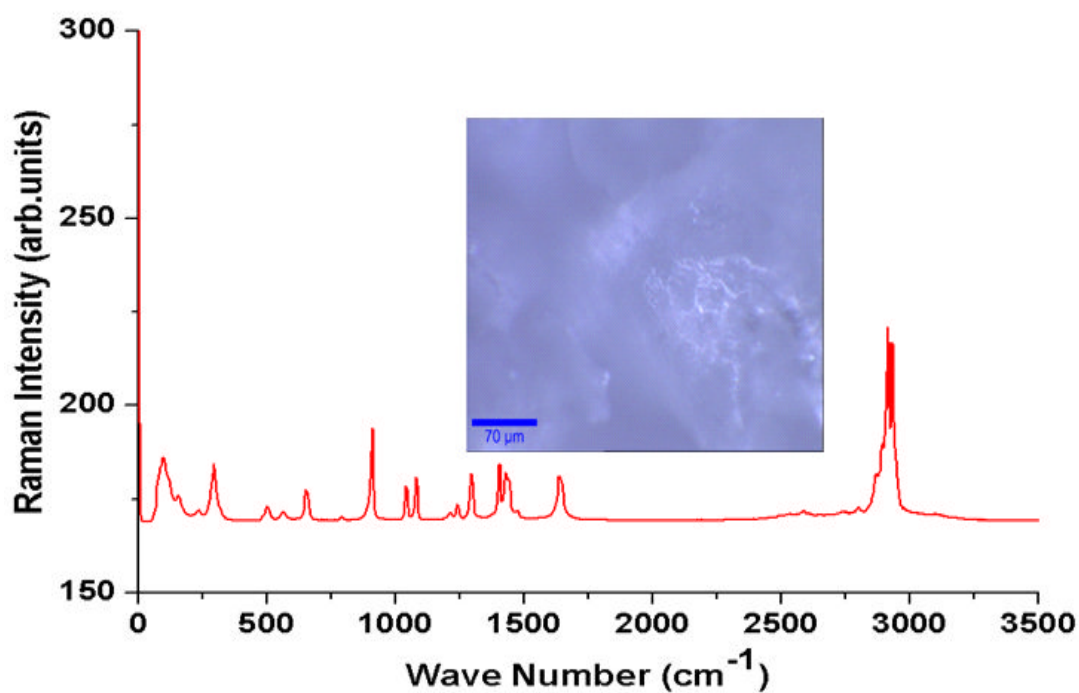


Figure 5.58: The Raman spectrum of Adipic acid control sample. The inset shows the optical microscope image of the control sample.

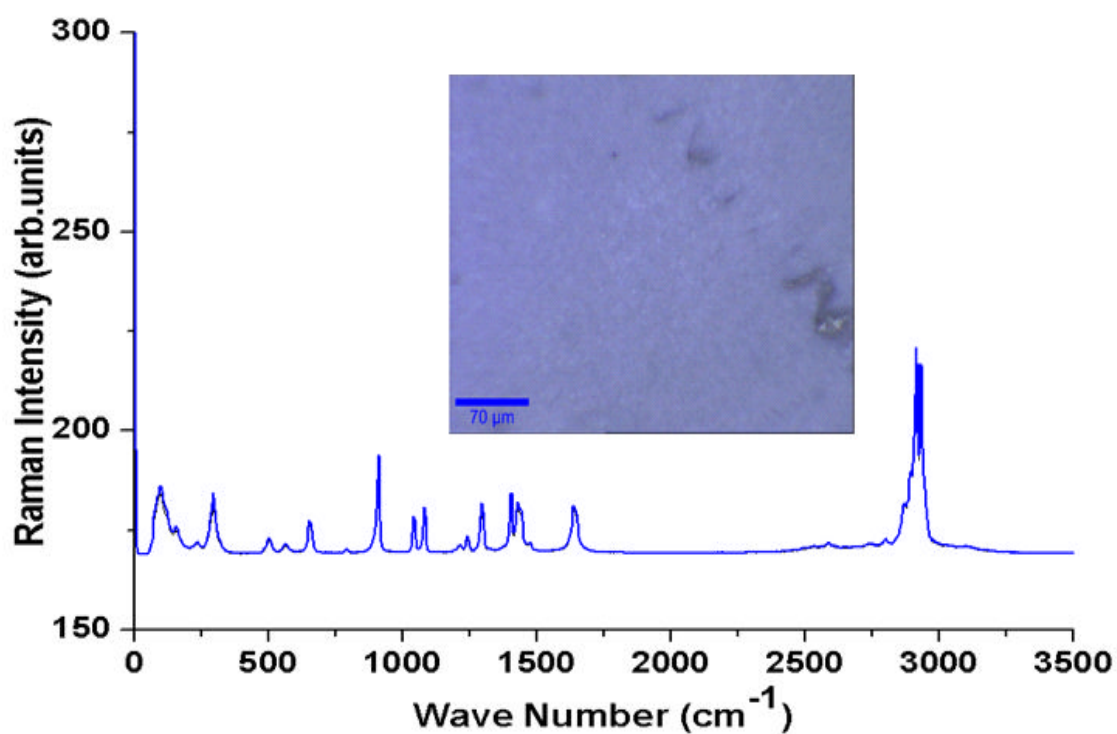


Figure 5.59: The Raman spectrum of Adipic acid deposited sample. The inset shows the optical microscope image of the deposited sample.

Figures 5.58 and **5.59** described that both spectrum are similar. Therefore, no change occurs in the chemical structure of Adipic acid. Raman spectrum of Adipic acid ($\nu_{\max}/\text{cm}^{-1}$) shows band at 2932 cm^{-1} (CH aliphatic). The large band is located at 1638 cm^{-1} corresponding to (C=O) at 1450 cm^{-1} for (CH₂ bend) and at 1273 cm^{-1} assigned to (OH bending). So, the presence of these bands also in deposited materials suggests the deposition of Adipic acid in exists successfully.

5.1.17 Structural engineering of Caffeine

5.1.17.1 SEM of Caffeine nano-microstructures

From **Figure 5.60** the SEM image of caffeine with different magnifications, the uniform structure with higher surface area appears clearly. Scanning electron microscope (SEM) images also show that our film products consist of densely-aggregated particles with average diameter $\sim 10\text{ nm}$.

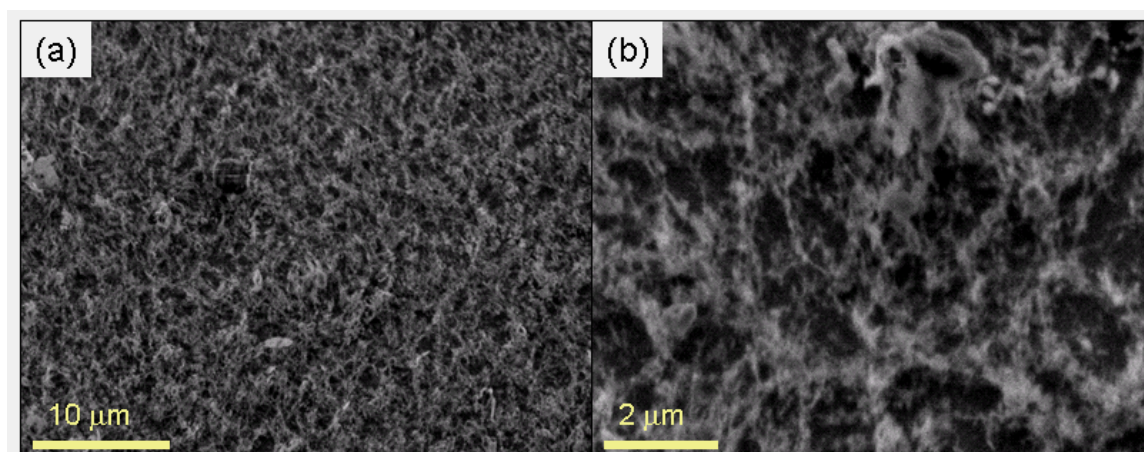


Figure 5.60: SEM images show different magnifications of Caffeine nanostructures deposited on Ti substrate.

5.1.17.2 Raman spectrum of Caffeine nano-microstructures

Visibly, both spectra are similar to each other as shown in **Figures 5.61** and **5.62**. Thus, the chemical composition of Caffeine is still the same after vacuum deposition. Raman spectrum is of Caffeine ($\nu_{\max}/\text{cm}^{-1}$) show characteristic peaks located at $\sim 3105.7\text{ cm}^{-1}$ and 2958 cm^{-1} which assigned to the (CH aromatic) and (CH aliphatic) respectively. It was noted that bands located at 1689.7 cm^{-1} and 1642.1 cm^{-1} which assigned to (2C=O) and peak at 1609 cm^{-1} for (C=C and C=N) and sharp peak located at 1319 cm^{-1} corresponding to (CH bend). The presence of these bands also in deposited materials implies the proper existence of Caffeine.

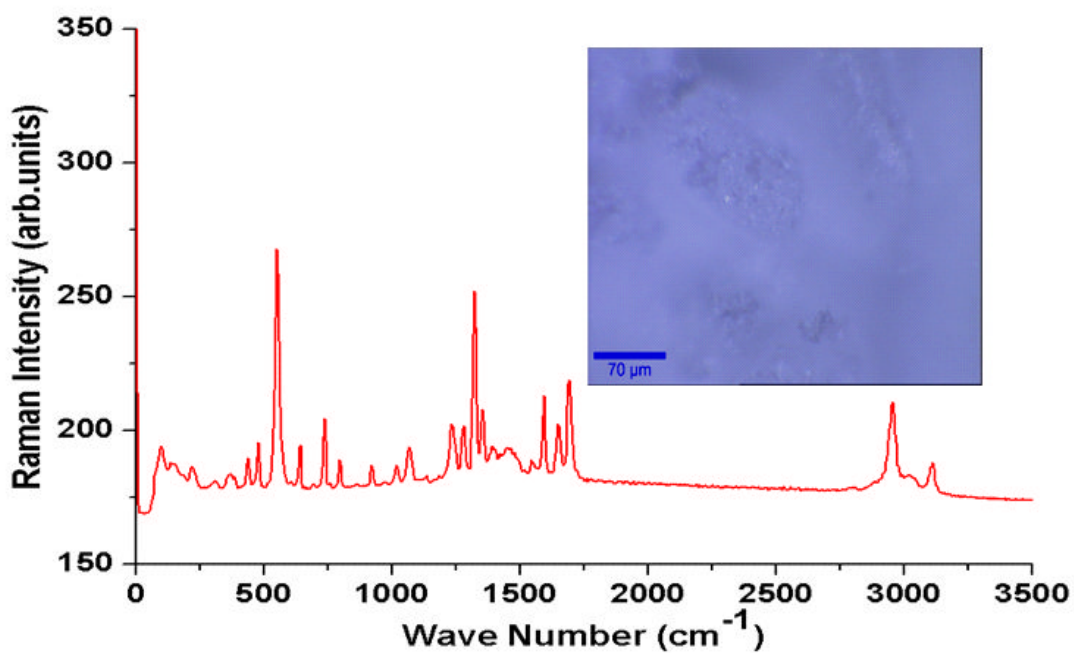


Figure 5.61: The Raman spectrum of Caffeine control sample. The inset shows the optical microscope image of the control sample.

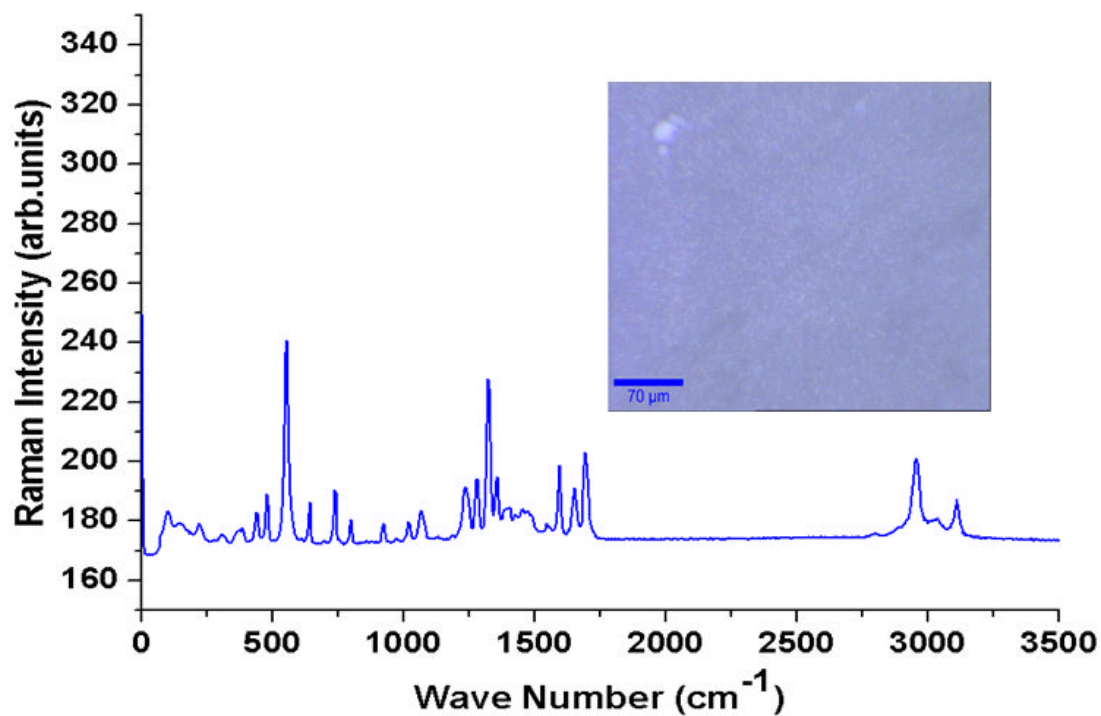


Figure 5.62: Caffeine sample after deposition with its appropriate optical image (inset) and Raman-spectrum.

5.1.18 Structural engineering of Cholesterol

5.1.18.1 SEM of Cholesterol nano-microstructures

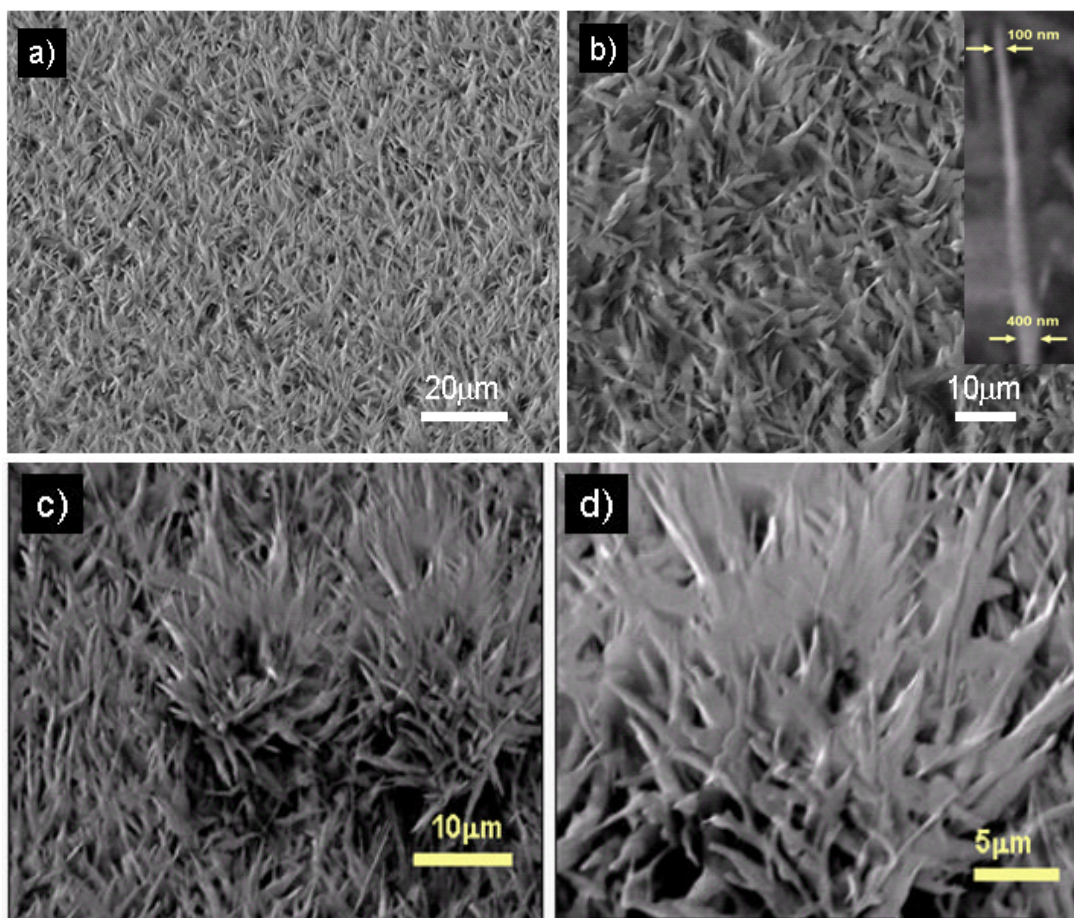


Figure 5.63: SEM image of Cholesterol nanostructures deposited on Ti (a, b) and Si coated with 4 nm Au thickness (c, d) with different magnifications.

The SEM image of Cholesterol shows a dense structure of nano needles and flower like structures that are distributed homogeneously and uniformly cover the surface of substrate using as shown in **Figure 5.63**. A uniform cover of the sample surface is achieved. The structure exhibits both needle and tetrapod forms which show high density and cross linking. The diameter of a needle is in the nanometer range of a few nm. As there are some free dark spaces one can presume that the growing of the structure arises from many small crystal nuclei.

5.1.18.2 Raman-spectra of Cholesterol nano-microstructures

For Cholesterol analysis, Raman-spectra have also been investigated the reference sample and deposited thin film of Cholesterol on Si coated with 4 nm Au thickness.

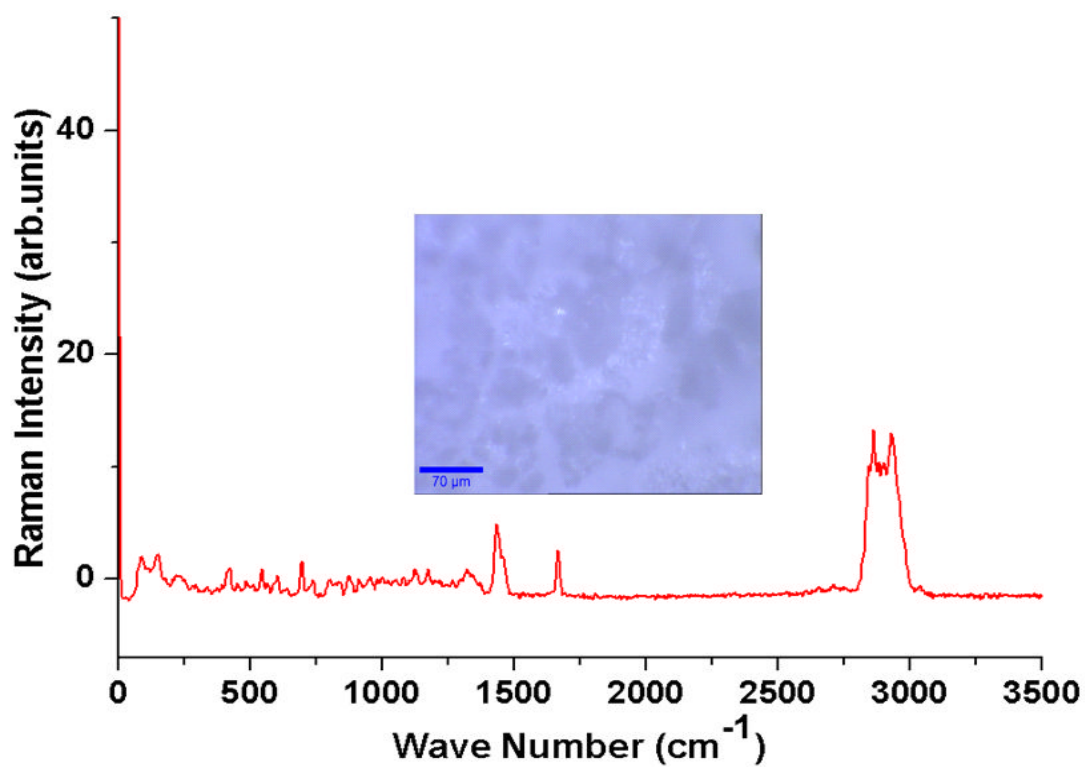


Figure 5.64: Raman spectrum and optical image (inset) of Cholesterol reference drug.

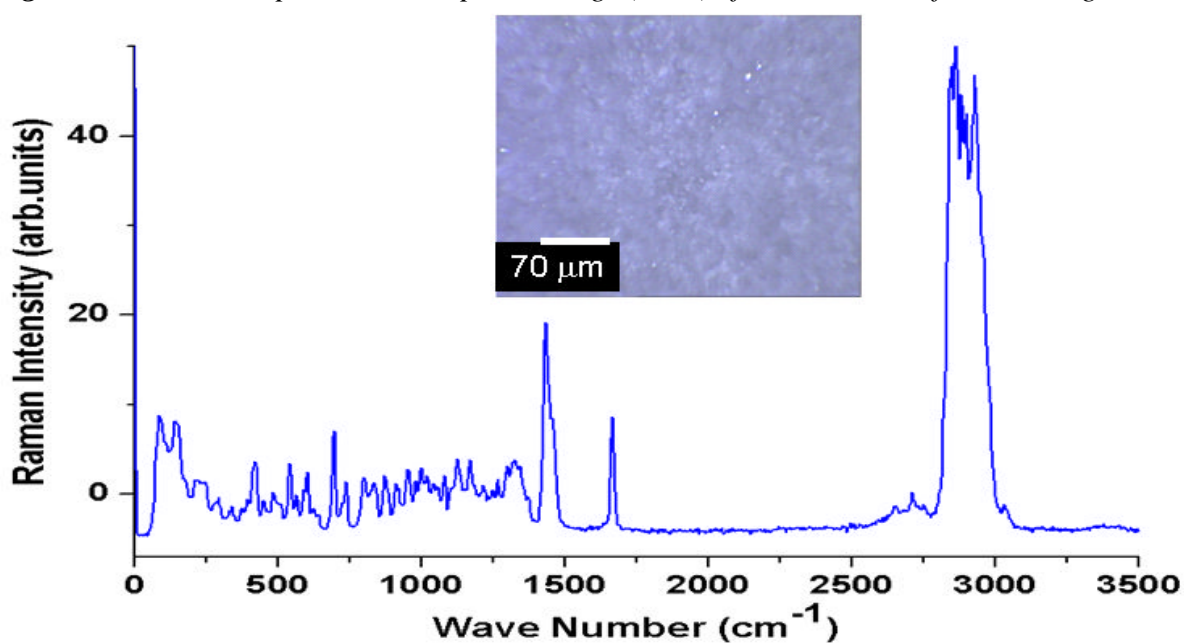


Figure 5.65: Raman-spectrum and optical microscope image (inset) of Cholesterol sample after evaporation.

Both spectra are likely related to the Raman shifts which imply that the deposited sample does not change in chemical composition. Raman spectra of Cholesterol (ν_{\max} / cm^{-1}) appear in **Figure 5.64.** and **Figure 5.65** showing the surface enhanced Raman intensity. Characteristic peaks at 2925-2874.6 cm^{-1} for (CH stretch).The large band is located at 1656 cm^{-1} for (C=C), 1436.1 cm^{-1} assigned to (CH₂ bend),1326 cm^{-1} for (CH₃ bend) and 1172 cm^{-1} due to the (OH bend), The occurrence of these bands in deposited materials suggests that the proper condition of the chemical structure of Cholesterol.

5.1.19 Structural engineering of SM nano-microstructures

5.1.19.1 Optical image of SM nano-micro structures

The material is deposited on glass and titanium; both results can be seen in **Figure 5.66.** The left image shows small droplets of SM on glass at a magnification of 50 x. They are < 500 nm as estimated from the scale bar. They are randomly distributed over the whole sample surface. They indicate that island growth is the predominant mechanism. The in the right figure is. SM nuclei seem to be a bit smaller and denser on titanium substrate if compared with glass substrate. But, they still follow the same growth mechanism as the nuclei form islands on the substrate. The optical image of the SM also does not show any interesting morphological features.

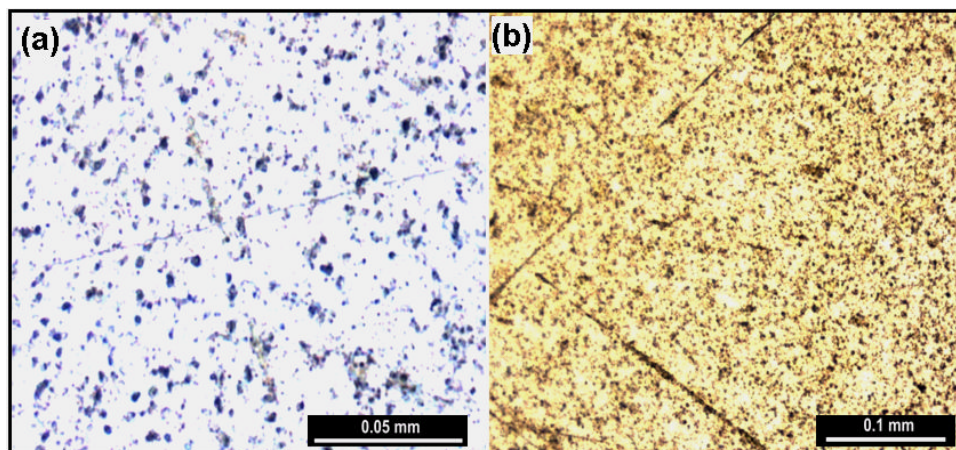


Figure 5.66: (a) Small droplets of SM directly after deposition on glass sample with a magnification of 50 x. (b) shows droplets of SM also directly after deposition but on titanium sample with a magnification of 20x.

5.1.19.2 SEM of SM nano-microstructures

SM is uniformly deposited onto Ti as seen in **Figure 5.67**. The structure appears to be uniformly and homogeneously composed of rods or pillars like structure that have rounded down head pieces. The pillars are thick in the submicron range and they increase of the surface area. A uniform cover of the surface with SM can be observed as well as the crystalline structure of the deposited material. The shape of the nanostructure peaks resembles rounded down rods.

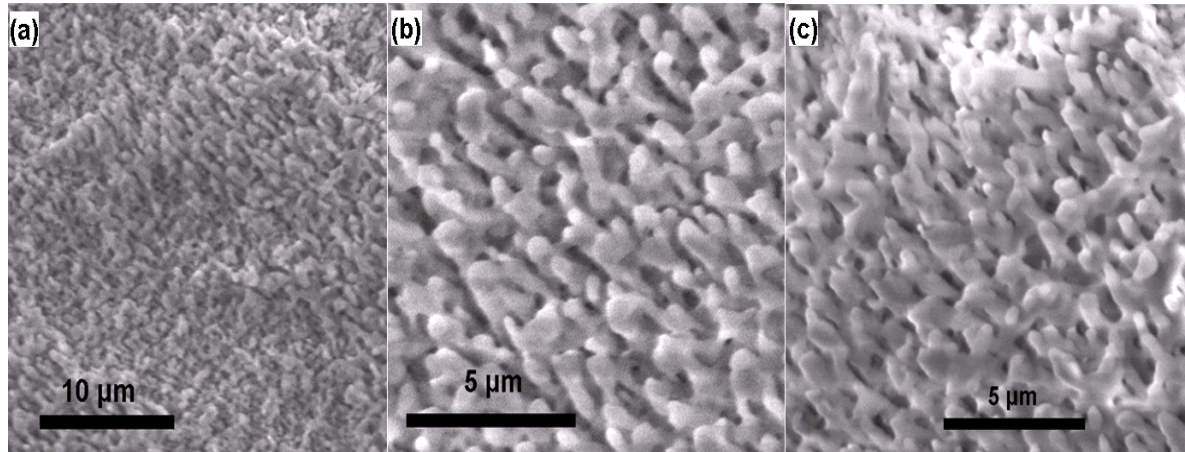


Figure 5.67: *a-c SEM images of SM grown on Ti with different magnifications revealing uniform dispersity.*

5.1.19.3 AFM of SM nano-microstructures

The two-dimensional topographical view of SM on Ti (**Figure 5.68**) depicts uniform crystalline shape covering the substrate. However, some white parts hypothesize that there are differences in the height.

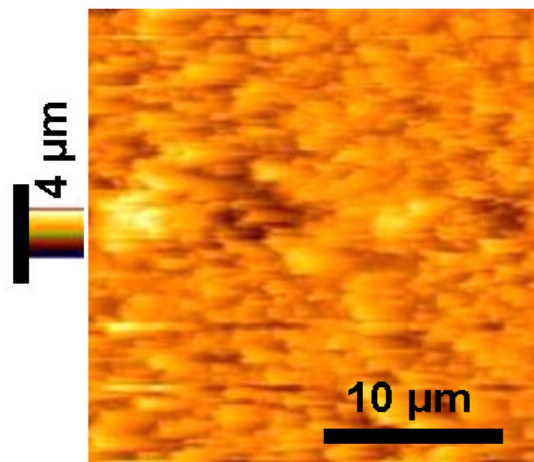


Figure 5.68: *AFM 2D image of SM on Ti substrate. The lighter parts in the image display particles that are higher than 2 μm. The particle size amounts roughly < 2 μm.*

The scan area is about $30 \times 30 \mu\text{m}^2$ and the size of crystallites is $< 2 \mu\text{m}$. Comparing this scan to the three-dimensional ones in **Figure 5.69** shows that SM is in fact crystallized uniformly. A height gradient from left to right is recognizable. The highest point in the left part of the scan is approximately $1.5 \mu\text{m}$ while on the right side it is around half of this value.

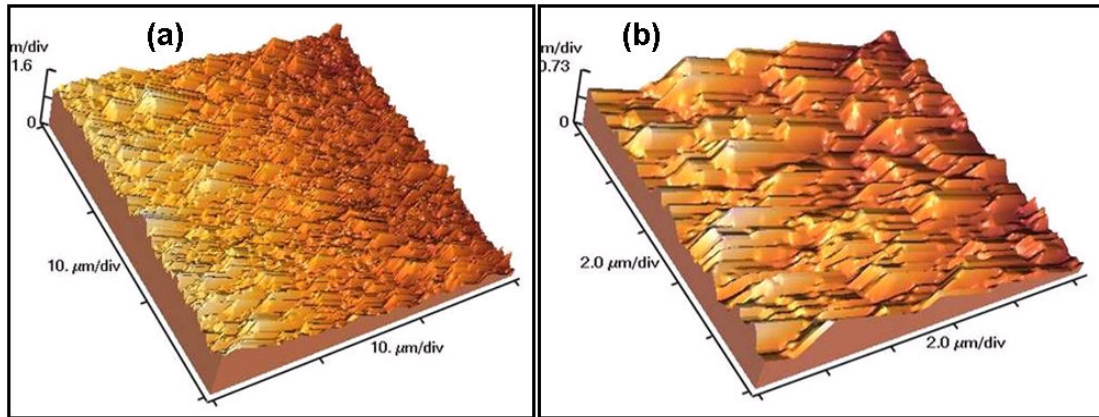


Figure 5.69: AFM 3D images of SM. (a) has a scan area of $10 \times 10 \mu\text{m}^2$ whereas (b) has a scan area of $2 \times 2 \mu\text{m}^2$. The maximum height is around $1.5 \mu\text{m}$.

5.1.20 Structural engineering of PLGA

5.1.20.1 SEM image of PLGA

Figure 5.70 shows the SEM image of PLGA which deposited on Ti substrate. The image is taken directly after evaporation with the exception of some island formations locally which are sufficiently separated from each other with average diameter of $5 \mu\text{m}$

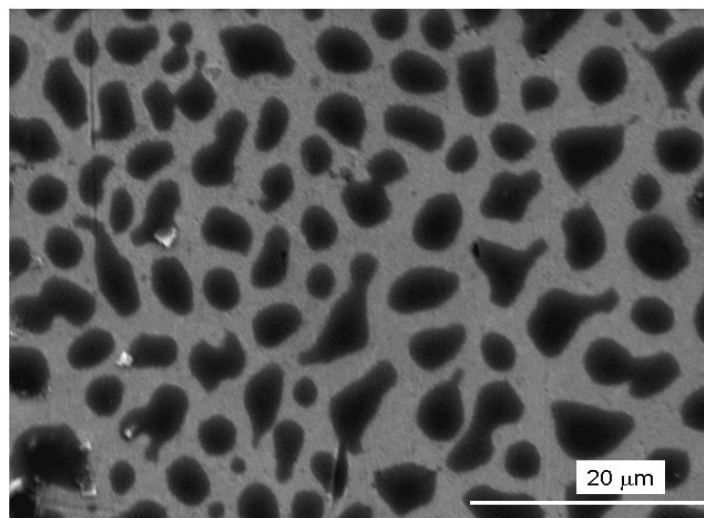


Figure 5.70: SEM image of PLGA on Ti substrate. The images are taken directly after evaporation. They show small droplets of PLGA.

5.1.21 Structural engineering of Indometacin

5.1.21.1 SEM of Indometacin nano-microstructures

The surface morphology of prepared Indometacin nano-microstructures has been characterized by SEM (see **Figure 5.71**). The surface of thin films consists of dendrite like structures. The hierarchical structures are essential for increasing the higher surface area to volume ratio.

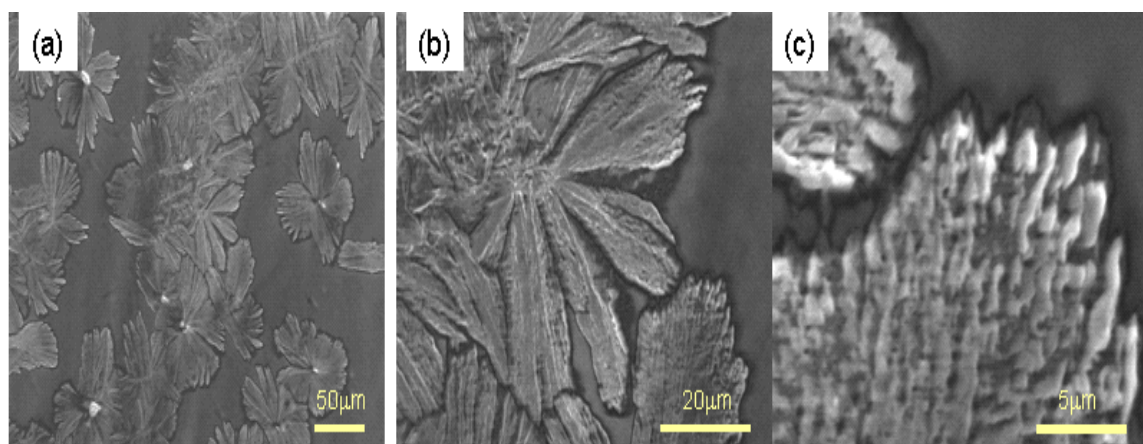


Figure 5.71: SEM images of Indometacin with hierarchical structures growing on Ti with different magnifications.

5.1.21.2 Raman spectrum of Indometacin nano-microstructures.

The reference substance of Indometacin shows a good Raman spectrum whereas the spectra derived from the samples are varying. The microscopic images from Indometacin deposited on Ti show an inhomogeneous surface with a thin film like layer with some incorporated crystals. Whereas the film spectrum does not resemble the reference spectrum at all, the crystal spectrum might be related to the reference. The foil carrier is very sensitive to energy input and shows an irregular surface with small “hairs”. The deposited layer shows a spectrum which is not truly comparable to the reference spectrum of Indometacin. Briefly, the vacuum deposition of Indometacin does not look very promising with respect to substance integrity 100 %.

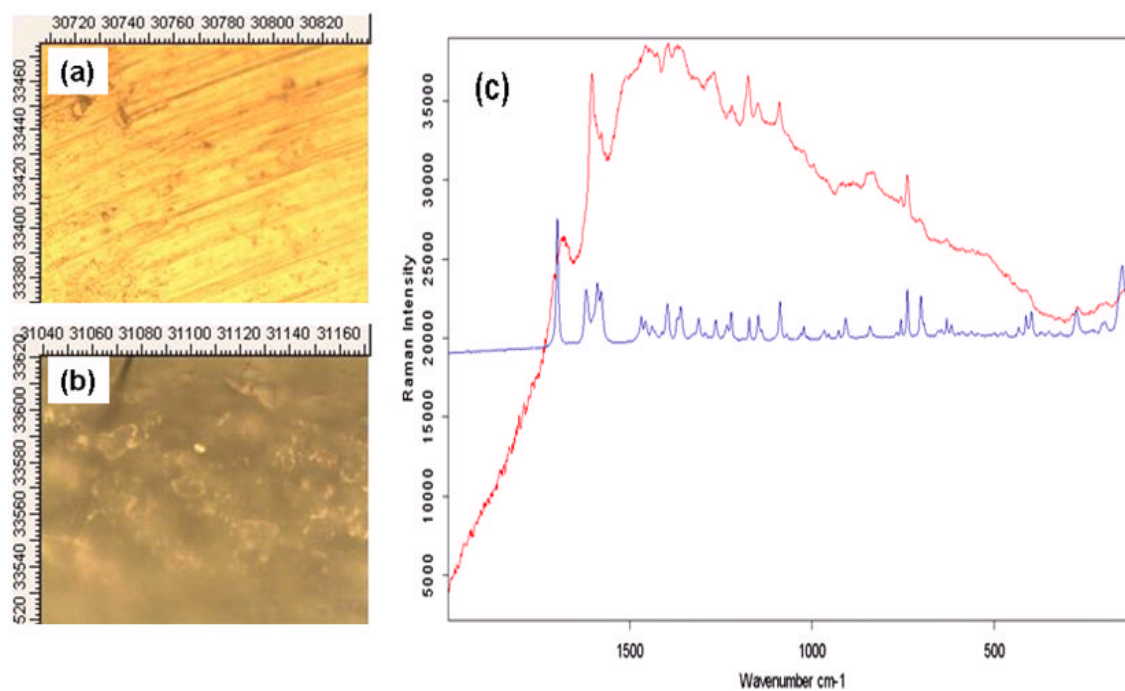


Figure 5.72: Microscopic image of Indometacin deposited on titan (film (a) reference sample (b) its Raman spectra of Indometacin reference substance (blue) and as film deposited substance on titanium substrate (red).

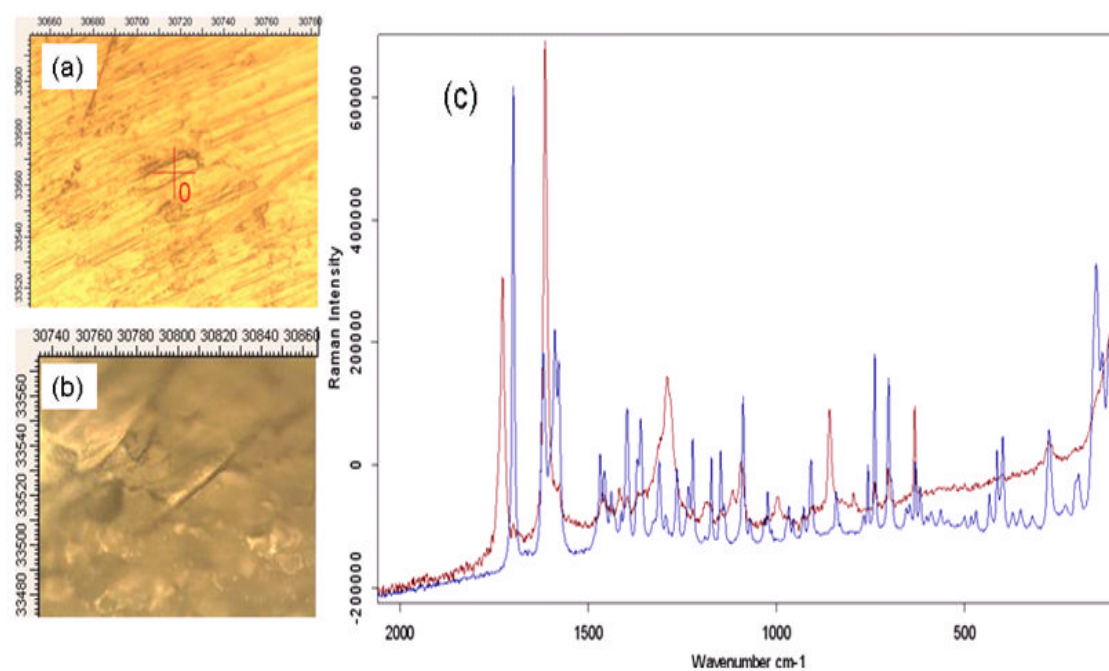


Figure 5.73: Microscopic image of Indometacin deposited on polymer foil (film (a) reference sample (b) its Raman spectra of Indometacin reference substance (blue) and as film deposited substance on polymer foil (red).

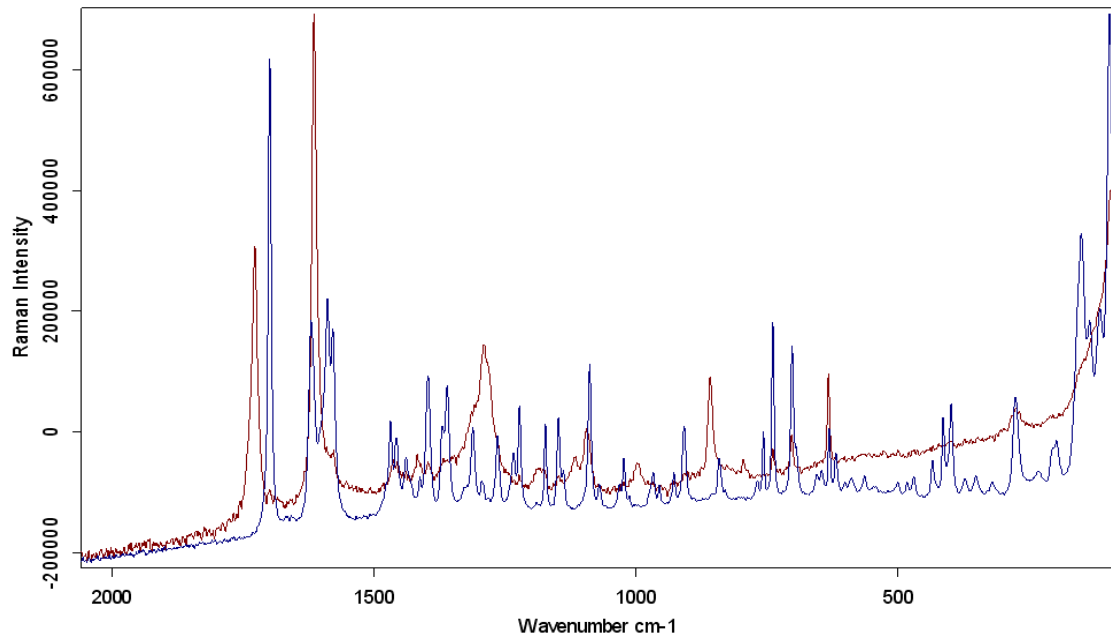


Figure 5.74: Raman spectra of Indometacin reference substance (blue) and deposited substance crystal on titanium substrate (red) after one week.

5.1.22 Structural engineering of multilayers

5.1.22.1 Characterization of two layers

Here, layer by layer deposition from antibiotic drug (Metronidazole) as first layer and PLGA as second layer which can be fabricated by using thermal evaporation to control the release of Metronidazole as illustrated in **Figure 5.75**. Drug release from bioerodible polymers require that the polymers break down into smaller molecular weight and nontoxic materials which removed or metabolized by the body.

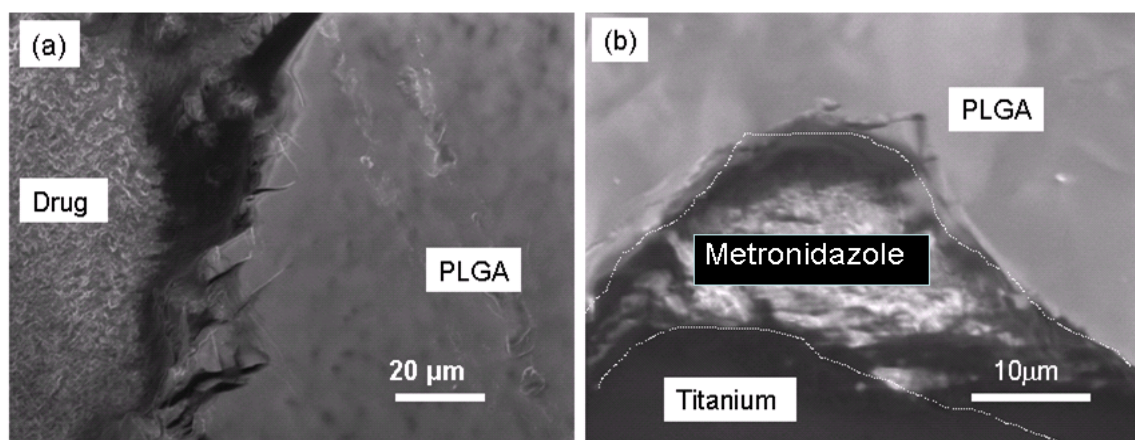


Figure 5.75: SEM of two layers sample composed of (1) Metronidazole, (2) PLGA with higher and lower magnification a and b respectively.

Paying attention to the properties of polymeric materials, such as physical and chemical stability, viscoelasticity, electric action, have extended the area of their applications to the biology and medicine.

5.1.22.2 Characterization of (4 Layers)

Investigating the adhesion between different layers and their growing process to form liposomes. Generation of a sample with 4 layers composed of (1) SM, (2) Cholesterol, (3) Fluorouracil and (4) SM (see **Figure 5.76**). From the SEM image, all materials are clearly seen deposited effectively on one another. They exhibit thicknesses in the nanometer range (for Fluorouracil) as well as in the micrometer range (for SM and Cholesterol).

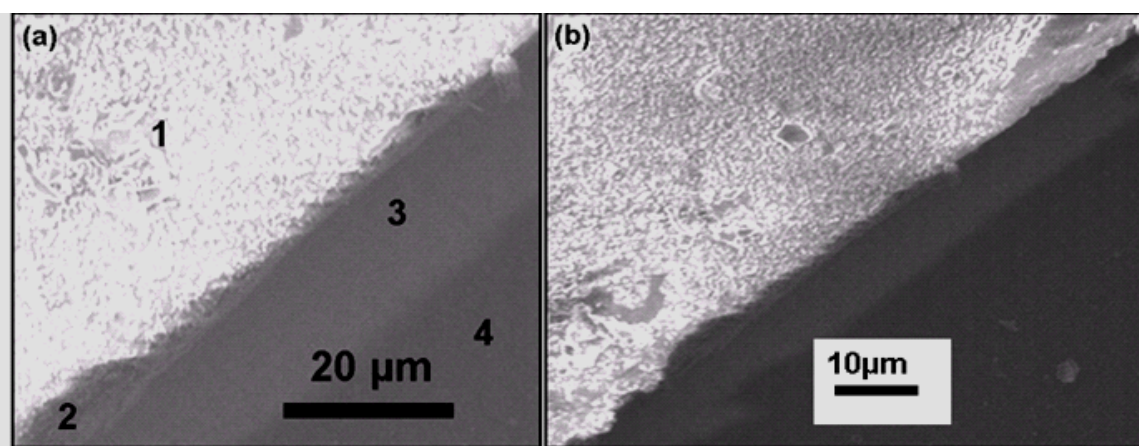


Figure 5.76: SEM of a four-layers sample composed of (1) SM, (2) Cholesterol, (3) Fluorouracil and (4) SM on Ti substrate with higher and lower magnification a and b respectively. Thicknesses of the single layers are: (1) $>20 \mu\text{m}$, (2) $15 \mu\text{m}$, (3) few nm, (4) $>20 \mu\text{m}$.

5.2 Discussion

5.2.1 Control over the crystallinity of the deposited drug films and their morphology

Thermal evaporation for pharmaceutical drugs is not so far reported in the literature which has been successfully established in this work [102]. Even though organic molecules for light emitting displays are of similar complexity like pharmaceutical molecules, surprisingly, their direct fabrication by thermal evaporation was not used in pharmaceutical engineering till now. A general precondition for TE is that the thermal

energy (here >300 °C meaning ~ 0.05 eV) injected into the molecules stays far away from the range of the intermolecular binding energies of typically 2-7 eV, which seems to be fulfilled. For getting a clearer view of the process, it should be understood in which steps of energy a single molecule can leave the different bonding force fields in its surrounding liquid and enter the vapour phase. Otherwise, energy barriers have to be taken in sequence to decompose a molecule. Such sophisticated calculations are difficult to carry out and not yet known. The large variety of possibilities for the molecules to wiggle, swing or rotate in its liquid state complicates it to foresee which of the molecules find their way into the gas phase and which decompose. Even if decomposition occurs in some fragments, a re-composition on the substrate may occur. This result seems to be confirmed by or arbitrary choice of molecules. But, an obvious prediction of the suitability for TE needs significant efforts to be done in future. When the vaporized atoms have reached the surface then condensed on it, extra mass transfer may occur by diffusive processes which may vary the shape, size and crystallinity of the organic material deposited. Different morphologies and structures may result when depositing from the vapour phase depending on the experimental parameters such as substrate surface, temperature [103] and evaporation rate. For example, the surface morphology of active pharmaceutical ingredients thin films show that the final film surface structure depends strongly on deposition rate. However, limited reports appear on organic thin film materials vs. deposition rate [104]. Organic molecules are often challenging to produce stable films on a substrate since they are often physisorbed, requiring a low surface energy at the film/substrate interface. Most organic materials have a low sublimation temperature where the vapour pressure is relatively high even at room temperature. These characteristics are in complete opposition with those of metal or inorganic materials which possess low vapour pressure even at high temperatures and often form strong chemical bonds with the substrate. The relationship between surface morphology and deposition parameters has been widely investigated, including metals, inorganic and organic thin film materials. However, the influence of vapour flux on surface morphology has not been confirmed to be the dominating factor. In order to evaluate the suitability of thermal evaporation for pharmaceuticals, several (>30) pharmaceutical substances under different parameters and several application examples have been demonstrated. Surprisingly, the vast majority of drugs ($>80\%$) show (see **Table 5.1**) the deposition of high quality crystalline films without decomposition. The formation of nano-micro scale pharmaceutical crystals on the substrate by thermal evaporation already indicates a high

Purity and high surface area to volume ratio if compared with the bulk material before evaporation as shown in **Figure 5.77**.

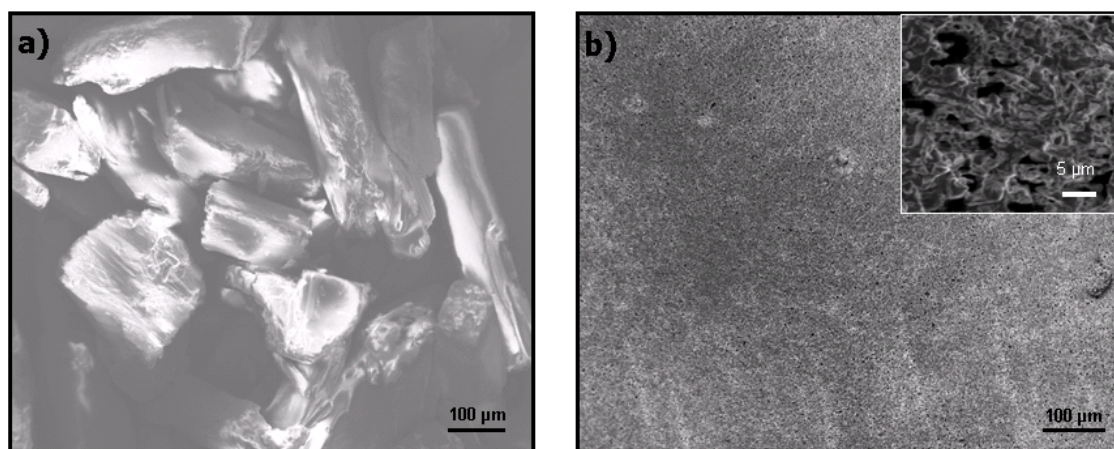


Figure 5.77: SEM images of Acetylsalicylic acid on Ti substrate after and before deposition a and b respectively. The inset shows higher magnification SEM image.

In view of a variety of molecules capable of thermally evaporated, there seems to be of no regularity which of the complex molecules stay intact and which decompose. In principle, the evaporation of the molecules may have a positive effect by purifying the evaporated substance since the contaminants with a lower melting point are evaporated early when the substrate is still covered by a shutter of the evaporation oven, or, in case of a higher melting point of the contaminant, it will not evaporate at all. With the molecules suitable for evaporation, the full versatility of thermal evaporation can be utilised. This means that by changing the deposition rate, the crystallinity of the deposited film can be controlled in a wide range from amorphous to almost single crystalline.

Figure 5.2 a-c illustrate this outcome with an example of a Nipasol drug film which might be amorphous or nanocrystalline in the case of deposition at $-100\text{ }^{\circ}\text{C}$ to crystalline film deposited at room temperature. With a liquid N_2 cooled substrate holder, even completely amorphous films can be deposited with a relatively high free surface energy. Also the coating thickness can be varied since the pharmaceutical drugs are used from a few nm to many μm simply by changing the evaporation rate and time as confirmed by AFM and profilometer measurements. Fabrication of nanostructured coatings of pharmaceutical drugs on desired substrates in a controlled manner is a very promising aspect of thermal evaporation technique after deposition. Moreover, the morphology of pharmaceutical molecules strongly depends on temperature, experimental condition,

compounds nature, substrate used and substrate temperature. For instance, when the evaporation temperature of Nipasol is reduced to ~ 165 °C or increased to ~ 220 °C as shown in **Figure 5.3**. The product is dominated by various dimensions and structures. **Figures 5.1, 5.9, 5.14, 5.29a-f, 5.38** and **5.42** demonstrate the morphology of pharmaceutical molecules which depends on the substrate surfaces. Besides, the nano-microstructures of the other compounds can be obtained by controlling the growth time and substrate surfaces. **Figure 5.29a-h** shows further examples of different nanoscale roughnesses and large surface areas formed by self organization during growth and appearance of thermally evaporated thin films of Tetracaine-HCl on different substrates as visualized by scanning electron microscopy. The inset images in **Figure 5.29 a-h** are the corresponding higher magnification SEM images showing a clear visibility of microstructural patterns of the deposited Tetracaine-HCl drugs. The choice of substrate may comprise a wide range of materials and even highly soluble substances employed to carry pharmaceutical thin films without the risk of side effects like dissolution of the substrate. The Tetracaine-HCl deposited films are strongly affected by the deposition conditions as confirmed in **Figure 5.29**. Branched nanostructures can be obtained by using 20 nm gold thickness deposited on Si substrate due to the aggregation of the particles along faces other than the polar faces [105] as illustrated in **Figure 5.78**. Rods form mostly in the direction of the dipole moment which fabricated by using 4 nm gold thickness (see **Figure 5.79**). In general, intermolecular compounds within the Tetracaine-HCl deposits, internal stress, and crystal coherency between Tetracaine-HCl deposited film and substrate are probably known to be the key to cause rods or other morphological formation. Interactions between internal stresses and intermolecular compounds formed within the Tetracaine-HCl deposits are still under investigation.

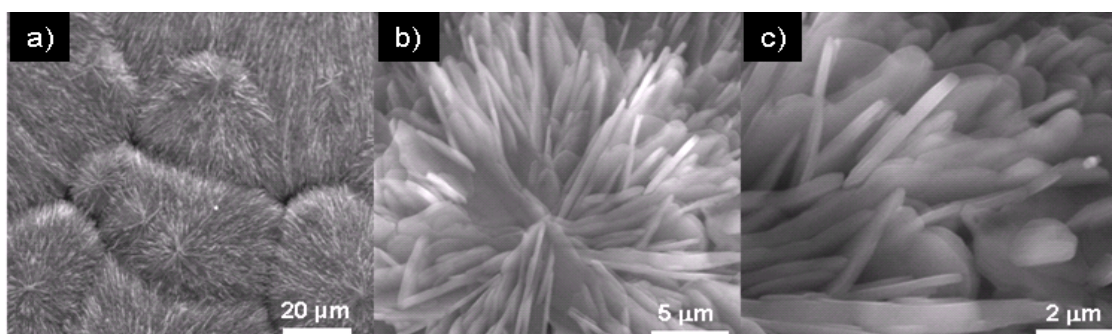


Figure 5.78: *a-c SEM images of Tetracaine HCl deposited on Si pre-coated with 20 nm Au thin film at different magnifications.*

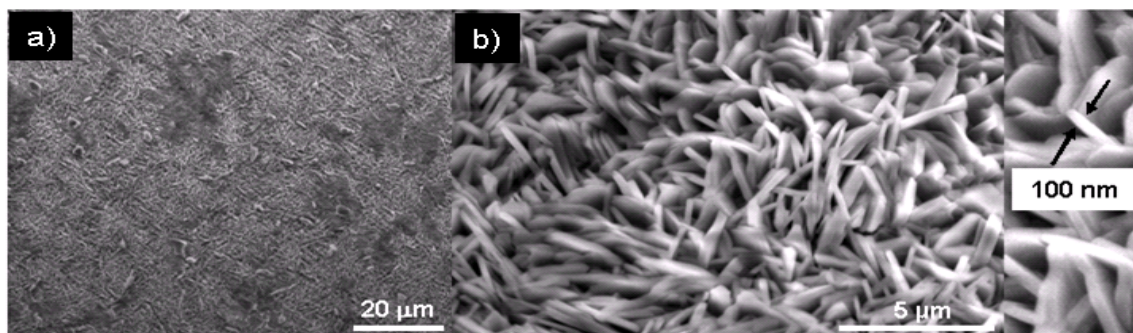


Figure 5.79: a-b SEM images of Tetracaine- HCl Si pre-coated with 4 nm Au thin film at different magnifications.

However, for the substitutional deposition, it is assumed that while the same conditions are used for deposition, the morphology of Tetracaine-HCl films are changed by the structure of the substrates, such as the crystal grain size and surface morphology. This is because by using the substitutional deposition, the rate of deposited film growth depends on the dissolution rate of the substrate. Additionally, the dissolution rate of the substrate mainly depends on the structures of the substrates such as grain size, orientation relationship and segregation of impurities. With the molecules suitable for evaporation, the full versatility of thermal evaporation can be utilised. This means that by changing the deposition rate, the crystallinity of the deposited film can be controlled in a wide range from amorphous to almost single crystalline. A limitation is given for pharmaceutical drugs which are instable or altered in vacuum. The 3D atomic force microscopy (AFM) image of the deposited Aspirin film in **Figure 5.36** depicts the formation of large Aspirin crystals. Similar investigations for several drug materials are performed and most of them are found to be structurally intact (see **Table 5.1**). For example, the deposition of nanostructures of Tetracaine-HCl and Cholesterol and drugs in the range of ~100 nm to ~500 nm thicknesses are shown respectively in **Figures 5.29 a-h)** and **5.67)**. These structures typically exhibit high surfaces which enable them to dissolve faster since they are solvent free if compared to their bulk counterparts. Typical for TE, the substrate has a large influence on the structure in terms of crystallinity and shape of the deposited drug. **Figure 5.9a)-e)** shows the differences in the deposition of Pilocarpine-HCl as active pharmaceutical drug on glass, polymer foil and titanium. Apart from the standard growth of nanoscale thin films with a certain degree of crystallinity, formation of rather complicated hierarchical structures may be triggered, as illustrated by SEM images for

Ascorbic acid shown in **Figure 5.56** at different magnifications. It should be noted that the hierarchical assembly of drug structures down to the nanoscale leads to a huge surface and volume ratio which significantly increases the solution kinetic processes by giving more possibilities for drug molecules to step into the liquid phase and to increase in solubility.

Figures 5.4, 5.38 show further examples for different nanoscale roughnesses and large surface areas formed by self organisation during growth. They also show the appearance of thermally evaporated films on different substrates visualised by scanning electron microscopy. The choice of substrate may comprise a wide range of materials and even highly soluble substances that can be employed to carry the pharmaceutical films without the risk of side effects like dissolution of the substrate. A limitation is given for pharmaceutical drugs which are instable or altered in vacuum.

5.2.2 Time-related Process

Optical microscope images show the time-related crystallization process by means of Chloramphenicol (see **Figures 5.23, 5.24, and 5.25**). Another example is Trimethoprim as illustrated in **Figure 5.50**. One can clearly see the increase of the particle diameters of the evaporated material through coalescence after certain waiting periods as one observed from **Figures 5.80**. The SEM mages of Chloramphenicol deposited on glass show the amorphous nature of deposited film (see **Figure 5.81**). The mobility of condensing particles on the substrate surface is more which provides the crystallization and the growth of large crystals after significant time. This phenomenon is explained by comprising energies, substrate and particle temperatures. To evaporate the material, energy is applied in form of heating until the melting point. When these particles condense and adsorb the substrate. In this study, post-deposition heat treatment processing methods have developed that are decoupled from the initial deposition conditions to induce different out-of-plane molecular orientations in Chloramphenicol thin film. As-deposited Chloramphenicol thin films lack any long-range order; subjecting it to post-deposition processing, such thermal annealing induces crystallization with increasing extents of preferential edge-on orientation. The XRD patterns of Chloramphenicol grown on glass substrate show the amorphous and crystalline nature of Chloramphenicol after deposition (see **Figure 5.82**). It noted that the crystallinity as a

function of time or temperature as demonstrated in **Figure 5.81** and **Figure 5.82**. The exhibited thermal energy of the particles is significant for the movement. Also the migration energy barrier has to be considered which is defined the minimum energy needed to move from one surface site to another. Now these energies have to be related for the prediction of motion of a particle. If the thermal energy is smaller than the migration energy barrier (see equation **5.1**), the particle sticks to its energetically favourable position.

$$k_B \cdot T \ll E_M \quad (5.1)$$

k_B is the constant Boltzmann. T is the Kelvin temperature and E_M is the migration energy. If the thermal energy exceeds these values due to the energy (or rather temperature) exchange between particle and substrate, the particle will carry out random jumps on the substrate surface. That means that the particle is distributed on the substrate surface and found at different places in different times. This process is called surface diffusion. Fick's first law suggests that the flux goes from regions of high concentration to regions of low concentration, with a magnitude that is proportional to the concentration gradient (spatial derivative). In one (spatial) dimension, the law is

$$J = -D \frac{\delta\phi}{\delta x} \quad (5.2)$$

where

- J is the "diffusion flux" (amount of substance) per unit area per unit time which measures the amount of substance that will flow through a small area during a small time interval.
- D is the diffusion coefficient or diffusivity in dimensions of [length² time⁻¹].
- ϕ (for ideal mixtures) is the concentration in dimensions of [amount of substance per unit volume].

x is the position [length].

Fick's second law predicts how diffusion causes the concentration to change with time:

$$\frac{\delta\phi}{\delta t} = D \frac{\delta^2\phi}{\delta x^2} \quad (5.3)$$

The particles perform these jumps until they reach their potential energy minimum. The frequency (f) of successful jumps is given by:

$$f = v_0 \cdot \left(\frac{-E_M}{k_B \cdot T} \right) \quad (5.4)$$

v_0 is in the order of vibrational frequency of atoms. The number of jumps per unit time is given by the diffusion constant D :

$$D = \frac{\langle [r(t'+t) - r(t')]^2 \rangle}{2dt} \quad (5.5)$$

Whereas $r(t)$ denotes a position of the particle at a given time, t and d is the dimension of the diffusion path. The surface diffusion considered in this case is 2. Combining equation 5.4 and 5.5 leads to the constant diffusion:

$$D = \frac{r(\Delta t)^2}{4} \cdot v_0 \cdot \left(\frac{-E_M}{k_B \cdot T} \right) \quad (5.6).$$

The particle can also fulfil rotations since molecules are assumed to be evaporated in this process. With material of higher concentration, interactions with other particles can occur as well. After random diffusion the particles arrive at neighbouring sites, they agglomerate and form clusters. It is also possible for clusters to move on the surface. As they have bigger mass they need higher energies to overcome the migration energy barrier. Due to the random movements and the condition for the constant diffusion, the crystallization process is a function of time-related process. [106, 107, 108].

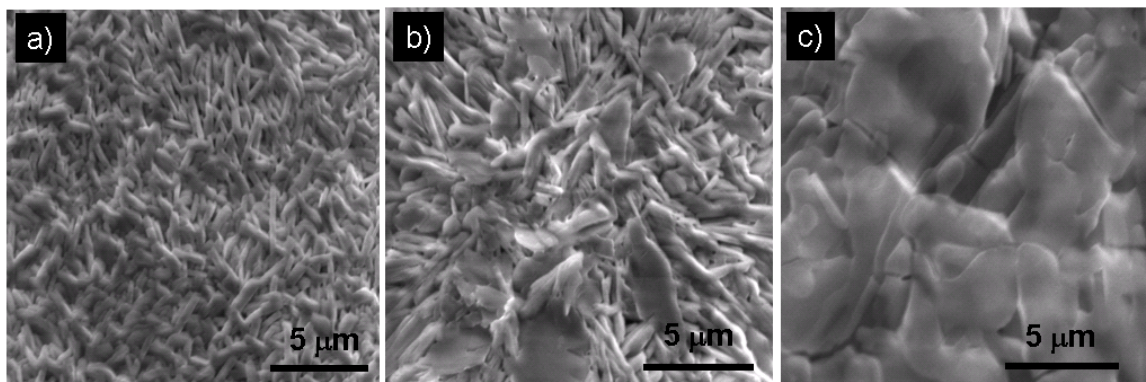


Figure 5.80: SEM images of Tetracaine-HCl grown on Si substrate at different evaporation times with 16 min (a), 23 min (b) and 30 min (c).

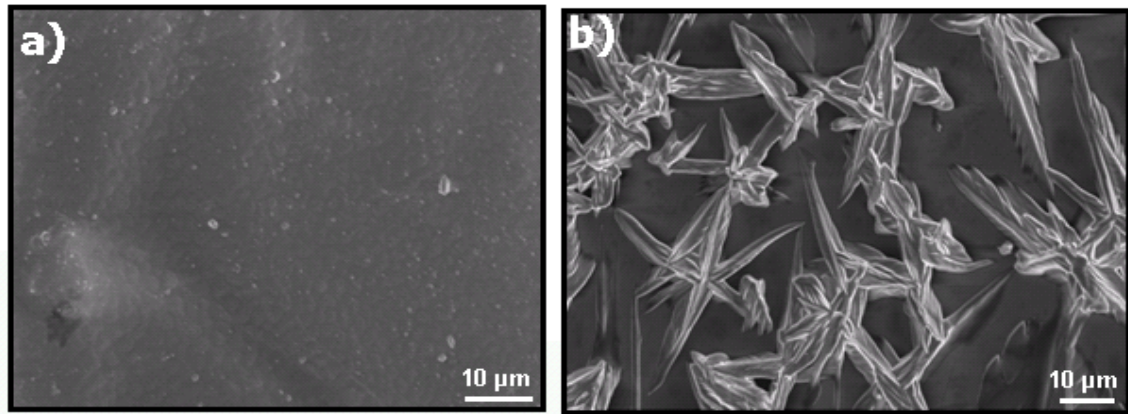


Figure 5.81: SEM images of Chloroamphenicol deposited on glass substrate which obtained after 3 h.(a) and 10 days(b) respectively.

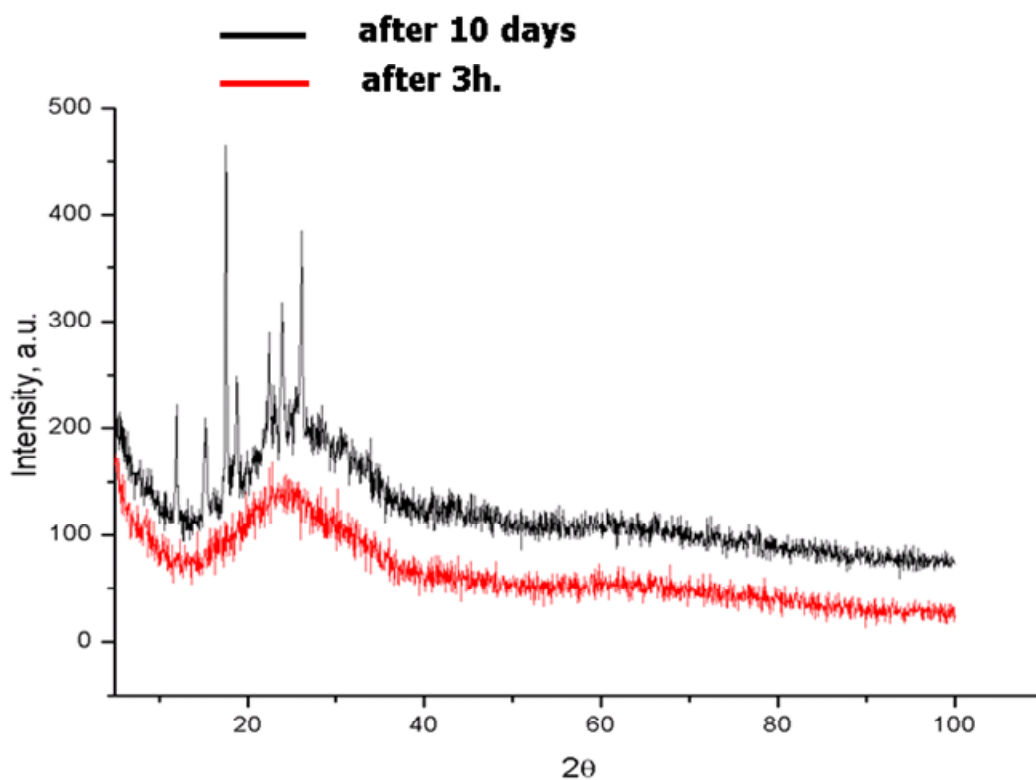


Figure 5.82: XRD pattern of Chloroamphenicol deposited on glass substrate at different times of 3h and 10 days.

5.2.3 Temperature-related Process

Chapter 5 illustrates the crystallization process is a function of growth temperature. This study showed that the effect of post-deposition annealing and changing in substrate temperature on the thermal stability and structural characteristics of the as-grown Chloramphenicol thin film. From equation (5.1), one can reckon that if the temperature is increased, the thermal energy will also increase. That is due to the fact that the particles

gain kinetic energy. Heat refers to the state of energy an object has in relation to the kinetic energy of its molecules or atoms. The more energy the particles have the higher the probability for them to overcome the migration energy barrier. That means that high frequency and coefficient diffusion will be much larger than normal diffusion processes without the assistance of heat. So, it is more probable for the particles to form clusters on the surface and withal nuclei. The time needed for crystallization of the evaporated material on the substrate diminishes here. The rapidness of the crystallization really depends on the amount of added heat. The structure-zone model proposed by Movchan and Demichishin is illustrated in **Figure 5.83** which correlates the substrate temperature with the structure of the appropriate thin film. The substrate temperature is mentioned as ratio of the melting temperature of the thin film material. In zone 1 the substrate temperature is low. Here, the assumptions in **Chapter 5.2.2** can be considered as the surface diffusion is low. Clusters form and grow through further particles sticking to them. But overall structure is not yet homogeneous. Zone 2 shows increased surface diffusion due to higher energy impact. The density of the structure is increased through bigger clusters that grow. Due to high temperature in zone 3 the particles attain high energies for diffusion mechanisms. A fast developing crystalline structure is the result. The problem with this model is that the pressure is disregarded. So, it is suggested for high vacuum processes. Also, the temperature depending on atmospheric pressure has to be considered. Therefore, the substrate temperatures have to be raised a bit more to maintain the same thin film structure.

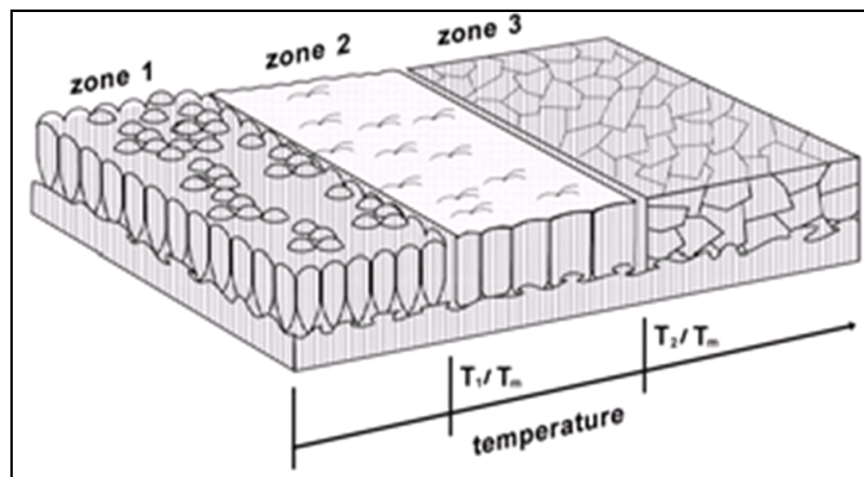


Figure 5.83: *Representative Structure-zone model after Movchan and Diminishin relating the substrate temperature to the corresponding arising thin film structure [109].*

5.2.4 Control over the lateral structuring of the deposited drug films

A lateral structuring, the positioning of thermal evaporated thin films, is relatively straightforward by utilising lithography or shadow masks. Possible applications for laterally structured systems are smart or multifunctional pharmaceutical drug coatings for implants or contact lenses. Specific examples are contact lenses for drug delivery [110] which should not affect the vision and thus require a lateral structuring as shown in **Figure 5.84** of the drug film. Selective area depositing pharmaceutical drugs on contact lenses is possible with TE technique using a suitable mask. Such a structuring could also be used in complex implant coatings like stents or dental implants that require different drugs in different places in contact with bone, mucosa or the oral cavity. Bacterial adhesion is an important step in the pathogenesis of an infection (periimplantitis). Placement of different antibacterial active molecules on specific areas of the implant surface (depending on the intraoral contact to bone, mucosa or the oral cavity) will also be possible with thermal evaporation. To demonstrate the possibilities, **Figure 5.84 a- b** shows thermally deposited Pilocarpine-HCl and Acetylsalicylic acid through a microscopic shadow mask resulting in lateral structuring of the deposited drug. The feature of lateral structuring also gives the possibility to cover the different surfaces such as inner and outer walls of stents with different drugs. Visionary, this micro-structured film could be used for multifunctional medical coatings that help to know the status of the drug layer like thickness. This 3D structuring may be used to build nano or microscopic particles with a predefined shape which might be beneficial for special applications like particulate drug uptake [111]. In principle, the demonstrated techniques of micro-structuring enable the formation of miniaturised drugs on micro or nanoscopic carriers which can be used to overcome the blood brain barrier or accumulated cancer tumours due to the enhanced permeability and retention (EPR) effect.

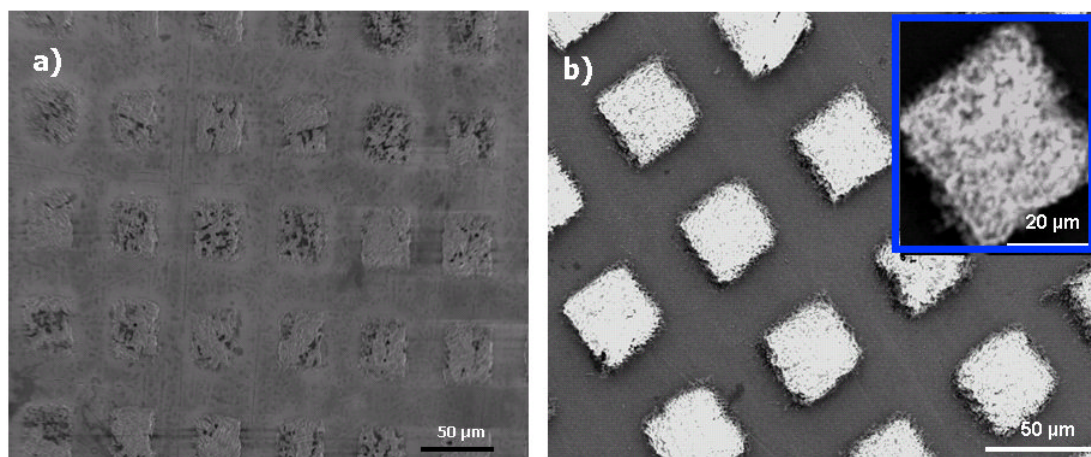


Figure 5.84: SEM images of lateral structures of Pilocarpine-HCl (a) and Acetylsalicylic acid (b) respectively.

5.2.5 Characterisation of chemical composition and Raman shifting

Relatively large molecules like Pindolol, Erythromycin or Tetracaine-HCl remain intact (confirmed, e.g. by Raman spectroscopy). The formation of micro-nanoscale pharmaceutical crystals on the substrate by thermal evaporation already indicates a high purity further confirmed in several cases by Raman spectroscopy investigations. For example, the Raman spectra of corresponding bulk and thermally evaporated Aspirin are similar to each other as shown in **Figure 5.37**. It clearly demonstrates that after thermal evaporation the micro-nanostructured film exhibits almost the same chemical structure if compared to its bulk (see **Figures 5.85, 5.86, 5.87** and **5.88**). The choice of substrate may comprise a wide range of materials and even highly soluble substances that can be employed to carry the pharmaceutical films without the risk of side effects like dissolution of the substrate. A limitation is given for pharmaceutical drugs which are instable or altered in vacuum. The possible causes of fibrous or rod formation has been discussed in this study. Most of the materials are still identical after evaporation.

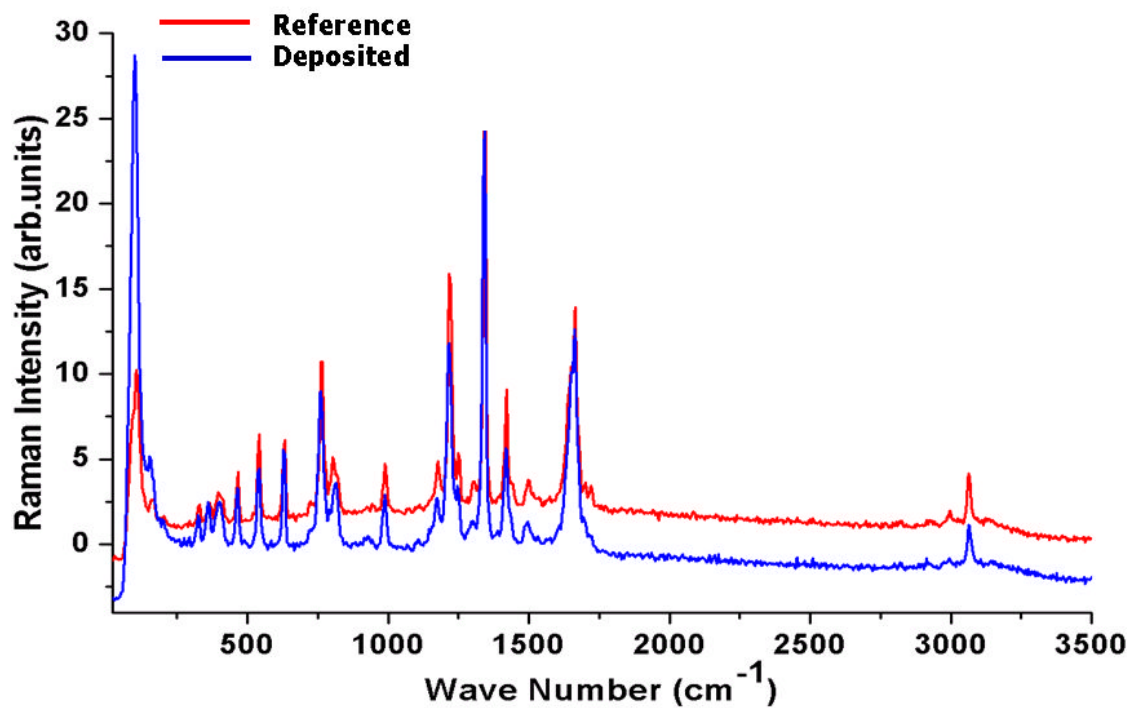


Figure 5.85: Raman spectra of the deposited and reference 5-Fluorouracil, showing clear Raman peaks in the thermally deposited 5-Fluorouracil on titanium substrate.

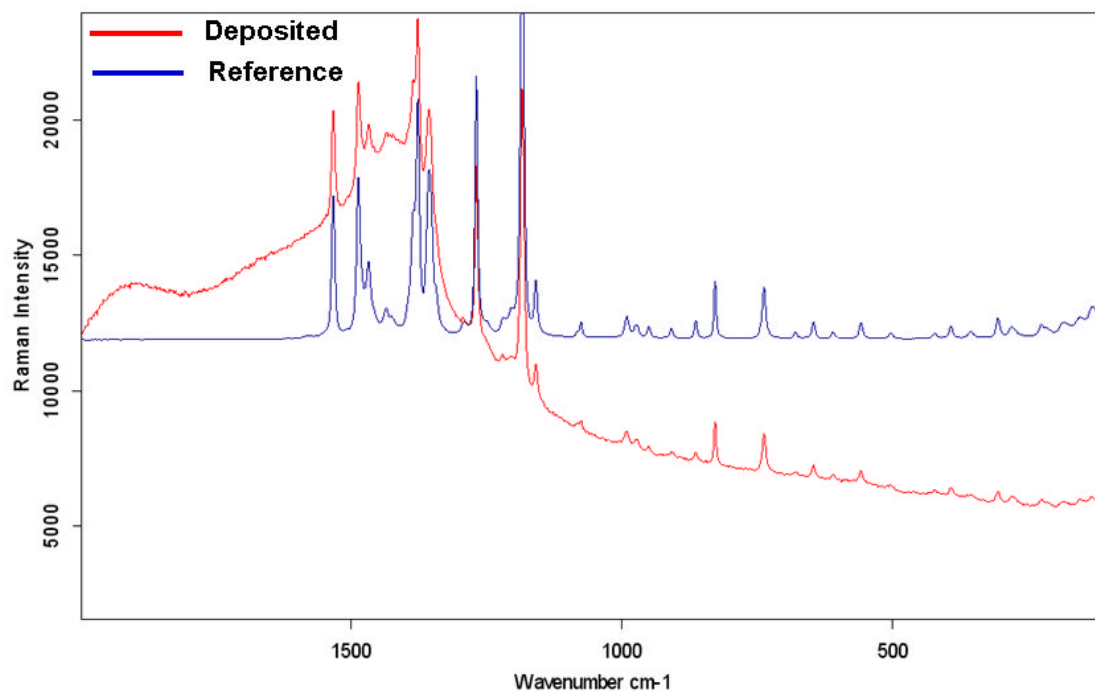


Figure 5.86: Raman spectra of the deposited and reference Metronidazole.

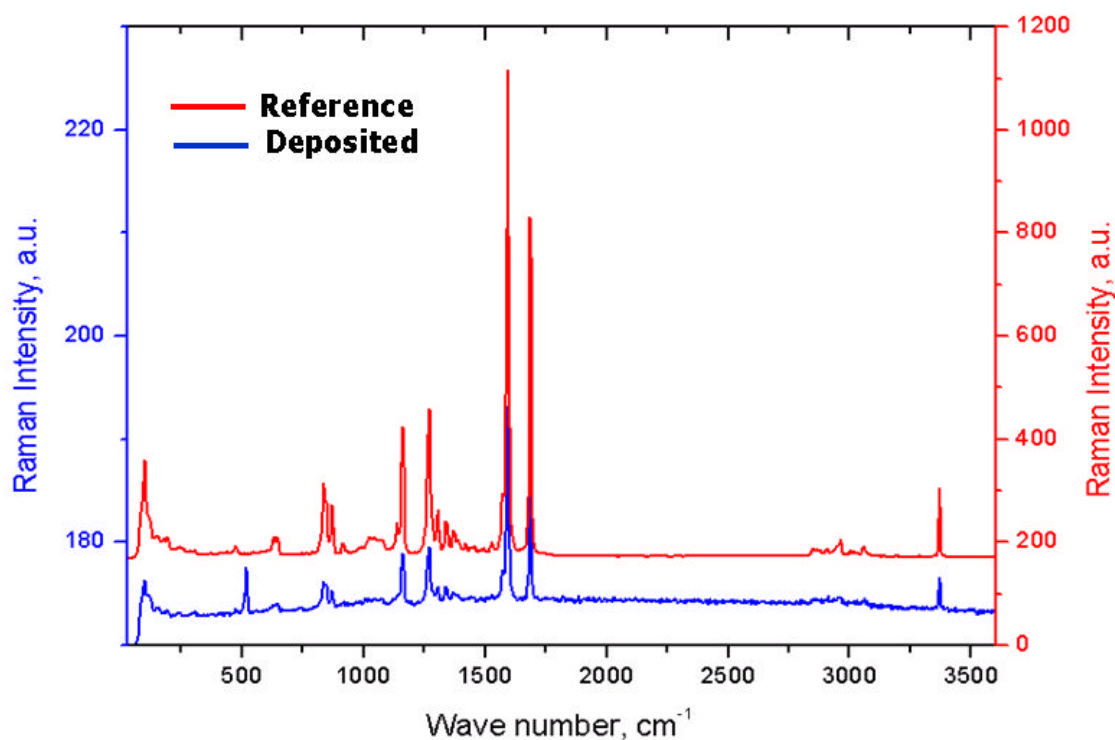


Figure 5.87: Raman spectra of the deposited and reference Clotrimazole.

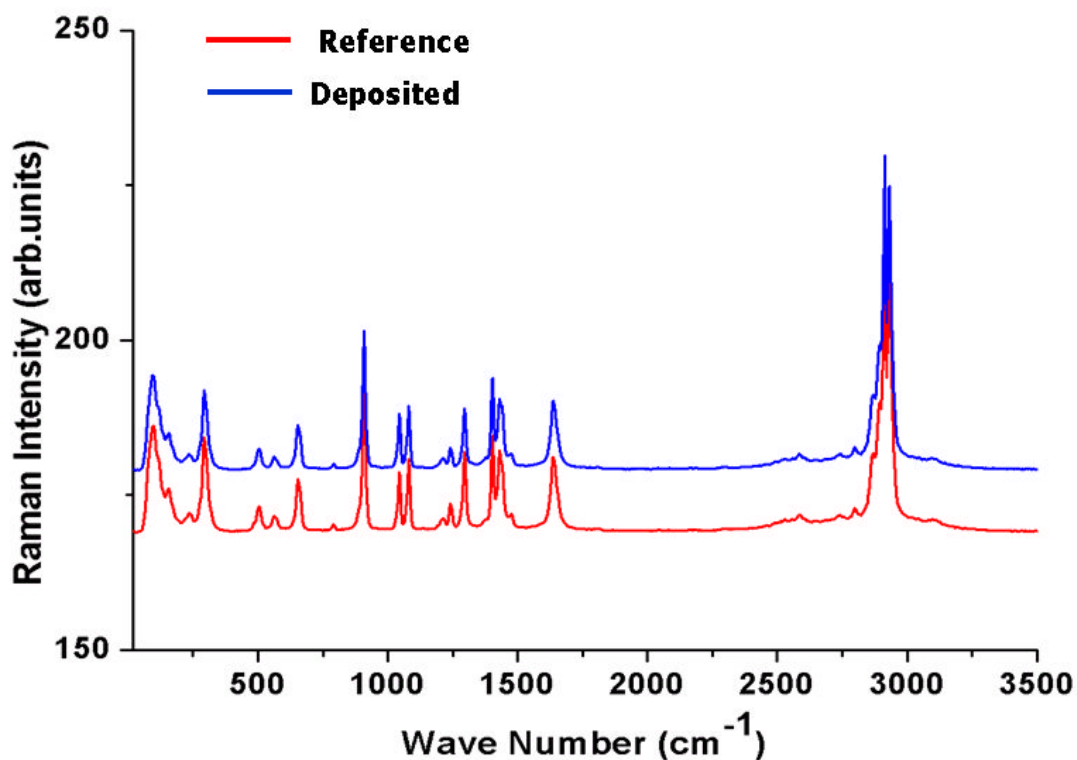


Figure 5.88: Raman spectra of the deposited and reference Adipic acid.

The sample has some defined peaks which do not belong to deposited materials and might derive from the substrate carrier. Other peaks are shifted to indicate a probable

change in the substance whereas the spectra derived from the samples are varying. Sometimes the microscopic images from deposited materials show an inhomogeneous surface with a thin film like layer with some incorporated crystals. Whereas the film spectrum does not resemble the reference spectrum at all due to things like the operator, the material thickness, intensity of laser beam, and substrate. From Raman microscopy data, if the thickness of materials is thinner and intensity of laser beam is higher, the material will start to decompose or burn. Therefore, the Raman is not identical. What one already observed here, some peaks or functional groups are missing due to atoms on the surface of the adsorbent; these atoms are not entirely surrounded by other adsorbent atoms. Therefore, the atoms cannot attract adsorbents. The exact nature of bonding depends on the details of the species involved. After some time, the molecules or atoms are arranged themselves and accumulated on the substrate surface to provide the formation of chemical bonds. Furthermore, the foil carrier is very sensitive to energy input and shows an irregular surface. The deposited layer shows a spectrum which is not truly comparable to the reference spectrum of deposited materials as shown in **Figure 5.89**. Also, in Raman spectrum, some sharp peaks are found enhanced with substrate used. From **Figures 5.64** and **5.65**, one can see the Raman signal of the deposited cholesterol enhanced with using gold as deposited on substrate. The increase in intensity of the Raman signal for adsorbates on particular surfaces occurs because of an enhancement in the electric field provided by the surface. When the incident light in the experiment strikes the surface, localized surface plasmons are excited. The field enhancement is greatest when the plasmon frequency. In order for scattering to occur, the plasmon oscillations must be perpendicular to the surface; if they are in-plane with the surface, no scattering will occur. It is because of this requirement that roughened surfaces or arrangements of nanoparticles are typically employed in SERS experiments as these surfaces provide an area on which these localized collective oscillations can occur [112]. In brief, the measured intensity of a Raman line is dependent up on number of factors, the relationship of which is given in equation [113].

$$I(\nu) = I_0K(\nu)C \quad (5.7)$$

Where $I(\nu)$ is the measured intensity of the Raman line, I_0 is the intensity of the excitation laser line, ν is the Raman shift, C is the concentration of the scattering species and $K(\nu)$ describes the overall spectrometer response. For Nipasol, the reference sample and another sample after evaporation are studied. The spectra are very similar to each other with only very subtle differences. Only very small wave number shifts in a number of

Raman scattering bands can be observed. Intensity changes in the spectra are taken into account. Both spectra contain the same functional groups. But, some peaks with lower density can be seen (see **Figure 5.6**). In the other hand, the Raman spectra of deposited Chloroamphenicol and Niopagin enhanced by time due to crystallinity has relationships with orientation and the polarizability of the material as illustrated in **Figures 5.90** and **5.91** respectively.

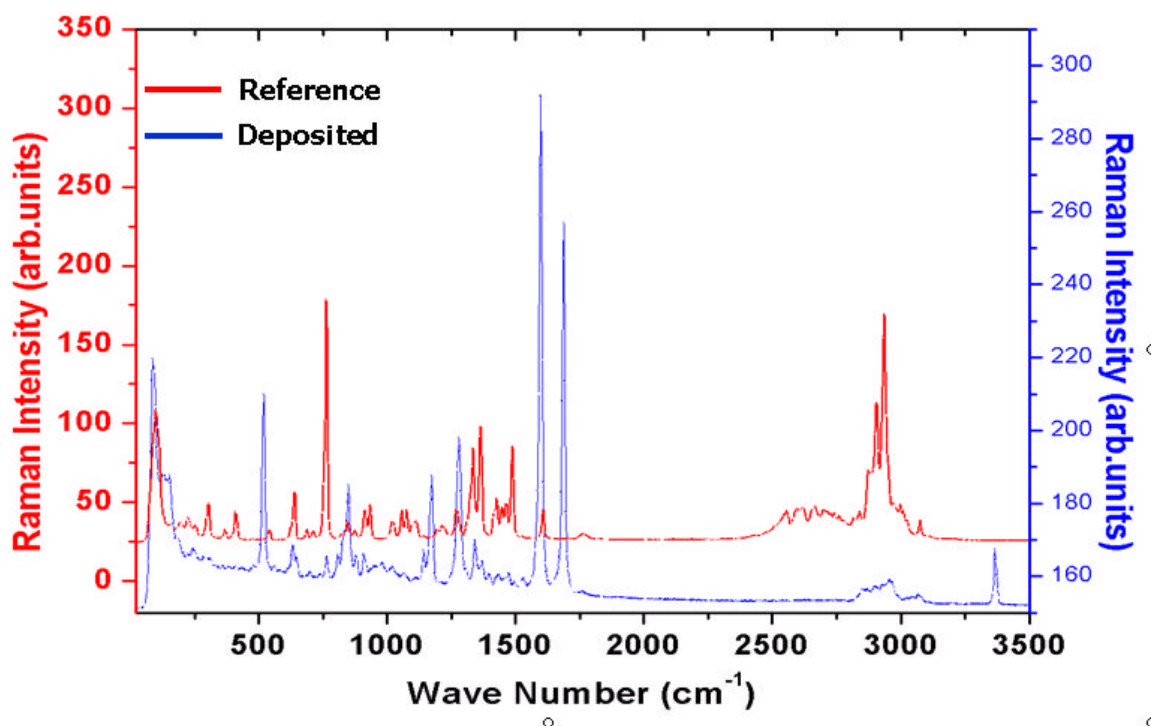


Figure 5.89: Raman spectra of the deposited (on polymer foil) and reference Pilocarpine-HCl.

Moreover, Raman of deposited of materials is based on many things like the laser intensity, operator, materials nature, sample thickness or volume. Some functional groups take time to reconnect and arrange themselves to find each other to deposit and diffuse on the substrate.

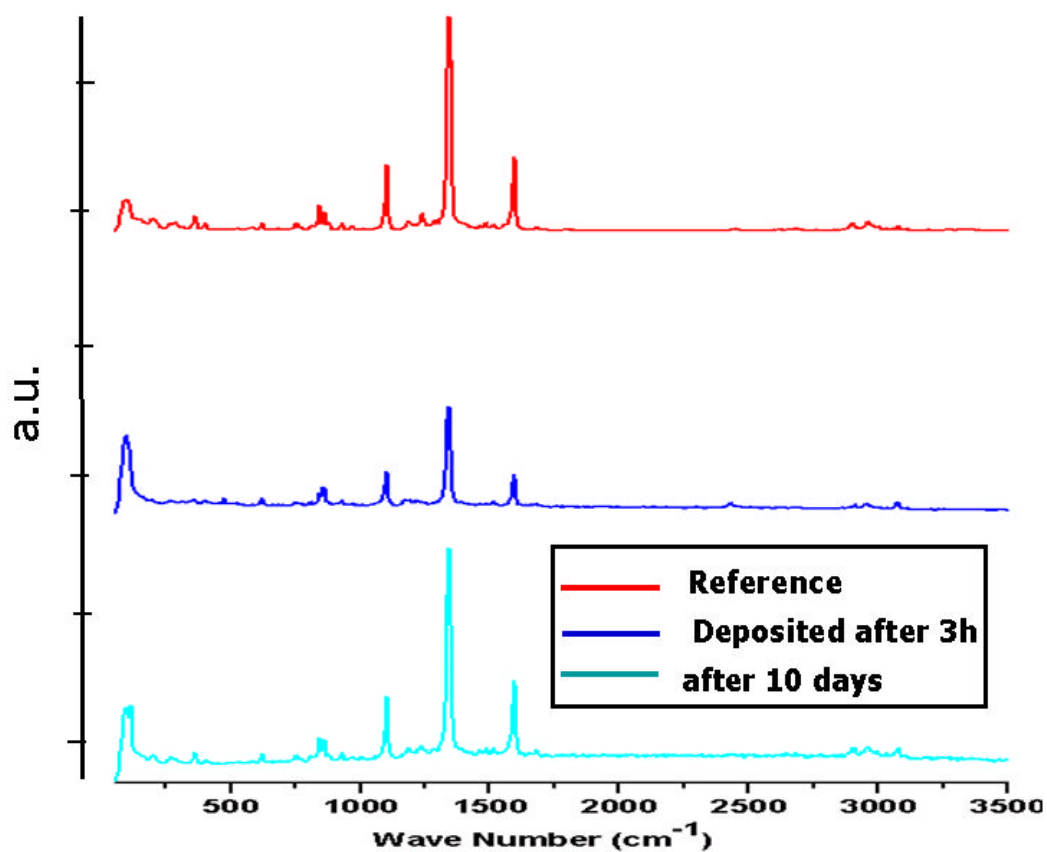


Figure 5.90: Raman spectra of the deposited (on glass at different time) and reference Chloroamphenicol.

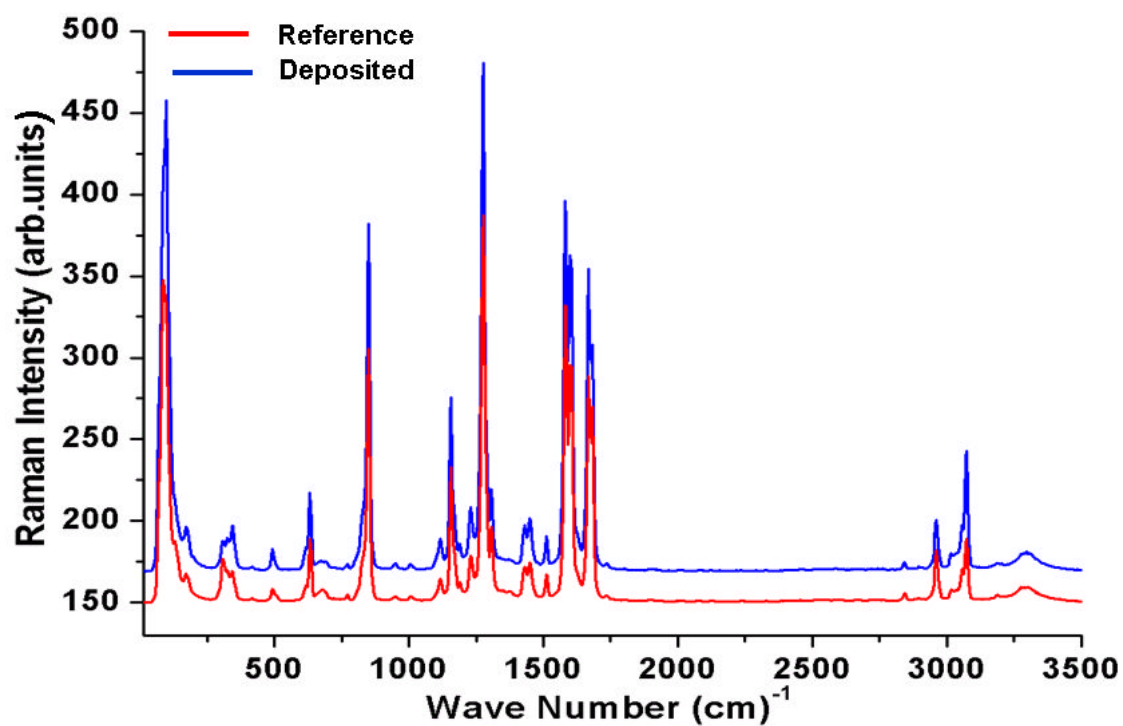


Figure 5.91: Raman spectra of the deposited and reference Nipagin.

5.3.6 Sequential deposition: Multilayers of different drugs and hybrid materials

The fabrication of pharmaceutical multilayers controls the drug release. A fast dissolving drug can be protected by a second layer that needs to be dissolved first. For example, a film of Metronidazole, being rapidly dissolved after TE, is covered with PLGA by subsequent depositions from two sources on a polished Ti-substrate. The release profile is shown in **Figure 5.75** and the effect of delayed drug release could be verified. Being a polymer, PLGA is expected to depolymerise during evaporation and to re-polymerise on the substrate. In addition to the delayed release, such multilayered systems may be used to release a combination of drugs in a desired time pattern, e.g., having a drug I for a few days, after completing dissolution of layer I, a subjacent drug II could be effective. This approach of fabricating multilayer pharmaceutical drugs by TE could be used for coronal stents, which first require an antiplatelet medication and subsequently an antiproliferative drug to prevent restenosis in coronary arteries and effect an optimal integration.

PLGA is one of the most accepted biocompatible and biodegradable polymer used in drug delivery and tissue engineering [114]. PLGA is produced from the polymerization of glycolic acid and lactic acid. In addition, PLGA is aliphatic polyester depending on the acid monomer ratios used. Different ratio of PLGA can be obtained. These polymers have a glass transition temperature of about 50 °C and show high solubility to a wide variety of nonpolar solvents. The degradation process occurs due to hydrolysis of ester bonds in water or physiological fluids. This process finally degrades or divides lactic acid and glycolic acid which enter the Krebs's cycle to produce carbon dioxide and water and removed during regular routes where by the duration can be changed by changing the monomer composition. **Figure 5.75** presents an example of a double layer of Metronidazole and PLGA. The image shows a cross section to visualise that the individual layers are maintained during thermal evaporation. Another promising route of a new drug designed thermal evaporation is the co-deposition from two evaporators simultaneously in a vacuum chamber. This allows the formation of a molecular scale mixing of pharmaceutical active substances or excipients to form nanostructured hybrid drugs exhibiting synergetic responses at the same time. With conventional solution based processing, such a mixing requires very special preconditions, e.g., the possibility for co-crystallisation. Evaporation of molecules from two different sources typically gives no

time for a demixing process on the substrate, as molecules directly lose most of their energy when they hit the substrate surface. A sample composed of four layers (1) SM, (2) Cholesterol, (3) Fluorouracil and (4) SM is produced (see **Figure 5.76**). Here, amorphous mixtures can be formed with structurally incompatible drugs, leading to synergistic effects. The approach is useful for controlling the dissolution of drugs. Furthermore, the solubility can be significantly increased. If a molecule with poor ability to dissolve is only surrounded by molecules of good solubility, a total increase in dissolution can be affected. This is very beneficial in increasing the solubility of poorly soluble drugs by deposition of a low soluble molecule in parallel with a highly soluble one and with this forming a solid solution. The co-deposition approach also allows the creation of a molecular mixture in terms of a solid solution from nearly every thermally evaporated drug. To show an example for such a combination, the efficacy of the above mentioned antifungal Itraconazole and antibacterial Erythromycin drugs were evaluated in combination by co-deposition. In agar plate diffusion tests, both antifungal and antibiotic effect of these combined deposits could be confirmed and were in the same degree as for the individual substances (as shown in **Chapter 6**).

Vapor phase of co-depositing noble metals and pharmaceuticals molecules such as Tetracaine-HCl is effective to produce Tetracaine-HCl /metal nanocomposite as illustrated in **Figure 5.92**.

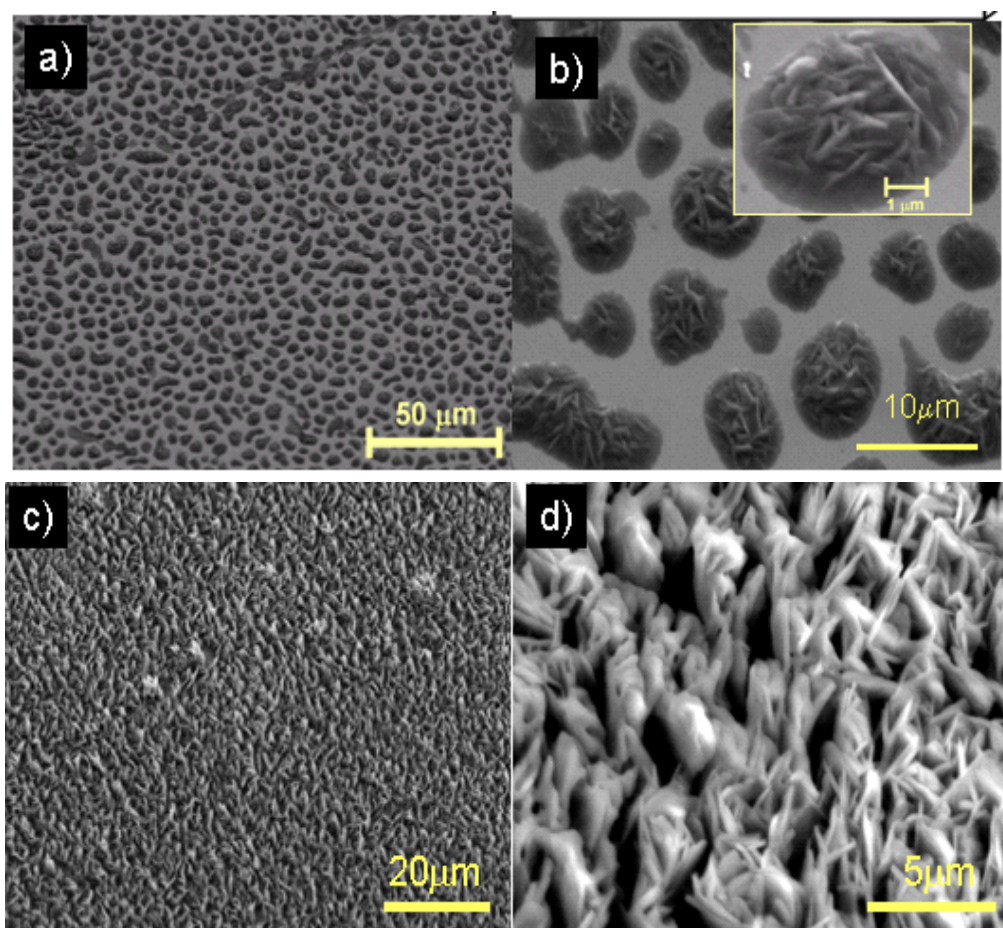


Figure 5.92: SEM images of co-deposition of Tetracaine-HCl with gold (a and b) and silver (c and d).

One can assume that the formation of metal nanoclusters in an organic matrix can be described analogously to cluster formation on an organic surface. When energetic metal atoms impinge on a organic surface, which grows simultaneously by organic fragment deposition and reconnection, the arriving metal atoms undergo various processes [115] including random walk on the organic surface, diffusion into the grown Tetracaine-HCl, or desorption. Within the diffusion distance, metal atoms may encounter each other or are captured by a surface defect. The metal volume fraction and the microstructures of co-evaporated composites depend strongly on the coefficient sticking of the metal atoms on the organic surface and the metal-organic molecules deposition rate ratio. A completely new way of pharmaceutical engineering is the combination of inorganic materials with pharmaceutical active substances. Such combinations could be potentially used as smart implant coatings that form nanoporous structures with medication filled pores in the inorganic material. In terms of the oral implant example given above, these molecules

may be embedded in nanoscale sponge like ceramic structures by co-evaporation to have a potential depot function of antibacterial factors in order to reduce the risk for periimplantitis. An example for such co-evaporation is shown in **Figure. 5.92c-d** where Ag and Tetracaine-HCl are combined.

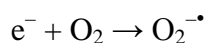
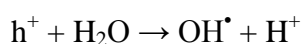
For comparison, **Figure 5.29a-f** shows the deposited Tetracaine-HCl without silver. The inorganic part of the hybrid structures could also be an active ingredient in wound dressings, e.g., silver nano-particles are known for their antimicrobial effect [116]. There has been increasing interest in deposition of pharmaceutical molecules like Nipasol on ZnO nano-micro structures (see **Figure 5.93**) due to their many exclusive characteristics. Zinc oxide (ZnO) nanostructures have been of great importance due to various fabrication methods available and different morphologies obtained. EDX spectra of the as synthesized Nipasol grown on ZnO nano structures which confirms the presence of Zinc, carbon as well as oxygen as shown in **Figure 5.94**.

The deposition of Nipasol nano microstructures on ZnO might provide the combination therapy for enhancement the antimicrobial activity and treatment of serious infections.

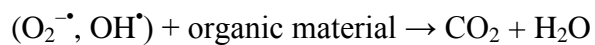
Generally, ZnO has a wide band gap of 3.37 eV with a large excitation binding energy (60 meV), exhibiting near UV emission, transparent conductivity and piezoelectricity. Sawai et al reported that ZnO possessed strong antibacterial activity [117]. Akiyama et al. also studied the efficiency of ZnO as a treatment for a topical dermatitis related to *S. aureus* [118]. The efficacy of ZnO for topical dermatitis may be based on the strong attraction between ZnO and *S. aureus* to inhibit the fibrin formation by coagulate of *S. aureus*. Furthermore, the higher antibacterial activity of ZnO against *Escherichia coli* is because H_2O_2 is generated from the surface of ZnO powder, when ZnO is irradiated by (UV or visible) which brings a separation of charge, creating a hole (h^+) in the valence band and an electron (e^-) in the conduction band:



At the surface of the excited ZnO particle, the valence band holes abstracts electrons from water and/or hydroxyl ions, producing hydroxyl radicals (OH^\bullet). Moreover, electrons can diminish O_2 to generate the superoxide anion $O_2^{\bullet-}$ [119]:



The obtained OH^\bullet and $\text{O}_2^{\bullet-}$ can induce lipid peroxidation in membranes. DNA damage occurs due to strand breakage or oxidized nucleotides and oxidation of amino acids and protein catalytic centres [120]:



Another possibility is the devastation of organic material in a direct reaction with positively charged ZnO particles.

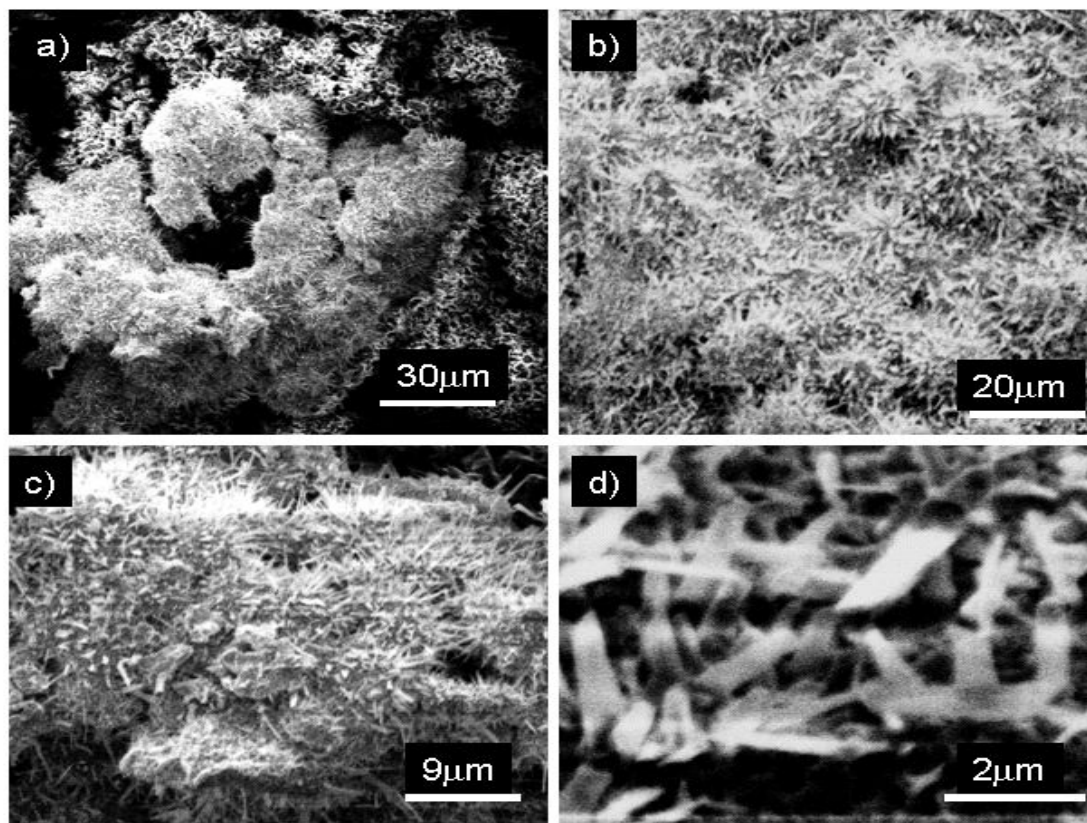


Figure 5.93: a-d SEM images of Nipasol coated on the surface of ZnO nano-microstructures.

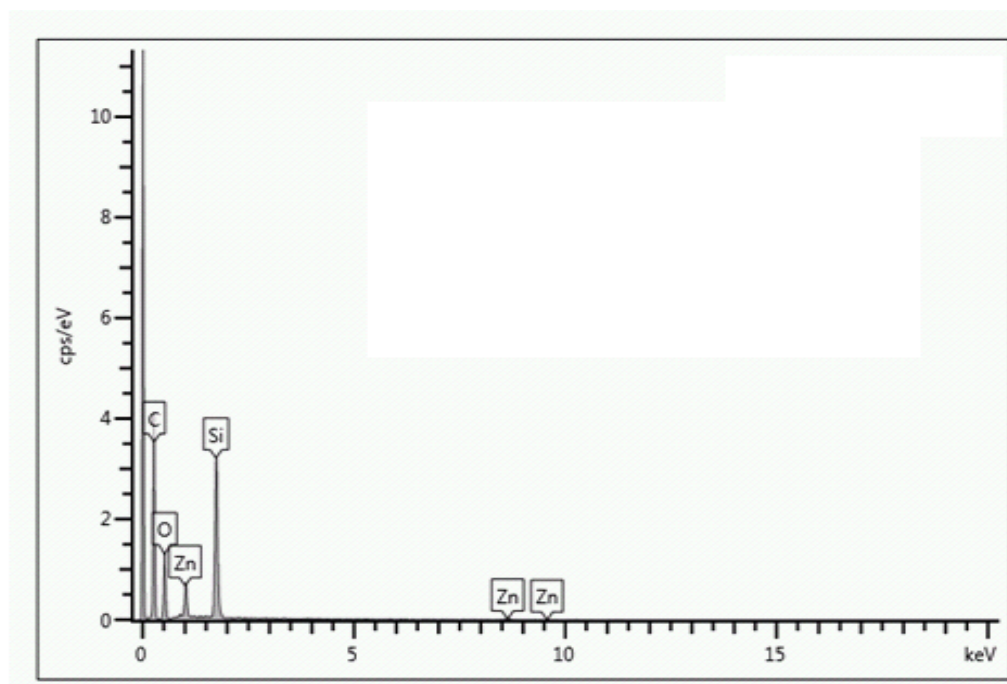


Figure 5. 94: EDX spectra of the as-synthesized Nipasol grown on ZnO nano structures which confirms the presence of Zinc, carbon as well as oxygen.

In addition, it is found that ZnO nano microstructures exhibits antiviral activity like Herpes simplex virus type-1 (HSV-1) [121]. It is regarded that ZnO is used as photosensitizer in photodynamic therapy for curing cancer with better selectivity for targeted tumour. When ZnO is exposed to light of exact wavelength, it is able to produce cytotoxic reactive oxygen species (ROS) such as hydroxyl radical, hydrogen peroxide and superoxide, making it possible for decomposition of some organic compounds and destroying the tumour cells [122]. Using combination therapy or nano sized drug carriers such as liposomes, polymeric micelles, dendrimers, superparamagnetic iron oxide crystals, and colloidal gold has been examined in cancer therapy in order to minimize the cytotoxicity of ZnO to the host cells, to decrease the side effects of anticancer drugs and to enhance the antitumoral drug effectiveness of the targeted therapies [123]. It is well known that ZnO has piezoelectric properties for passing electrical charge through the guidance channel during mechanical deformation to accelerate the healing of neural tissue and reduce the sticking and density of staphylococcus epidermidis which colonized the implanted biomaterials [124].

Chapter 6

6-Application of Thermal Evaporation

This chapter describes some application scenarios of the pharmaceutical thin films obtained by thermal evaporation in vacuum. This includes the antimicrobial screening, experiments for the control about the drug release profiles and some basic electronic properties.

6.1 Antimicrobial screening:

The vacuum deposited antimicrobial substances revealed bacteriostatic and accordingly fungistatic activities in similar degrees compared to the controls (see material and methods **chapter 4**). The substances which were tested are listed in **Table 6.1** and **6.2**. The maximum extent of inhibition areas around titan plates was mostly observed in front of the coated surfaces while at the small sides and the non-coated backside the bacteriostatic activity was reduced. The present study examines vitro activities of series of antimicrobial agents. **Figures 6.1** and **6.4** make it clear that inhibition areas of vacuum deposited Erythromycin and Itraconazole are presented on agar plates with *Staphylococcus aureus* or *Candida albicans*, respectively. Major changes are in the use of antimicrobial agents for growth promotion. In the case of antimicrobial substances, the nanostructured thin films were deposited directly on titanium substrates and their antibacterial or antifungal activities were tested (**Table 1**). Even very poorly water soluble substances such as Metronidazole, Erythromycin and Itraconazole have been found to be more active when deposited by thermal evaporation. The test objects are discs made of titanium at one side coated with the test drug by vacuum deposition.

Some of the agar test plates with TE drugs are compared to the controlled sample where they all are compared with their higher doses (30 µg) conventionally controlled. This significant increase in the area of inhibition zones for thermally evaporated antibacterial drugs and also antibiotics are compared to their control samples as seen in (**Figures 6.1, 6.3, 6.4** and **6.6** respectively) and **Tables 6.1** and **6.2**. They are clearly visible and can be explained by increasing the dissolution rate which is due to an almost amorphous

assembly of the deposited drugs or reducing the particles size after deposition if compared with reference drug as shown in **Figures 6.2** and **6.5**.

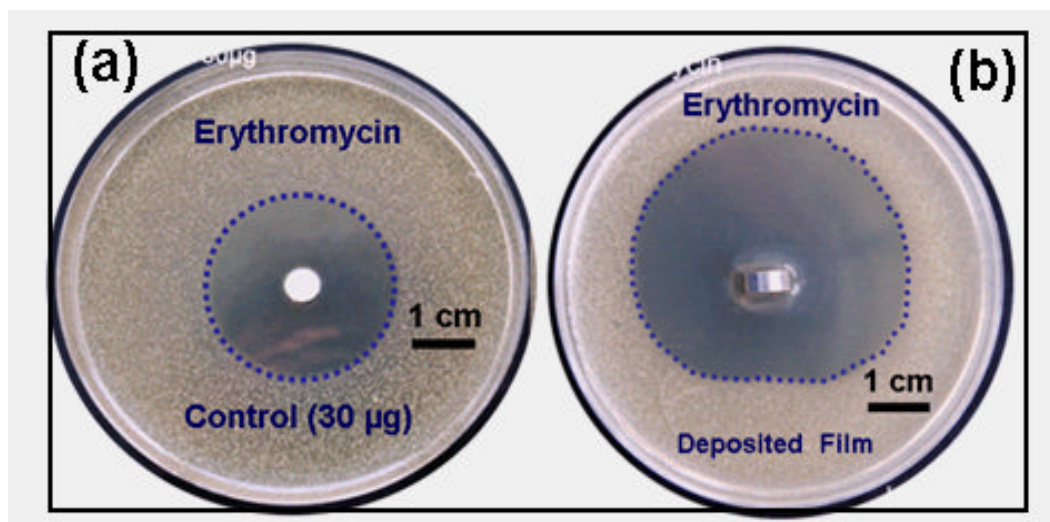


Figure 6.1: shows the antimicrobial activity of Erythromycin against Staphylococcus aureus, positive control (a), deposited film (b).

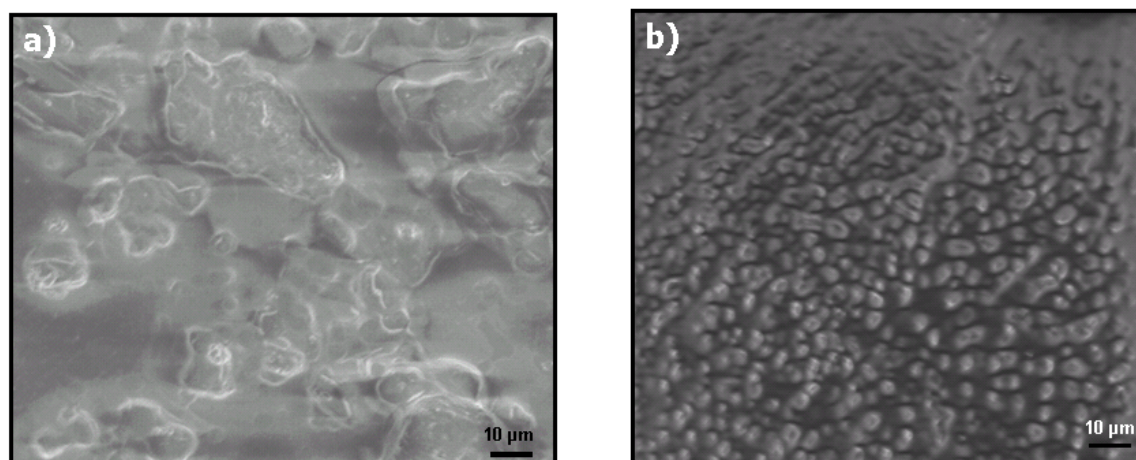


Figure 6.2: SEM images of Erythromycin as bulk material before evaporation (a) and deposited film after evaporation (b).

The antimicrobial activity of vacuum deposited films of Nipasol and Tetracycline-HCl, Chloramphenicol were measured by using test organism *Staph. Aureus* as illustrated in **Figure 6.3**. When titanium plates are placed in agar medium, inhibition zones are measured after 24 h at 34 ° C. Inhibition zones for Tetracycline and Chloramphenicol are the area around the whole platelets, Tetracycline - 3 samples in a Petri dish in the middle Filter paper disk with Tetracycline control. It is found that the deposited films have higher inhibition zone if compared with control samples.

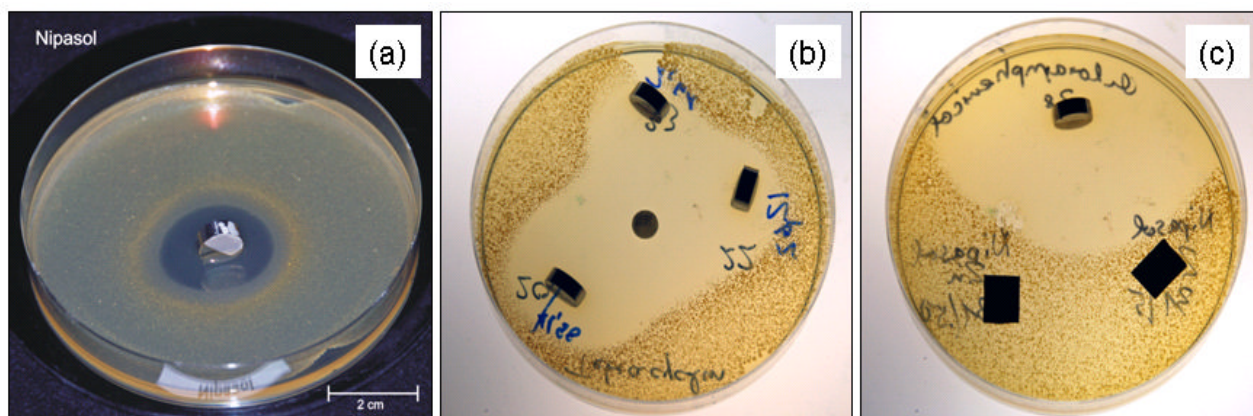


Figure 6.3: illustrates the antimicrobial activities of deposited films of Nipasol (a), Tetracycline-HCl (b), Chloramphenicol (c) against *Staphylococcus aureus*.

The process of superimposition on a titanium surface without prior dissolution of a substance appears to have no reducing effect on its antimicrobial efficacy. Evidence for the integrity of the chemical structures is established by Raman analyses in the case of the substances investigating Erythromycin and Clotrimazole (see **Chapter 5**).

Test substance	Maximum extent of inhibition area [cm ²]	
	experimentals (titanium plates)	controls (paper, 30 µg/disc)
Chloramphenicol	2.55	1.36
Erythromycin(base)	3.11	1.38
Metronidazole	2.06	1.67
Nipasol	1.16	0
Neomycinsulfate	0.57	0.68
Novobiocin sodium salt	3.95	1.64
TetracyclinH ₂ O	1.44	1.82
Tetracyclin HCl	1.65	not performed
Vancomycin HCl	0.67	0.80

Table 6.1: shows the bacteriostatic effect of various antibiotics and of Nipasol deposited by evaporation under vacuum against *Staphylococcus aureus* ATCC 6538.

Test substance	Maximum extent of inhibition area [cm ²]	
	Experimentals (titanium plate)	Controls (paper, 30 µg/disc)
Clotrimazole	1.76	1.72
Itraconazole	1.82	0.97
Ketoconazole	2.83	1.07

Table 6.2: The fungistatic effect of antimycotics deposited by evaporation under vacuum against *Candida albicans* ATCC 10231.

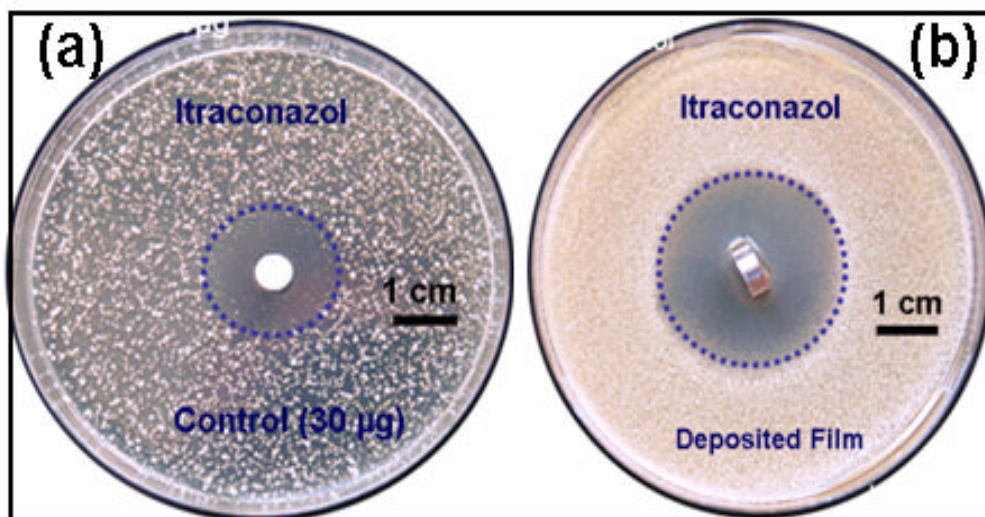


Figure 6.4: The antimicrobial activity of Itraconazole against *Candida albicans*, positive control (a), deposited drug (b) by evaporation under vacuum.

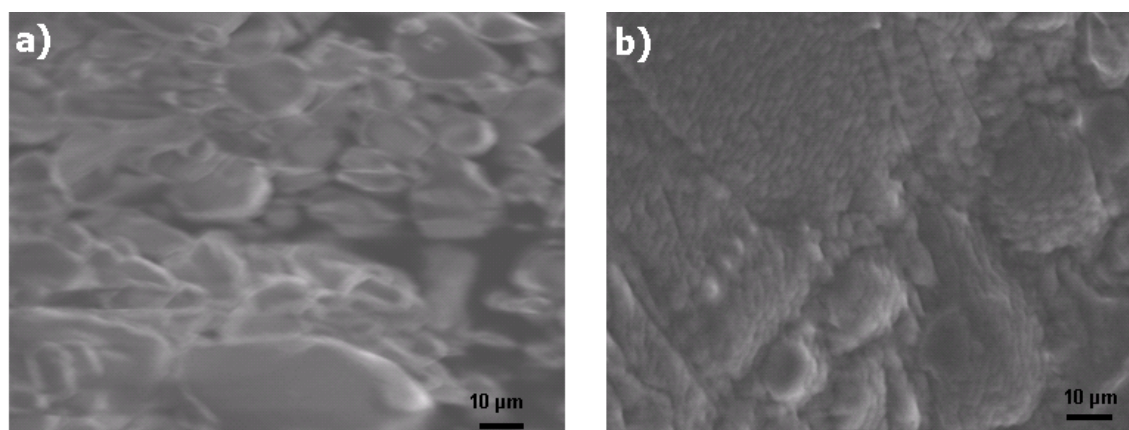


Figure 6.5: SEM images of Itraconazole as bulk material (a) and deposited drug (b) by evaporation under vacuum.

Another promising route of a new drug design by thermal evaporation is the co-deposition of two different drugs from two separate evaporators simultaneously in a vacuum chamber. This allows the formation of a molecular scale mixing of pharmaceutical active substances or excipients to form nanostructured hybrid drugs exhibiting synergetic responses at the same time. With conventional solution based processing, such a mixing requires very special preconditions, e.g., the possibility for co-crystallisation. Evaporation of molecules from two different sources typically gives no time for a demixing process on the substrate, as molecules directly lose most of their energy when they hit the substrate surface. Here, amorphous mixtures can be formed with structurally incompatible drugs leading to synergistic effects. The approach is very helpful for controlling the dissolution of drugs. In addition, the solubility can be significantly increased. If a molecule with poor ability to dissolve is only surrounded by molecules of good solubility, a total increase in dissolution can be affected. This is very beneficial in increasing the solubility of poorly soluble drugs by deposition of low soluble molecules in parallel with a highly soluble one and with this forming a solid solution. Thermal evaporation also provides amorphous deposited film which has a random structure and is completely and more easily dissolved.

The co-deposition approach also allows the creation of a molecular mixture in terms of a solid solution from every thermally evaporated drug (overviewed **Table 3.1**). To show an example for such a combination, the efficacies of the above mentioned antimicrobial agents such as Erythromycin and Itraconazole were evaluated in combination. In agar plate diffusion tests, both antifungal and antibiotic effect of these combined deposits could be confirmed and were in the same degree as for the individual substances (as shown in **Figures 6.1** and **6.4**). From our first biological tests, it is obvious that thermally evaporated substances can in principle exhibit higher activities as compared to their conventionally controlled sample. However, further biological experiments with other pharmaceuticals should be performed to reveal the full potential of thermal evaporation for pharmaceutical engineering.

It is obvious that superimposition on a surface by evaporation under vacuum particularly in the case of poorly water soluble substances like Chloramphenicol, Erythromycin,

Nipasol, Clotrimazole and Itraconazole is a very appropriate technique to provide an antimicrobial ambience without the necessity to dissolve the substance.

Additionally, Chloramphenicol and Tetracylin-HCl were evaporated under vacuum on glass plates. The antibacterial efficacy of these objects could also be confirmed. As shown above, vacuum deposition on surfaces of different materials is effective.

The application of materials with surfaces antimicrobial equipped by this technique may be many-sided. But, particularly for the use of implantable devices as bone pins or artificial teeth, it may open new perspectives in the defence of infections. Therefore, the production of vacuum-deposited coatings, from which antimicrobials are released over a long period, is to be established. Furthermore, structural factors, such as defects or guest ions in the crystal, can facilitate dissolution by reducing the bond strength in the crystal. Lowering the lattice energy could facilitate dissolution although enthalpy and entropy of dissolution probably play a role for antimicrobial agents after deposition by vacuum technique. This material has still anti-microbial properties to decrease the chances of bacterial and fungal infections.

The antimicrobial activity of Tobramycin against Staph aureus (**Figure 6.6**) is demonstrated in Agar plate with 15 ml Caso-Agar (Petri-dish) using Staph aureus as pathogenic bacteria with Absorption: 0.116 (Factor: 7.3×10^8) \diamond 1:10 dilution 0.1 ml into 5 ml Caso-Agar incubating at 24 hours at 37 C°. Clearly, from the **Figure (6.6)**, Tobramycin after deposition by thermal evaporation technique is still active. However, the activity depends on the substrate used and the surface morphology.

The results of utilizing Titanium oxide substrate coated with Tobramycin show much higher Inhibition zone: 24.70 mm which is measured by Gauge (diameter) after 24 h as compared to the Positive Control, 25 μ m Tobramycin has Inhibition zone: 22.64 mm. This significant increasing in the area of inhibition zones for thermally evaporated Tobramycin if compared to its control samples as seen in **Figure 6.6**. It was found that the Inhibition zone based on the employed substrate: titanium substrate gives 21.47 mm inhibition zone in the other hand stainless steel provides 15.98 mm inhibition zone. No inhibition is observable after 1 day. For the negative control which is measured without any deposition (Anod. Ti type II).

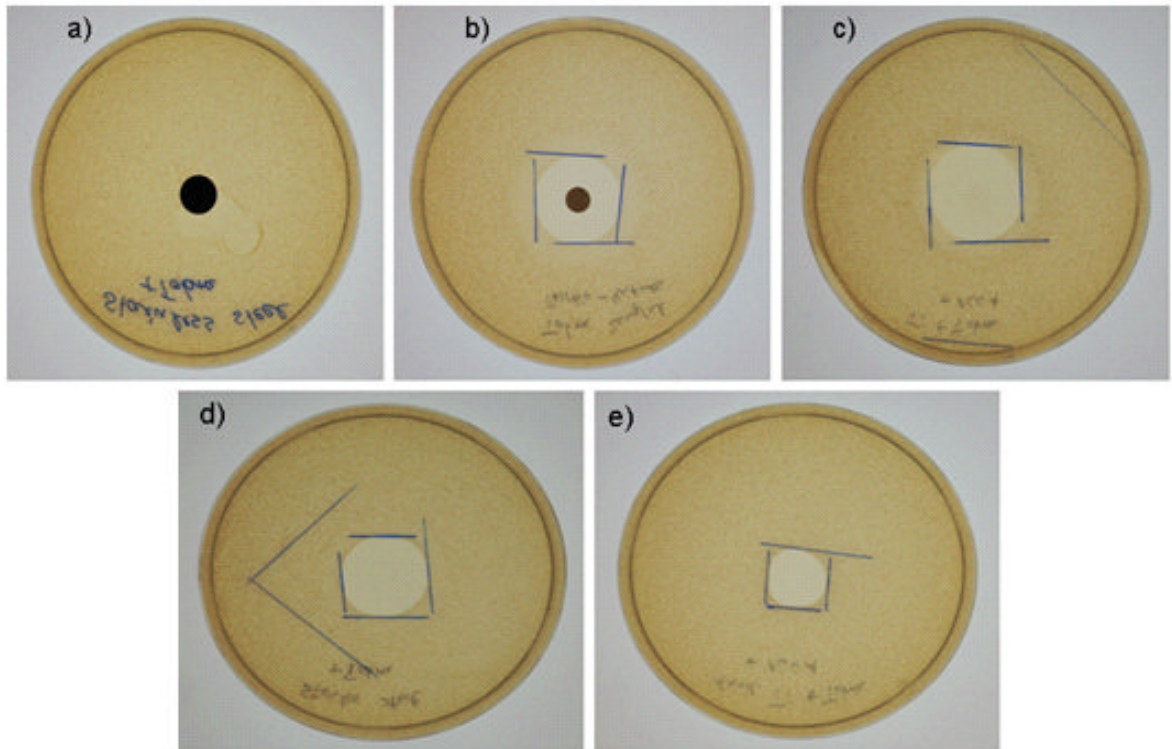


Figure 6.6: Illustrates the antimicrobial activity of Tobramycin against *Staph aureus*, Negative Control (Anod. Ti type II) (a), Positive Control (Tobramycin) (b), deposited Tobramycin film grown on Titanium oxide (c), Titanium (d), stales steel (e).

In Summary, The antimicrobial activity of Erythromycin inhibits the growth of *Staphylococcus aureus* by higher inhibition zone than the same amount of control experiments. The fungistatic effect of antimycotics (Intracanzol) deposited by evaporation under vacuum against *Candida albicans* ATCC 10231 shows significant inhibition zone if compared with the control sample. The activity of Tobramycin against *Staph aureus* (**Figure 6.6**) is questionable as it suggests a more detailed research. Thus, the growth of the colonies *Staph aureus* completely inhibited in the presence titanium oxide substrate gives much higher Inhibition zone than the reference drug.

According to the interpretation suggested for thermal evaporation coating process. These results revealed that this procedure provides a stable and homogeneous coating with higher surface area as illustrated in **Figure 6.7**.

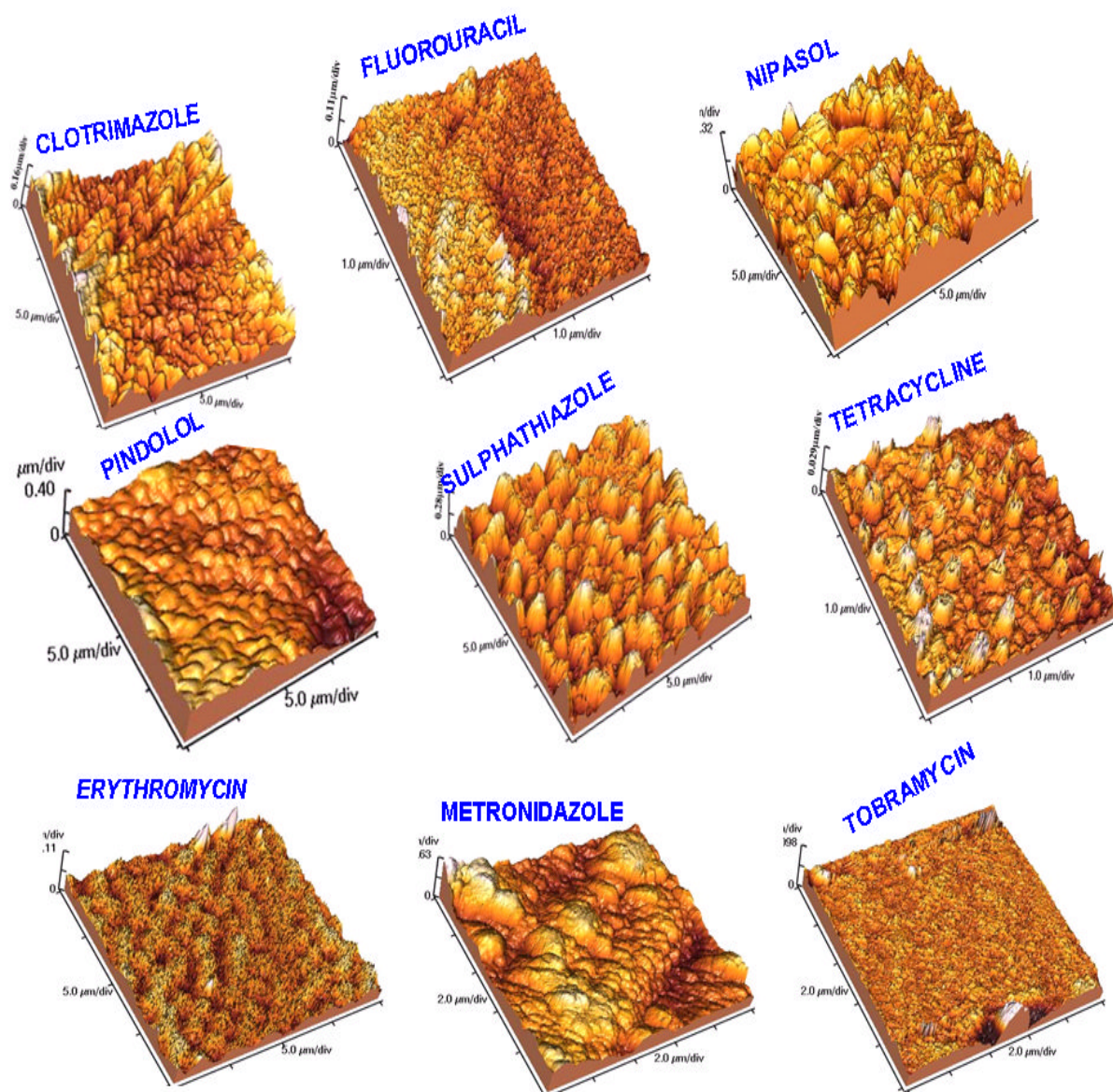


Figure 6.7: 3D AFM images of nano-microstructured pharmaceutically active molecules.

Antimicrobial activity was strongly dependent on particle size of antimicrobial agents, with smaller sized nano-microstructures having more efficient antibacterial activity than larger size. The vacuum deposition of active anti microbial agents is found to enhance surface reactivity due to their extremely small size and high surface area. Higher surface area of active molecules allows many particles to cover the bacteria cells to a high extent and bring deposited molecules in an active form in high concentration in proximity to the cell. This indicates that, after reduction of particle size, increased saturation solubility, an

enlarged surface area, and a thinner diffusion layer could dramatically increase the dissolution velocity as described by Noyes Whitney equation [38].

$$\frac{dc}{dt} = \frac{DA}{vh}(C_s - C_x) \quad (6.1)$$

Where dC/dt = dissolution rate, D = diffusion coefficient, A = surface area, V = the volume of the dissolution medium, C_s = saturation solubility, C_x the drug concentration of bulk solution and h = hydrodynamic boundary layer thickness.

6.2 Controlled drug release from biodegradable polymers

In **Figure 6.8** Metronidazole is detectable in the elution profile in phosphate buffer, pH 7.4 at 35 °C. The titanium plate was dissolved in 1 ml sterile phosphate buffer, pH 7.2 and incubated in closed tubes. Where each 10 μ l of sample is removed, diluted with 3 ml of buffer and measured, mmodified release formulations show a sustained (= extended = delayed) release of the drug. The modified release concept is suitable for drugs with short half life to maintain therapeutic plasma concentrations over a longer period of time. The administration intervals can be reduced.

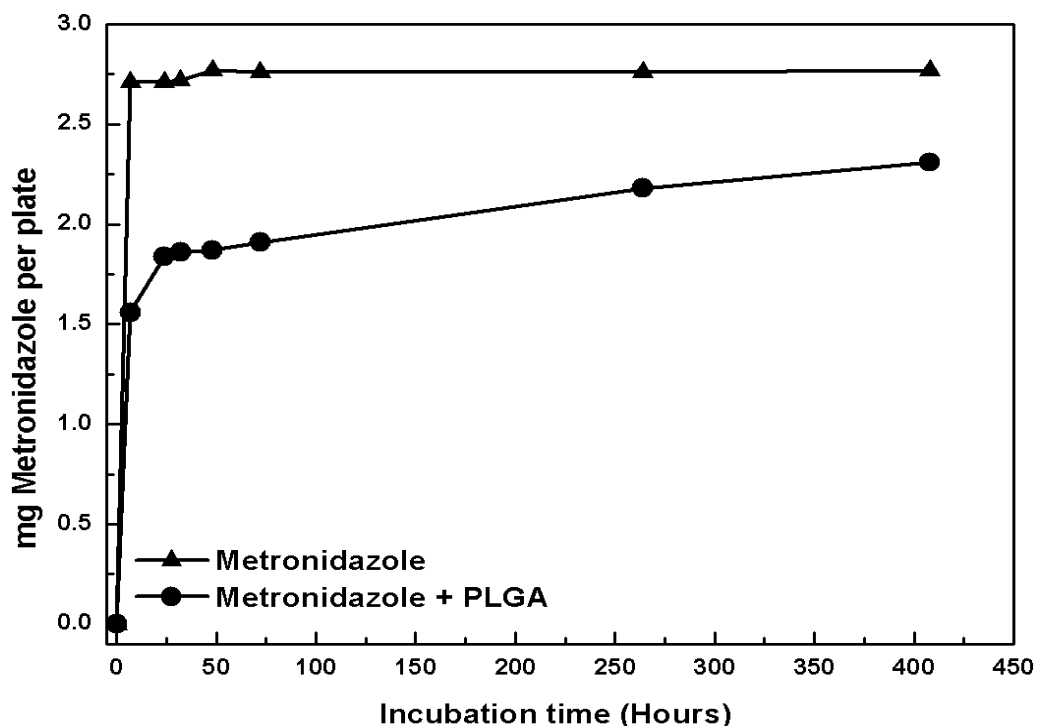


Figure 6.8: Illustrates drug release profile of Metronidazole.

Moreover, high plasma peak levels which go along with side effects that can be optimized. Modified release formulations are important for long-term treatment. In the test with the layer by layer deposition (PLGA (50/50) with Metronidazole), stronger

release takes place after five days period. Additional to the delayed release, such multilayered systems may be used to release a combination of drugs in a desired time pattern, e.g., having a drug I for a few days, after complete dissolution of layer I, a subjacent drug II could take effect. In this case a thin film of Metronidazole, being rapidly dissolved after TE (see **Figure 6.9 b**) which is covered with PLGA by subsequent depositions from two sources on a polished Ti-substrate. The construction of multilayer's by chemical method is difficult due to the nature of fluids. From the release kinetics shown in **Figure 6.8** the effect of delayed drug release could be verified. Being a polymer, PLGA is expected to depolymerise during evaporation and to repolymerise on the substrate. This approach of fabricating multilayer pharmaceutical drugs by TE could be used for coronal stents, which first require an antiplatelet medication and subsequently an antiproliferative drug to prevent restenosis in coronary arteries and effect an optimal integration. The morphology at the interface between the individual layers also plays very important role in controlling the drug release kinetics.

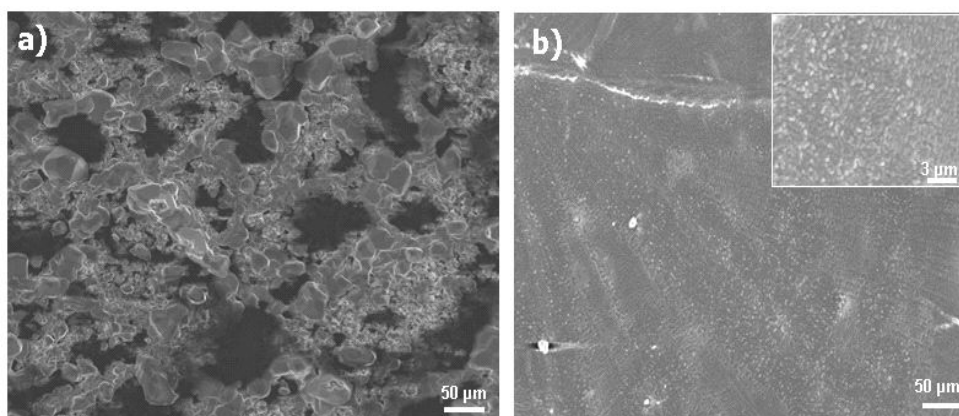


Figure 6.9 : SEM images of Metronidazole as bulk material (a) and deposited drug (b) by vacuum evaporation. The inset shows higher magnification SEM image.

6.3 Thermal evaporation for enhanced activities

By using thermal evaporation approach, it was possible to produce different concentration from the deposited drug starting from lower to higher concentration depending on the experimental conditions. The amount of material deposited on the substrate was calculated by measuring four samples from Tetracycline hydrate, different weights 3.25 μg , 4.8 μg , 5.14 μg and 7.99 μg were obtained. In case of Pilocarpine-HCl, three samples are measured, different weights also 1.78 mg, 1.87 mg and 1.87 mg appear. With Tetracaine-HCl, two samples were also investigated to provide (205.7 μg and 230.0

µg). Furthermore, the antibacterial activity against pathogenic bacteria and fungi powerfully depended on the specific surface area of the deposited film of the active pharmaceutical molecules. The activity increases with the increase of the surface area, irrespective of the shape and the crystallinity of their deposited films. In the case of *Staphylococcus aureus*, however, it was found that there was difference in the activity if compared to the reference drugs. Using of biodegradable polymers to control the release of pharmaceutical agents, these polymers have great efficacy for the control release of different drugs like antibiotic, antimicrobial, vaccines, human growth hormone, insulin, anti-tumour agents, contraceptives and vaccines. Long circulation of drugs in the body explains how drug delivery and drug targeting to the site of desired action. Definitely, surface modification is helpful in attaining these goals. Manufacture of nanostructures by using the environmentally processes like thermal evaporation is fairly a promising area of research to develop the materials liberated from the unwanted toxic residual solvents. Although many important goals have been reached in achieving stabilization of drugs in circulation, more investigations are needed to expand the novel products in this area.

6.4 Pharmaceutical field effect transistor (PFET)

Organic semiconductors have appeared as an enticing alternative for the development of low cost electronics. These materials have the potential to be solution processed which lowers production costs and increases substrate compatibility. Anyway, in contrast to organic light emitting diodes, organic field effect transistors couldn't be realized in a sufficient manner till today. Due to the similarities of the utilized molecules for the pharmaceutical thin films used here and the type of molecules used for organic field effect transistors, In order to fabricate a pharmaceutical field effect transistor, Pilocarpine-HCl semiconductors were chosen as active layer due to its conductivity behaviour. This conduction mechanism can be either ballistic or diffusive of the charge carriers through deposited layers or based on tunnelling in nature. Charge transport in conductive organic materials is dependent on π -bonding orbitals and quantum mechanical wave-function overlap.

Visionary, the thermal evaporation approach could be useful for fabrication of a PFET in future for different potential applications such as bioelectronic devices and biosensors. Another promising possibility can be by coat integrated silicon chips to design a PFET

for different applications ranging from new generations of organic electronic devices to biomedical engineering [125, 126].

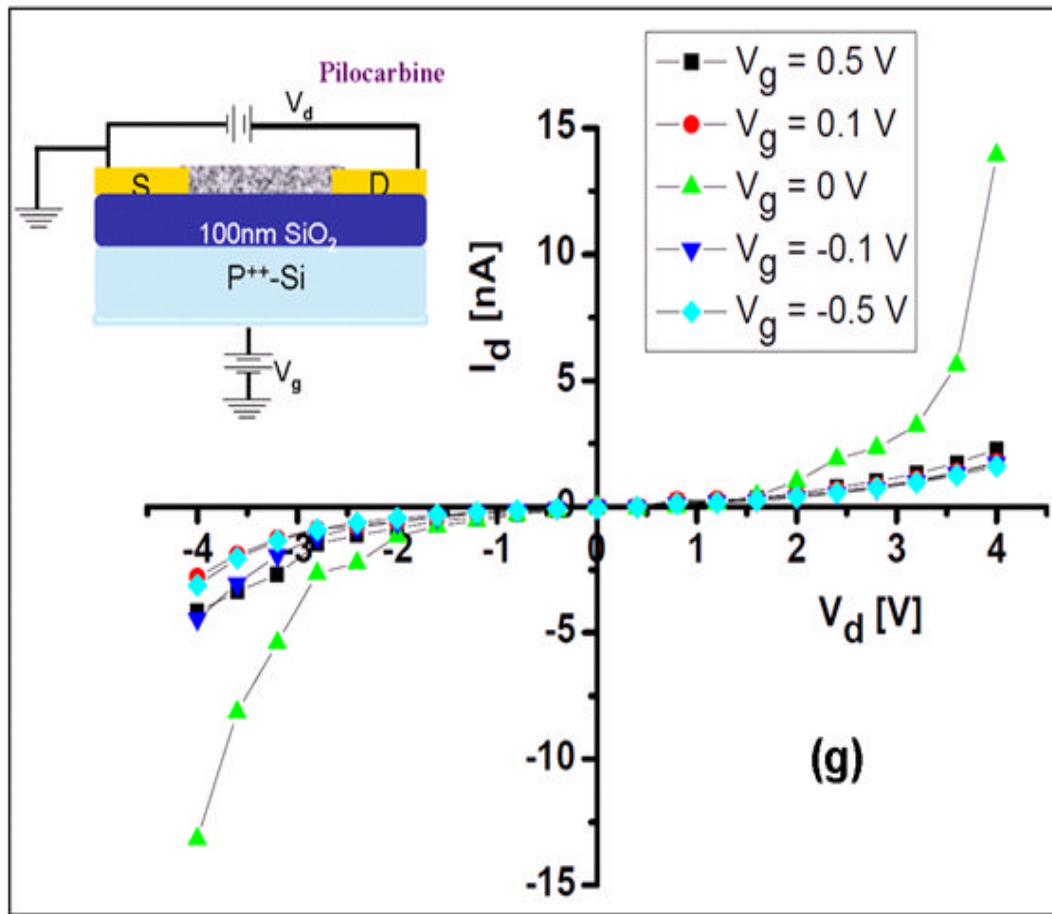


Figure 6.10: The basic layout and conductivity curves of a PFET based on Pilocarpine-HCl by deposition through a shadow mask directly on a silicon microchip.

Figure 6.10 shows the basic layout and conductivity curves of a PFET based on Pilocarpine-HCl by deposition through a shadow mask directly on a silicon microchip. A gate voltage allows blocking a source-drain current. Visionary, this micro-structured film could be used for multifunctional medical coatings that help to know the status of the drug layer like thickness. When the Gate is made more negative, it depletes the majority carriers from a larger depletion zone around the gate. This reduces the current flow for a given value of Source-to-Drain voltage. Modulating the Gate voltage modulates the current flow through the device.

6.5 Room Temperature Current - Voltage Characteristic

Challenge with other electrically conductive pharmaceutical materials that have recently been explored for photo-thermal therapy is that these materials are absorbed across wide range of infrared light in order to optimize both biological transport and heat transfer. In therapeutical conductive substances, several studies have been done for example in bone repairing which has semiconductor behaviour in some respects. For instance, the basic functional unit in bone appears to be a PN junction diode formed by exactly molecular association between collagen fibres (N-type material) and the mineral apatite crystals (P-Type material). Basically, the conductivity is determined by the number of free charge carriers and their mobility. The charge carriers are sensitive to radiation which used in clinical situation [127]. Moreover, the conductive drugs used for Iontophoresis [128] which has many advantages as drug administration method. Inonotphoresis used for delivery the conductive drugs through the surface tissues by using a small electric charge.

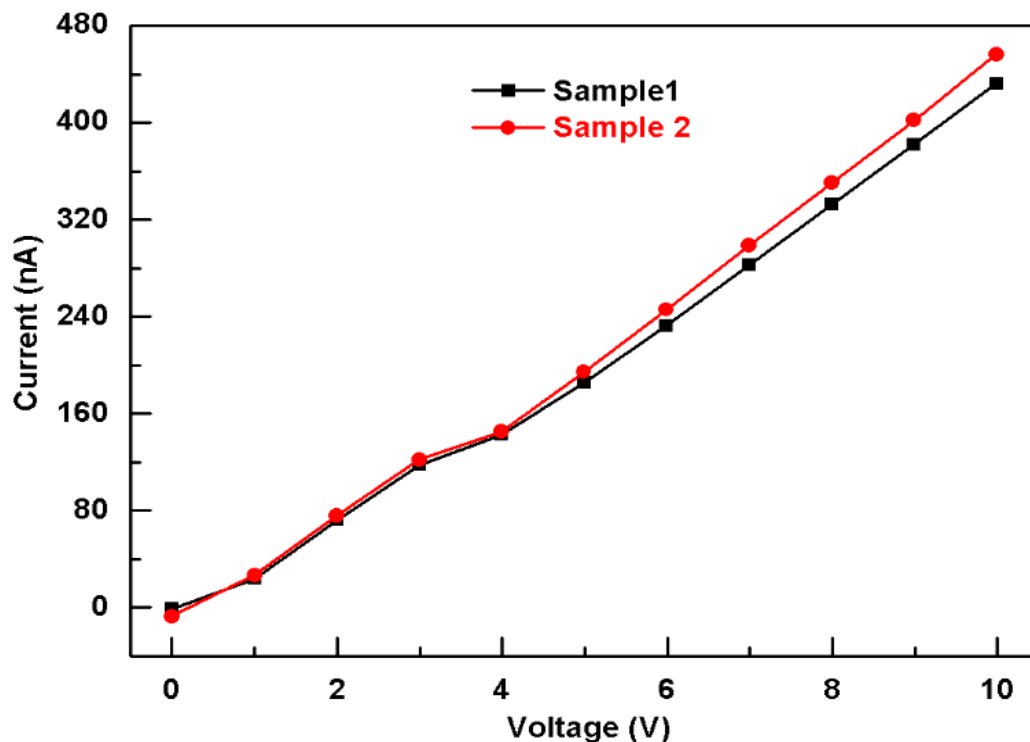


Figure 6.11: The I-V characteristic of pilocarpine-HCl thin film deposited on glass substrate.

Here, Pilocarpine-HCl was selected as an example for conductivity measurement. The room-temperature electrical measurements were performed under ambient conditions by using Au contact pins connected to the fabricated micro or nanostructure circuits. The current through the micro-nanostructure circuit was measured by using a Keithley 6485 picoamperemeter (which is optimized for measuring the extremely small electrical signal)

while increasing the voltage from 0 to 10 V. The resistance of Pilocarpine- HCl thin film was extracted from the slope of the current-voltage (I-V) curve. **Figure 6.11** shows a set of I-V curves Pilocarpine-HCl thin film which acts like semiconductor behaviours. Actually, conducting organic materials have backbones of contiguous sp² hybridized carbon centres. One valence electron on each centre resides in a p_z orbital, which is orthogonal to the other three sigma-bonds. Thus, the conjugated p-orbitals form a one-dimensional electronic band, and the electrons within this band become mobile when it is partially emptied.

6.6 The unique requirements of thermal evaporation

Indeed, thermal evaporation technology has been investigated as an alternative and attractive technique to prepare and engineering the micro- and nano structures from drugs and pharmaceutical excipients. Thermal evaporation is solvent free and environmentally friendly. A good variety of drugs can be produced with this technique. These drugs would require least amount of dosage because of higher solubility and also least side effects owing to higher purity. Thermal evaporation offers a considerable promise as alternative technique for formation a multi-component mixture making micro-nanostructures rapid, efficient and suitable for coating the surface implants. In this work, the versatile fabrication of solvent free micro-nanostructured pharmaceutical drugs had been introduced in a controlled way on various substrates.

Designing delivery systems, and the unprecedented recent growth in the field, has driven a great deal of research into novel means of drug delivery. The search for techniques that offer formulations that are stable, bioavailable, manufacturable, and acceptable to the patient, has led to major advances in development of transdermal and implantable delivery and controlled release technology. The conventional area of formulation technology has achieved scientific advances to meet the needs of these compounds. s. Biomaterial-associated bacterial infections present common and challenging complications with medical implants. As a result, prevention of bacterial colonization and biofilm formation is an important consideration and may be supported by the use of antiseptic surface coatings.

Results showed an initial peak of release layer by layer test after 5 days. Then stronger release takes place faster. Drug release from bioerodible polymers is used in both topical

and systemic applications. Both of them require that the polymers break down to nontoxic materials, and polymers used in systemic applications must also degrade to low-molecular-weight fragments that can be removed or metabolized by the body. In topical applications, retainment of high molecular weight of the degradation products is desirable, since systemic absorption of the polymer will occur, and toxicological hazards will be reduced.

A lateral structuring, the positioning of thermal evaporated thin films, is relatively straightforward by utilising lithography or shadow masks. Possible applications for laterally structured systems are smart or multifunctional pharmaceutical drug coatings for implants [129] or contact lenses. Specific examples are contact lenses for ophthalmic drug delivery [130] which should not affect the vision and thus require a lateral structuring as shown in **Figure 5.35** of the drug film. Selective area for depositing pharmaceutical drugs on contact lenses is possible with TE technique through suitable microscopic shadow mask. Such a structuring could also be used in complex implant coatings like stents or dental implants that require different drugs in different places in contact with bone, mucosa or the oral cavity. Bacterial adhesion is an important step in the pathogenesis of an infection (periimplantitis). Placement of different antibacterial active molecules on specific areas of the implant surface (depending on the intraoral contact to bone, mucosa or the oral cavity) will also be possible with thermal evaporation. Highly complicated drug delivery systems are developed to apply their effects after they are injected to the body, particular, into the systemic circulation. The study of drug delivery expands and proves that the reduction of poorly soluble active ingredients to nanoscales increases the solubility, bioavailability, controlled release and biological site-specific targeting. This new group of delivery systems is definitely an important component of modern drug delivery technology. Many novel drug delivery technologies are under development and significant progress nearly in all branches of drug delivery and local pharmacodynamic effects by physical or chemical binding of the drug to a carrier system.

Chapter 7

7 Summary and Outlook

The aim of this thesis was to evaluate whether vacuum evaporation of drugs could be utilized as a new method to create thin film coatings that possess potential pharmaceutical use.

Briefly, it was found that thermal evaporation of pharmaceutical molecules can be utilized as a completely solvent free technique where drugs as powders or crystalline materials are directly formulated into desired nano or micro structures and shapes on preferred substrates. Thermal evaporation is based on the principle of physical vapor deposition. The drugs and the drug carrier materials were heated up in a crucible to their melting temperature. The whole procedure was carried out in a vacuum chamber. High-vacuum (10^{-5} - 10^{-7} mbar) guaranteed a long mean free path of the evaporated particles on their way to the substrate as well as the avoidance of contaminations.

The performed deposition experiments and their structural analyses suggest that by thermal evaporation technique, most of pharmaceutical substances (>80%) can be micro-nanostructured in different desired complex forms as illustrated in **table 5.1**. Other pharmaceutical molecules such as Triclosan and PEG used in this study could not be structured by thermal evaporation, they tend to decompose irreversibly.

To examine the resulting structures and morphologies, diverse techniques were used. These techniques include optical microscopy, SEM, AFM, Raman-spectroscopy, XRD and profilometry (see **chapter 5**). In order to avoid the structural damage in the structures and charging, acceleration voltages in the SEM were kept as small as possible down to 2 kV and reduced currents were applied. In order to get the actual morphologies of thermal evaporated pharmaceuticals by using SEM, further coating (of carbon or gold thin film) was performed on deposited drugs. Raman spectra of raw (control) drugs as well as thermally evaporated layers on different substrates were recorded to ensure the identity of structured pharmaceutical substances.

The spectral and microscopic data show that substrate surface and employed temperatures have a strong influence on structural evolutions of the pharmaceutical drugs during thermal evaporation as shown in **Figures 5.1, 5.2 and 5.9** respectively. Thermal evaporation as fabrication technique for drug delivery systems has many advantages such as simple process, solvent free and low cost if compared to other techniques. It appears that the chemical structures of the evaporated materials such as Chloramphenicol are unmodified for offering crystalline structures as illustrated in **Figures 5.23, 5.24 and 5.25** respectively. It is important to note that it takes some time after evaporation for the sample to become crystalline due to diffusion processes. Further attempts have been made to improve the crystallization process by annealing of the deposited pharmaceutical substance at certain temperatures as demonstrated in **Figure 5.50**. It turned out that the energy imparted in heating leads to a faster crystallization process. Relevant parameters are taken into account in relation to the thin film structures including the concentration of the material to be evaporated, the temperature, the vacuum and the deposition time.

In general, an appropriate delivery system is very necessary for drugs with poor solubility. At the same time, one needs to minimize side effects. So, site-specific delivery (i.e., drug targeting) would be the most desirable aspect. In addition, one of the main challenges in medications is the dosage, for which the most helpful schedule is determined by the toxicity of the clinical agents used. The observed features of vacuum deposited films like enhanced solubility, activity and controlled release movement of synthesized drugs in present case seem to be a powerful alternative for the traditional physical structuring of pharmaceutical drug molecules. The variety of new possibilities for pharmaceutical engineering utilizing thermal evaporation is expected to cover a wide range and will be potentially beneficial for many branches of medicine, pharmacy and engineering. Since a large number of drugs are accessible to the approach, thermal evaporation tests could result in reduction of dose and side effects for many approved drugs. The possibility of smart designing like hybrid, multilayer and/or implant coatings or solid solutions could lead to a re-assessment of insoluble molecules and thus could be very promising for many new therapies. So, the thermal evaporation technique can be versatily employed for micro-nanostructuring of different pharmaceutical drugs in various desired forms with increasing responses. A completely new way of pharmaceutical engineering is the combination of inorganic materials with pharmaceutical active substances. Such combinations could be potentially used as smart

implant coatings i.e., in form of nanoporous structures with medication filled pores in the inorganic material. An example for such co-evaporation is shown by SEM measurement in **figure 5.29** where Ag and Tetracaine-HCl are combined.

Furthermore, it was possible with thermal evaporation to design multiple layers of different desired active and non-active ingredients. They can be used to increase the activity of the drug, control the drug release and in combination therapy. Co-deposition approach also allows the creation of a molecular mixture in terms of a solid solution from nearly every thermally evaporated drug. The efficacies of the antimicrobial agents such as Erythromycin and Itraconazole are an example for such a combination. In agar plate diffusion tests, both antifungal and antibiotic effect of these combined deposits could be confirmed and were in the same degree as for the individual substances (as shown in **Figure 6.1** and **Figure 6.4**) for Erythromycin and Itraconazole respectively. It appears that the pure titanium plate polishing does not show antibacterial properties, but the antimicrobial effect of deposited film after evaporation from antimicrobial agents and antibiotic is confirmed as illustrated in table 6.1 and 6.2. The results show that the deposition of pharmaceutical molecules is reproducible and their biological activities are very efficient.

The first biological tests starting in this research project make it obvious that thermally evaporated substances can in principle exhibit higher activities as compared to their conventional control sample. However, further biological experiments with other pharmaceuticals should be performed to reveal the full potential of thermal evaporation for pharmaceutical engineering. It is confirmed that thermal evaporation can be used to effect a delayed release, such multilayered systems may be used to release a combination of drugs in a desired time pattern. For example, having a drug I for a few days, after complete dissolution of layer I, a subjacent drug II could take effect. In this case, a thin film of Metronidazole, being rapidly dissolved after thermal evaporation is covered with PLGA by subsequent depositions from two sources on a polished Ti-substrate. Being a polymer, PLGA is expected to depolymerize during evaporation and to re-polymerize on the substrate. This approach of fabricating multilayer pharmaceutical drugs by thermal evaporation could be used for coronal stents, which first require an antiplatelet medication and subsequently an antiproliferative drug to prevent restenosis in coronary arteries and affect an optimal integration. Experimentally, in this study, thermal evaporation of pharmaceutical molecules is applied in a field effect transistor. Another

promising possibility can be to coat the integrated silicon chips to design a pharmaceutical field of the effect transistor (PFET) for different applications ranging from new generations of organic electronic devices to biomedical engineering. The basic layout and conductivity curves of a PFET are based on Pilocarpine-HCl by deposition through a shadow mask directly on a silicon microchip. Results suggested that the deposition of pharmaceutical molecules is more reproducible and the biological activities are very efficient due to the higher surface area and reducing the particle size of the drugs.

An essential point for pharmaceutical practices that should not be ignored is that many solvents have been used to combine active and non-active ingredients which may provide acute toxicity *in vivo*. The chemical compositions of deposited material are a significant factor in the field of biomedical applications to assure that there are no changes occurring from abnormalities in the chemical structures. It also rendered possible to reduce the particle size to nano-micro-range and increase the surface area. These facts advance the acceptance to mammalian cells. They also help to change the dosages well. Thermal evaporation of drugs and drug carriers offers great opportunities concerning biomedical applications like coating surfaces of stents and implants in particular. It is used to prevent these from bacterial affections to avoid restenosis and osteomyelitis. This dissertation pays our attention to the fabrication of various thin films from various materials such as pharmaceutical compounds, polymer and metals by using physical vapor deposition process. Finally, this dissertation explores thermal evaporation of pharmaceutical molecules to achieve drugs solubility and reduce their toxicity towards normal tissues.

As an outlook, the use of thermal evaporation is not limited to the drugs listed but also it can be employed for developing and restructuring unrestricted pharmaceutical materials into new forms of medications with improved responses. It is hoped that this will enable and contribute further detailed examinations of various thin film deposition from many more pharmaceutical substances, metals and semiconductors which can be used in medical devices. Visionary, the improvements in solubility and the absence of toxic solvents could lead to novel therapies and finally to increased patients survival.

Bibliography

- [1] The Royal Society and The Royal Academy of Engineering, Nanoscience and nanotechnologies: opportunities and uncertainties. London, UK, (2004).
- [2] Nishiguchi, K. and Oda, S., Self-aligned double-gate single-electron transistor derived from 0.12- μm -scale electron-beam lithography., *Appl. Phys. Lett.*,78: pp.2070-2072 (2001).
- [3] Seiji, H., Masao, N., Kenji, S., Hiroyuki, K., Yasuo, T., Katsumi, M., Mechanism of Potential Profile Formation in Silicon Single-Electron Transistors Fabricated Using Pattern-Dependent Oxidation, *Japanese Journal of Applied Physics.*, 40: pp. L29-L32 (2001).
- [4] Ono, Y., Takahashi, Y., Yamazaki, K., Nagase, M., Namatsu, H., Kurihara, K., and Murase, K., Fabrication Method for IC-Oriented Si Single-Electron Transistors., *IEEE transactions on electron device*, 47(1): pp. 147-153 (2000).
- [5] Shegai, O. A., Zhuravlev, K. S., Markov, V. A., Nikiforov, A. I., Pchelyakov, O. P., Photoresistance of Si/Ge/Si Structures with Germanium Quantum Dots., *Semiconductors*, 34: pp.1363-1367(2000).
- [6] Wang, Y., Deng, K., Gui, L., Tang, Y., Zhou, J., Cai, L., Qiu, J., Ren, D., Preparation and Characterization of Nanoscopic Organic Semiconductor of Oxovanadium Phthalocyanine., *J. Colloid Interface Sci.*, 213: pp.270-272 (1999).
- [7] Yang, J., Maria, J., Ferreira, F., Weng, W., and Tang, Y., Sol–Gel Preparation and Electrorheological Activity of $\text{SiO}_2\text{--TiO}_2$ Composite Powders., *J. Colloid Interface Sci.*, 195: pp. 59-65 (1997).
- [8] Liao, Y. C., Lin, S. Y., Lee, S. C. and Chia, C. T., Spherical SiGe quantum dots prepared by thermal evaporation, *Appl. Phys. Lett.*,77: p. 4328 (2000).
- [9] Lin, W., Lin, S. Y., Lee, S. C., and Chia, C. T., J., Structural and optical properties of germanium nanoparticles., *Appl. Phys.* 91: p. 1525 (2002).
- [10] Che, G., Lakshmi, B. B., Martin, C. R., and Fisher, E. R., Chemical Vapor Deposition Based Synthesis of Carbon Nanotubes and Nanofibers Using a Template Method., *Chem. Mater.* 10: pp.260-267(1998).
- [11] He, Y., Yin, C., Cheng, G., Wang, L. and Liu, X., The structure and properties of nanosize crystalline silicon films., *J. Appl. Phys.*,75: pp.797-803 (1994).
- [12] Mandich, N. L., Bondybey, V. E., and Reents, W. D., Reactive etching of positive and negative silicon cluster ions by nitrogen dioxide., *J. Chem. Phys.*, 86: pp. 4245-4257 (1987).

-
- [13] Hahn, H. and Averbach, R. S., The production of nanocrystalline powders by magnetron sputtering., *J. Appl. Phys.* 67: pp. 1113-1115 (1990).
- [14] Taneja, P., Ayyub, P., and Chandra, R., *Phys. Rev. B* 65: p. 245412 (2002).
- [15] Pankhurst, Q. A ., Connolly, J., Jones, S. K., and Dobson, J., *J. Phys. D: Appl. Phys.*, 36: pp.R167–R181(2003).
- [16] Bergström, C. A. S., Wassvik, C. M., Johansson, K., Hubatsch, I., Poorly soluble marketed drugs display solvation limited solubility, *J. Med. Chem.* 50: pp.5858-5862 (2007).
- [17] Langer, R., Drug delivery and targeting., *Nature.* 392 (6679 Suppl.): pp. 5-10 (1998).
- [18] Lipinski, C. A., Drug-like properties and the causes of poor solubility and poor permeability, *J Pharm Toxicol Methods* 44: pp.235–249 (2000).
- [19] Kumar, A., Sahoo, S. K., Padhee, K., Kochar, P. P. S., Satapathy, A. and Pathak, N., Review on solubility enhancement techniques for hydrophobic drugs, *Pharmacie Globale (IJCP)*, 3 (03) (2011).
- [20] Lipinski, C. A., Solubility in water and DMSO: issues and potential solutions. In *Pharmaceutical Profiling in Drug Discovery for Lead Selection*, Borchardt RT, Kerns E H, Lipinski CA, Thakker DR, Wang B. Eds.; AAPS Press: Arlington, V. A., pp.93-125 (2004).
- [21] Takagi T, Ramachandran C, Bermejo M, Yamashita S, Yu, LX, Amidon, G. L., A provisional biopharmaceutical classification of the top 200 oral drug products in the United States, Great Britain, Spain, and Japan., *Mol Pharm* 3: pp.631–643(2006).
- [22] James K; “Solubility and related properties”, vol. 28, Marcel Dekker, Newyork, 986, pp.127 –146, 355 – 395.
- [23] Leuner, C., Dressman, J., Improving drug solubility for oral delivery using solid dispersions., *Eur J Pharm Biopharm.* Jul;50(1): pp.47-60 (2000).
- [24] Patel, R. P., Patel, M.P., Suthar, A. M., Spray drying technology: an overview., *Indian J Science and Technology.*, 2: pp.44-47 (2009).
- [25] Mishima, K. Biodegradable particle formation for drug and gene delivery using supercritical fluid and dense gas., *Adv Drug Delivery Rev.*, 60: pp.411–432 (2008).
- [26] Chrisey, D. B., Pique, A., McGill, R. A., Horwitz, J. S., Ringeisen, B. R., Laser deposition of polymer and biomaterial films., *Chem Rev.*, 103: pp.553-576(2003).
- [27] Kipp, J. E., The role of solid nanoparticle technology in the parenteral delivery of poorly water-soluble drugs, *International Journal of Pharmaceutics.*, 284 (1-2): pp. 09–122 (2004).
- [28] Singhal, D., Curatolo, W., Drug polymorphism and dosage form design: a practical perspective, *Advanced Drug Delivery Reviews.*, 56: pp.335– 347(2004).

-
- [29] Singla, A. K., Garg, A., Agarwal, D., Paclitaxel and its formulations, *Int J Pharm*; 235: pp.179–192 (2002).
- [30] Gelderblom, H., Verweij, J., Nooter, K., Sparreboom, A., Cremophor EL: the drawbacks and advantages of vehicle selection for drug formulation., *Eur J Cancer*, Sep; 37(13): pp.1590-8 (2001).
- [31] Yang, T., Cui, F. D., Choi, M. K, Lin, H., Chung, S. J., Shim, C. K., Kim, D. D. , Liposome formulation of paclitaxel with enhanced solubility and stability., *Drug Deliv. Jul*;14(5): pp.301-8 (2007).
- [32] Blagden, N., de Matas, M., Gavan, P. T., York, P., Crystal engineering of active pharmaceutical ingredients to improve solubility and dissolution rates., *Advanced Drug Delivery Reviews.*, 59: pp. 617–630 (2007).
- [33] Birnbaum, D. T., Kosmala, J. D., Henthorn, D. B., Peppas, L. B., Controlled release of beta-estradiol from PLGA microparticles: The effect of organic phase solvent on encapsulation and release., *J. Control. Rel.* 65: pp. 375–387(2000).
- [34] Soppimath, K. S., Aminabhavi, T. M., Kulkarni, A. R., Rudzinski, W. E., Biodegradable polymeric nanoparticles as drug delivery devices., *J Controlled Release*, 29: pp 1-20 (2001).
- [35] Dubey, R., Pure drug nanosuspensions impact of nanosuspension technology on drug discovery and development., *Drug Del. Tech.* (2006).
- [36] Merisko-Liversidge, E. M, Liversidge, G. G, Drug Nanoparticles: Formulating Poorly Water-Soluble Compounds., *Toxicologic Pathology*, 36: 43-48 (2008).
- [37] Ginty, P. J., Whitaker, M. J., Shakesheff, K. M., Howdle, S. M., Drug delivery goes supercritical., *Materials Today*, 8: pp.42-48 (2005).
- [38] Noyes, A. A., and Whitney, W. R., The rate of solution of solid substances in their own solutions., *J. Am. Chem. Soc.* 19: p. 930 (1897).
- [39] Patel, J. N., Rathod, D. M. , Patel, N A. , and Modasiya, M. K., Techniques to improve the solubility of poorly soluble drugs., *Int. J. of Pharm. & Life Sci. (IJPLS)*, 3: pp.1459-1469 (2012).
- [40] Daniher, D. I., Zhu, J., Dry powder platform for pulmonary drug delivery., *Particuology*, 6 (4): pp.225–238 (2008).
- [41] Mattox, D. M., The foundation of vacuum coating technology., Noyes publications/ William Andrew Publishing Norwich New York. U.S.A., (2003).
- [42] Yang, Y., Liu, Y., Park, S., Lee, K., Koh, K. H., Ji, H., Wang, X., Ong, J. Development of sputtered nanoscale titanium oxide coating on osseointegrated implant devices and their biological evaluation., *Vacuum*, 83: pp.569–574(2009).

-
- [43] Kulkarni, A. P., Tonzola, C. J., Babel, A., Jenekhe, S. A., Electron transport materials for organic light-emitting diodes. *Chem Mater* 16: pp4556-4573 (2004).
- [44] Weszka, J. P., Jarka, P., Pakuła, D., Dobrzański, L. A., Domański, M., Jurusik, J. Studying of kinetic growth of organic thin films, *J Achievements Mat Manufact Engineering* 35: pp.29-36 (2009).
- [45] Venables, J. A., *Introduction to Surface and Thin Film Processes*, Cambridge University Press (2000).
- [46] Wang, W. C., Zhong, D. Y., Zhu, J., Kalischewski, F., Dou, R. F., Wedeking, K., Wang, Y., Heuer, A., Fuchs, H., Erker, G., and Chi, L. F., Patterned nucleation control in vacuum deposition of organic molecules., *Phys Rev Lett* 98: pp.225504-225508(2007).
- [47] Mang, T., Bobzin, K., Bartels, T., *Surface Engineering, Industrial Tribology*, Wiley-VCH Verlag, (2011).
- [48] Donald, L. Smith, *Thin Film Deposition, Principals & practice*
- [49] Kratz, F., Müller, I. A., Ryppa, C., Warnecke, A., Prodrug strategies in anticancer chemotherapy., *ChemMedChem*, 3: pp.20-53 (2008).
- [50] Male, K. B., Lachance, B., Hrapovic, S., Sunahara, G., Luong, J. H. T., Assessment of Cytotoxicity of Quantum Dots and Gold Nanoparticles Using Cell-Based Impedance., *SpectroscopyAnal. Chem.*, 80: pp.5487-5493 (2008).
- [51] Brown, S. D., Nativo, P., Smith, J-A., Stirling, D., Edwards, P. R., Venugopal, B., Flint, D. J., Plumb J. A., Graham, D., and Wheate, N. J., Gold Nanoparticles for the Improved Anticancer Drug Delivery of the Active Component of Oxaliplatin, *J. Am. Chem. Soc.* 9: 132, pp. 4678-4684 (2010).
- [52] Kelemen, L. E., The role of folate receptor α in cancer development, progression and treatment: Cause, consequence or innocent bystander? *Int. J. Cancer* 119: pp.243-250 (2006).
- [53] Rfsler, A., Vandermeulen, G. W., Klok, H. A., Advanced drug delivery devices via self-assembly of amphiphilic block copolymers. *Adv Drug Delivery Rev*, 53:pp.95- 108 (2001).
- [54] Cherukuri, P., Glazer, E. S., Curley, S. A., Targeted hyperthermia using metal nanoparticles , *Advanced Drug Delivery Reviews*, 62: pp.339–345 (2010).
- [55] Feng, Q. L., Wu, J., Chen, G. Q., Cui, F. Z., Kim, T. N., Kim, J. O., A mechanistic study of the antibacterial effect of silver ions on *Escherichia coli* and *Staphylococcus aureus*, *J. Biomed Mater, Rev*, 52: pp.662-668 (2000).
- [56] Baram-Pinto, D., Shukla, S., Gedanken, A., Sarid, R., Inhibition of HSV-1 attachment, entry, and cell-to-cell spread by functionalized multivalent gold nanoparticles., *Small* 6: 1044–1050 (2010).

-
- [57] Baram-Pinto, D., Shukla, S., Perkas, N., Gedanken, A., Sarid, R., Inhibition of herpes simplex virus type 1 infection by silver nanoparticles capped with mercaptoethane sulfonate., *Bioconjug Chem*, 20: pp.1497–1502 (2009).
- [58] Rutnakornpituk, M., Baranauskas, V., Riffle, J. S., Connolly, J., St Pierre, T. G., Dailey, J. P., Polysiloxane fluid dispersions of cobalt nanoparticles in silica spheres for use in ophthalmic applications, *Eur. Cells Mater.*, 3: pp.102–5 (2002).
- [59] Ecke, A. G., Fachpraktikum Mikroelektronik und Sensorik Versuch: Hochvakuumbedampfung, Technische Universität Ilmenau, (2004).
- [60] Palisaitis, J. Vasiliaskas, R., Epitaxial Growth of Thin Films, Linköping University, (2008).
- [61] Deniz, D., Texture evolution in metal nitride (aluminum nitride, titanium nitride, hafnium nitride) thin films prepared by off-normal incidence reactive magnetron sputtering, Ph.D. Thesis, (2008).
- [62] Anantharaju, N., Panchagnula, M. V, Vedantam, S., Length Scale Effects in Wetting of Chemically Heterogeneous Surfaces., *Contact Angle, Wettability and Adhesion*, 6: pp.53-64 (2009).
- [63] Petros, R. A., DeSimone, J. M., Strategies in the design of nanoparticles for therapeutic applications. *Nat Rev Drug Discov.*, Aug; 9(8): pp.615-27(2010).
- [64] Choi, H. S., Liu, W., Misra, P., Tanaka, E., Zimmer. J. P., Ipe, B. I., Bawendi, M. G., Frangioni, J. V., Renal clearance of quantum dots., *Nat. Biotech.*, 25: pp. 1165–1170 (2007).
- [65] Ilium L., Davis, S. S, Wilson, C. G., Thomas, N. W., Frier, M., Hardy J. G., Blood clearance and organ deposition of intravenously administered colloidal particles. The effects of particle size, nature and shape., *Inter. J. of pharmaceutics*, 12(2-3): pp. 135-146 (1982).
- [66] Robby, A. P., and Joseph, M. D., Strategies in the design of nanoparticles for therapeutic applications., *Nature Review Drug discovery*, 9: pp. 615-627 (2010).
- [67] Dubin, C. H., Special delivery: pharmaceutical companies aim to target their drugs with nano precision., *Mech Eng Nanotechnol*, 126(Suppl): pp.10 - 2 (2004).
- [68] Dass, C. R., Su, T., Particle-mediated intravascular delivery of oligonucleotides to tumors: associated biology and lessons from gene therapy., *Drug Delivery*, 8: pp.191-213 (2001).
- [69] Courier, H. M., Butz, N., Vandamme, T. F., Pulmonary drug delivery systems: recent developments and prospects., *Crit Rev Ther Drug Carrier Syst*, 19: pp.425- 498 (2002).
- [70] Lloyd-Jones, D., Adams, R., Carnethon, M., De Simone, G., Ferguson, T. B., Flegal, K., et al. Heart disease and stroke statistics—2009 update: a report from the American Heart

Association statistics committee and stroke statistics subcommittee, *Circulation*, 119: pp.480–6 (2009).

[71] Cutlip, D. E., Chauhan, M. S., Baim, D.S., Ho, K. K. L., Popma, J. J., Carrozza, J. P., et al. Clinical restenosis after coronary stenting: perspectives from multicenter clinical trials., *J Am Coll Cardiol*;40: pp.2082–9 (2002).

[72] Patel, S. J., Perera, D. and Redwood, S. R., Stents and restenosis: the development of drug-eluting stents., *Journal of Renovascular Disease*, 2: 17–33 (2003).

[73] Htay, T. and Liu, M. W., Drug-eluting stent: a review and update *Vascular Health and Risk Management*.,1(4): pp.263-276 (2005).

[74] Serruys, P., Gershlick, A. H., *Handbook of Drug-Eluting Stents*, Taylor & Francis; (2005).

[75] Papat, K. C., Eltgroth, M., LaTempa, T. J., Grimes, C. A., Desai, T. A., Decreased *Staphylococcus epidermis* adhesion and increased osteoblast functionality on antibiotic-loaded titania nanotubes., *Biomaterials*, 28: pp.4880–4888 (2007).

[76] Young, A. M., Ho, S. M., Drug release from injectable biodegradable polymeric adhesives for bone repair., *Journal of Controlled Release* 127: pp. 162–172 (2008).

[77] Henderson, B. and Nair, S. P., Hard labour: bacterial infection of the skeleton., *Trends in Microbiology*, 11 (12): pp. 570–577 (2003).

[78] Donlan, R. M., *Biofilms: Microbial Life on Surfaces*., *Emerging Infectious Diseases*, 8(9):pp.881-890 (2002).

[79] Rosenthal, V. D., Maki, D. G., Graves, N., The international nosocomial infection control consortium (INICC): Goals and objectives, description of surveillance methods, and operational activities., *Am. J. Infect. Control*, 36: pp.e1-e12 (2008).

[80] Bearman, G. M. L., Munro, C., Sessler, C. N., Wenzel, R. P., Infection control and the prevention of nosocomial infections in the intensive care unit., *Sem. Resp. Crit. Care Med.*, 27: pp.310-324 (2006).

[81] Thevenot, P., Hu, W., Tang, L. Surface chemistry influences implant biocompatibility, *Curr. Top. Med. Chem.*, 8: pp.270-280 (2008).

[82] Vroman, L., Methods of investigating protein interactions on artificial and natural surfaces., *Ann. N. Y. Acad. Sci.*, 516:pp.300-305 (1987).

[83] Stutz, H., Protein attachment onto silica surfaces—A survey of molecular fundamentals, resulting effects and novel preventive strategies in CE. *Electrophoresis*, 30: pp.2032-2061 (2009).

-
- [84] Fang, F., Szleifer, I., Kinetics and thermodynamics of protein adsorption: A generalized molecular theoretical approach., *Biophys. J.*, 80: pp.2568-2589 (2001).
- [85] O'Toole, G., Kaplan, H. B., and Kolter, R., Biofilm formation as microbial development., *Annu. Rev. Microbio*, 54: pp.49–79 (2000).
- [86] Pavithra, D., Doble, M., Biofilm formation, bacterial adhesion and host response on polymeric implants—issues and prevention., *Biomed. Mater.*, 3: pp.1-13 (2008).
- [87] Hoiby, N., Bjarnsholt, T., Givskov, M., Molin, S., Ciofy, O., Antibiotic resistance of bacterial biofilms., *Int. J. Antimicrob. Agents*, 35: pp.322-332 (2010).
- [88] Knetsch, M. L. W., and Koole. L. H., New Strategies in the Development of Antimicrobial Coatings: The Example of Increasing Usage of Silver and Silver Nanoparticles., *Polymers*, 3, 340-366 (2011).
- [89] Hall-Stoodley, L., Stoodley, P., Evolving concepts in biofilm infections, *Cell. Microbiol.*, 11: pp. 1034-1043 (2009).
- [90] Donlan, R. M. Biofilms: Microbial life on surfaces. *Emerg. Infect. Dis.*, 9: pp.891-890 (2002).
- [91] Probst J, Gbureck U, Thull R: Binary nitride and oxynitride PVD coatings on Titanium for Biomedical applications., *Surface and Coatings Technology*, 148 :pp.226-33 (2001).
- [92] Binnig, G. and Quate, C. F., Atomic Force Microscope., *Phys. Rev. Lett.*, 56: p. 930 (1986).
- [93] Wiesendanger, R., Scanning probe microscopy and spectroscopy, Cambridge University press, (1994).
- [94] Fuchs, E., Oppolzer, H., Rehme, H., Particle Beam Microanalysis, Fundamentals, Methods, and Applications, (1990).
- [95] Murata, K., Matuskawa, T. and Shimizu, R., Monte Carlo Calculations on Electron Scattering in a Solid Target., *Jap. J. Appl. Phys.*, 10: p. 678 (1971).
- [96] Shimizu, R., Ikuta, T. and K. Murata, The Monte Carlo technique as applied to the fundamentals of EPMA and SEM, *J. Appl. Phys.*, 43: p.4233 (1972).
- [97] C. Richard Brundle, J. S. W., Charles A. Evans, *Encyclopedia of Materials Characterization*, Manning Publications Co. (1992).
- [98] FUCHS E., OPPOLZER H., REHME H.; Particle Beam Microanalysis
- [99] Cullity, B. D., and Stolk, S. R. *Elements of X- Ray Diffraction 3rd edition*
- [100] Iwatsu, F., Kobayashi, T. and Uyeda, N., *Phys. Chem.*, 84: p.3223 (1980).
- [101] Ohring, M., *The Materials Science of Thin Films*, Academic Press, Boston, (1992).

-
- [102] Zarie, E. S., Kaidas, V., Gedamu, D., Mishra, Y. K., Adelung, R., Furkert, F. H., Scherließ, R., Steckel, H., Schreiber, B. G., Solvent free fabrication of micro and nanostructured drug coatings by thermal evaporation for controlled release and increased effects., *PLoS ONE*,7(8):pp.40746 (2012).
- [103] Inchidjuy, P., Pukird, S., Nukeaw, J., The Effects of Substrate Temperature on Optical Properties and Surface Morphology of Nickel Phthalocyanine Thin Films Grown by Organic Evaporator System *Advanced Materials Research.*, 55–57: pp.593–596 (2008).
- [104] Burrows, P. E., Forrest, S. R., Sapochak, L. S., Schwartz, J., Fenter, P., Buma, T., Ban, V. S., Forrest, J. L., Organic vapor phase deposition: A new method for the growth of organic thin films with large optical non-linearities., *J. Cryst. Growth*, 156: pp. 91–98 (1995).
- [105] Ethayaraja, M. and Bandyopadhyaya, R., Mechanism and Modeling of Nanorod Formation from Nanodots., *Langmuir*, 23,pp. 6418-6423 (2007).
- [106] Wuttig, M., Liu, X., Ultrathin metal films: magnetic and structural properties, Springer Berlin Heidelberg, (2004).
- [107] Barth, J. V., Mobility of complex organic species at metal surfaces, *Advanced Materials and Process Engineering Laboratory Departments of Chemistry and Physics & Astronomy, University of British Columbia, Vancouver*, pp.269-286 (2006).
- [108] Jensen, P., Barabasi, A. L., Larralde, H., Havlin, S., Stanley, H. E., A Fractal Model for the First Stages of Thin Film Growth., *Fractals*, 4: pp.321-329 (1996).
- [109] Mattox, D. M., *Handbook of Physical Vapour Deposition (PVD) Processing*, Elsevier, Oxford (2nd Ed.) (2010).
- [110] Xinming, L., Yingde, C., Lloyd, A. W., Mikhalovsky, S. V., Sandeman, S. R., Howel C. A., Liewen, L., Polymeric hydrogels for novel contact lens-based ophthalmic drug delivery systems: A review., *Contact Lens and Anterior Eye.*, 31: pp.57–64 (2008).
- [111] Gratton, S. E. A., Ropp, P. A., Pohlhaus, P.D., Luft, J. C., Madden, V. J., et al. The effect of particle design on cellular internalization pathways., *Proc Natl Acad Sci U S A*,105: pp.11613–11618 (2008).
- [112] Smith, E., Dent, G., *Modern Raman Spectroscopy: A Practical Approach*
- [113] Gamberini, M. C., Baraldi, C., Tinti, A., Rustichelli, C., Ferioli, Gamberini, V. G., Solid state characterization of chloramphenicol palmitate. Raman spectroscopy applied to pharmaceutical polymorphs, *Journal of Molecular Structure*, 785: pp. 216-224 (2006).

-
- [114] Hile, D. D. and Pishko, M. V., “Solvent-free Protein encapsulation within biodegradable polymer foams,” *Drug Delivery*, 11: pp. 287–293 (2004).
- [115] Faupel, F., Thran, A., Keine, M., Strunskus, T., Zaporojtchenko, V., Behnke, K., *Diffusion of Metals in Polymers and During Metal/Polymer Interface Formation*, chapter 8, pp. 221–251, Springer-Verlag Berlin Heidelberg New York (2003).
- [116] Zaporojtchenko, V., Podschun, R., Schürmann, U., Kulkarni, A., Faupel, F., *Physico-chemical and antimicrobial properties of co-sputtered Ag-Au/PTFE nanocomposite coatings.*, *Nanotechnology* 17: pp. 4904–4908 (2006).
- [117] Sawai, J., Doi, R., Maekawa, Y., Kojima, H., *Indirect conductimetric assay of antibacterial activities.*, *J. Ind. Microbiol. Biotech.*, 29: pp.296– 298 (2002).
- [118] Akiyama, H., Yamazaki, O., Kanzaki, H., Tada, J., Arata, J., *Effect of zinc oxide on the attachment of Staphylococcus aureus.*, *J. Dermatol. Sci.* 17: pp. 67– 74(1998).
- [119] Brunet, L., Lyon, D. Y., Hotze, E. M., Alvarez, P. J. J., Wiesner, M., “Comparative photoactivity and antibacterial properties of C60 fullerenes and titanium dioxide nanoparticles”., *Environ. Sci. Technol.*, 43: pp. 4355–4360(2009).
- [120] Zvekić, D., Srđić, V. V., Karaman, M. A., Matavulj, M. N., *Antimicrobial properties of ZnO nanoparticles incorporated in polyurethane varnish.*, *Processing and Application of Ceramics* 5 [1]:pp. 41–45 (2011).
- [121] Mishra, Y. K., Adelung, R., Röhl, C., Frank Spors, D. S., Tiwari, V., *Virostatic potential of micro–nano filopodia-like ZnO structures against herpes simplex virus-1.*, *Antiviral Research*, 92: pp. 305–312(2011).
- [122] He, X. X., Wu, X., Wang, K. M., Shi, B. H., Hai, L., *Methylene blue-encapsulated phosphonate-terminated silica nanoparticles for simultaneous in vivo imaging and photodynamic therapy.* *Biomaterials*, 30:pp.5601-9 (2009).
- [123] Zhang, H., Chen, B., Jiang, H., Wang, C., Wang, H., Wang, X., *A strategy for ZnO nanorod mediated multi-mode cancer treatment* , *Biomaterials*, 32: pp1906-1914 (2011).
- [124] Seil, J. T., and Webster, T. J., *Decreased astroglial cell adhesion and proliferation on zinc oxide nanoparticle polyurethane composites*, *International Journal of Nanomedicine*, 3(4): pp.523–531(2008).
- [125] Katz, H. E., Huang, J. *Thin-Film Organic Electronic Devices.*, *Annu Rev Mater Res.*, 39: pp.71–92 (2009).
- [126] Urban, G. A., *Micro- and nanobiosensors–state of the art and trends.*, *Meas Sci Technol* 20: 012001 (2009).

[127] Behari, J., Guha, S. k., and Agarwal, P. N., The effect of ultraviolet radiation of the electrical conductivity of human bone., *Calcif. Tiss. Res.*, 19: pp 223-227 (**1975**).

[128] Gangarosa , L. P., Park, N. H., Fong, B. C., Scott, D. F., and Hill, J. M., Conductivity of drugs used for Iontophoresis., *Journal of pharmaceutical sciences*, 67(10): p.1439 (**1978**).

[129] Persson, L. G., Lekholm, U., Leonhardt, A., Dahlén, G., Lindhe, J., Bacterial colonization on internal surfaces of Brånemark system implant components., *Clin Oral Implants Res.* Jun;7(2): pp.90-5 (**1996**).

[130] Gulsen, D. and Chauhan, A., Ophthalmic Drug Delivery through Contact Lenses., *invest. Ophthalmol. Vis. Sci.*, July 45(7): pp.2342-2347 (**2004**).